R-758 NASA CR-112311

AEROSOL PHYSICAL PROPERTIES FROM SATELLITE HORIZON INVERSION

BY
Carlton R. Gray, Harvey L. Malchow, Dennis C. Merritt,
Robert E. Var, and Cynthia K. Whitney

MASSACHUSETTS INSTITUTE OF TECHNOLOGY
DEPARTMENT OF METEOROLOGY
AND
CHARLES S. DRAPER LABORATORY, INC.

FINAL REPORT
CONTRACT NAS 1-11092

PREPARED FOR
NATIONAL AERONAUTICS AND SPACE ADMINISTRATION
LANGLEY RESEARCH CENTER
Hampton, Virginia 23365

JULY 1973

1. REPORT NO.	2. GOVERNMENT ACCESSION NO.	3. RECIPIENT'S CATALOGUE NO.
CR-112311		

4. TITLE AND SUBTITLE	5. REPORT DATE
Aerosol Physical Properties from Satellite Horizon Inversion	JULY 1973
	6. PERFORMING ORGANIZATION CODE: DSR–73734
7. AUTHOR(S): C.R. Gray, H.L. Malchow, D.C. Merritt, R.E. Var, and C.K. Whitney	8. PERFORMING ORGANIZATION REPORT NO.: AER–24–F
	10. WORK UNIT NO.
9. PERFORMING ORGANIZATION NAME AND ADDRESS: Massachusetts Institute of Technology, Dept. of Meteorology and the Charles S. Draper Laboratory, Inc. Cambridge, Massachusetts	11. CONTRACT OR GRANT NO.: NAS 1–11092
12. SPONSORING AGENCY NAME AND ADDRESS: National Aeronautics and Space Administration Washington, D. C. 20546	13. TYPE OF REPORT AND PERIOD COVERED: Contractor Report
	14. SPONSORING AGENCY CODE

15. SUPPLEMENTARY NOTES

16. ABSTRACT

An investigation is made into the feasibility of determining the physical properties of aerosols globally in the altitude region of 10 to 100 km from a satellite horizon scanning experiment. The investigation utilizes a horizon inversion technique previously developed and extended herein. Aerosol physical properties such as number density, size distribution, and the real and imaginary components of the index of refraction are demonstrated to be invertible in the aerosol size ranges (0.01–0.1μ), (0.1–1.0μ), (1.0–10μ). Extensions of previously developed radiative transfer models and recursive inversion algorithms are displayed.

17. KEY WORDS [SUGGESTED BY AUTHOR(S)]	18. DISTRIBUTION STATEMENT
Aerosols, Ozone, Horizon Inversion, Remote Sensing, Scattering	Unclassified – unlimited

19. SECURITY CLASSIF. (OF THIS REPORT)	20. SECURITY CLASSIF. (OF THIS PAGE)	21. NO. OF PAGES
Unclassified	Unclassified	211

TABLE OF CONTENTS

TABLE OF CONTENTS (Cont)

1.0 INTRODUCTION

This report represents an extension and refinement of programs and techniques developed for determining the vertical distributions of various atmospheric constituents (aerosols, ozone, and neutral atmospheric density i.e. Rayleigh scattering air molecules) from radiance measurements of the earth's horizon (Newell and Gray, 1972). Surveyed in the previously reported study were the techniques required for determining selected constituent distributions and the observability conditions and instrument characteristics necessary for the successful measurement inversion. This report extends the radiance inversion technique to the determination of aerosol physical characteristic distributions. In the previous study stratospheric aerosols were found to exhibit gross extinction features so that they could be observed by the proposed technique. Because of increasing interest in these particles as products of various pollution sources, it was decided to investigate further (Gray et al, 1972) the potential of the horizon inversion technique for determining other physical characteristics of the stratospheric and mesospheric aerosols besides total extinction. Thus an analysis of the capability of the technique to deduce information about the particulate size distribution and index of refraction was undertaken.

These investigations were centered around the refinement and extended development of the techniques previously employed. Here the state vector in the inversion computer code was extended to include the desired aerosol characteristics. The radiative transfer simulation was refined to include arbitrary (noncoplanar) azimuth angles and opaque (thick) clouds. These refinements were tested for accuracy against other less efficient codes. To supplement these activities an efficient empirical aerosol model was developed from data generated by a more complex Mie code computation of the aerosol optical properties. With the empirical aerosol model, quantities such as the partial derivatives of the angular scattering function with respect to the real part of the index of refraction can be easily computed. These refined techniques and aerosol models were then used to simulate an aerosol inversion procedure for obtaining the vertical distributions of aerosols and their gross physical properties.

The measurement technique used here is to scan the earth's sunlit horizon as shown in Figure 1.0-1 with a multiwavelength photometer and to record the radiant intensities measured at a predetermined sequence of angular positions. These measured intensities are then processed as shown in the flow chart Figure 1.0-2.

The estimation procedure begins with an input of the geometry which includes primarily the sun direction and the measurement platform altitude. The geometric data along with an a priori estimate of the atmospheric state (constituent densities and aerosol characteristics) is used to compute a theoretical prediction of the intensity profile and its partial derivatives with respect to state elements. This is done with a radiative transfer simulation for the first selected wavelength and scan angle. The theoretical partial derivatives, theoretical intensities, and the measured intensity are then fed to the filter equations where an optimal estimate of the atmospheric state is produced based upon the difference between measured and predicted intensities, the state covariance, and the measurement noise. The optimal state estimate is then fed back through the intensity calculations and a new intensity is computed and compared to the next measurement. The loop continues until all wavelength channels and scan angles have been sampled. The result is an optimal estimate, in a minimum variance sense, of the atmospheric state including aerosol number density, size distribution parameters, and index of refraction.

Section 2 of the report discusses the aerosol inversion capability of the scattered sunlight experiment, stellar occultation inversion, and radiance effects from a horizon profile parameter study. The aerosol inversion simulations show the relative invertability of the various aerosol characteristics under a range of conditions including different altitudes and assumed a priori uncertainties. The efficacies of several wavelength bands are compared. Three aerosol size ranges are considered, (0.01-0.1μ), (0.1-1.0μ) and (1.0-10μ). The effects of changes in variables such as season, latitude, satellite altitude, solar zenith and azimuth angles, and albedo on horizon profiles are investigated.

Section 3 details the filter and radiative transfer model development and inversion procedure refinement work that was carried out to make aerosol inversion possible. Included are discussions of the augmented state filter, the refined radiative transfer simulation, and the empirical aerosol models.

Section 4 provides a review of our conclusions and recommendations on the invertibility of aerosols, model development and satellite data requirements.

Section 5 appends supplementary information.

Appendix 1. A parameter study of horizon profile intensity variability as a function of season, latitude, albedo, sun azimuths, and zenith and wavelength is illustrated.

Appendix 2. The regression formulation of the aerosol model used for the size ranges (0.01-0.1μ), (0.1-1.0μ) and (1.0-10.0μ).

Appendix 3. The multiple scattering code C.K.W. is discussed.

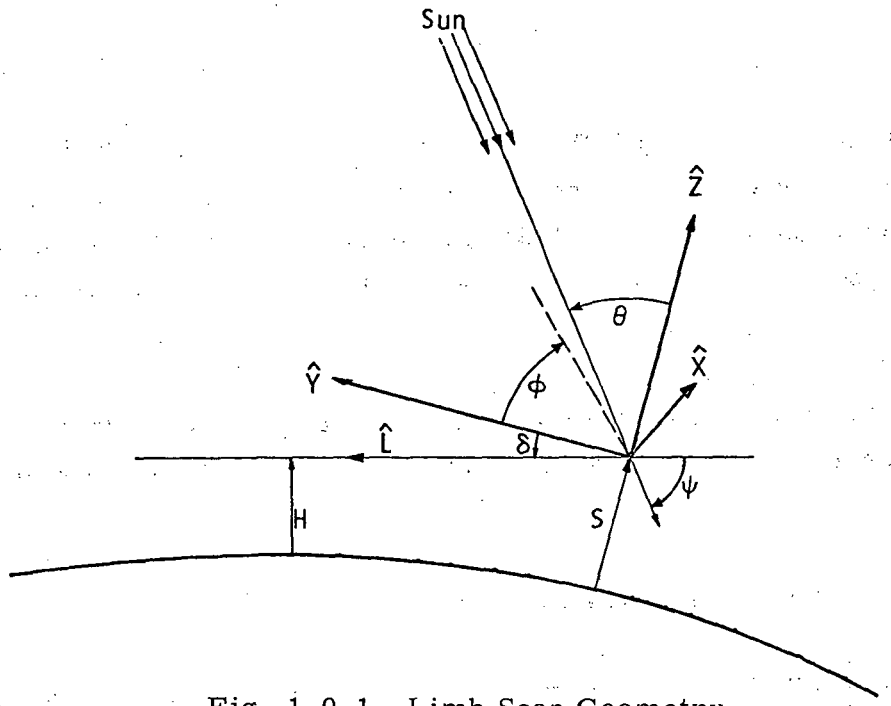

Fig. 1.0-1 Limb Scan Geometry

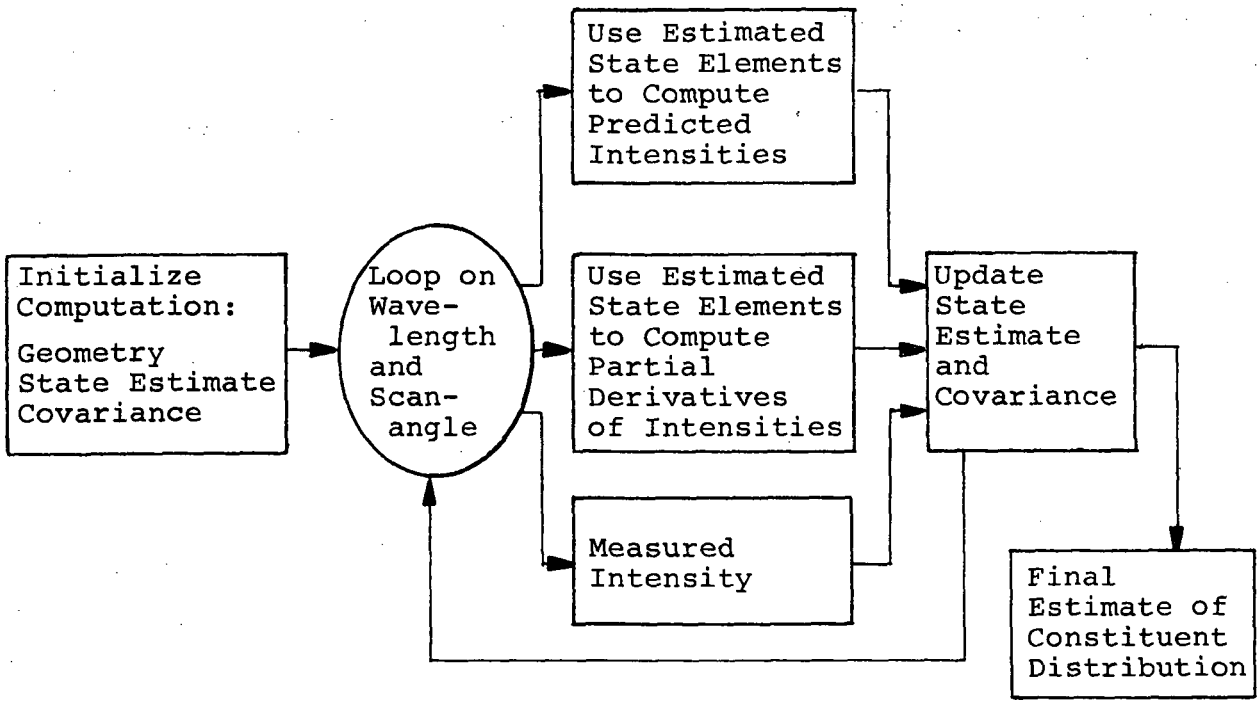

Fig. 1.0-2 Atmospheric Data Inversion Procedure

REFERENCES

SECTION 1

1) Gray, C. R., H. L. Malchow, D. C. Merritt, and R. E. Var, "Aerosol Monitoring by Satellite Horizon Scanning", J. Spacecr. Rockets, 10, 71-76, January, 1973.

2) Newell, R. E., and C. R. Gray, "Meteorological and Ecological Monitoring of the Stratosphere and Mesosphere", NASA Contractor Report, NASA CR-2094, August, 1972.

2.0 RADIANCE INVERSION AND SIMULATION

2.1 AEROSOLS – IMPLICATIONS OF INVERSION

2.1.1 Introduction

Using a Kalman-Bucy filter to invert horizon profile data produces both an estimate of the atmospheric state and a covariance matrix describing the accuracy of the estimates. By propagating the covariance matrix through a proposed measurement schedule it is possible to predetermine which parameters will or will not be affected by the measurements, and what linear combinations of parameters will be well known. A function called sensitivity has been defined which is a measure of the amount of information obtained about a particular state element in a measurement. The sensitivity curves are computed very rapidly, but fail to predict quantitatively the final variances and covariances of the parameters which are obtained by a covariance propagation. They do, however, qualitatively predict which parameters will have small variances at the end of a measurement schedule, and so they are used extensively in the following discussion.

A sensitivity analysis was applied to the problem of determining which aerosol parameters are observable from a horizon scan experiment. It has been demonstrated (Newell and Gray, 1972) that aerosol extinction per unit volume is readily recovered from limb scan data at all altitudes between 10 and 85 km with an idealized instrument having a noise value of 10^{-3} times the maximum horizon signal and between 10 and 100 km for a noise value of 10^{-4}. The sensitivity study, therefore, is aimed at determining the observability of four different parameters, namely aerosol number density (ρ), size distribution parameter (α), real index of refraction (n), and imaginary (complex) index of refraction (n'). The size distribution parameter (α) is the radius exponent where the power law size distribution is of the form $n(r) = Ar^{-\alpha}$. The results are broken into three groups representing three assumed aerosol size ranges: 0.01-0.1μ, 0.1-1.0μ, and 1.0-10μ. For these size ranges solar zenith angles were varied from $+60^{\circ}$

to -30^{o} with resulting scattering angles varying from approximately 50^{o} to 140^{o}. Constituent results based on these variable conditions are developed in Figures 2.1-1 to 2.1-12. Analysis shows how the invertability of the parameters is affected by 1) the geometry 2) the instrument noise, and 3) the statistics of the initial estimates of the aerosol parameters. This analysis was conducted for spherical aerosols and nonspherical aerosol shape factors which have a spherical equivalent.

2.1.2 (0.1-1.0μ) Aerosol Inversion Simulations

For this aerosol size range (0.1-1.0μ), as is also the case for the other size ranges, the aerosol number density is initially adjusted so that extinction at 5500 A is equal to the extinction used as the standard state (Newell and Gray, 1972) based on Elterman, 1966 and 1970, given the initial estimate that $\alpha = 3$, $n = 1.5$, and $n' = 0$. Because of the proportionality between extinction and cross section for a given number density there will be an increased number density for the (0.01-0.1μ) range over the (0.1-1.0μ) range and conversely a decrease for the (1.0-10μ) range. For the range (0.1-1.0μ) the number density runs from approximately 10^{3} /cm^{3} at ground to 10^{-5} /cm^{3} at 100 km.

For all of the three aerosol size ranges the instrument white noise was assumed to be 10^{-7} μwatts/cm^{2} (RMS). It has been shown previously (Newell and Gray, 1972) that varying the noise simply varies the maximum altitude from which information can be retrieved. The maximum useful altitude can be approximated by observing the intensity versus altitude curves of Section 2.3 and noting at what altitude the intensity reaches the noise level i.e. S/N = 1. At a few kilometers above this point the initial estimates of constituents are as good as the filtered values and no significant changes are affected in the estimates.

Sensitivity curves were produced for a number of different scattering angles and wavelengths with an instrument having a finite field of view. Sensitivity is a function derived from the filter equations, which indicates

the relative information content from constituent to constituent and altitude to altitude for every measurement condition i.e. (wavelength and tangent height). Given a measurement, the information content for a particular constituent and altitude (state element) is reflected in a decrease in the variance associated with that element and it is natural to look at the covariance update equation for the definition of sensitivity:

$$P(m+1) = P(m) - K(m+1)B(m+1)P(m) \qquad (2.1\text{-}1)$$

the term of interest here is K(m+1)B(m+1)P(m), which is the decrease in the covariance for a particular measurement condition. Normalizing by P(m) yields the sensitivity matrix K(m+1)B(m+1). Of particular interest in the sensitivity matrix are the diagonal elements which indicate the relative decrease in variance of the elements of the state vector. To isolate the effects of the measurement vector on the sensitivity, the covariance is assumed to maintain its initial value. With this assumption the sensitivity of the jth element of the state vector is

$$s_j(m) = \left(\frac{\partial h(x,m)}{\partial x_j}\right)^2 P_{jj} \Bigg/ \left[\left(\sum_i \left(\frac{\partial h(x,m)}{\partial x_i}\right)^2 P_{ii}\right) + R\right] \qquad 2.1\text{-}2$$

In choosing an instrument's wavelengths it is desirable to have as many linearly independent measurements as possible. That is, each measurement should be sensitive to a different combination of parameters. The functions which relate extinction and phase function to aerosol parameters change slowly with respect to wavelength. For this reason a wide spread of wavelengths over the region 2500 to 7000 A is best suited for the inversion (see Figure 2.1-1 or 2.1-4). Thus the wavelengths 3000, 4000, 5000, 6000, and 7000 A, which span the visible region with a minimum of wavelength channels necessary for the inversion, have been arbitrarily selected as working values. In this case the actual wavelengths chosen are not as important as the separation between the wavelengths and in an actual experiment more wavelengths would be run for greater accuracy.

The total scattered sunlight radiance at the horizon is a composite of the radiance contributed by aerosols and Rayleigh scatterers. For each scattering constituent the radiance contribution is proportional to the product of its scattering cross section and angular scattering function (phase function). If the scattering cross sections for both aerosol and Rayleigh scatterers are equal then the relative contribution of each constituent to the horizon radiance depends only upon the relative values of the phase functions at a given scattering angle. For most scattering angles away from the forward region the aerosol phase function will be smaller than the Rayleigh function thus reducing the relative contribution of aerosols to the radiance, however this effect can be partly offset by an increase in the relative scattering cross section of aerosols at longer wavelengths.

Both the effects of changes in wavelength on cross section and changes in scattering angle on the phase function can be observed by examining the sensitivity curves of Figures 2.1-2 and 2.1-4. In Figure 2.1-2 it can be seen that the aerosol number density sensitivity "AEROSOL" increases at longer wavelengths while the "NEUTRAL" molecule scattering decreases. This is the cross-section effect. Figure 2.1-4 differs only by a change in solar zenith from Figure 2.1-2. The scattering angle for Figure 2.1-4 is less favorable (i.e. less forward, $\approx 110^{\circ}$ versus $\approx 50^{\circ}$) for aerosols. Therefore, the aerosol sensitivity is lowered relative to Figure 2.1-2 while the neutral molecule scattering sensitivity increases.

The most serious problem encountered is in the uncertainty of the initial statistics associated with the initial estimate. The updating of estimates by the filter inversion routine depends in part on the RMS values of the initial estimate. If a parameter is well known it will not receive much of an update and its variance will decrease relatively slowly. This is particularly critical in the case of the aerosol parameters where there is a large sensitivity to aerosol extinction per unit volume, however, the particular aerosol parameters which receive these updates are determined partly by their initial variances.

Sensitivity computations in the (0.1-1.0μ) size range were made with initial RMS error values of 600% for (ρ), 1 for (α), 0.05 for (n), and 0.005 for (n') along with realistic estimates of neutral density and ozone (Malchow, 1971) RMS values as a function of altitude (Figure 2.1-3). Curves run with these values showed a large sensitivity to aerosol number density and only a small additional sensitivity to (n') below 30 km. Other runs with 100% RMS error on (ρ) (Figure 2.1-1) showed all parameters except (n) to be readily observable at all altitudes. Thus varying the initial RMS estimates varies the final RMS estimates and the sensitivity, and until realistic data are collected about these parameters the covariance matrices associated with the parameter estimates will be unreliable.

The sensitivity curves indicate a potential problem with regard to observability. Since the wavelength dependence of sensitivity is basically the same for both number density(ρ) "AEROSOL" and size distribution(α) "ALPHA" there is the possibility that no two measurements are linearly independent in these two parameters, therefore making it impossible to estimate either in one. This similarity in wavelength dependence occurs because increasing either (α) or (ρ) has the effect of lowering the wavelength dependence of the total received signal by increasing the effective aerosol to Rayleigh scattering ratio. A complete propagation of the covariance matrix was made to determine if this was the case. The results indeed showed a high correlation (0.6 to 0.8) between the two parameters but also showed a significant factor of five decrease in variance for both parameters in a coarse inversion (only three wavelengths and a four kilometer separation of tangent heights). The final variances were $\sigma_\alpha = \pm 0.2$ and $\sigma_\rho = \pm 20\%$ which indicates that the two quantities are separable and observable.

Covariance propagations were performed for each of the particle size ranges. The results of these propagations show numerically how the initially assumed variances of the aerosol parameters are reduced by the information gained in a measurement sequence.

Initial values of the aerosol parameter RMS uncertainties were chosen to reflect the range of values occurring in the literature (Newell and Gray, 1972, and Malchow, 1971). Number density (ρ) was assumed to vary over one order of magnitude $\pm 3\sigma$, thus the σ_ρ used was 166%. This is consistent with the large observed variations in the number density of stratospheric aerosols related to volcanic activity. The size parameter (α) was assumed to cover the entire observed range $0<\alpha<6$, thus $\sigma_\alpha = 1$. The real part of the index of refraction ranges from that of water (1.33) to fused silica (1.65) thus yielding a $\pm 3\sigma$ range of 0.32 and a σ_n of 0.05. Finally the complex part of the index of refraction was assumed to be as large as 0.015 ($+3\sigma$) which is felt to be conservative (Volz, 1973) with a $\sigma_{n'}$ value of 0.005. Both the real and complex parts of the index of refraction are assumed to be wavelength independent. All initial RMS values are assumed constant with altitude.

Figure 2.1-13 shows graphically the reduction in RMS uncertainty resulting from a covariance propagation for the (0.1-1.0μ) particle size range. The solid line indicates the assumed initial value of a particular quantity, and the error bars show the final RMS uncertainty. Numerical values corresponding to the error bars are listed in Table 2.1-1. Considerable reduction of the number density uncertainty occurs for all altitudes although it is especially prominent at 10 and 20 km where the aerosol turbidity is at a maximum. A similar pattern of error reduction is displayed for the size parameter (α). Uncertainty in the complex part of the index of refraction is reduced, however, the improvement is not as striking as in the case of the other parameters. In general the covariance propagation for this size range shows that substantial reductions in the initial uncertainties of aerosol number density, imaginary index, and size parameters are effected by the inversion. The uncertainty in the real part of the index of refraction is however reduced only slightly. This result is consistent with the sensitivity curves in Figures 2.1-1 and 2.1-2 which show little sensitivity to the real index of refraction at any altitude.

2.1.3 (0.01-0.1μ) Aerosol Inversion Simulations

The aerosol number density was adjusted to preserve the standard extinction versus altitude curve for 5500 A with α = 3, n = 1.5, and n' = 0. For this range the density varied from $1.4 \times 10^{7}/cm^{3}$ at the ground to 5.5×10^{-2} $/cm^{3}$ at 100 km. Since the phase function for this size range varies less with angle than in the (0.1-1.0μ) range only a few zenith angles were run. The results of these runs show that the constituent sensitivities did not significantly change with zenith angle (see Figures 2.1-6 and 2.1-7).

The most notable difference between this size range and the two others is the lack of sensitivity to (n'). For these small particles only number density and the size distribution parameter (α) are observable because the partial derivatives of the scattering phase function with respect to (n) and (n') for this size range are near zero. A change from 300% to 100% uncertainty in number density enhances the (α) sensitivity rather than increasing (n') sensitivity (see Figure 2.1-6 and 2.1-5 respectively).

Analysis of the two sensitivity curves for (ρ) and (α) indicates a potential problem in distinguishing between the two parameters. The fact that the sensitivities for both parameters have the same wavelength dependence implies that the measurement equations at different wavelengths are not totally linearly independent (see Figure 2.1-8). However a coarse covariance propagation was run (five wavelengths and four kilometer tangent height separation) which indicates that the two are separable. The correlations were indeed high (0.6 to 0.8) between the parameters but there is a factor of two decrease in number density variance and a factor of ten decrease in size distribution variance from the initial values.

The two parameters (ρ and α) are highly observable from 10 to 100 km or until instrument noise becomes dominant. Typically an instrument noise of 10^{-3} times the maximum horizon signal restricts the altitude sensitivity range to 85 km while a noise value of 10^{-4} extends the altitude sensitivity to approximately 100 km. Thus the interference that comes

about from increased uncertainties in neutral density at higher altitudes does not reduce the observability of the two aerosol parameters significantly.

Figure 2.1-14 illustrates the RMS error reduction for the particles in this size range. The numerical values are listed in Table 2.1-II. The results are generally similar to those obtained for the (0.1-1.0μ) size range except that there is a smaller reduction of the number density uncertainty. Somewhat surprising, in view of the near zero sensitivity for (n') shown in Figure 2.1-6, is the substantial reduction of the uncertainty in (n') after a covariance propagation. This indicates that the factor causing the error reduction is a buildup of correlations between (n') and the other parameters as opposed to a partial derivative effect which dominates the sensitivity results. When the sensitivity and covariance propagation results differ significantly as in this case it is important to consider the differences between the abbreviated covariance propagation used to produce these working numbers and a real covariance propagation used in an actual inversion. To insure the ultimate convergence of the state vector estimate it is often required to reduce the covariance update by means of a numerical multiplier. This results in a smaller reduction of the initial covariance after a given number of reiterative updates than would be indicated by the unweighted propagation used here.

2.1.4 (1.0-10μ) Aerosol Inversion Simulations

The large particles in this range are the furthest from Rayleigh in their scattering properties, i.e., in their cross-section wavelength dependence and in the shape of their phase function. Because of their large cross section the number density is low, running from 23.4 /cm^3 at the ground to 7.7×10^{-8}/cm^3 at 100 km.

The great difference between these particles and other atmospheric constituents makes them the most readily inverted of all size ranges. It is possible to invert all four aerosol parameters from a given horizon scan when the phase function is not minimized by an unfavorable scattering angle

i.e. sun angle. Although the four sensitivities are reasonably close, results from the previous size ranges indicate that all four physical characteristics are separable. Variable scattering angles are readily obtainable for nearly all conceivable orbits from equatorial to polar orbits with the exception of the 600 and 1800 local hour angle near polar-orbits.

There is, however, a problem with this size range that does not appear in the other ranges. That is, when the scattering angle approaches 110^{o}, the phase function is so small that the aerosol energy contribution and respective sensitivities drop drastically and only number desity is highly invertible from the data (Figure 2.1-12). The variations in sensitivity with changing solar angle can be clearly seen in Figures 2.1-9 through 2.1-12.

Covariance propagation results for the large particles are shown in Figure 2.1-15 and the corresponding numerical values are listed in Table 2.1-II. In the case of the large particles all the parameter uncertainties are substantially reduced including the real part of the index of refraction which was essentially unaffected for the other particle size ranges.

2.1.5 Modeling Errors

With the standard filter approach to the inversion problem it is theoretically possible to drive the variances on all the parameters as close to zero as desired by taking enough measurements. However, since there are inherent errors in the radiative transfer modeling a near perfect variance is unrealistic. The purpose of this section is to determine the effects of aerosol modeling errors on the final accuracy obtainable in an inversion. This is done by computing the vectors $(k, \Delta x)$ and the scalar (ΔI) in the equation $\Delta x = k\,(\Delta I)$ where Δx is the state error, (k) is the filter gain, and ΔI is the intensity error.

The results are presented in sets of tables. The first table of each set (Table 2.1-IV) illustrates the gain (k) which is used to compute errors in the state given errors in intensity. This is done with a geometry having

a zenith angle = 30^{o} and an azimuth angle = 0^{o} for all size ranges, with standard initial errors (see section 2.1.2), and using a 300% initial uncertainty in aerosol number density. The additional tables of each set are the computed state error Δx for errors in the albedo and aerosol models and for an instrument bias. The state errors are based upon the gain (k) of the first table.

It is important to realize that the initial uncertainties are important in the propagation of error. For example, a parameter which has both a large partial derivative and a large initial uncertainty will receive a large update and become more in error by inaccurate models than a parameter with a small initial variance and partial derivative. The numbers given represent the maximum error that will occur in an inversion using 3000, 4000, 5500, and 7000 A as wavelength channels. It should be noted that the (k) values for 3000 A at 20 and 40 km, and for 4000 A at 20 km are set equal to zero. This is because these wavelengths are saturated at the designated altitudes and therefore yield no information about the densities.

Tables 2.1 -V, VI, IX, X, XV, and XVI list the errors in the state vector elements produced by errors in the aerosol extinction and phase function models. The model errors used here are representative of the errors associated with the aerosol models presented in Section 3.3 of this report. Tables 2.1 -V, VI list the state errors for aerosols in the (0.01-0.1μ) size range. The modeling errors for this size range are small ($\approx$2% in extinction and $\approx$5% in phase function) and consequently the effects on the state are also small. The largest resulting error is due to the phase function error, and is a 12.3% error in the particle number density at 60 km as shown in the fourth column of Table 2.1 -VI.

The (0.1-1.0μ) particle size range has larger associated errors and consequently larger effects on the state. Tables 2.1 -IX, X list the state errors associated with this size range. As with the smaller size range, the phase function error (10%) produces larger state errors than the extinction error (5%). The largest error induced is in the aerosol number

density at 60 km, and is 26%. This error is still small compared to the assumed initial number density uncertainty of 300%, and is less than the 60% uncertainty obtained after a coarse covariance propagation.

For the large particle range the state errors are presented in Tables 2.1 -XV, XVI. Again the number density estimates are primarily affected, and the errors are comparable to the final state estimates obtained via a covariance propagation.

Table 2.1 -XII shows the effects of the assumption of the wrong size range for aerosols, i.e., the table shows what errors result if the size range is assumed to be (0.1-1.0μ) whereas the actual size range is (.01-0.1μ). The resulting errors are large as expected since the extinctions differ by two orders of magnitude for the two size ranges. Aerosol number density is shown to be in error by one order of magnitude or $\approx$ 1000% at 40 km. Other state elements are also strongly affected. The neutral density estimate is in error by 52% at 80 km, and the ozone density by 242% at 60 km. Errors in the other aerosol parameters are significant though not large (these are given in absolute units). At 40 km, the error in (α) approaches one which represents a significant alteration of the size distribution. The results of this size range shift emphasize the importance of either knowing rather accurately the particle size limits, or expanding the state vector to include these limits.

Table 2.1 -XIII shows the effects of the introduction of a 10% instrument bias error in each wavelength channel. The error induced in the aerosol number density is moderately large because the signal contribution by the aerosol to the total signal is small. Since the aerosol number density uncertainty is large, the filter attempts to correct the signal error by adjusting mainly the aerosol number density.

Finally, Tables 2.1 -VII, XI, and XVII show the effects on the state of the introduction of an unestimated effective surface albedo deviation from the expected value. The effect of an albedo uncertainty is similar to the

effect of an instrument bias, i.e., there is a broad-band shift in the measured intensity away from the expected value. Since aerosol density is assumed to have a relatively large initial uncertainty, it is this quantity which is mainly adjusted to account for the intensity shift. The amount of adjustment done to the aerosol number density is inversely proportional to the contribution that the aerosol makes to the total intensity. Error values in Table 2.1 -VII, XI, and XVII are based upon a scattering angle that coincides with the minimum in the angular scattering functions for the medium and large-sized particles.

Thus these aerosols are making a minimal contribution to the total intensity at the receiver, and therefore the errors related to an uncertain albedo are maximized. Tables 2.1 -VII, XI, and XVII illustrate this effect dramatically. Each aerosol size range is defined to have the same extinction. As the particle size increases, the scattering phase function decreases (at the chosen sun angle) and the error increases rapidly for the same extinction in each size range. There are two implications of these results. One is that the albedo should be added to the state vector and estimated to minimize its uncertainty. The other implication is that the solar scattering angle for primary radiation should be chosen to minimize the effect of albedo uncertainties. At more desirable scattering angles the large particle errors (Table 2.1 -XVII) are substantially reduced, and are comparable to the small particle errors (Table 2.1 -VII). For example, the 1160% error in number density for large particles at a scattering angle of 80° (Table 2.1 -XVII, 40 km) is reduced to 60% when the scattering angle is changed to 30°.

	Initial RMS Error	FINAL RMS ERROR					
		0km	10km	20km	30km	40km	50km
ρ	166%	26%	9%	6%	13%	31%	20%
α	1.0	0.143	0.065	0.060	0.244	0.276	0.200
n	0.05	0.048	0.044	0.043	0.044	0.010	0.038
n'	0.005	0.003	0.002	0.001	0.001	0.001	0.002

Table 2.1-I. RMS Uncertainties From Covariance Propagation with Five Wavelengths, 0.1 to 1.0μ Particle Size Range.

	Initial RMS Error	FINAL RMS ERROR					
		0km	10km	20km	30km	40km	50km
ρ	166%	46%	30%	27%	25%	25%	46%
α	1.0	0.064	0.058	0.049	0.036	0.045	0.241
n	0.05	0.047	0.045	0.040	0.045	0.046	0.048
n'	0.005	0.002	0.002	0.001	0.001	0.001	0.002

Table 2.1-II. RMS Uncertainties From Covariance Propagation with Five Wavelengths, 0.01-0.1μ Particle Size Range.

	Initial RMS Error	FINAL RMS ERROR					
		0km	10km	20km	30km	40km	50km
ρ	166%	22%	25%	10%	24%	26%	28%
α	1.0%	0.235	0.253	0.072	0.053	0.035	0.657
n	0.05	0.04	0.018	0.011	0.025	0.026	0.024
n'	0.005	0.002	0.001	0.001	0.001	0.001	0.001

Table 2.1-III. RMS Uncertainties From Covariance Propagation with Five Wavelengths, 1.0-10μ Particle Size Range.

TABLE 2.1-IV

FILTER GAIN (k) FOR (0.01-0.1μ) AEROSOL SIZE RANGE

Zenith Angle 30°, Azimuth = 0°

Alt.	λ	Number Density (/cm^3)			Aerosol Parameters		
(km)	(Å)	Neutral	Ozone	Aerosol	α	n	n'
20	3000	0.00E 0	0.00E 0	0.00E 0	0.00E 0	0.00E 0	0.00E 0
20	4000	0.00E 0	0.00E 0	0.00E 0	0.00E 0	0.00E 0	0.00E 0
20	5500	3.22E 14	-5.36E 9	1.22E 5	-6.44E- 1	4.47E- 3	-7.90E- 6
20	7000	3.93E 14	-9.05E 8	1.66E 5	-8.89E- 1	6.10E- 3	4.25E- 5
40	3000	0.00E 0	0.00E 0	0.00E 0	0.00E 0	0.00E 0	0.00E 0
40	4000	8.19E 15	-1.62E 8	2.05E 4	-9.53E 0	6.66E- 2	-7.84E- 6
40	5500	1.42E 16	-5.23E 11	4.88E 4	-2.31E 1	1.80E- 1	8.37E- 5
40	7000	3.24E 16	-1.81E 11	1.24E 5	-5.95E 1	4.09E- 1	4.15E- 3
60	3000	9.69E 16	-1.48E 12	2.68E 4	-2.14E 2	1.50E 0	-3.01E- 4
60	4000	4.33E 16	-4.72E 7	1.92E 4	-1.58E 2	1.10E 0	-2.84E- 4
60	5500	7.34E 16	-1.44E 11	4.41E 4	-3.72E 2	2.58E 0	6.90E- 4
60	7000	1.82E 17	-5.10E 10	1.22E 5	-1.04E 3	7.18E 0	7.01E- 2
80	3000	1.20E 17	-1.88E 10	2.41E 4	-3.47E 3	2.44E 1	-2.59E- 4
80	4000	5.77E 16	-7.00E 5	1.86E 4	-2.74E 3	1.92E 1	-2.70E- 4
80	5500	9.90E 16	-2.16E 9	4.32E 4	-6.51E 3	4.52E 1	3.13E- 2
80	7000	2.48E 17	-7.76E 8	1.20E 5	-1.83E 4	1.26E 2	1.30E 0

TABLE 2.1-V

STATE ERROR (ΔX) FOR (0.01-0.1μ) AEROSOL SIZE RANGE

WITH A 2% EXTINCTION ERROR

Zenith Angle = 30°, Azimuth = 0°

Alt.	Number Density (percent error)			Aerosol Parameter (absolute error)		
(km)	Neutral	Ozone	Aerosol	α	n	n'
20	1.06E- 4	-2.43E- 3	2.06E 0	-3.52E- 3	2.44E- 5	1.36E- 7
40	8.17E- 3	-1.83E- 2	4.41E 0	-7.36E- 3	5.14E- 5	3.18E- 7
60	5.95E- 2	-4.79E- 1	4.92E 0	-8.21E- 3	5.75E- 5	2.82E- 7
80	6.96E- 2	-2.68E- 2	4.44E 0	-7.42E- 3	5.19E- 5	2.68E- 7

TABLE 2.1-VI

STATE ERROR (ΔX) FOR (0.01-0.1μ) AEROSOL SIZE RANGE

WITH A 5% PHASE FUNCTION ERROR

Zenith Angle = 30°, Azimuth = 0°

Alt.	Number Density (percent error)			Aerosol Parameter (absolute error)		
(km)	Neutral	Ozone	Aerosol	α	n	n'
20	4.24E- 4	-9.69E- 3	8.20E 0	-1.40E- 2	9.71E- 5	4.99E- 7
40	2.15E- 2	-5.22E- 2	1.16E 1	-1.94E- 2	1.35E- 4	1.22E- 6
60	1.50E- 1	-1.21E 0	1.23E 1	-2.07E- 2	1.44E- 4	1.26E- 6
80	1.74E- 1	-6.72E- 2	1.11E 1	-1.87E- 2	1.30E- 4	1.21E- 6

TABLE 2.1-VII

STATE ERROR (ΔX) FOR (0.01-0.1μ) AEROSOL SIZE RANGE

WITH (.1) ALBEDO ERROR FOR A CLOUD 0.5 ALBEDO AT 4KM

Zenith Angle = 30°, Azimuth = 0°

Alt.	Number Density (percent error)			Aerosol Parameter (absolute error)		
(km)	Neutral	Ozone	Aerosol	α	n	n'
20	2.25E- 3	-5.14E- 2	4.35E 1	-7.42E- 2	5.15E- 4	2.91E- 6
40	1.54E- 1	-4.70E- 1	1.03E 2	-1.78E- 1	1.22E- 3	1.24E- 5
60	8.68E- 1	-8.05E- 1	1.33E 2	-2.31E- 1	1.58E- 3	1.54E- 5
80	9.83E- 1	-4.80E- 2	1.22E 2	-2.10E- 1	1.45E- 3	1.50E- 5

TABLE 2.1-VIII

FILTER GAIN (k) FOR (0.1-1 μ) AEROSOL SIZE RANGE

Zenith Angle = 30°, Azimuth = 0°

Alt.	λ	Number Density (/cm^3)			Aerosol Parameters		
(km)	(A)	Neutral	Ozone	Aerosol	α	n	n'
20	3000	0.00E 0	0.00E 0	0.00E 0	0.00E 0	0.00E 0	0.00E 0
20	4000	0.00E 0	0.00E 0	0.00E 0	0.00E 0	0.00E 0	0.00E 0
20	5500	1.76E 15	-1.92E 10	4.06E 1	-8.54E- 1	1.13E- 2	3.54E- 3
20	7000	5.02E 14	-8.14E 8	3.12E 1	-7.57E- 1	8.89E- 3	2.52E- 3
40	3000	0.00E 0	0.00E 0	0.00E 0	0.00E 0	0.00E 0	0.00E 0
40	4000	3.19E 17	-5.00E 9	1.71E 1	-2.72E 1	3.88E- 1	1.47E- 1
40	5500	7.22E 16	-2.10E 12	1.57E 1	-2.97E 1	3.79E- 1	1.20E- 1
40	7000	3.17E 16	-1.42E 11	1.85E 1	-3.95E 1	4.49E- 1	1.32E- 1
60	3000	1.25E 18	-1.60E 13	3.16E 0	-7.50E 1	1.11E 0	5.69E- 1
60	4000	1.09E 16	-9.91E 8	1.04E 1	-2.95E 2	4.18E 0	1.66E 0
60	5500	3.54E 17	-5.80E 11	1.36E 1	-4.60E 2	5.83E 0	1.94E 0
60	7000	1.74E 17	-4.43E 10	1.80E 1	-6.85E 2	7.77E 0	2.40E 0
80	3000	1.92E 16	-2.52E 11	3.81E 0	-1.53E 3	2.21E 1	1.16E 1
80	4000	1.25E 16	-1.26E 7	8.84E 0	-4.40E 3	6.18E 1	2.55E 1
80	5500	4.55E 17	-8.34E 9	1.30E 1	-7.62E 3	9.75E 1	3.37E 1
80	7000	2.27E 17	-6.46E 8	1.74E 1	-1.18E 4	1.32E 2	4.23E 1

TABLE 2.1-IX

STATE ERROR (ΔX) FOR (0.1-1μ) AEROSOL SIZE RANGE

WITH A 5% EXTINCTION ERROR

Zenith Angle = 30°, Azimuth = 0°

Alt.	Number Density (percent error)			Aerosol Parameter (absolute error)		
(km)	Neutral	Ozone	Aerosol	α	n	n'
20	4.90E- 4	-7.55E- 3	4.56E 0	-4.74E- 3	5.59E- 5	1.62E- 5
40	8.04E- 2	-7.33E- 2	9.90E 0	-1.03E- 2	1.17E- 4	3.53E- 5
60	2.36E- 1	-8.74E- 1	1.04E 1	-1.09E- 2	1.24E- 4	3.83E- 5
80	2.32E- 1	-8.16E- 2	9.42E 0	-9.86E- 3	1.10E- 4	3.53E- 5

TABLE 2.1-X

STATE ERROR (ΔX) FOR (0.1-1μ) AEROSOL SIZE RANGE

WITH A 10%PHASE FUNCTION ERROR

Zenith Angle = 30°, Azimuth = 0°

Alt.	Number Density (percent error)			Aerosol Parameter (absolute error)		
(km)	Neutral	Ozone	Aerosol	α	n	n'
20	2.13E- 3	-3.20E- 2	1.84E 1	-1.70E- 2	2.26E- 4	7.07E- 5
40	2.65E- 1	-1.94E- 1	2.50E 1	-2.54E- 2	2.94E- 4	9.52E- 5
60	7.92E- 1	-1.79E 0	2.62E 1	-2.74E- 2	3.11E- 4	1.01E- 4
80	7.70E- 1	-1.23E- 1	2.35E 1	-2.46E- 2	2.78E- 4	9.19E- 5

TABLE 2.1- XI

STATE ERROR (ΔX) FOR (0.1-1μ) AEROSOL SIZE RANGE

WITH (.1) ALBEDO ERROR FOR A CLOUD 0.5 ALBEDO AT 4KM

Zenith Angle = 30°, Azimuth = 0°

Alt.	Number Density (percent error)			Aerosol Parameter (absolute error)		
(km)	Neutral	Ozone	Aerosol	α	n	n'
20	1.23E- 2	-1.85E- 1	1.06E 2	-9.88E- 2	1.31E- 3	4.09E- 4
40	6.23E 0	-1.89E 0	5.31E 2	-4.12E- 1	5.88E- 3	2.23E- 3
60	2.35E 1	-3.24E 0	4.66E 2	-3.63E- 1	5.13E- 3	2.04E- 3
80	2.29E 1	-1.84E- 1	3.67E 2	-2.86E- 1	3.96E- 3	1.63E- 3

TABLE 2.1-XII

STATE ERROR (ΔX) FOR (0.1-1μ) AEROSOL SIZE RANGE
WITH (0.01-0.1μ) AEROSOL CHARACTERISTICS UTILIZED
Zenith Angle = 30°, Azimuth = 0°

Alt.	Number Density (percent error)			Aerosol Parameter (absolute error)		
(km)	Neutral	Ozone	Aerosol	α	n	n'
20	2.49E- 2	-3.73E- 1	2.15E 2	-1.99E- 1	2.64E- 3	8.26E- 4
40	1.40E 1	-2.24E 0	1.19E 3	-9.27E- 1	1.32E- 2	5.02E- 3
60	3.61E 1	-2.42E 2	2.97E 2	-2.76E- 1	3.49E- 3	1.16E- 3
80	5.21E 1	-1.68E 1	6.35E 2	-4.96E- 1	6.86E- 3	2.83E- 3

TABLE 2.1-XIII

STATE ERROR (ΔX) FOR (0.1-1μ) AEROSOL SIZE RANGE
WITH A 10% INSTRUMENT BIAS
Zenith Angle = 30°, Azimuth = 0°

Alt.	Number Density (percent error)			Aerosol Parameter (absolute error)		
(km)	Neutral	Ozone	Aerosol	α	n	n'
20	4.42E- 3	-6.64E- 2	3.82E 1	-3.53E- 2	4.69E- 4	1.46E- 4
40	3.92E 0	-6.69E- 1	3.33E 2	-2.59E- 1	3.69E- 3	1.40E- 3
60	1.82E 1	-1.22E 2	3.00E 2	-2.33E- 1	3.30E- 3	1.31E- 3
80	2.63E 1	-8.49E 0	2.37E 2	-1.85E- 1	2.56E- 3	1.05E- 3

TABLE 2.1-XIV

FILTER GAIN (k) FOR (1-10 μ) AEROSOL SIZE RANGE

Zenith Angle = 30°, Azimuth = 0°

Alt.	λ	Number Density (/cm^3)			Aerosol Parameters		
(km)	(Å)	Neutral	Ozone	Aerosol	α	n	n'
20	3000	0.00E 0	0.00E 0	0.00E 0	0.00E 0	0.00E 0	0.00E 0
20	4000	0.00E 0	0.00E 0	0.00E 0	0.00E 0	0.00E 0	0.00E 0
20	5500	1.19E 17	-1.20E 12	4.09E 0	2.40E- 1	-2.98E- 1	-1.12E- 2
20	7000	1.35E 16	-2.12E 10	2.00E 0	-4.78E- 1	-1.05E- 1	-2.49E- 3
40	3000	0.00E 0	0.00E 0	0.00E 0	0.00E 0	0.00E 0	0.00E 0
40	4000	2.39E 18	-3.69E 10	1.80E- 1	3.14E 0	-8.30E- 1	-6.53E- 2
40	5500	2.00E 18	-5.77E 13	8.95E- 1	-2.46E 1	-4.33E 0	-1.59E- 1
40	7000	6.08E 17	-2.73E 12	1.00E 0	-3.95E 1	-4.38E 0	-8.70E- 2
60	3000	1.33E 18	-1.68E 13	2.97E- 3	5.00E 0	-2.80E- 1	-2.45E- 2
60	4000	2.48E 18	-2.21E 9	3.03E- 2	1.48E 1	-2.73E 0	-2.15E- 1
60	5500	5.10E 18	-8.26E 12	3.87E- 1	-1.64E 2	-3.42E 1	-1.30E 0
60	7000	3.19E 18	-7.98E 11	9.10E- 1	-6.01E 2	-7.07E 1	-1.49E 0
80	3000	2.05E 18	-2.66E 11	4.76E- 3	8.26E 1	-4.55E 0	-5.58E- 1
80	4000	2.44E 18	-2.43E 7	2.60E- 2	9.56E 1	-3.36E 1	-2.92E 0
80	5500	5.32E 18	-9.62E 10	3.21E- 1	-3.05E 3	-4.71E 2	-1.82E 1
80	7000	3.75E 18	-1.05E 10	8.27E- 1	-1.07E 4	-1.12E 3	-2.31E 1

TABLE 2.1-XV

STATE ERROR (ΔX) FOR (1-10μ) AEROSOL SIZE RANGE

WITH A 20%EXTINCTION ERROR

Zenith Angle = 30^{o}, Azimuth = 0^{o}

Alt.	Number Density (percent error)			Aerosol Parameter (absolute error)		
(km)	Neutral	Ozone	Aerosol	α	n	n'
20	-5.02E- 2	6.95E- 1	-5.43E 1	-1.67E- 3	2.06E- 3	7.83E- 5
40	-5.01E- 1	4.98E- 1	-1.12E 1	1.79E- 3	3.15E- 4	1.15E- 5
60	-6.21E- 1	5.28E- 1	-8.24E 0	1.14E- 3	2.38E- 4	9.10E- 6
80	-5.23E- 1	-2.70E- 2	-6.05E 0	1.05E- 3	1.62E- 4	6.29E- 6

TABLE 2.1-XVI

STATE ERROR (ΔX) FOR (1-10μ) AEROSOL SIZE RANGE

WITH A 30%PHASE FUNCTION ERROR

Zenith Angle = 30^{o}, Azimuth = 0^{o}

Alt.	Number Density (percent error)			Aerosol Parameter (absolute error)		
(km)	Neutral	Ozone	Aerosol	α	n	n'
20	6.57E- 2	-9.10E- 1	7.12E 1	-6.82E- 3	-2.71E- 3	-1.02E- 4
40	9.26E- 1	-2.44E 0	6.79E 1	-1.55E- 2	-1.72E- 3	-5.68E- 5
60	2.15E 0	-1.83E 0	6.65E 1	-1.47E- 2	-1.73E- 3	-3.67E- 5
80	1.92E 0	-8.58E- 2	5.61E 1	-1.38E- 2	-1.44E- 3	-2.98E- 5

TABLE 2.1-XVII

STATE ERROR (ΔX) FOR (1-10μ) AEROSOL SIZE RANGE

WITH (.1) ALBEDO ERROR FOR A CLOUD 0.5 ALBEDO AT 4KM

Zenith Angle = 30^{o}, Azimuth = 0^{o}

Alt.	Number Density (percent error)			Aerosol Parameter (absolute error)		
(km)	Neutral	Ozone	Aerosol	α	n	n'
20	6.35E- 1	-1.15E 1	9.05E 2	-4.91E- 2	-3.44E- 2	-1.30E- 3
40	4.67E 1	-5.19E 1	1.16E 3	-1.86E- 1	-3.28E- 2	-1.20E- 3
60	5.42E 1	-4.61E 1	7.85E 2	-1.69E- 1	-2.08E- 2	-7.94E- 4
80	4.79E 1	-2.13E 0	6.57E 2	-1.56E- 1	-1.63E- 2	-5.76E- 4

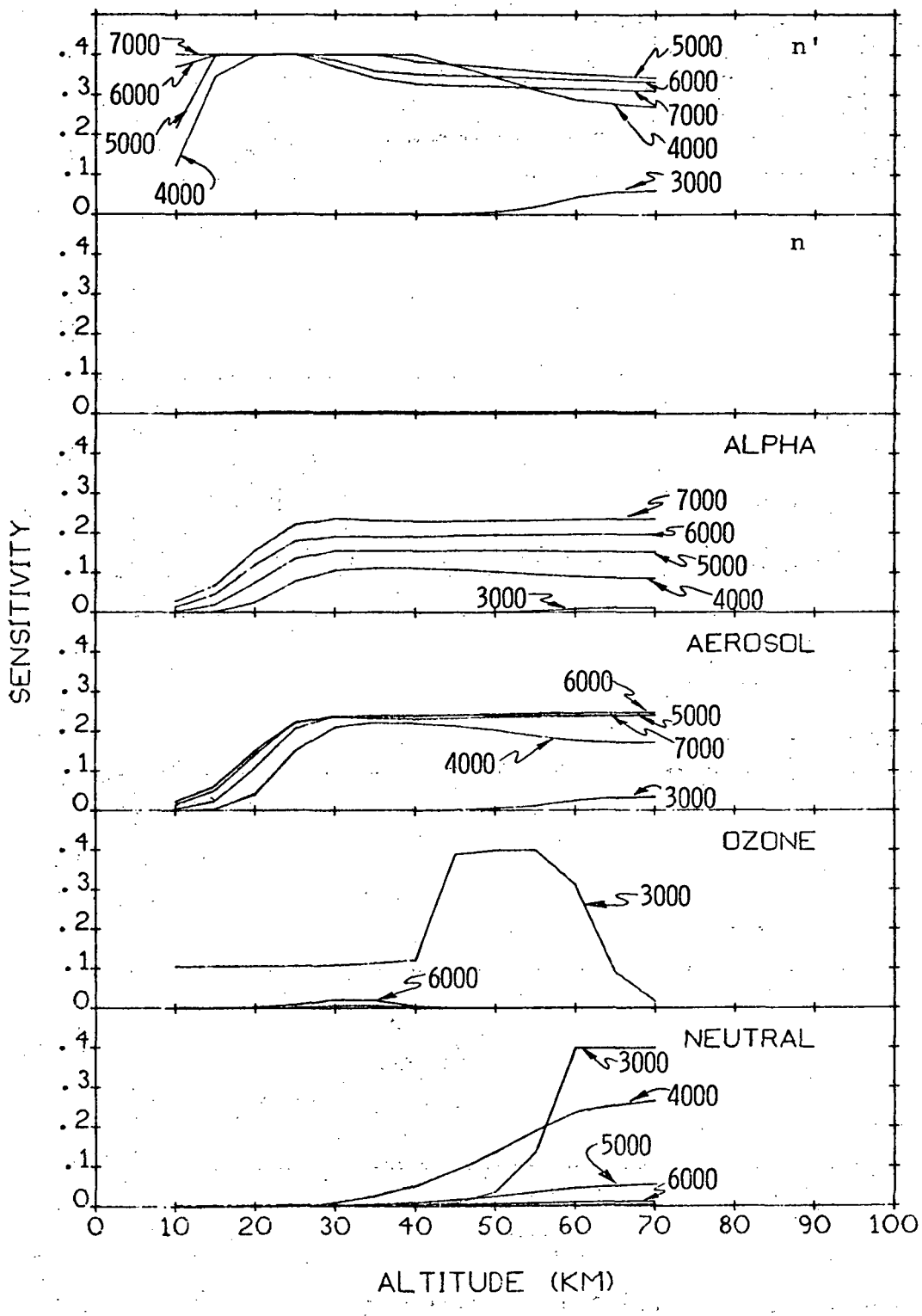

Fig. 2.1-1 Scattered Sunlight Constituent Sensitivities for Aerosol Size Range (0.1-1.0μ), Zenith Angle = 60°, Azimuth Angle = 0°, and 1σ values (ρ=100%, α=1, n=0.05, n'=0.005), Wavelength in Angstroms.

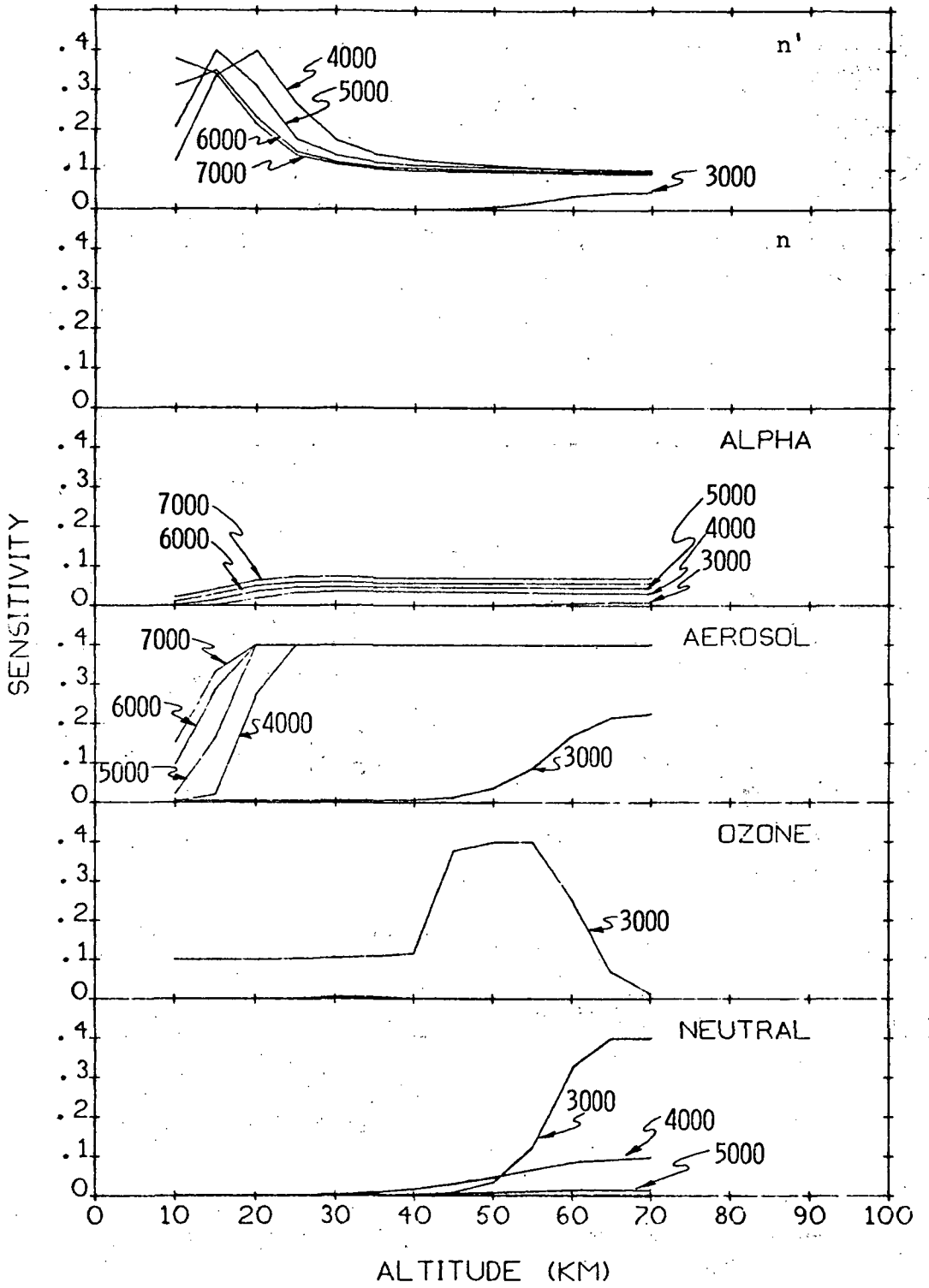

Fig. 2.1-2 Scattered Sunlight Constituent Sensitivities for Aerosol Size Range (0.1-1.0μ), Zenith Angle = 60°, Azimuth Angle = 0°, and 1σ values (ρ=300%, α=1, n=0.05, n'=0.005), Wavelength in Angstroms.

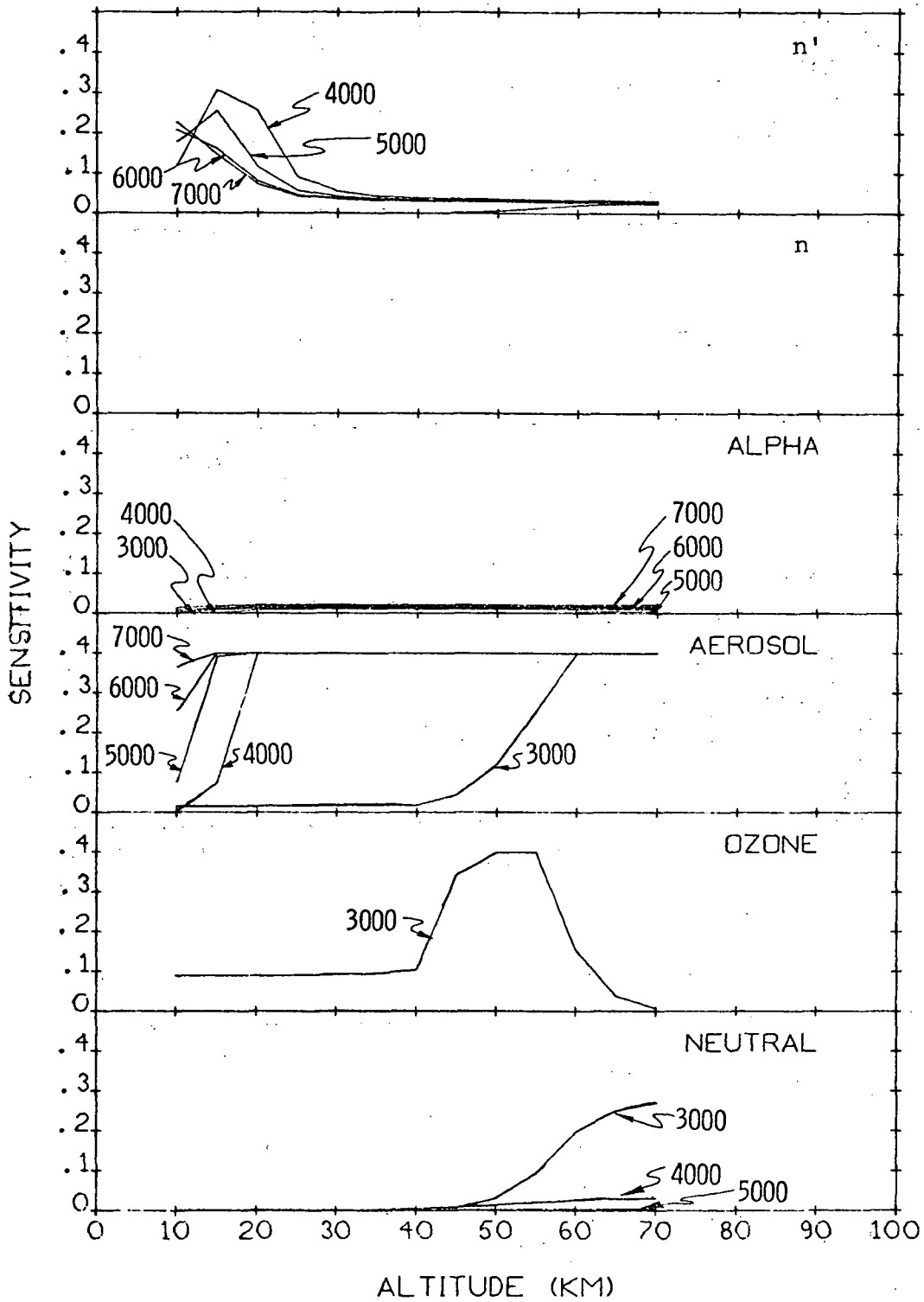

Fig. 2.1-3 Scattered Sunlight Constituent Sensitivities for Aerosol Size Range (0.1-1.0μ), Zenith Angle = 60°, Azimuth Angle = 0°, and 1σ values (ρ=600%, α=1, n=.05, n'=.005), Wavelength in Angstroms.

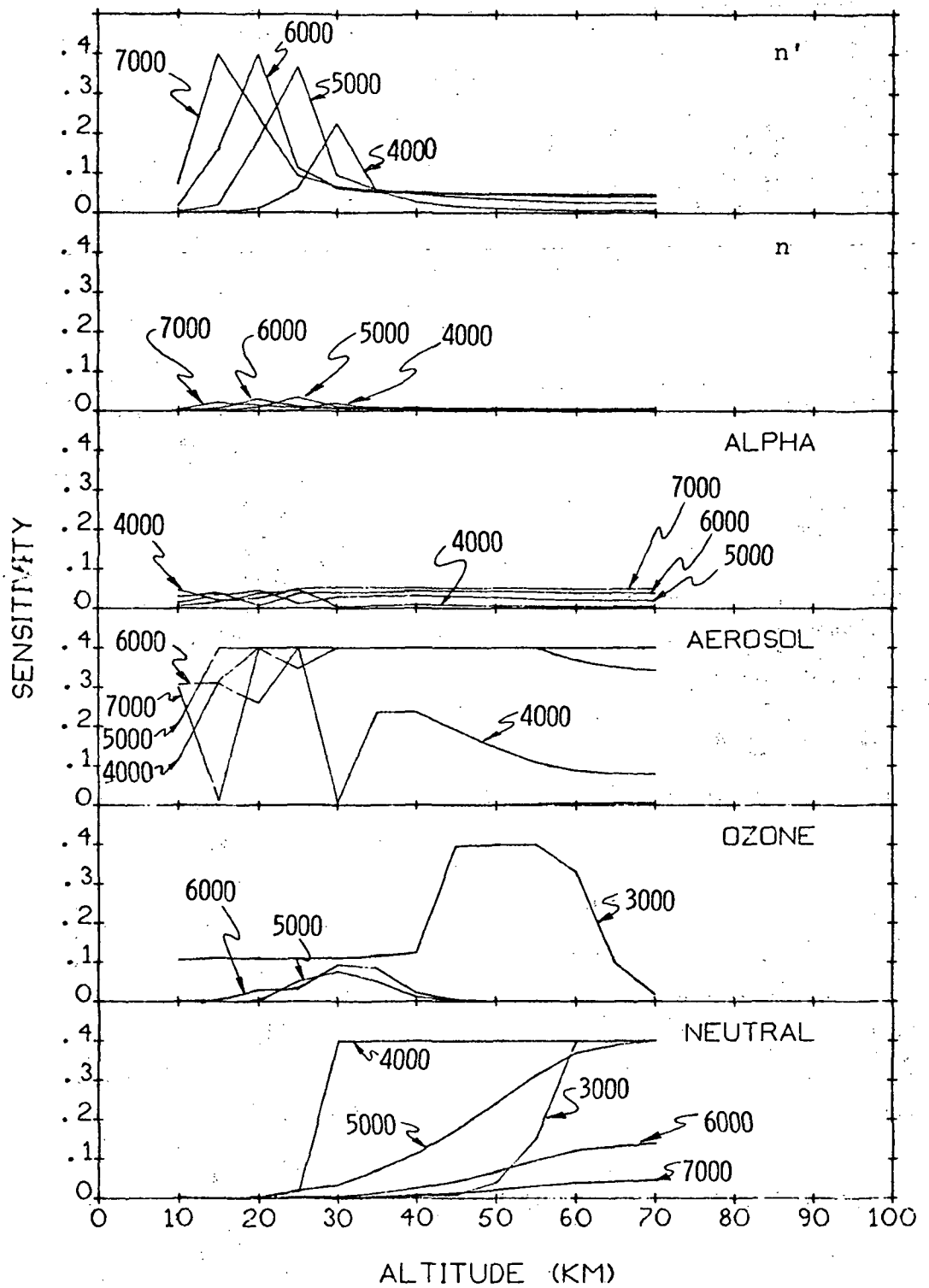

Fig. 2.1-4 Scattered Sunlight Constituent Sensitivities for Aerosol Size Range (0.1-1.0μ), Zenith Angle = 0^{o}, Azimuth Angle = 0^{o}, and 1σ values (ρ=300%, α=1, n=.05, n'=.005), Wavelength in Angstroms.

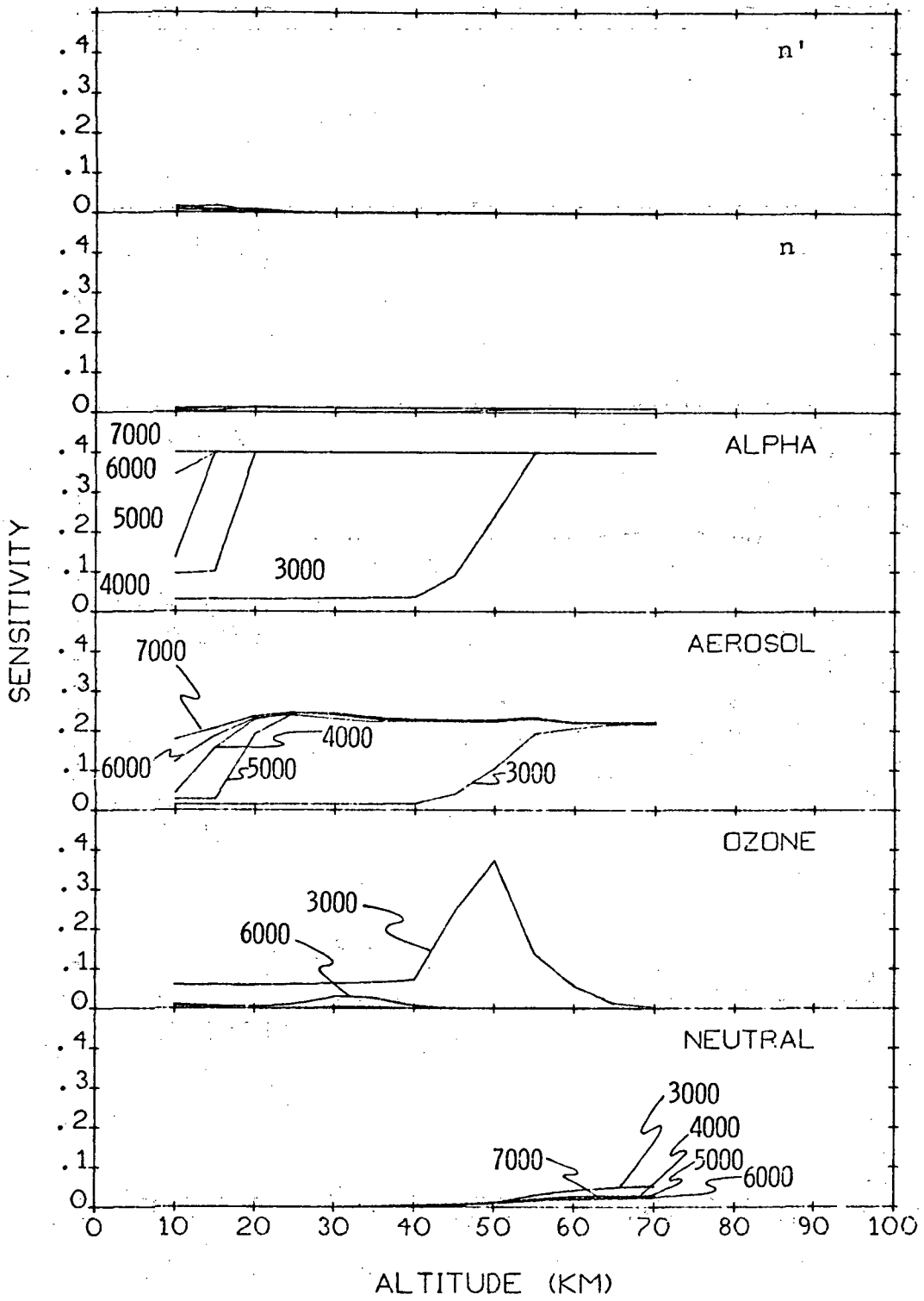

Fig. 2.1-5 Scattered Sunlight Constituent Sensitivities for Aerosol Size Range (0.01-0.1μ), Zenith Angle = 60°, Azimuth Angle = 0°, and 1σ values (ρ=100%, α=1, n=.05, n'=.005), Wavelength in Angstroms.

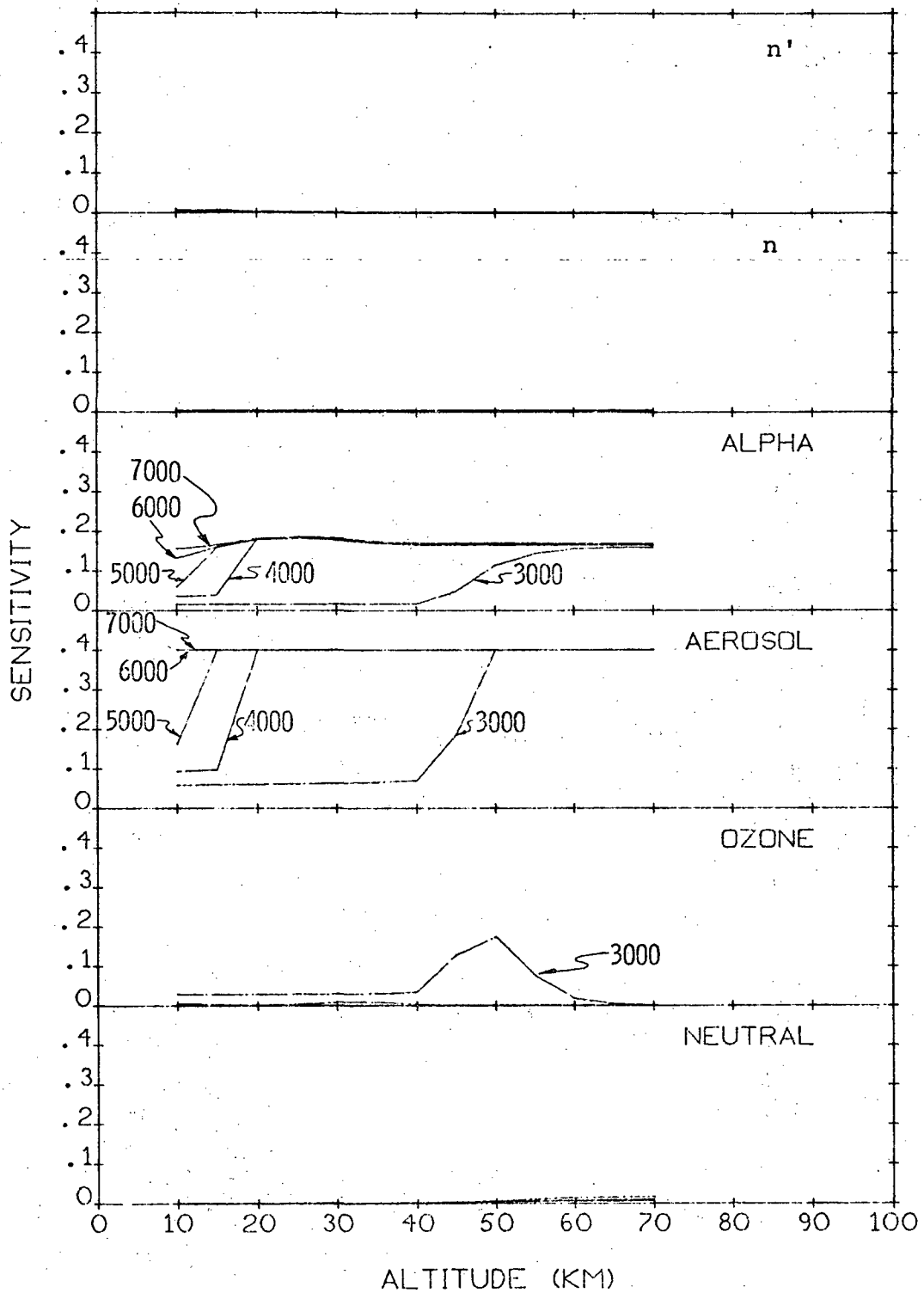

Fig. 2.1-6 Scattered Sunlight Constituent Sensitivities for Aerosol Size Range (0.01-0.1μ), Zenith Angle = 60°, Azimuth Angle = 0°, and 1σ values (ρ=300%, α=1, n=.05, n'=.005), Wavelength in Angstroms.

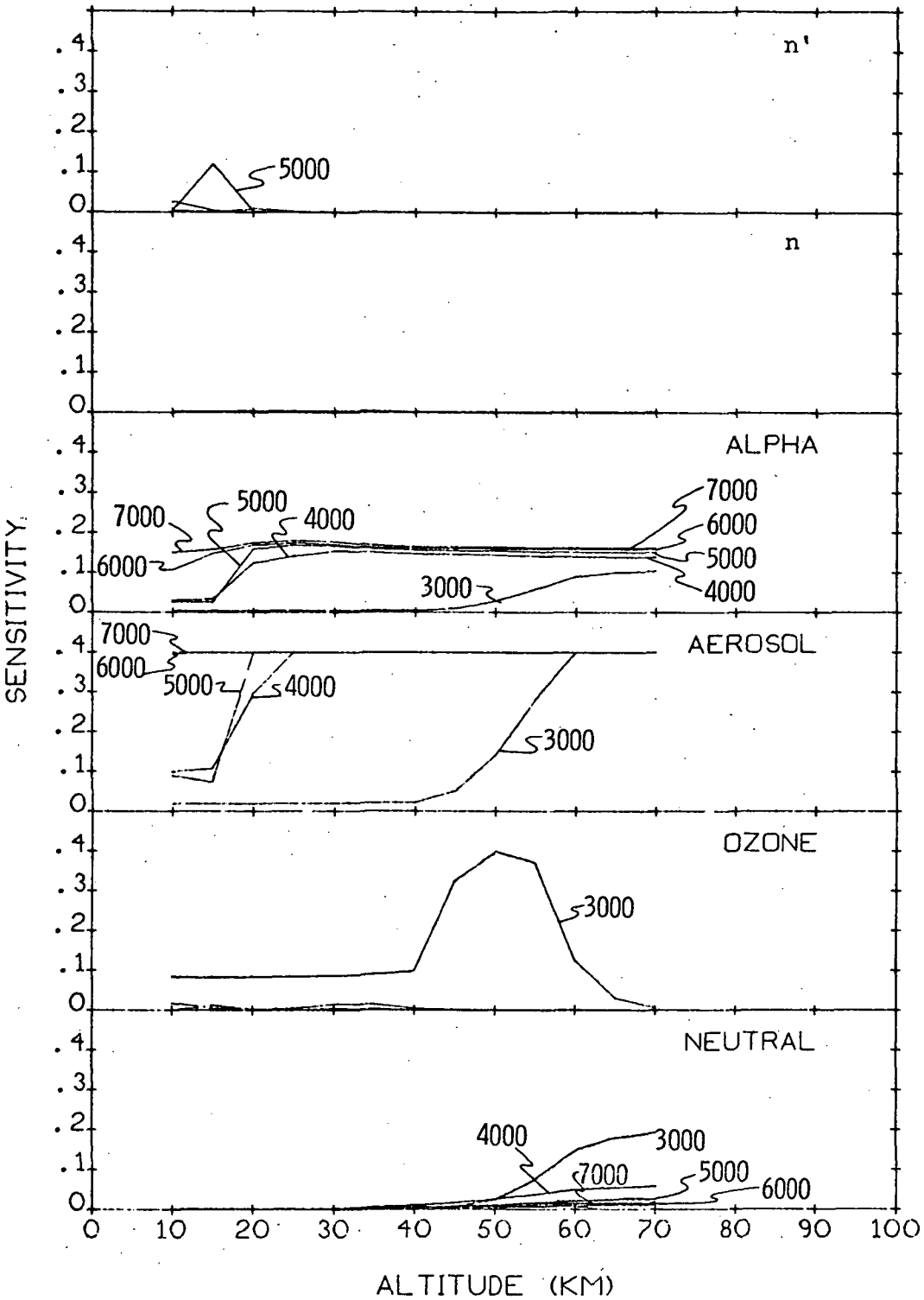

Fig. 2.1-7 Scattered Sunlight Constituent Sensitivities for Aerosol Size Range (0.01-0.1μ), Zenith Angle = 0^{o}, Azimuth Angle = 0^{o}, and 1σ values (ρ=300%, α=1, n=.05, n'=.005), Wavelength in Angstroms.

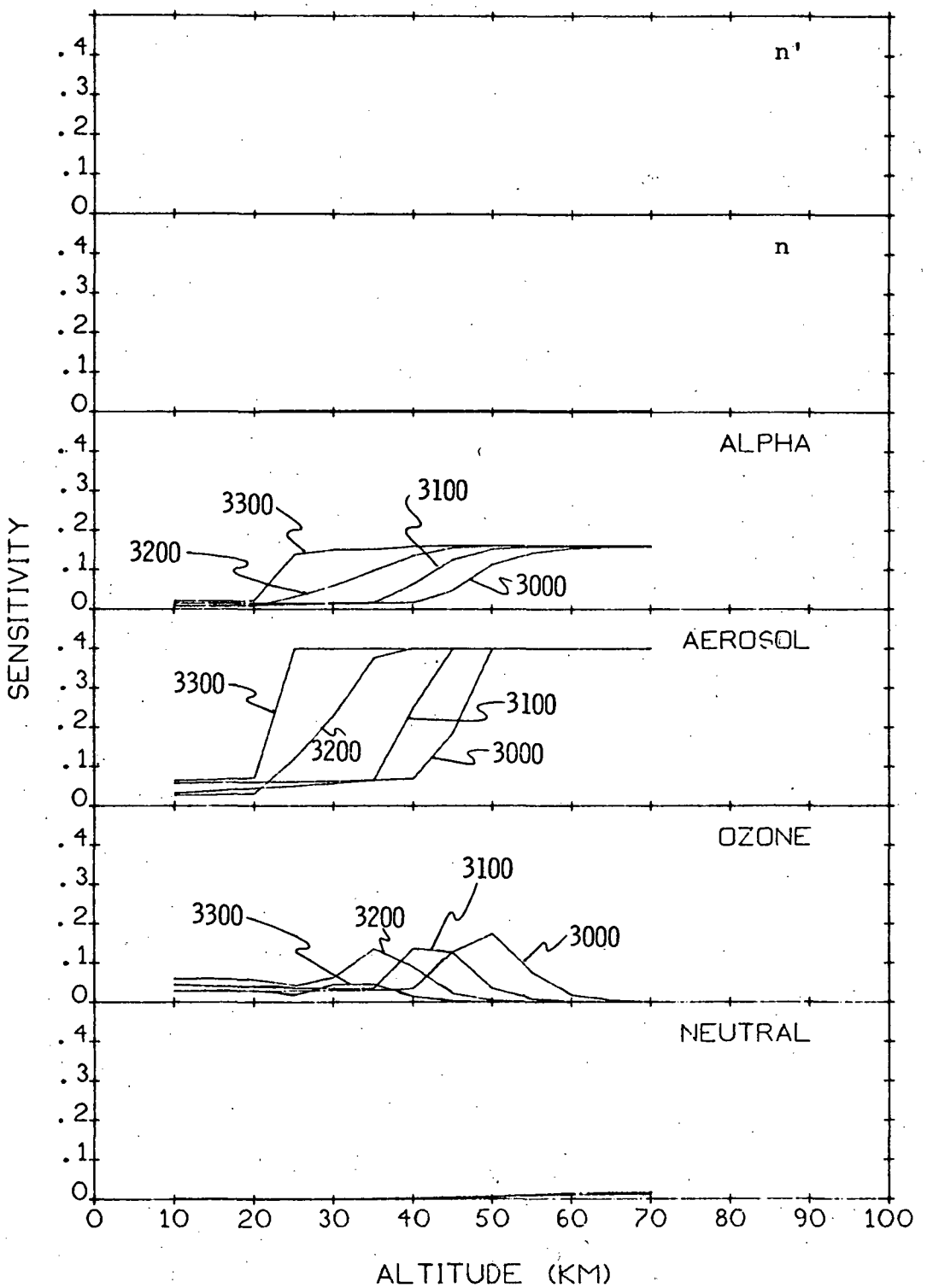

Fig. 2.1-8 Scattered Sunlight Constituent Sensitivities for Aerosol Size Range (0.01-0.1μ), Zenith Angle = 60°, Azimuth Angle = 0°, and 1σ values (ρ=300%, α=1, n=.05, n'=.005), Wavelength in Angstroms.

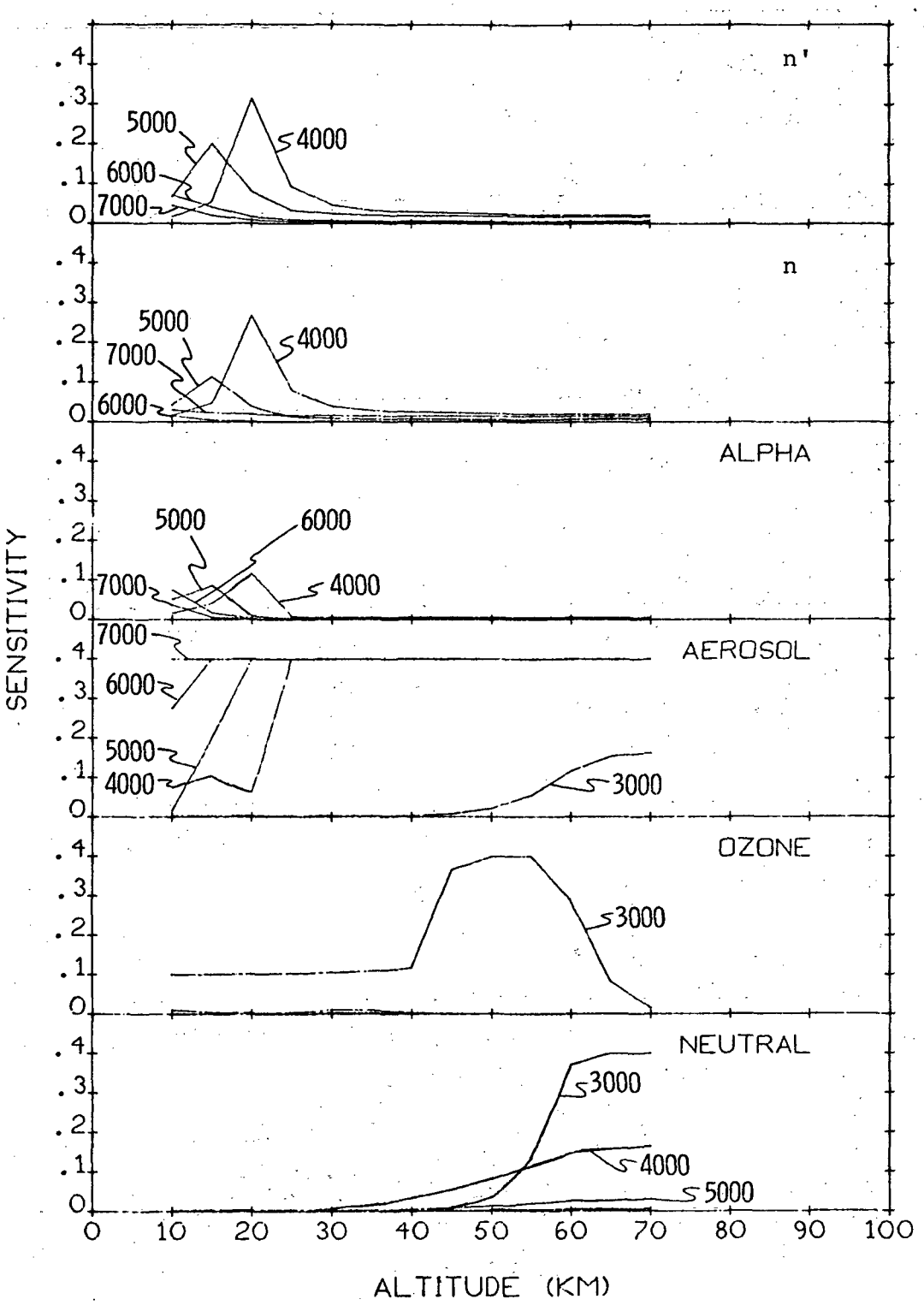

Fig. 2.1-9 Scattered Sunlight Constituent Sensitivities for Aerosol Size Range (1.0-10μ), Zenith Angle = 60^{o}, Azimuth Angle = 0^{o}, and 1σ values (ρ=300%, α=1, n=.05), n'=.005), Wavelength in Angstroms.

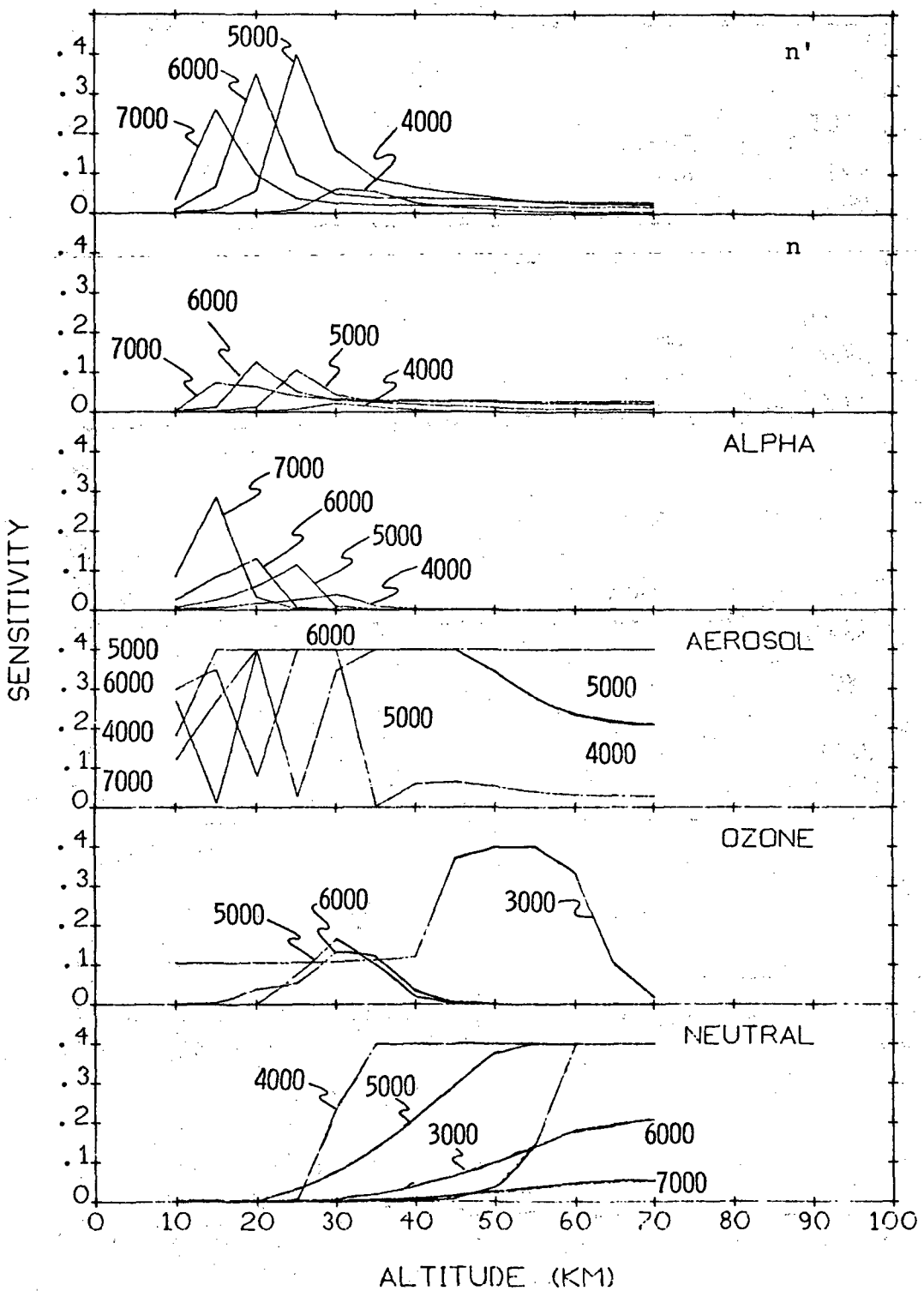

Fig. 2.1-10 Scattered Sunlight Constituent Sensitivities for Aerosol Size Range (1.0-10μ), Zenith Angle = 90°, Azimuth Angle = 0°, and 1σ values (ρ=300%, α=1, n=.05, n'=.005), Wavelength in Angstroms.

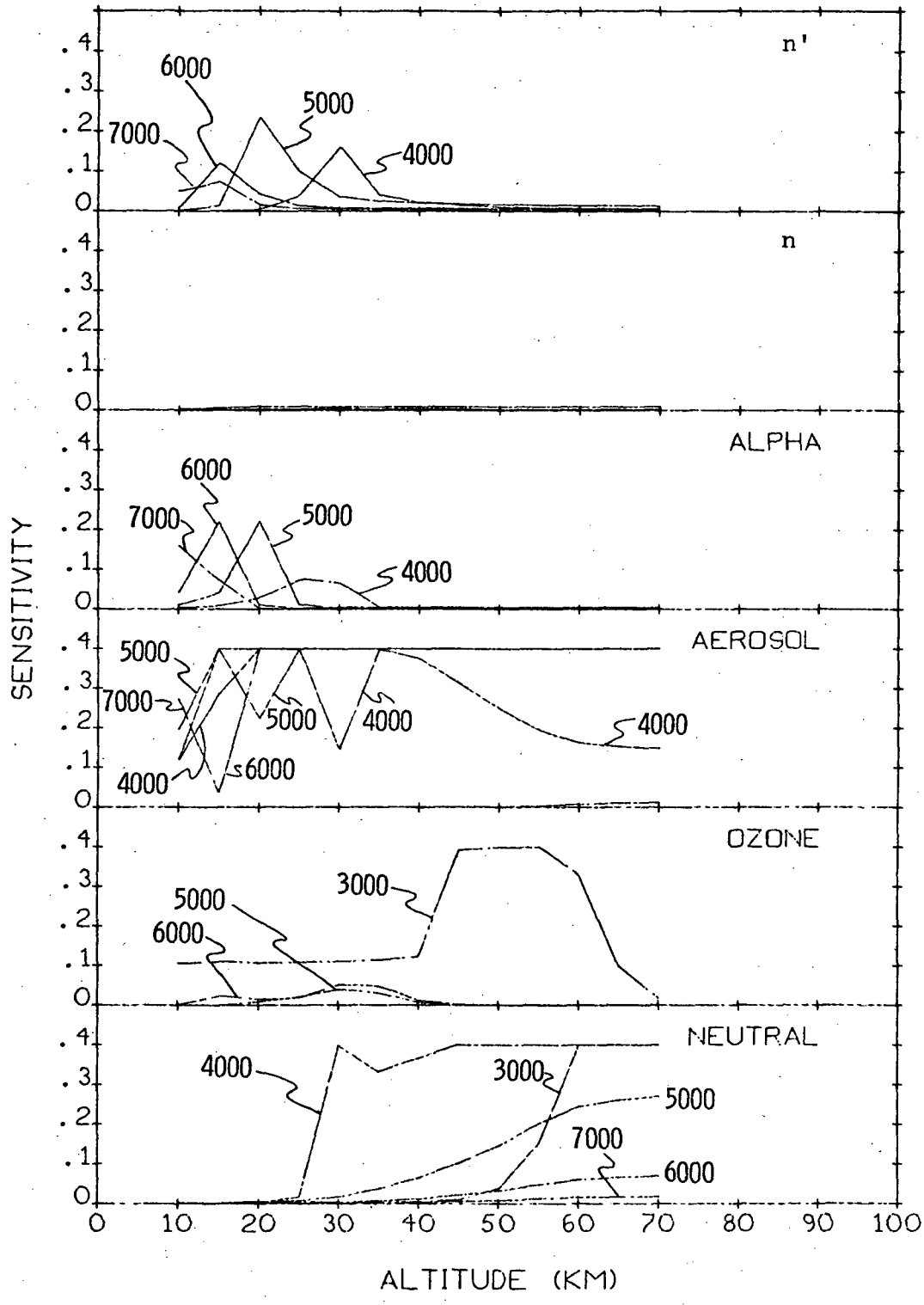

Fig. 2.1-11 Scattered Sunlight Constituent Sensitivities for Aerosol Size Range (1.0-10μ), Zenith Angle = 50°, Azimuth Angle = 180°, and 1σ values (ρ=300%, α=1, n=.05, n'=.005), Wavelength in Angstroms.

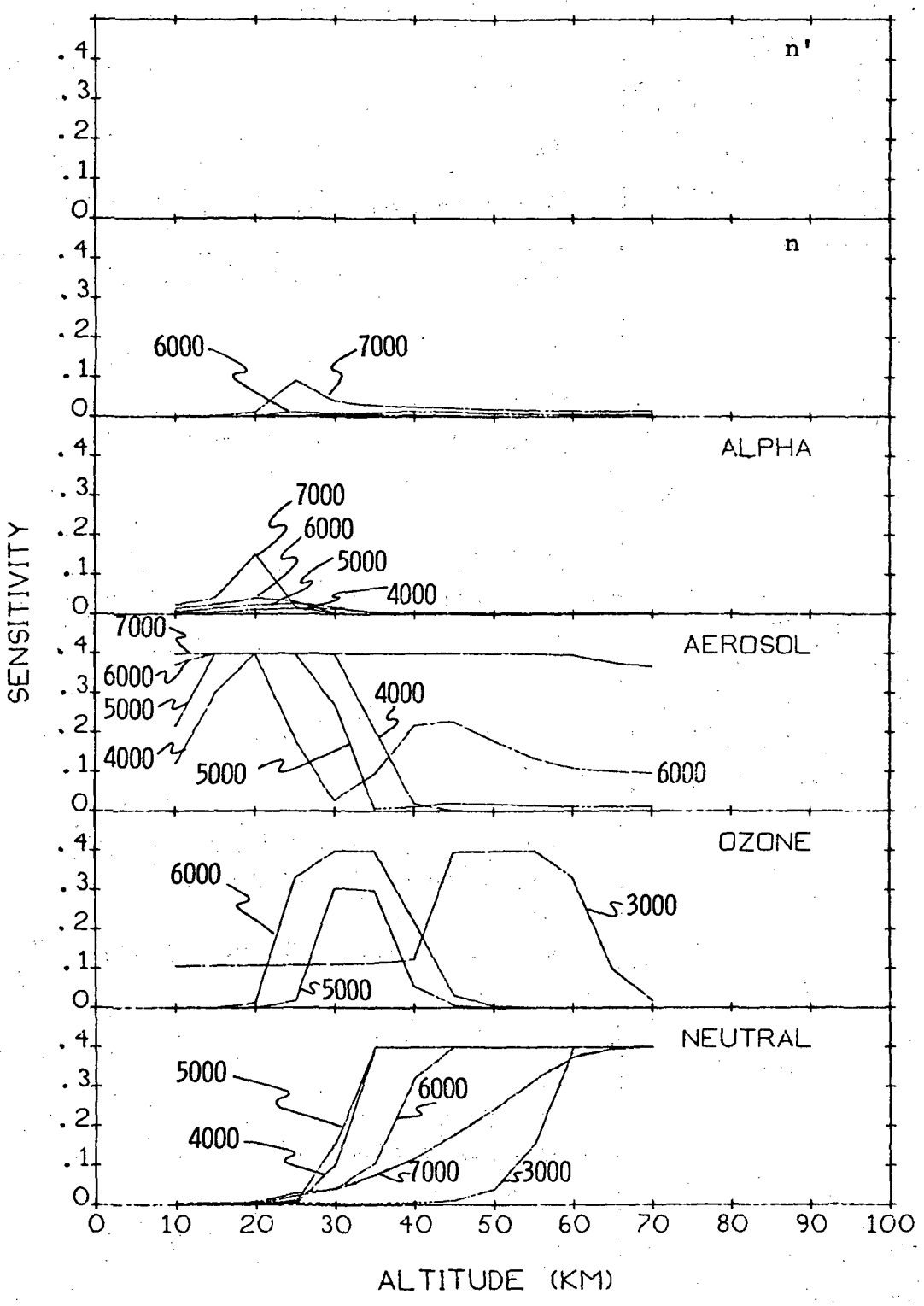

Fig. 2.1-12 Scattered Sunlight Constituent Sensitivities for Aerosol Size Range (1.0-10μ), Zenith Angle = 0^{o}, Azimuth Angle = 0^{o}, and 1σ values (ρ=300%, α=1, n=.05, n'=.005), Wavelength in Angstroms.

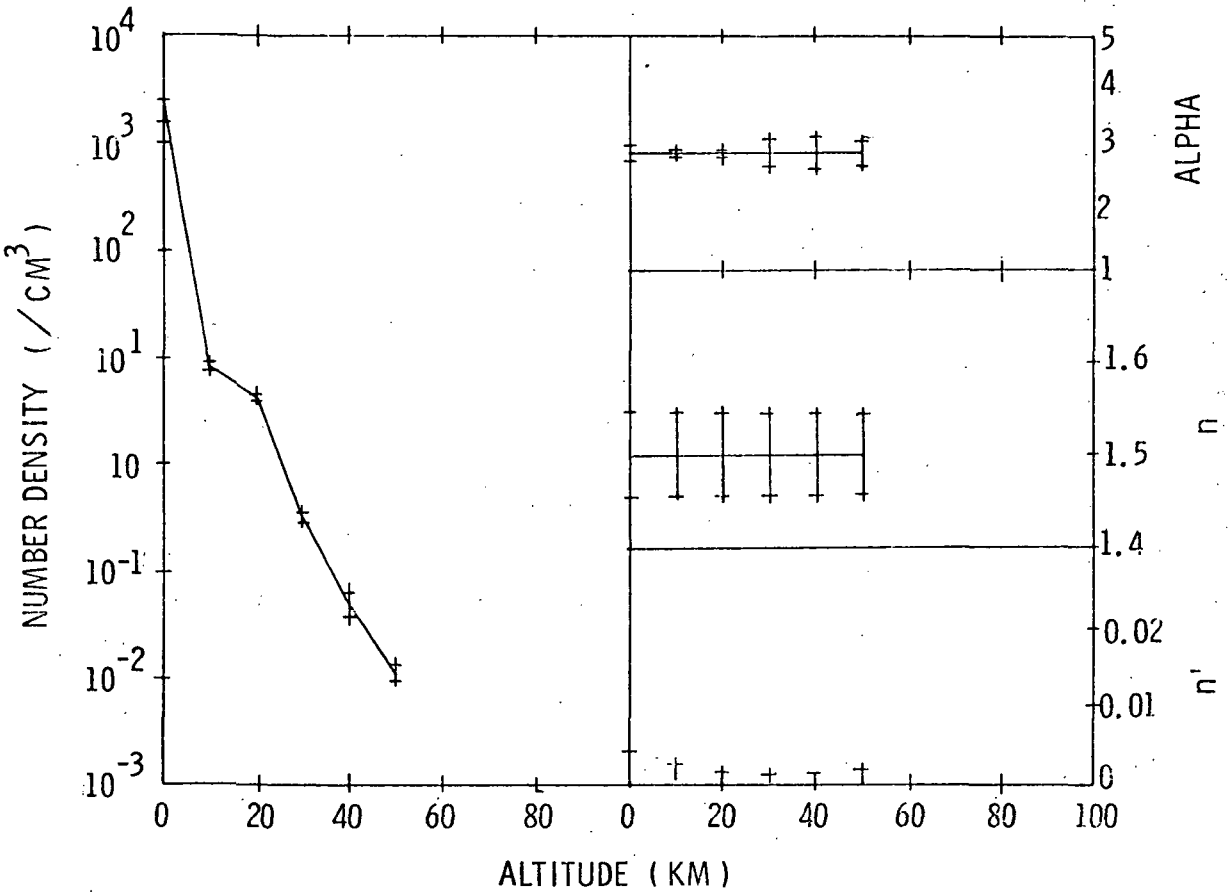

Fig. 2.1-13 Covariance Propagation for Aerosol Size Range (0.1-1.0μ), Zenith Angle = 60°, Azimuth Angle = 0°, and 1σ values (ρ=166%, α=1, n=.05,n'=.005), Wavelengths of 3000, 4000, 5000, 6000, and 7000 Å, and Tangent Heights Spaced at 4 km.

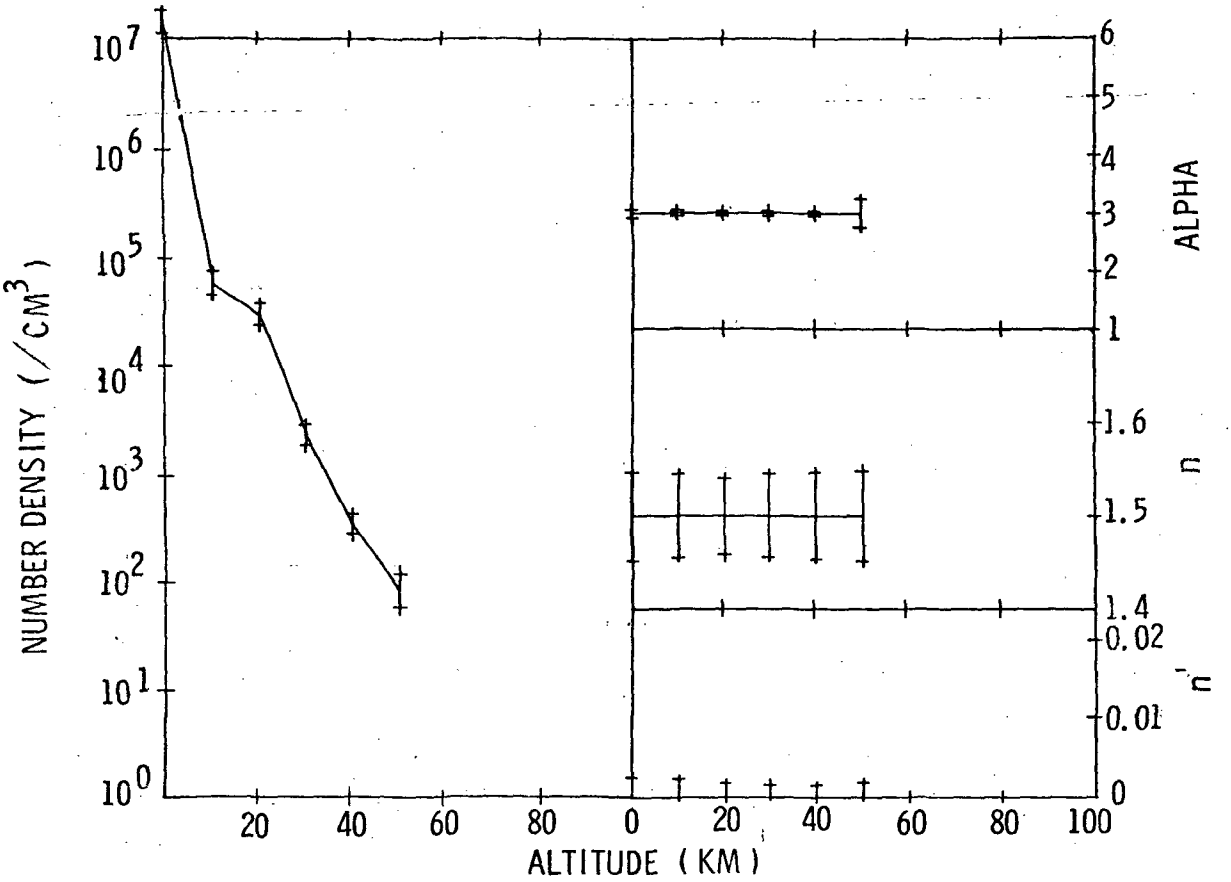

Fig. 2.1-14 Covariance Propagation for Aerosol Size Range (0.01-0.1μ) Zenith Angle = 60°, Azimuth Angle = 0°, and 1σ values (ρ=166%, α=1, n=.05, n'=.005), Wavelengths of 3000, 4000, 5000, 6000, and 7000 Å, and Tangent Heights Spaced at 4 km.

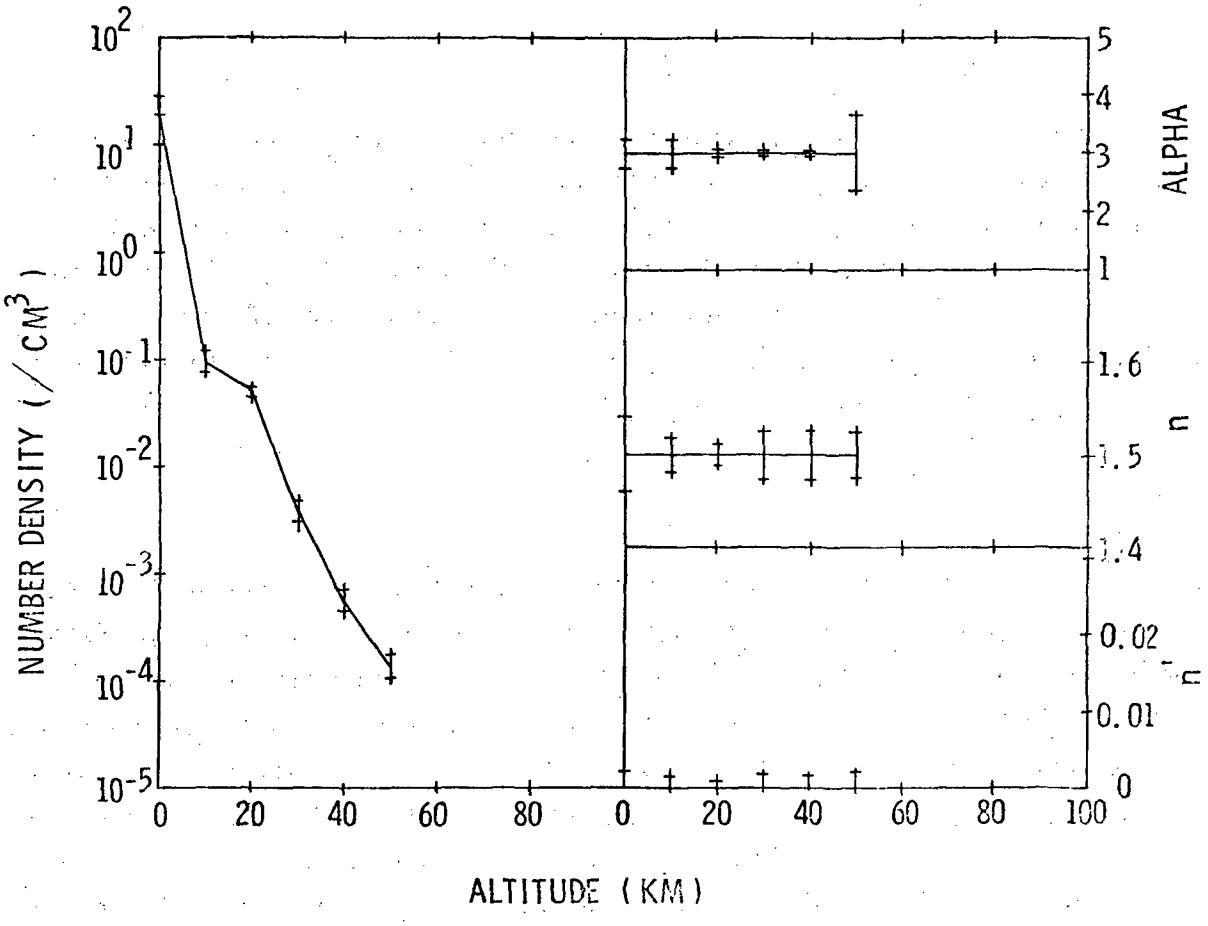

Fig. 2.1-15 Covariance Propagation for Aerosol Size Range (1.0-10μ), Zenith Angle = 60°, Azimuth Angle = 0°, and 1σ values (ρ=166%, α=1, n=.05, n'=.005), Wavelengths of 3000, 4000, 5000, 6000, and 7000 Å, and Tangent Heights Spaced at 4 km.

2.2 STELLAR OCCULTATION SIMULATION

2.2.1 Introduction

One of the contract subtasks was concerned with the application of the Kalman-Bucy filter to the inversion of stellar occultation data. The data, however, was unobtainable during the contract period. The inversion scheme was nevertheless developed and a sensitivity analysis was performed. Several computer runs were made using simulated data which illustrates the invertibility of high altitude aerosol layers with a star occultation experiment.

2.2.2 Sensitivity

The sensitivity function for stellar occultation is identical to that used for scattered light. The partial derivatives are, however, applied to a different radiative transfer model. Figure 2.2-1 shows the envelope of peak sensitivities for a complete stellar occultation scan at several wavelengths. It can be seen from this figure that both ozone and neutral density will be invertible down to an altitude of 20 km. The curves indicate ozone cannot be inverted below this level. This is because the intensity attenuation of ozone sensitive wavelengths below 20 km is too great to permit measurement of the signal with the assumed instrument signal to noise ratio of 100:1.

Figure 2.2-2 shows the effect of a high altitude aerosol layer (50 km, one order of magnitude anomalous increase) on the stellar occultation sensitivity curves. It can be seen that standard levels of aerosols do generate a sufficient signal increase to be detected, however, an anomalous increase of this nature will be measured and inverted for the assumed 100:1 signal to noise ratio.

2.2.3 Selected Simulation Results

For the purpose of simulation, fictitious, but realistic, density distributions other than standard were used to generate simulated data e.g. anomalous layers were included based on measurements of Rossler, 1968 and Elliot, 1971. The data was then processed by the inversion routine. In Figure 2.2-3 the crosses represent the estimate of the density with two error bars given for each point. The horizontal bar represents the uncertainty in the altitude at which the average density occurs while the vertical bar represents the density uncertainty. The density error bars are derived from the filter while the altitude error bars are derived a priori in simulations. The solid line represents the fictitious density or "right" answer. If the densities fall within the RMS error bars 67% of the time the simulation is considered a success.

Figure 2.2-3 is a simulation in which an order of magnitude anomalous aerosol layer at 50 km was used to generate fictitious data. The inversion results demonstrate the ability of the inversion technique to determine such layers if they exist with a 100:1 signal to noise ratio and wavelengths of 3000, 4000, 5000, and 7000 A.

2.2.4 Conclusion

The Kalman-Bucy filter is easily adapted to the inversion of stellar occultation data and produces excellent results. Although a simplified radiative transfer model was used in these simulations there is no reason why a more sophisticated model incorporating refraction and dispersion effects could not be used. This would extend the range of invertibility well below 30 km for both neutral density and aerosols in addition to providing more accurate results above 30 km.

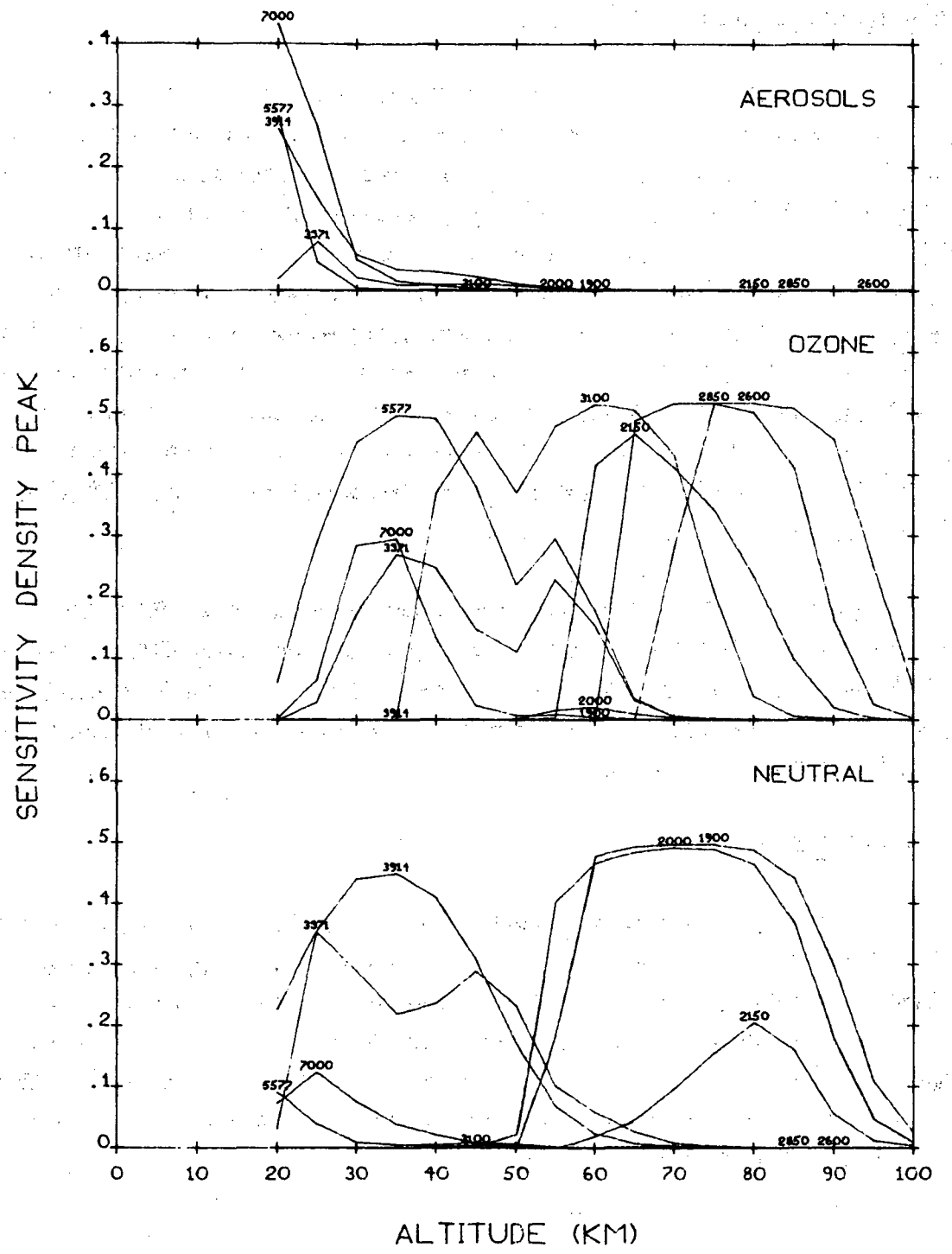

Fig 2.2-1 Stellar Occultation Constituent Peak Sensitivity Profiles with 100:1 signal to noise and standard densities.

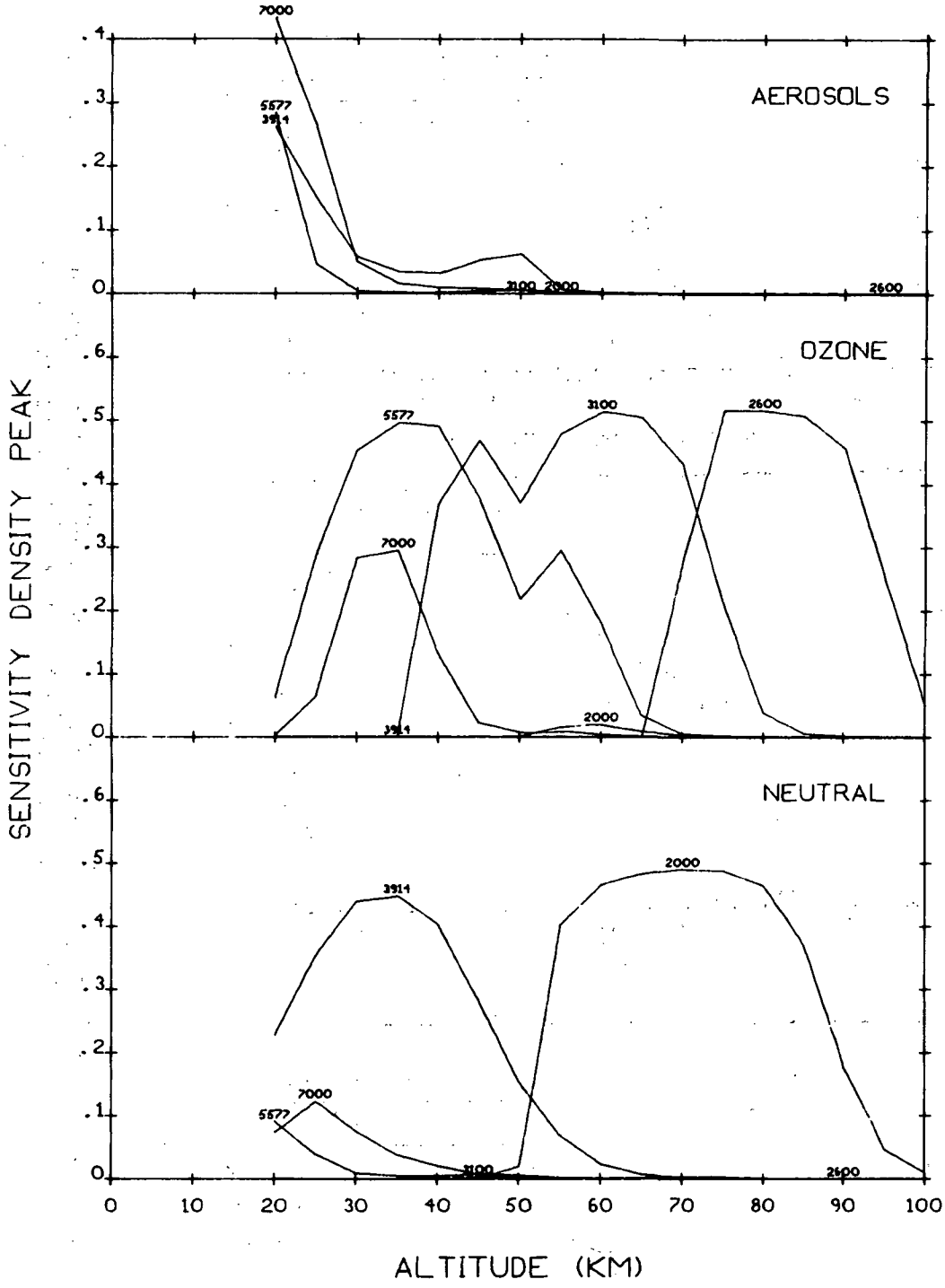

Fig. 2.2-2 Stellar Occultation Constituent Peak Sensitivity Profiles with 100:1 signal to noise and an (order of magnitude increase) anomalous aerosol layer at 50 km.

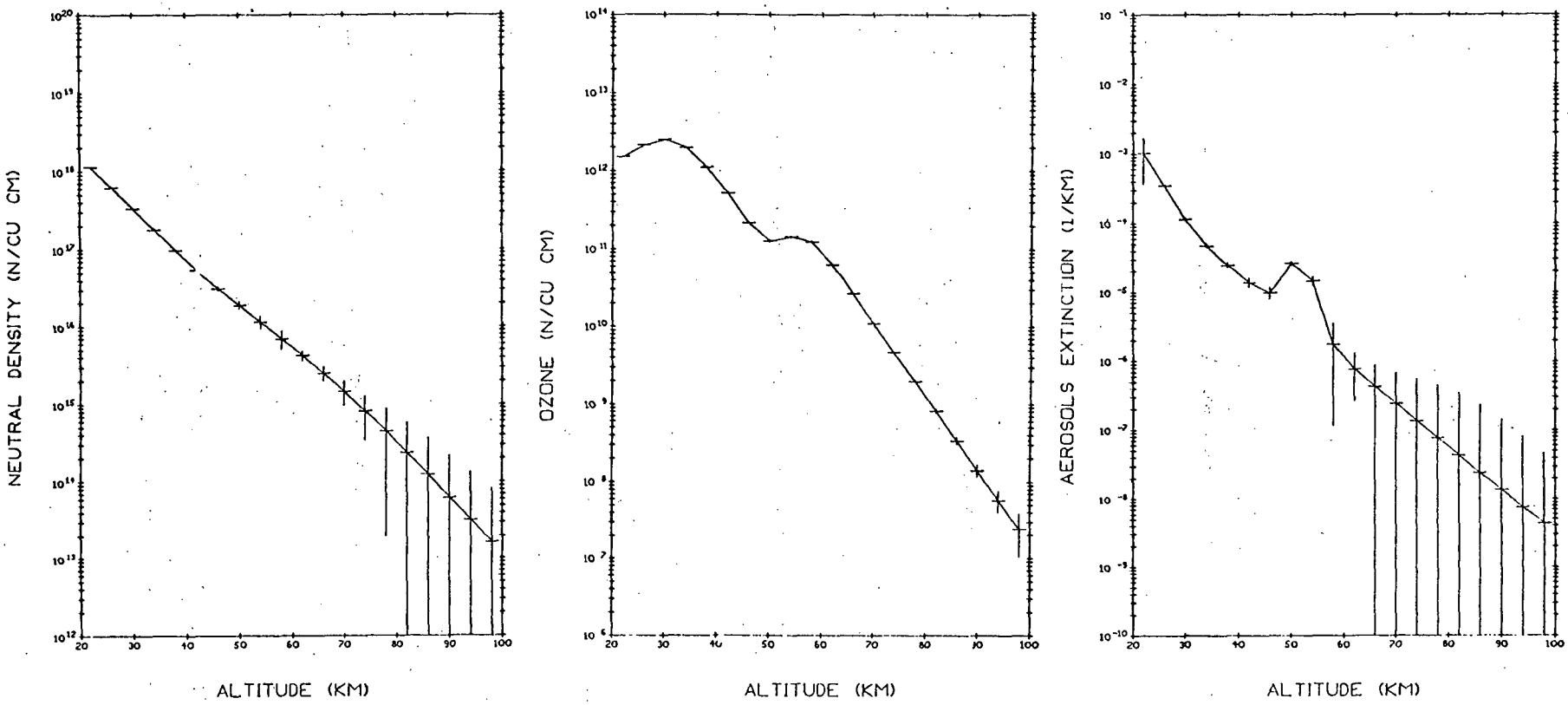

Fig. 2.2-3 Inversion of Simulated Stellar Occultation Data in the presence of an anomalous aerosol layer at 50 km.

2.3 HORIZON PROFILE PARAMETER SIMULATION

2.3.1 Introduction

In this section we discuss the results of a horizon profile parameter study aimed at determining how horizon profiles are altered by changes in the various measurement parameters. These include season, latitude, satellite altitude, solar zenith and azimuth angles, and either the earth's albedo or the altitude and albedo of a cloud layer. The newly developed mulitple scattering code (C.K.W.) was used to produce 324 radiance profiles representing various combinations of the measurement parameters. The horizon profiles are plotted in multiples of from three to five profiles per graph and are compiled in Appendix 5.1. Figure 2.3-1 is a sample profile set showing zenith angle as a variable. The measurement parameter being varied in each graph is identified at the top of the graph and values of a given variable corresponding to a given profile are listed to the right of each graph. The fixed parameters for each profile set are listed in the legend. The right hand graph in each figure displays the fractional change of each radiance profile relative to one member of the set.

Figure 2.3-2 shows the limb scan geometry, defining the tangent height (H), the satellite altitude (S), and the line of sight (L). The direction of the sun's rays are specified in relation to a Cartesian coordinate frame attached to the satellite, with $(\hat{Z})$ along the local vertical and with $(\hat{Y})$ in the plane defined by $(\hat{Z})$ and $(\hat{L})$. The solar zenith angle (θ) is measured relative to $(\hat{Z})$ and the solar azimuth angle (ϕ) is measured in the $(\hat{X},\hat{Y})$ plane relative to $(\hat{Y})$. The angle which $(\hat{L})$ makes with $(\hat{Y})$, i.e., the scan angle, is defined as (δ).

All of the horizon profiles given in this report pertain to a satellite altitude of 500 km. The scan angle (δ) therefore varies from about 19.5° to 22° as the tangent height varies from 100 km to zero. The single scattering angle is determined by the angles $(\theta, \phi,$ and $\delta)$ through the expression $\cos\psi = (\cos\phi\sin\theta\cos\delta - \cos\theta\sin\delta)$. Thus, for the coplanar cases ($\phi=0^{\circ}$ and $\phi=180^{\circ}$) $\psi=90^{\circ}+\delta-\theta$ and $\psi=90^{\circ}+\delta+\theta$, and for the $\phi=90^{\circ}$ case $\cos\psi$ is simply given by $(-\cos\theta\sin\delta)$.

2.3.2 Discussion of Results

For reasons of organizational convenience the 84 figures for this parameter study are located in Section 5.1. In each case the atmosphere was considered to have two-kilometer layers (DZ = 2) that extended to an altitude of one hundred and twenty two kilometers (ATM = 122). The seasonal and latitudinal distributions for the mean neutral and ozone densities used in determining these profiles are shown in Figures 5.1-73 to 5.1-84. Figures 5.1-1 to 5.1-12 show the variations in horizon profiles resulting from seasonal variations in the neutral and ozone densities for each of twelve latitide-wavelength conditions (latitude = 0, 40, and 70°N and λ = 3000, 4000, 5500 and 7000 Angstroms). At 0°N latitude the same neutral density distribution was used for all seasons. The changes in the profiles with season at 0°N latitude reflect, therefore, only the changes in the ozone density distribution. This profile set represents the only case where the differential horizon profiles can be interpreted simply in terms of the changes occurring in just one of the atmospheric constituents. These changes, which are referenced to the winter profile, are greatest at 3000 A and smallest at 4000 A in agreement with the known spectral characteristics of the ozone absorption cross section (Wu, 1970). The remaining horizon profiles in this parameter study are arbitrarily based upon the latitude and seasonal choices of 40°N latitude, winter.

Figures 5.1-13 to 5.1-24 show the variations in horizon profiles with wavelength for twelve cloud-zenith angle conditions (a zenith angle of 30° and 80° and a cloud at 4, 7, and 10 km with an albedo of 0.4 and 0.8). The solar irradiances at 3000, 4000, 5500, and 7000 A are 5.14, 14.92, 17.25, and 13.25 μwatts/cm^2-A respectively (Thekaekara and Drummond, 1970). Figures 5.1-25 to 5.1-28 show the variations in horizon profiles with wavelength for four zenith angles (0, 30, 50, and 80 degrees) and a ground albedo of 0.3. These figures show that clouds are only observable at the longer wavelengths like 5500 and 7000 A which penetrate deepest into the atmosphere. In addition, these figures show that the enhancement of radiance

due to an increase in cloud albedo is strongly dependent upon the zenith and azimuth angles, which determine the scattering angle (ψ) and hence the fraction ($\sin\psi$) of the solar irradiance that is actually incident upon the cloud surface.

Figures 5.1-29 to 5.1-64 show the variations in horizon profiles with zenith angle for 36 combinations of azimuth angle, wavelength, and ground albedo (azimuth angle = 0, 90, and 180 degrees; λ = 3000, 4000, 5500, and 7000 Angstroms; ground albedo = 0.2, 0.5 and 0.8). The differential horizon profiles are all referenced to the zero zenith angle profile. These figures show that the shape of a profile is not affected greatly by changes in the albedo and in the solar azimuth and zenith angles. For the brightest profile (80° zenith and 0° azimuth) there is little albedo effect because $\sin(\psi)$ is relatively small and therefore most of the signal is produced by strong forward scattering high in the atmosphere. Albedo effects are most prominent for azimuth and zenith angle combinations that make the scattering angle $(\psi) \approx \pi/2$.

Figures 5.1-65 to 5.1-72 show the variations in horizon profiles with ground albedo for eight combinations of zenith angle and wavelength (zenith angle = 30 and 80 degrees; λ = 3000, 4000, 5500, and 7000 Angstroms). The differential horizon profiles are referenced to the albedo = 0 profile. These figures show that the enhancement of the line of sight radiance due to the earth's albedo is strongly dependent upon wavelength and scattering angle.

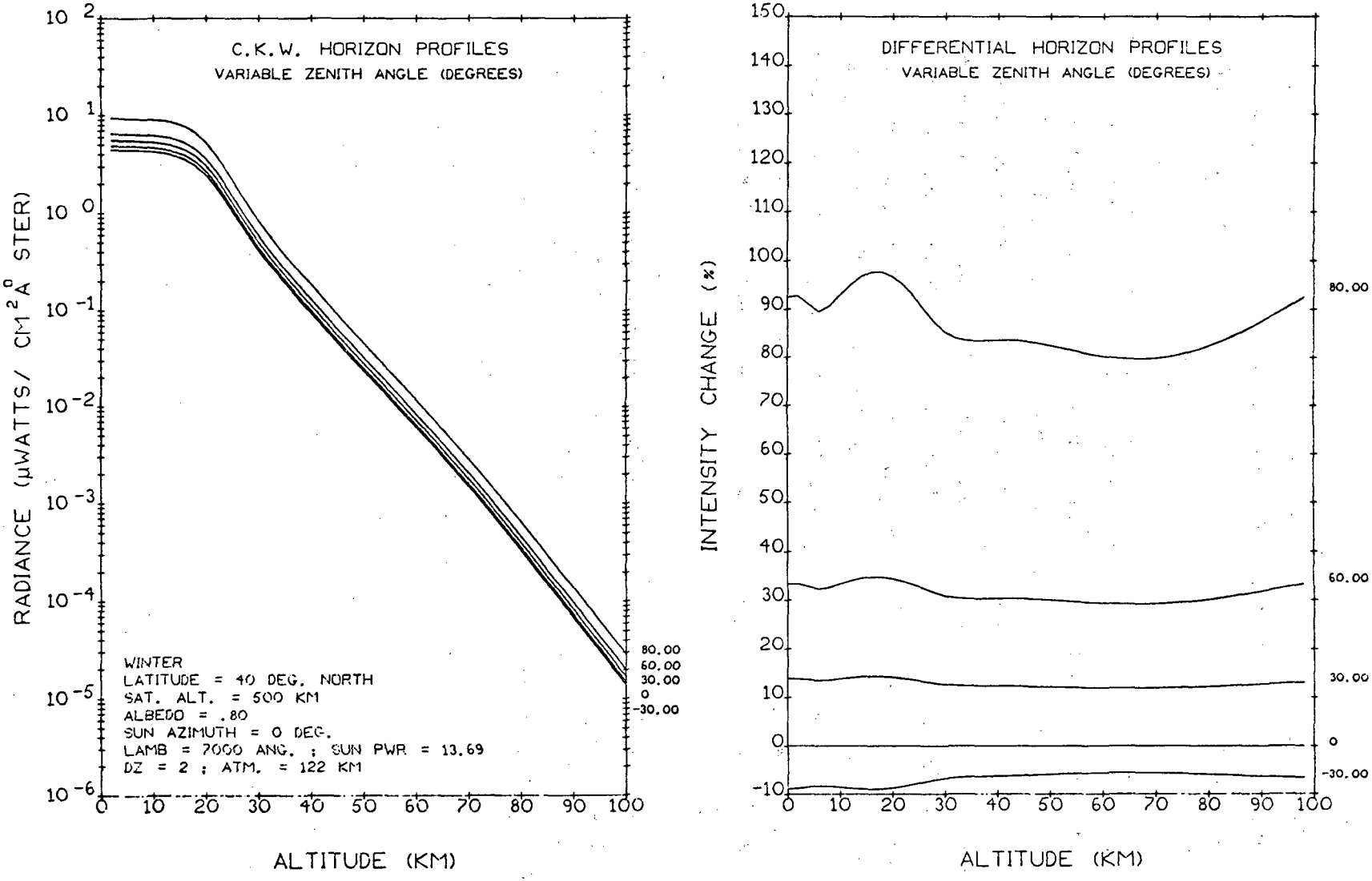

Fig. 2.3-1 Variable Zenith Angle Horizon Profiles

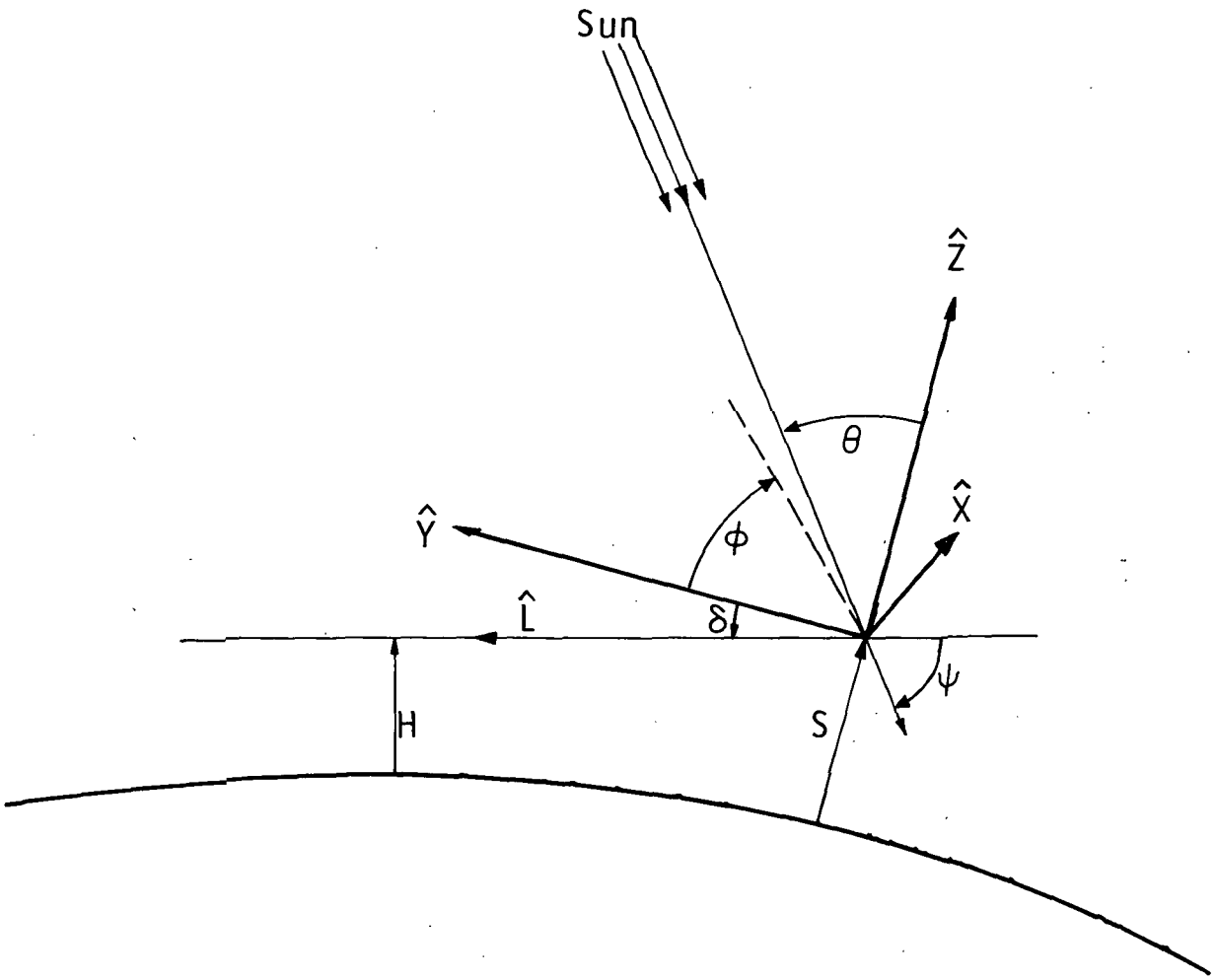

Fig. 2.3-2 Limb Scan Geometry

REFERENCES

SECTION 2

1) Elliott, D.D., "Effect of a High Altitude (50Km) Aerosol Layer on Topside Ozone Sounding", Space Res., 11,857-861, 1971.

2) Elterman, L., "Vertical-Attenuation Model with Eight Surfaces Meteorological Ranges 2 to 13 Kilometers", AFCRL Report 70-0200, March, 1970.

3) Elterman, L., "An Atlas of Aerosol Attenuation and Extinction Profiles for the Troposphere and Stratosphere", AFCRL Report 66-828, December, 1966.

4) Malchow, H.L., "Standard Models of Atmospheric Constituents and Radiative Phenomena for Inversion Simulation", MIT Aeronomy Program Internal Report No. AER 7-1, January, 1971.

5) Newell, R.E., and C.R. Gray, "Meteorological and Ecological Monitoring of the Stratosphere and Mesosphere", NASA Contractor Report, NASA CR-2094, August, 1972.

6) Rossler, F., "The Aerosol Layer in the Stratosphere", Space Res., 8, 633-636, 1968.

7) Thekaekara, M.P., and A.J. Drummond, "Standard Values for the Solar Constant and its Spectral Components", Nature, Phy. Sci., 229, 6-9, January 4, 1971.

8) Volz, F.E., "Infrared Optical Constants of Ammonium Sulfate, Sahara Dust, Volcanic Pumice, and Flyash", Appl. Opt., 12, 564-598, March, 1973.

3.0 MODELING

3.1 FILTER DEVELOPMENT

3.1.1 Introduction

There are a number of approaches to the problem of inverting aerosol parameters, neutral atmospheric density, and ozone density from horizon profile data. Ideally the method chosen should provide a best estimate (in some statistical sense) of the desired parameters incorporating not only the data, but the instrument characteristics and previous knowledge of the parameters as well. What follows is a discussion of several techniques which have been considered as well as the reasoning behind the choice of the Kalman-Bucy filter.

3.1.2 Comparison of Techniques

The first and most obvious approach to the inversion problem is to attempt an analytic solution of the equations of radiative transfer, that is solving for density as a function of intensity. This technique has been used (Anderson, 1969) for atmospheric probing; however, even for simple geometries with single scattering and only one unknown constituent several simplifying assumptions must be made in order to reach an analytic solution. Also, once the solution is reached it is difficult to perform a meaningful error analysis on the final answer. Thus given the stated goals of the method to be chosen and the complexity of the radiative transfer equations for horizon scan geometry, it is clear that this approach to the inversion problem is limited.

Since it is not practically feasible to solve the equations analytically the next possibility to consider is an indirect solution to the equations using partial derivatives and some iterative scheme to arrive at an approximate solution to a set of simultaneous equations. This would probably be possible and would give reasonable answers, however, there would be no statistical

error analysis. Also if there were more data points than needed to solve the simultaneous equations only the first data taken would be used. Thus this technique involves incomplete data utilization and does not provide for the desired error analysis.

Next, a regression technique might be considered. A regression would provide not only a best estimate in a least squares sense but error statistics as well. However there are some problems with the application of a regression and these are: 1) Previous knowledge of the parameters is not incorporated in the estimate or the statistics, 2) Instrument noise is not incorporated, and 3) The large amount of data must be processed simultaneously rather than sequentially. However this would be a good technique if there was not a better approach to the problem.

The use of Bayesian statistics makes possible the incorporation of previous knowledge and instrument noise in the inversion scheme. It also allows data to be processed one point at a time thus incorporating each new datum into the estimate of the statistics of the estimate. There are a number of Bayesian approaches to the problem such as maximum likelihood estimation, Bayesian regression, weighted least squares, and the Kalman-Bucy filter.

For the case in which the equations relating the measurement and the state are linear, and noises are Gaussian, all these techniques are equivalent. However in real physical situations these assumptions are often invalid and the techniques differ. The Kalman-Bucy filter was chosen because: 1) It has all the advantages of Bayesian statistics, 2) The filter equations are simple and easy to understand and code, and 3) Because of the simplicity of the equations the filter readily lends itself to iterative techniques which ensure convergence in spite of the nonlinearity of the equations.

3.1.3 Filter Review

The Kalman-Bucy filter is a recursive technique for estimating the state (in this case aerosol parameters, neutral atmospheric density, and ozone) of a system (the atmosphere) from measurements of that system (horizon profile data). At each recursion the previous estimate of the state is updated. The degree and distribution among parameters of the update is determined by the measurement, the previous estimate of the state, the instrument noise, and the statistics (covariance matrix) associated with the estimate of the state. After the state is updated the covariance matrix is also updated so that it reflects the current knowledge of the state.

The updating procedure is done in three steps. First is the calculation of the filter gain which determines the degree and distribution of the update among the elements of the state vector.

$$K(m+1) = P(m)\, B^T(m+1) \left[B(m+1)\, P(m)\, B^T(m+1) + R\right]^{-1} \quad (3.1\text{-}1)$$

where

(m) is an index of measurement
(K) is the filter gain
(P) is the covariance matrix
(B) is the measurement vector whose elements are

$$b_i = \partial h(x, m+1)/\partial x_i$$

h(x, m+1) is the predicted value of the intensity based on the state estimate and measurement parameters

and

(R) is the instrument noise.

The second step is the updating of the state estimate

$$\hat{x}(m+1) = \hat{x}(m) + K(m+1)\left[I\,(m+1) - h(x,\, m+1)\right] \qquad (3.1\text{-}2)$$

where $(\hat{x})$ is the state estimate and (I) is the measurement.

Thirdly the covariance matrix is updated to incorporate the knowledge gained of the state.

$$P(m+1) = P(m) - K(m+1)\, B(m+1)\, P(m) \qquad (3.1\text{-}3)$$

As can be seen from the equations there are three steps which must be taken before applying a filter to the problem of limb scan data inversion. First a computer code giving a direct solution to the equations of radiative transfer is needed for the calculation of $h(x, m)$ and $\partial h(x, m)/\partial x$ (partials are usually calculated by the approximation $\Delta h(x, m)/\Delta x$). Second the state (x) must be defined, and third some initial estimate of the covariance matrix P(0) must be made to start the recursive process.

Two computer codes are available for the first requirement and these are discussed in detail in Section 3.2. For all of the inversion work to date the hybrid single scattering code has been used since the multiple scattering code had not been completed. However, the characteristic shape of the hybrid profile agrees well with the multiple scattering code. Also, the hybrid codes use less computer time and it is simpler to extract the partial derivatives from the single scattering code. It is important to note that one of the advantages of the filter inversion technique is the capability of incorporating any solution into the equations of radiative transfer no matter how complex. Thus in an actual experiment the more accurate multiple scattering code would be used.

The definition of the state has been previously discussed (Newell and Gray, 1972) for the purposes of inverting three constituent densities. Basically that scheme had density points defined at arbitrary altitude

increments. The elements of the state were the logs of the densities (or extinction in the case of aerosols) at each altitude. By using this definition of the state at intervals of from 3-10 km along with a finer integration step of 1 km in the radiative transfer codes it was found that the filter would converge (Newell and Gray, 1972) for realistic densities that would be encountered in the atmosphere.

3.1.4 Sensitivity Review

For this current work the state definition was expanded to include the log of aerosol number density (ρ), size distribution parameter (α), and both real and complex indices of refraction (n and n') at each chosen altitude. This expanded state was first analyzed through sensitivity studies and then through covariance propagation to determine the feasibility of estimating each parameter. The results of this study are discussed in Section 2.1.

The sensitivity vector is derived from the filter equations and indicates the relative information derived about each constituent parameter at each altitude for every measurement condition (i.e. wavelength and viewing angle). Since after each measurement the covariance matrix records the information gained from the measurement it is natural to look at the covariance update equation for the definition of sensitivity. The term of interest here is K(m+1) B(m+1) P(m), which gives the decrease in the covariance after the (m+1) measurement. Normalizing by P(m) yields the sensitivity matrix K(m+1) B(m+1) whose diagonal elements comprise the sensitivity vector. For practical data presentation and speed in calculation, the sensitivity vector can be defined by assuming that the covariance matrix maintains its initial variances and has zero cross correlation. With these assumptions the sensitivity of the j^{th} element of the state vector is

$$s_j(m) = \left(\frac{\partial h(x,m)}{\partial x_j}\right)^2 P_{jj} \Bigg/ \left[\left(\sum_i \left(\frac{\partial h(x,m)}{\partial x_i}\right)^2 P_{ii}\right) + R\right] \qquad (3.1\text{-}4)$$

It is important at this time to realize both the usefulness and drawbacks of sensitivity analysis. The main purpose of the analysis is to show just which constituent parameters and altitude regions are important in a measurement. Thus sensitivity analysis will reveal for example that at 4000 A and a tangent height of 20 km with a certain set of initial uncertainties the greatest information will be derived about aerosol number density and aerosol absorption in the region from 20 to 23 km. The analysis will also reveal that at 3000 A and 20 km the only information derived is from ozone between 40 and 50 km. (This is due to the strong ozone absorption which prohibits this wavelength from penetrating below 30 km.)

The one disadvantage of the sensitivity analysis stems from the assumption that each update has zero cross correlation. It often happens that a set of measurements do not yield linearly independent sensitivity vectors. For example consider a simple experiment designed to determine aerosol number density and neutral density at 50 km by two measurements at 3800 and 4000 A. The sensitivity vectors would be high for both constituents at both wavelengths seemingly indicating that both are readily observable. However, the actual final covariance matrix of such an experiment would show that little has been learned of either constituent since there is no way to distinguish between constituents from the measurements. Therefore, the covariance matrix would indicate that the sum of both constituents is well known.

This is not a serious problem however since visual inspection of sensitivity vectors is often sufficient to determine whether or not there will be a problem with ambiguous measurements. If there seems to be some doubt then a complete propagation of the covariance matrix can be made to determine exactly what information is recoverable from the data.

3.1.5 Stellar Occultation

The stellar occultation inversion technique is essentially the same as the inversion of scattered sunlight (Newell and Gray, 1972). There are, however, some aspects of the stellar occultation radiative transfer model

that make improvements possible in the construct of the state elements. These improvements yield finer data resolution and more accurate error statistics. The next few paragraphs describe the essential differences between the two inversions.

The radiative transfer model used for the stellar occultation work is

$$I = I_o e^{-\tau} \qquad (3.1\text{-}5)$$

where (I) is the measured intensity, (I_o) is the star intensity, and (τ) is the optical depth along the line of sight. The model used assumes a linear line of sight and neglects dispersion and multiple scattering effects. These assumptions will not cause errors in excess of 10% above 30 km (Hayes and Roble, 1968). This altitude is approximately the maximum depth to which ozone information can be retrieved.

Since the Kalman-Bucy filter assumes linearity in the measurement equation it is desirable to obtain a radiative transfer model which is as nearly linear as possible. In the case of stellar occultation it is possible to create an exact linear equation by measuring the log of the intensity rather than the intensity thus giving the new measurement equation

$$\ln(I) = \ln(I_o) - \tau \qquad (3.1\text{-}6)$$

In the scattered light case discussed previously it is necessary to estimate densities at a resolution approximately two to three times as coarse as the tangent height data. This was necessary along with a gain damping term to insure convergence of the filter. For the linearized stellar occultation case it is possible to estimate density at each tangent height and also to dispense with the gain damping factor. The final density estimates are therefore average densities of a layer between two tangent heights.

3.2 RADIATIVE TRANSFER MODELING

3.2.1 Introduction

This section discusses the extension of computer algorithms for simulating the horizon profile caused by radiative transfer within the earth's atmosphere (previously reported in Newell and Gray, 1972). Here, we begin by reviewing the computational problems to which these codes are addressed and introduce briefly computer codes applicable to related problems. Their applicability to present work objectives is discussed, with emphasis on the unsolved problems that required the development of new codes. These new codes, a simple, modified single scattering code and a more sophisticated, full multiple scattering code, are compared in terms of accuracy obtainable versus computational burden required. The various applications to which they have been put are presented.

3.2.2 The Computational Problem

The problem of horizon profile simulation is a difficult one because in the earth's atmosphere there are important polarization effects in the presence of multiple scattering involving not only Rayleigh but also aerosol scatterers, as well as absorption. Furthermore, there is the nonhomogeneous structure of the atmosphere, and its slight curvature in conformity with the earth. Many of these factors contribute substantial difficulty. Polarization requires a matrix rather than a scalar treatment, thus increasing the complexity of operations and the amount of storage space required. Multiple scattering is a well-known primary source of difficulty in all radiative transfer calculations. Rayleigh scattering and absorption are straightforward, but aerosol scattering is characterized by an exceedingly complicated ill-behaved phase function, or angular pattern, that is difficult to incorporate in a radiative transfer model. The nonhomogeneous structure of the atmosphere imposes an altitude dependence of the scattering into any given solid angle. Finally, the curvature of the earth entails formidable geometry problems.

3.2.3 Codes Applicable to Related Problems

Basic computational techniques for radiative transfer modeling that existed at the outset of our work are reviewed by Hunt (1971). We shall refer to the two basic approaches he discusses as the matrix operator method and the Monte Carlo method. The matrix operator method represents the atmosphere (or any sub-layer of it) as a matrix operator that transforms an input column vector of stream irradiances to an output column vector of stream irradiances. This matrix formulation is not to be confused with the matrix formulation required by the inclusion of polarization in the problem; the matrix operator method has matrices even if polarization is ignored. The Monte Carlo method represents the atmosphere with a random number generator that chooses scattering locations, angles etc. for individual photons, very large numbers of which are followed to accumulate a horizon profile.

The matrix operator method has been used mainly in homogeneous plane parallel atmospheres, where application of the doubling technique makes it impressively efficient. It has not, however, yet been developed to handle inhomogeneous curved atmospheres. Thus, while it was available in principle at the outset of our work, in practice, its use would have required extensive development. By contrast, the Monte Carlo method has actually been applied to essentially our problem in a program called FLASH written by Collins and Wells, 1970. The FLASH program will indeed accommodate every one of the sources of difficulty mentioned in the preceeding section. Furthermore, the program existed at the outset of our activities. It would have been an attractive solution to our problems except for one factor: it requires a large amount of computing time (approximately 2000 seconds of CDC 6600 cpu time per horizon scan to achieve an accuracy of approximately four percent).

3.2.4 The Radiative Transfer Codes

Within the Draper Laboratory, there are now two radiative transfer codes that simulate horizon profiles. One is a refinement and completion of the code REV.HYBRID which is described briefly in the earlier report by Newell and Gray, 1972 and in greater detail in an internal report by Var, 1971. It is based essentially on single scattering plus an effective planetary or cloud albedo as a secondary source. The second code (C.K.W.) is a more recently developed full multiple scattering model with polarization. It is based on mathematical techniques described in Newell and Gray, 1972 and in more detail in a recent journal article by Whitney, 1972. Some of the computational procedures involved in implementing the model are described in Appendix 5.3 of this document.

Considerable effort has been expended to provide a basis for judging which of the two radiative transfer codes should be used for any particular application. The remainder of this section reports on these activities. There are three main areas of comparison: accuracy achievable, run time requirements, and suitability for specific applications.

In attempting to establish the absolute accuracy of the C.K.W. code we compared its results to FLASH results through the courtesy of the Air Force Cambridge Research Laboratory. Differences between FLASH and C.K.W. were found to be small and related primarily to fluctuations in the Monte Carlo results or differences between the details of layer definitions in the two codes.

The run times for both the C.K.W and the REV.HYBRID codes appear to be significantly less than those required for Monte Carlo simulations, in spite of the fact that specific comparisons are complicated by a number of operational and statistical factors. Our comparisons have been based rather arbitrarily on the times required to produce horizon profiles which are in apparent agreement with each other. Typically, the C.K.W code produces a horizon profile in approximately twenty seconds, and

REV.HYBRID in approximately seven seconds, both on an IBM 360/75, while the Monte Carlo code of FLASH uses approximately two thousand seconds of CDC 6600 time to produce comparable results. The significant comparison here is between the C.K.W. code and the Monte Carlo code, since only they are really addressed to the full multiple scattering problem. A tentative estimate of the time saving with C.K.W. code is a factor of several hundred.

In general, one would anticipate that multiple scattering would increase observed radiances to those that have been scattered directly into the receiver field of view. The magnitude of that contribution as determined by the C.K.W. code is illustrated in Figures 3.2-1 and 3.2-2. The enhancement of the radiance occurs without substantially altering the profile shape. Such an effect can be simulated also with the REV.HYBRID code by introducing a fictitious planetary albedo. The ficticious albedo required to match multiple scattering results depends upon sun angle and wavelength. Figures 3.2-3 and 3.2-4 show the effects of an albedo range of zero to unity upon REV.HYBRID horizon profile at 4000 and 5500 A. At 5500 A the vertical optical depth of the atmosphere is smaller than at 4000 A, thus more sunlight reaches the surface and is reflected back into the atmosphere. The reflected radiation is scattered into the receiver field of view adding substantially more radiation than when the albedo is zero causing a significant variation in the enhancement for the two wavelengths.

There is no way that the enhancement required to make REV.HYBRID conform to the C.K.W. code can be derived from basic principles. Thus we feel it is wise to use the full multiple scattering code (C.K.W.) for applications requiring absolute radiances, rather than simply horizon profile shape. Where only shape is required, REV.HYBRID is sufficiently accurate.

We come now to the question of suitability for different applications. There are two important applications to consider here: the generation of horizon profiles for the inversion simulations used to produce the aerosol invertibility results of Section 2.1, and the generation of the 324 sample horizon profiles in Appendix 5.1 illustrating the effects of varying wavelength,

latitude, season, cloud height, zenith and azimuth angles. For the inversion simulations, the single scattering REV.HYBRID was judged suitable because the simulation does not require absolute radiances but rather fractional changes in radiances induced by small perturbations in each of the quantities defining elements of the state vector. Furthermore, the calculation of these differential changes would have required the calculation of many complete horizon profiles, and hence a considerable amount of computer run time with C.K.W. This is not the case with REV.HYBRID; differential changes can be obtained without recalculating complete profiles. By contrast, for the parametric horizon profile study, the computer code (C.K.W.) was used because the effects of the parameters to be illustrated could not have been accurately obtained from REV.HYBRID.

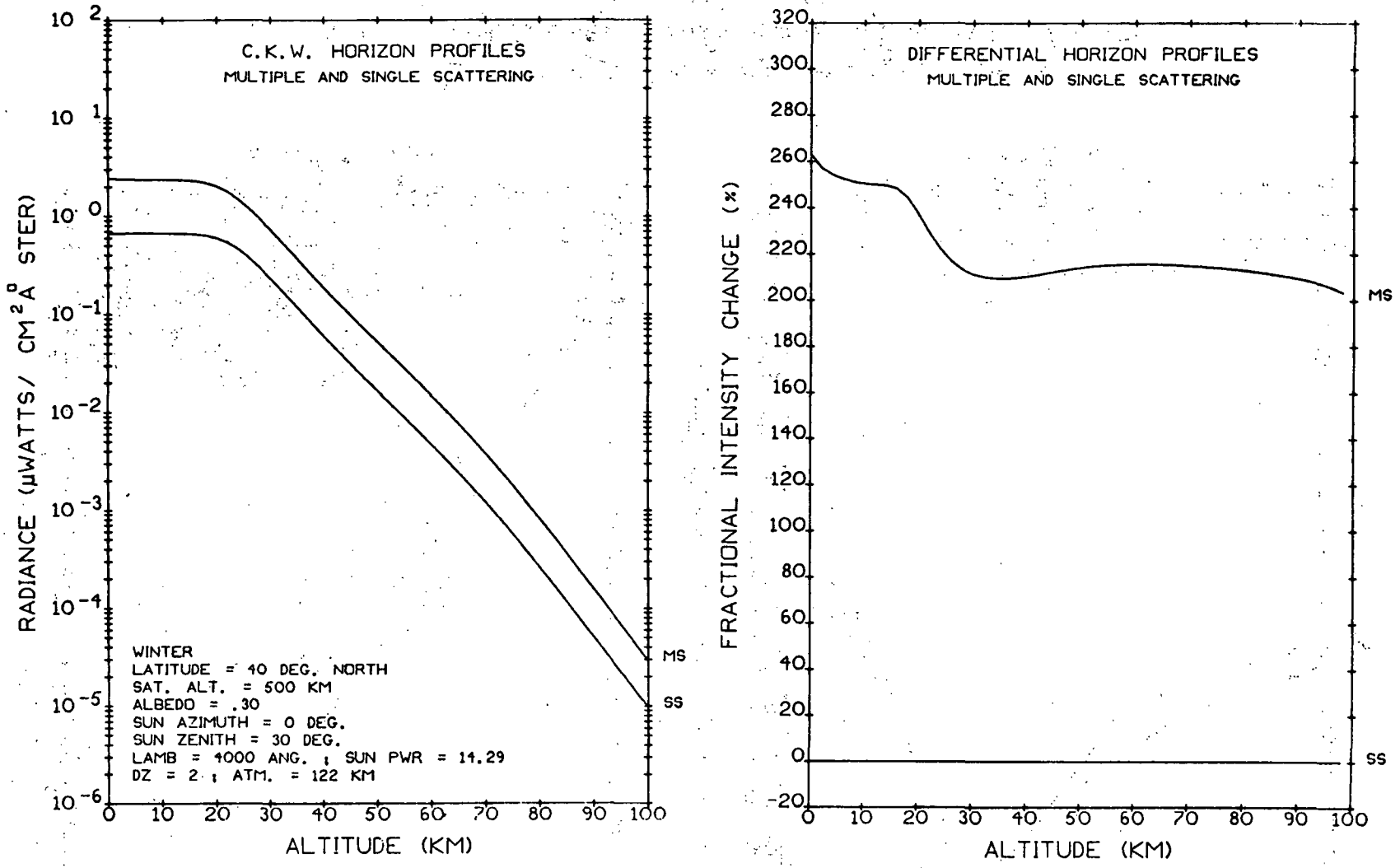

Fig. 3.2-1 Multiple and Single Scattering Horizon Profiles (Zenith Angle = 30°, λ=4000 Å)

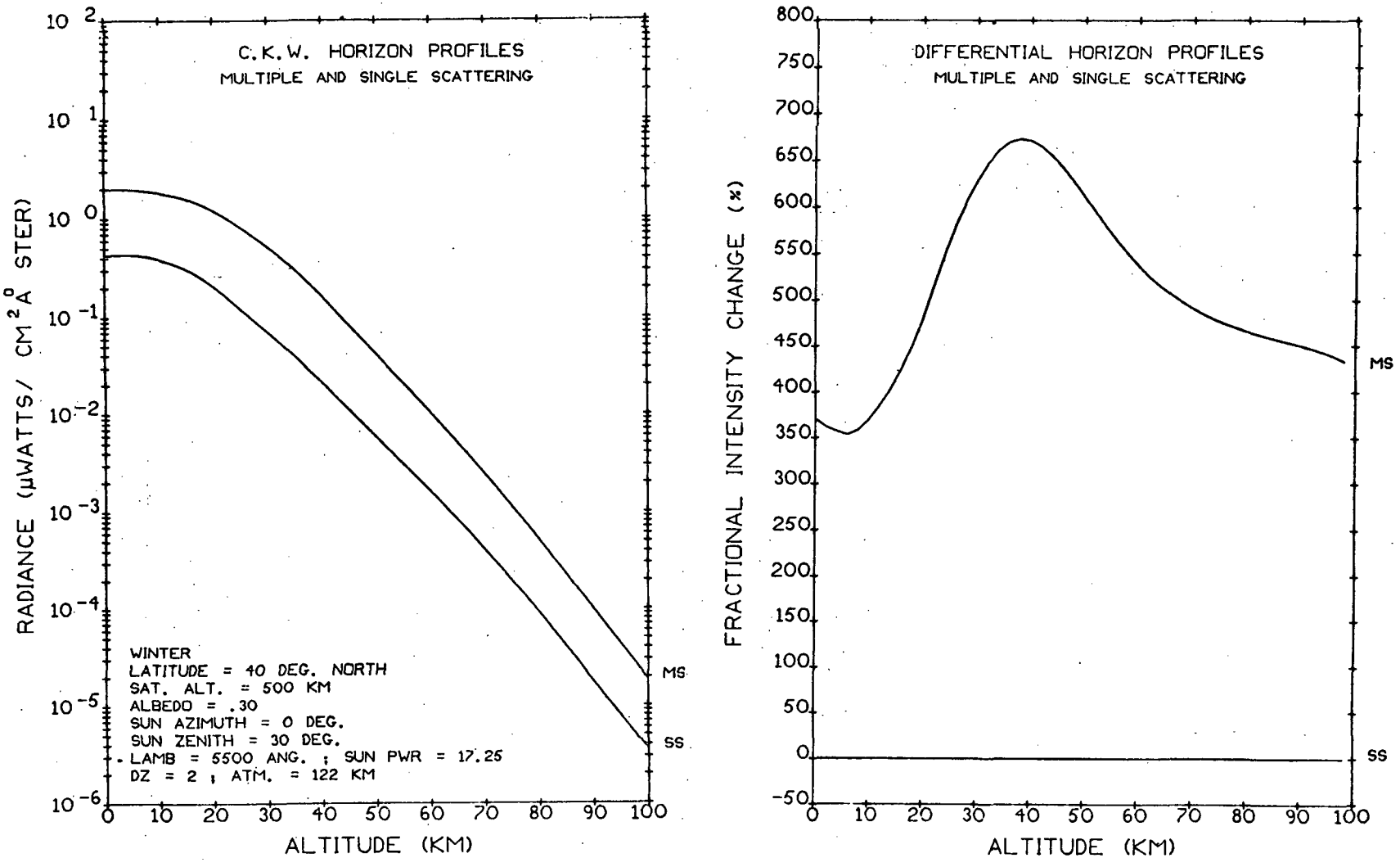

Fig. 3.2-2 Multiple and Single Scattering Horizon Profiles
(Zenith Angle = 30^{o}, λ=5500 $\mathring{A}$)

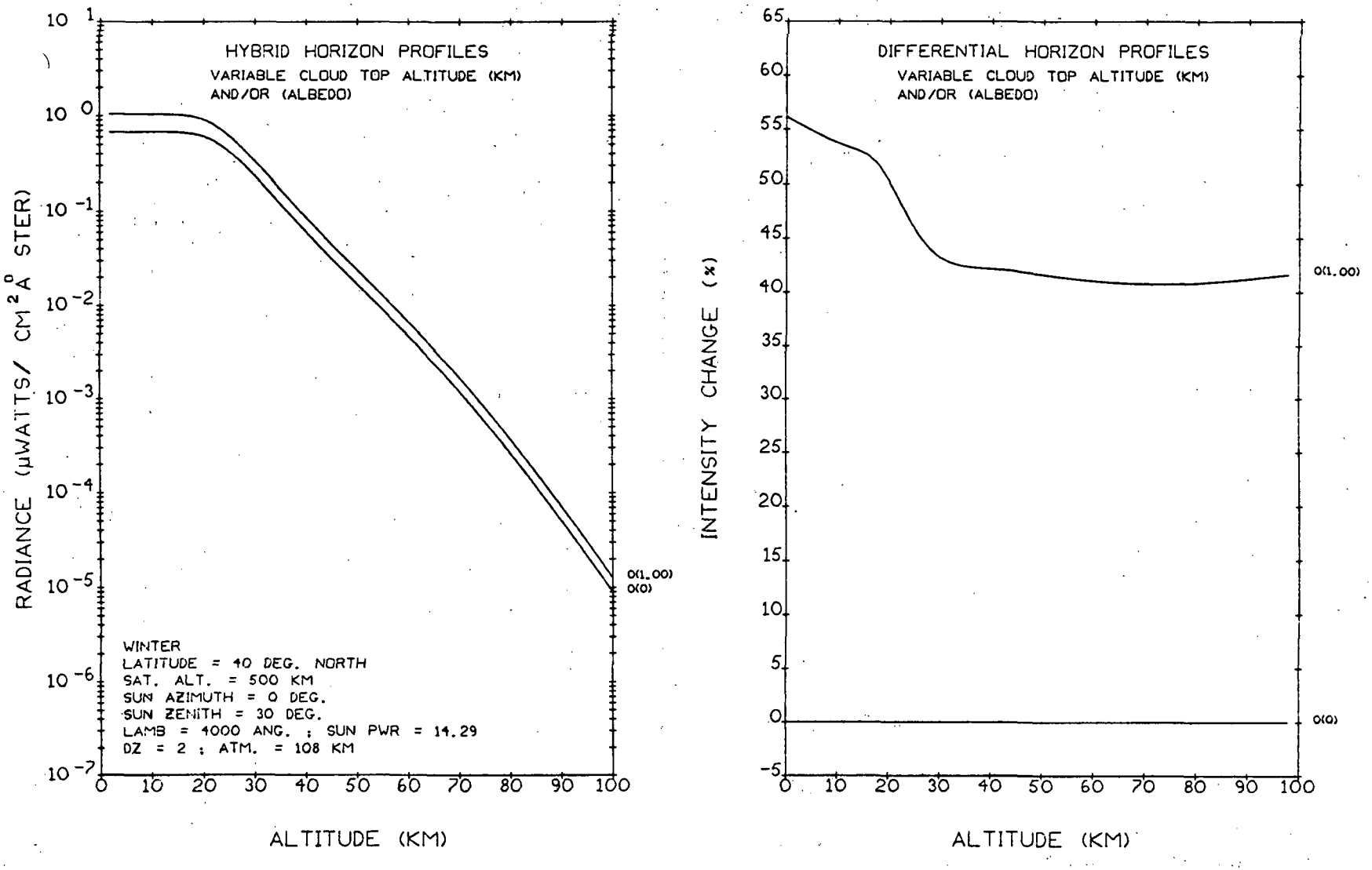

Fig. 3.2-3 Single Scattering REV.HYBRID Horizon Profiles for Planetary Albedos of 0 and 1.0 at 4000 Å.

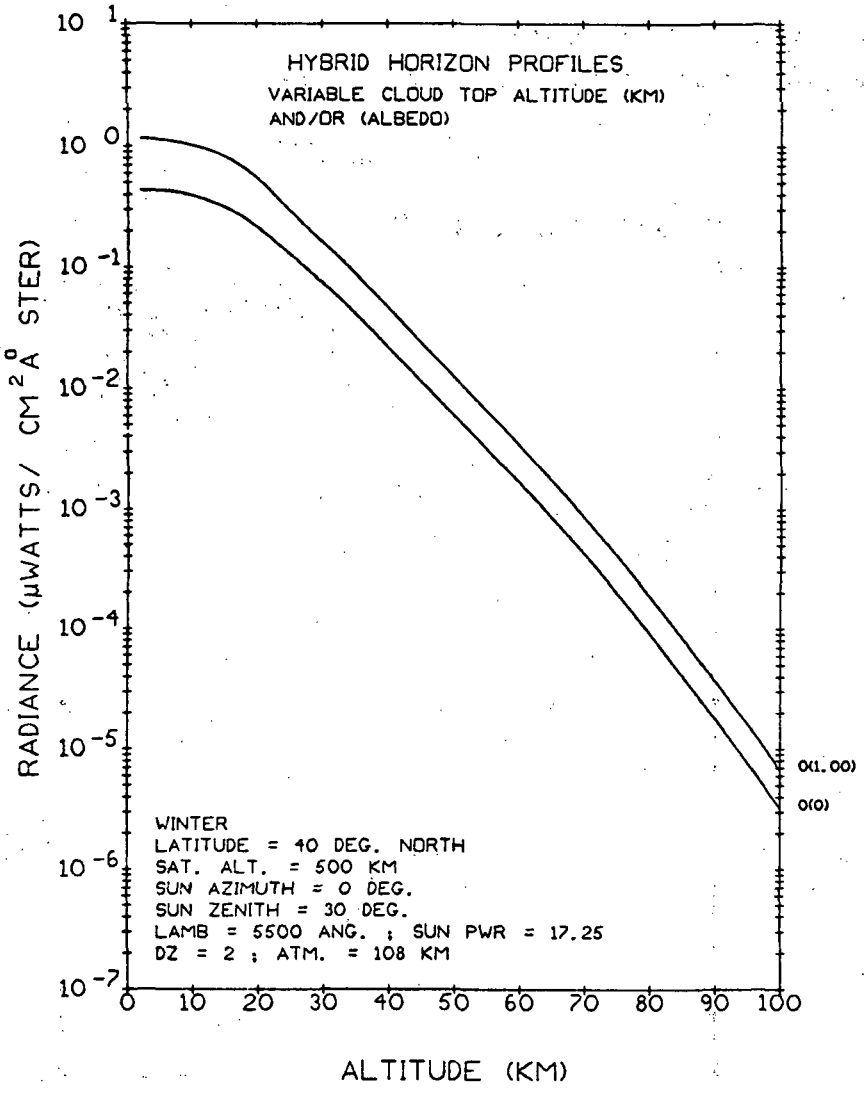

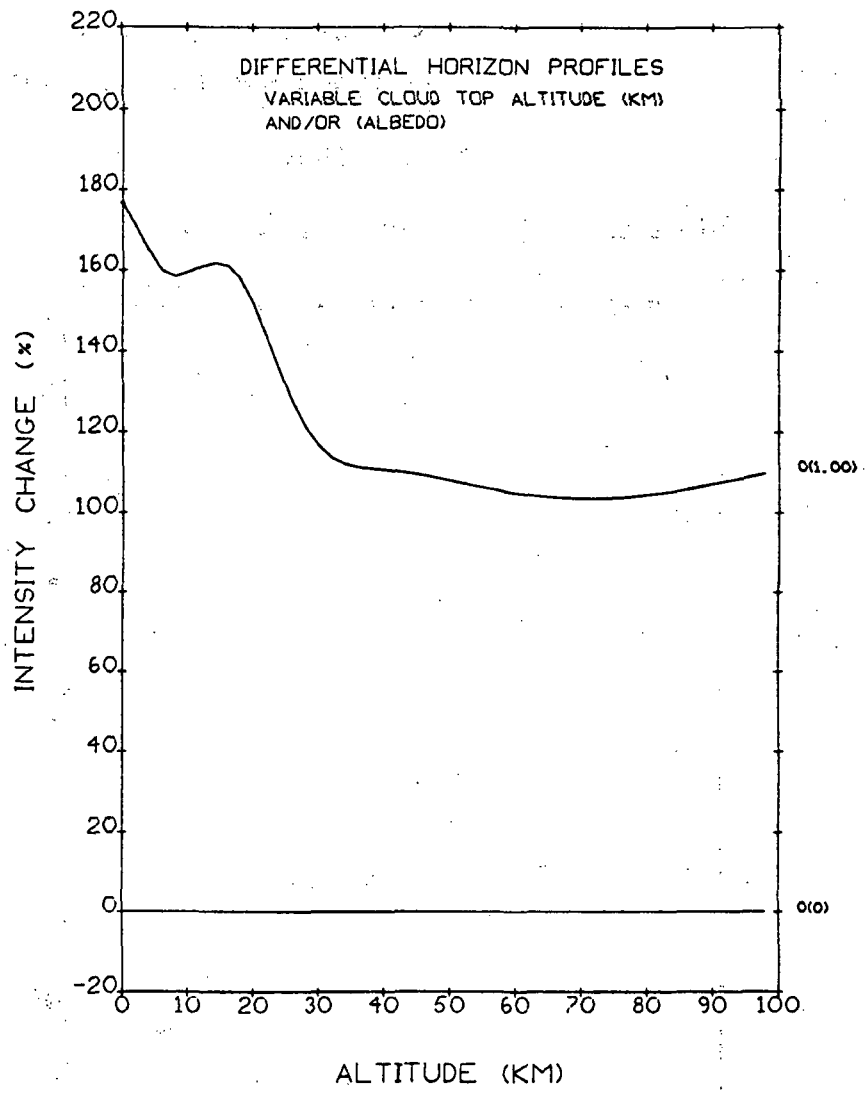

Fig. 3.2-4 Single Scattering REV.HYBRID Horizon Profiles for Planetary Albedos of 0 and 1.0 at 5500 Å.

3.3 AEROSOL MODELING

3.3.1 Introduction

The application of recursive filter algorithms to limb profile inversion of aerosols requires that at each recursion the aerosol optical properties be recomputed given an updated physical characteristic estimate. Aerosol optical and physical properties are related theoretically through the Mie equations which express the angular scattering contributions and cross section as a function of the physical parameters such as size and index of refraction. At each recursion the filter requires recomputed values of these quantities and also the partial derivatives of radiant intensity with respect to those physical characteristics that are included in the state vector. For example the partial derivative of intensity with respect to index of refraction is of the general form $\partial I/\partial n = (\partial I/\partial \tau)\ (\partial \tau/\partial n) + (\partial I/\partial P\ (\theta))\ (\partial P\ (\theta)/\partial n)$. Evaluation of $\partial \tau/\partial n$ and $\partial P\ (\theta)/\partial n$ involves the use of detailed aerosol models. Since computational times on the order of a minute are involved in determining these quantities using the Mie series, the total computer time required for inverting a single scan would be on the order of hours per scan just for aerosol calculations. Such an amount of time would be out of proportion to other calculational requirements posed by the filter algorithm, and inconsistent with the goal of near-real-time inversion capability.

The implications of this calculational complexity when matched with the desire for computational economy are that multicalculations with the Mie series are to be avoided, and some alternate procedure must be provided.

3.3.2 Choice of Models

Several alternate procedures for the Mie computations are suggested. For the simple one parameter size distribution with which we are concerned, there are four parameters to consider within each size range. These are wavelength (λ), size distribution parameter (α) (used in the distribution

law $n(r) = Ar^{-\alpha}$), and the two part index of refraction $m = (n) - i\,(n')$. Thus each scattering phase function and associated cross section is a function in four dimensions $P(\theta; \alpha, \lambda, n, n')$ and $\sigma(\alpha, \lambda, n, n')$. The empirical fit problem is thus to find a set of four dimensional functions to fit computed data to within some accuracy criterion. In addition the (θ) dependence of (P) must be described for any chosen set of parameters.

One approach would be to establish a four dimensional array of computed points and to interpolate between them. It was felt however that the search times involved in this procedure would be longer than desirable, and that the four dimensional interpolation procedure would be excessively complex.

Another approach, and the one taken here, is to fit, in a least squares sense, the computed data with continuous functions of the four variables. This has been done by applying a multivariate regression analysis to the computed Mie data for the extinction, scattering, and absorption cross sections (σ_T, σ_s and σ_a), and to the computed Mie phase function data at six selected angles, viz., 0^o, 20^o, 60^o, 110^o, 164^o, 180^o. The Mie data for each function (P, σ) was obtained for 81 points corresponding to all possible combinations of the three values assigned to each parameter, viz., α = 2, 4, 7; λ = 4000, 6000, 8000A; n = 1.3, 1.4, 1.5; and n' = 0, 0.02, 0.04. The continuous functions thus obtained for the phase functions and cross sections are listed in Appendix 5.2.

There are several options for the choice of a "goodness of fit" criterion. In general one can force fit with a least path moment weight called the best L_P approximation (Kahng, 1972). When $p = \infty$ the result is the Chebyshev "maximum residual" fit. When p = 2 we have the usual least squares fit. For this problem some (p) in between would perhaps be desirable; however since a multivariate computer code was readily available only for p = 2, this fit criterion was used and the resulting functions are least squares fits in four dimensions.

Phase Function Interpolation

To obtain $P(\theta; \alpha, \lambda, n, n',)$ for (θ) values other than $\theta_i = 0^o$, 20^o, 60^o, 110^o, 164^o, 180^o, an interpolation formula is required. A least squares polynomial fit could be made to the selected angle points, however, comparable accuracy was found to be obtainable by fitting log-linear straight lines between the function values P_i at the selected angles θ_i. Thus between the selected θ_i, values of $P(\theta)$ are given by

$$P(\theta_i \leq \theta \leq \theta_{i+1}) = P(\theta_i) \exp\left[\frac{\ln P(\theta_{i+1}) - \ln P(\theta_i)}{(\theta_{i+1} - \theta_i)}\right](\theta - \theta_i) \qquad (3.3\text{-}1)$$

Normalization

The interpolation formula has the advantage that it can be easily normalized to insure proper conservation of scattering by shifting each modeled (P) up or down by an amount determined by a closed form integral. The constant of normalization is just

$$c = 1/2\pi \sum_{i=1}^{5} P(\theta_i) \exp(-m_i \theta_i) \frac{\{\exp(m_i \theta_{i+1})\gamma_i - \exp(m_i \theta_i)\beta_i\}}{1 + m_i^2} \qquad (3.3\text{-}2)$$

where

$$\gamma_i = m_i \sin\theta_{i+1} - \cos\theta_{i+1} \qquad (3.3\text{-}3)$$

$$\beta_i = m_i \sin\theta_i - \cos\theta_i \qquad (3.3\text{-}4)$$

and

$$m_i = \{\ln P(\theta_{i+1}) - \ln P(\theta_i)\}/(\theta_{i+1} - \theta_i) \qquad (3.3\text{-}5)$$

3.3.3 Error Sources

It is possible to have considerable error in the phase function models for a particular set of parameters and still gain useful information from a model. The important thing is that the model represent an average over an ensemble of computed points that are representative of the phase function over the range of the parameters. For example if a modeled $P(\theta)$ has an RMS deviation of 25% at some angle, but variations of a parameter (say n') over its range cause $P(\theta)$ to change by say 200% then reliable partial derivatives and the concomitant inversion sensitivities can be obtained. The error sources and related limitations are described in the following subsections.

Several strong trends in the data that should outweigh the RMS residuals are evident. These are noted below.

1.0-10μ Size Range

1. There is a strong (n') dependence at both 164° and 180° as well as other angles in this region. The phase function is generally an order of magnitude lower for n' = 0.02 than for the n' = 0 case. The n' = 0.04 case drops $P(\theta)$ another 50%.
2. The $P(0^{\circ})$ values are twice as high for the n' = 0.02, 0.04 cases as for the n' = 0 case.
3. (n') effects are also strong at 20° and 60° (200% to 500% variation), as well as at other intermediate angles.
4. (λ) effects are strong (300%) at 0° and 180°. As expected, the (λ) dependence changes from $P(0^{\circ}) \propto 1/\lambda$ to $P(180^{\circ}) \propto \lambda$.
5. (α) effects are as much as 400% at $P(0^{\circ})$ and diminish with increasing (θ). Beyond 110° complicated forms result.
6. (n) effects are most noticeable and consistent at 164° (up to 300% variation). As (n) increases, $P(\theta)$ increases.

0.1-1.0μ Size Range

1. The (n') dependence at 164° and 180° is strong; (200% to 500%) unless $\alpha = 7$, elsewhere it is very weak (10%).
2. (n) effects are up to 200% at 164° and 180°, but diminish with increasing α and λ.
3. (λ) dependence is strongly linked to (α) over all (θ).
4. (n) effects at 164° are strong (200% to 300%) unless $\alpha = 7$, $\lambda = 8000$A.
5. (α) effects are strong at 0° (up to an order or magnitude), but correlated with (λ), $P(0^{\circ}) \propto 1/\alpha\lambda$.

0.01-0.1μ Size Range

1. (n') dependence is negligibly small over the range of all the other parameters.
2. (n) dependence is at most a 10% effect at the larger angles for $\alpha = 2$.
3. (α) and (λ) both strongly influence the phase function, but the effects are on a smaller (200%) scale than for the larger size ranges.

Mie Code Errors

To normalize the phase function generated by the weighted size distribution average, the Mie code performs a trapezoidal integration between the selected defining points, and adjusts the amplitudes by the proper constant to achieve conservative scattering. However, since much of the accumulated value of the normalizing integral $2\pi \int p(\theta) \sin\theta \, d\theta$ is obtained at small angles, the adjustment of the entire functional amplitude is very sensitive to the fineness of the angular defining intervals. This is particularly important for the larger particles which have rapidly decreasing phase function values near $\theta = 0$. In the (1.0-10μ) size range, a decrease in the small angle (θ) step size from 10° to 0.2° results in a factor of twenty adjustment of the phase function upward. The upwards adjustment is caused by the excessive integral accumulation under the trapezoidal function between 0° and the first defined point at 10° in the coarse sample.

Figure 3.3-1 shows an extreme case of this with angle step increments of 0.2^{o} and 10^{o}. Both curves in Figure 3.3-1 are normalized by integration to unity. The dashed curve is the actual curve under which the trapezoidal integration is performed rather than the computer-drawn straight line connecting the 0^{o} and 10^{o} points. In general the error due to the overall phase function adjustment for normalization is proportional to the difference between the scattering cross section as predicted by the evaluation of the $\theta = 0^{o}$ Mie series and the value obtained by integration of the phase function. For the (1.0-10μ) size range the maximum value of this error is about 25% for the $\Delta\theta$ intervals that were used in the calculations. In the (0.1-1.0μ) range the error is about 5% or less, and for the (0.01-0.1μ) range the error is less than 0.3%.

Size Distribution Sampling Errors

The power law distribution $n(r) = Ar^{-\alpha}$ is sampled at discrete (r) values within the chosen size ranges. Each (r) choice corresponds to a particular Mie scattering result for a particle of radius (r), and the resulting phase functions are averaged by combining the individual (r) phase values with the $(-\alpha)$ weight. Since this process has the effect of averaging out the oscillations related to the Bessel and Legendre series within the Mie series, the results depend somewhat on the fineness of the Δr integration steps. Table 3.3-I shows an example for the size range (1.0-10μ) with complex index of refraction. Differences between the phase function values for the range of 10 to 200 radius sample points are generally of the order of a few percent except for the 180^{o} values which differ by 20%. In Table 3.3-II similar values are shown for non-absorptive aerosols ($n' = 0$). Thirty percent differences in the phase function values occur here for a few angles, and indicate that the number of radius steps required for a few percent accuracy is nearer 100 than 10. However the required computer time is directly proportional to the number of integration steps.

TABLE 3.3-I

PHASE FUNCTION VALUES

NOMINAL CASE, $\alpha=2$, $\lambda=.4$, $n=1.4$, $n'=.02$, 1-10μ

NO. OF STEPS IN INTERVAL	PHASE ANGLE 0°	20°	60°	110°	164°	180°
10	372	.0367	.00406	.00120	.00126	.00122
50	368	.0373	.00411	.00122	.00118	.00164
100	368	.0371	.00418	.00119	.00124	.00152
200	368	.0372	.00418	.00120	.00123	.00154

TABLE 3.3-II

PHASE FUNCTION VALUES

$\alpha=2$, $\lambda=.4$, $n=1.4$, $n'=0$, 1-10μ

NO. OF STEPS IN INTERVAL	PHASE ANGLE 0°	20°	60°	110°	164°	180°
10	256	.205	.0151	.00264	.0114	.0578
50	249	.236	.0190	.00285	.0134	.0676
100	253	.203	.0196	.00245	.0141	.0728
200	253	.204	.0196	.00276	.0138	.0731

The derived aerosol model is based upon a 10 step integration, thus 30% errors may be expected in the (1.0-10μ) size range from this error source. Figure 3.3-2 shows a plot of the differences between the phase function values resulting from 10 step and 200 step size distribution sampling. The differences are expressed as a percentage of the phase function value for the 200 sample case. It shows that the effects of changing the sample step size are essentially random with regard to angular position.

Errors Related to Piecewise Function Fitting

The errors just discussed were related to the computational uncertainty of the phase function at a particular angle. The modeling procedure we have chosen connects the points f($P(\theta_i)$, θ_i) with exponential curves of the form $P(\theta) = A\exp(B\theta)$; thus even if the parameter model $P(\theta_i; n, n', \alpha, \lambda)$ were perfectly accurate there would be errors caused by the fluctuations of $P(\theta)$ between the select model points $P(\theta_i)$. This would be true whether the points were connected by exponential curves or by, e.g. a least squares polynomial fit. This error source would decrease in magnitude if the $P(\theta_i)$ sample points were more closely spaced, however the six chosen θ_i represent a compromise between accuracy and the need to limit model complexity. Each new θ_i requires a new L_P fit to find the modeled $P(\theta_i; n, n', \alpha, \lambda)$, however the data shows that the θ_i choices should be optimized for each size range separately. For example, Figure 3.3-3 shows the log-linear fit to the (0.01-0.1μ) case having the most curvature. The fit is in error by a maximum of 14%. The RMS error for this case is 7%. For some of the better fits in this size range the RMS error is about 4%. The case illustrated in Figure 3.3-3 could be improved by the addition of points defined around 30°, 90°, and 110°. However the choice of defining angles for a given size range is not a simple matter to be solved by examination of a single curve. The noticeable structure in the curves in the backscatter region moves over a range of (θ) when the various parameters are changed.

Figure 3.3-4 shows the six point fit to one of the worst-fit cases in the (0.1-1.0μ) range. In this size range the points of fit correspond quite

closely with the major points where curvature changes, however it can be seen from the figure that additional defining points would be helpful here at 130^{o} and 176^{o}. The maximum error for the $(0.1\text{-}1.0\mu)$ case is 56%, with an RMS error of 21.5%, 1σ.

In the $(1.0\text{-}10\mu)$ size range the standard points of definition do not fit the Mie curves well, and three or four additional points should be used for a better fit. A particularly bad-fitting case is shown in Figure 3.3-5. The minimum for the phase function is at 130^{o} and is missed by the approximate fit point at 110^{o} causing large errors at 130^{o}. The 6-point function also ignores the secondary peak at 150^{o}, and fits badly at 10^{o}. Over the range of parameters considered, the position of the phase function minimum for the $(1.0\text{-}10\mu)$ size range varies over the interval $110^{o}\text{-}130^{o}$. Thus, improved modeling of this size range would require inclusion of extra defining points within this interval. The maximum error for this case is 630% at 130^{o}. The RMS error is 400%.

The RMS errors listed in this section are based upon the sequence of discrete angles used in the Mie computations. Since these angles are defined with smaller increments at small and large angles, there is a built-in weighting which may adjust the RMS error value somewhat either upward or downward (depending on the particular fit) from the RMS error which would result from a uniform disbursement of sample points.

In summary, the errors due to the piecewise log-linear fit at six preselected angles are moderate but within useable limits for the $(0.01\text{-}0.1\mu)$ and $(0.1\text{-}1.0\mu)$ size ranges. The errors are too large for the large particle range $(1.0\text{-}10\mu)$ which implies that an optimization procedure should be constructed for choosing the angular points of definition.

Parametric Fluctuations

It is of interest to examine the effects of small changes in the defining parameters (α, λ, n, n') to see whether or not the phase function is undergoing rapid fluctuations near the selected nominal parameter values. If this were the case there would be no guarantee that the value of $P(\theta)$ at the nominal

parameter value was actually representative of $P(\theta)$ in the region around the selected value.

This problem was investigated by means of a set of Mie calculations with small perturbations from the standard points. Deviations from the case $\alpha = 2$, $\lambda = 4000$A, $n = 1.4$, $n' = 0.02$ were considered by running cases with $\alpha = 2.1$, $\lambda = 4100$A, $n = 1.41$ and $n' = 0.021$. The (1.0-10μ) size range was considered because it exhibits the most erratic behavior and should represent a worst case. The results are tabulated in Table 3.3-III.

TABLE 3.3-III

LINEARITY PARAMETER ξ FOR A 1-10μ CASE

Phase Angle	(α)	(n)	(n')	(λ)
0°	ξ=2.3	2.4	0.12	4.2
20°	9.0	1.6	0.2	7.7
60°	0.36	5.0	2.7	18.0
110°	0.91	0.18	0.27	1.0
164°	1.2	1.6	0.12	2.1
180°	0.39	0.63	0.027	6.7

The number in the table is $\xi = \frac{\Delta P}{\delta P} \frac{\Delta x}{\delta x}$ where ΔP and Δx are the ranges of the phase function and the parameter expressed as a percent of the nominal value. The quantities δP and δx are the perturbed phase function and parameter values also expressed as a percent or fraction of the nominal values. If all the functional behavior were linear these values would be unity. Typical changes in the phase function indicate the $\xi = 4$ corresponds

to quadratic dependence. The results show that at λ = 4000A one has a rapidly varying phase function at 60^{o}, however the excursion from the value at 4000A to the value at 4100A is a variation of 21% which is comparable to the scale of other errors for this size range. Otherwise the fluctuations are relatively calm. The small values for (n') are related to the fact that P changes rapidly in the forward and backward directions for very small deviations of (n') from zero. Thus the range of P is large between values corresponding to n' = 0 and n' = 0.02, hence the small values of (ξ) for (n'). Since the modeling functions used were primarily quadratic, one expects to find relatively smooth behavior of the phase functions with respect to parametric variations over the parameter range.

Summary of Phase Function Modeling Errors

The models listed in Appendix 5.2 exhibit a complex error structure in general. However one can estimate the maximum RMS errors by assuming that the various sources of error are independent and thus that the errors can be added. The error sources are, in approximately decreasing order of importance, regression residuals, piecewise fitting errors, size distribution sampling errors, Mie Code normalizing errors, and higher order parametric fluxuations.

The regression residuals are listed in Table 3.3-IV with both maximum and RMS values given.

At the defined angles the total error consists of the regression error, the size distribution sampling error, and the normalizing error. If we take the typical size distribution sampling errors of Table 3.3-I as 1σ values, and the normalizing errors discussed above and combine them by means of a root mean sum of squares, the errors in Table 3.3-V are obtained at the defined phase function angles.

TABLE 3.3.-IV

RMS AND MAXIMUM RESIDUALS FOR PHASE FUNCTION PARAMETER MODEL

Phase Angle	0.01 – 0.1μ		0.1 – 1.0μ		1.0–10μ	
	σ(%)	Max.(%)	σ(%)	Max.(%)	σ(%)	Max.(%)
0°	0.3	0.9	3	8	3	10
20°	0.2	0.5	1.8	5	11	45
60°	0.1	0.3	4	9.5	8	23
110°	0.4	2.7	4.5	17	18.9	97
164°	0.25	0.6	6	15	31	120
180°	0.2	0.5	10	25	32	127

TABLE 3.3.-V

RMS ERRORS AT DEFINED ANGLES
INCLUDING NORMALIZATION AND SAMPLING INTERVAL ERRORS

Phase Angle	0.01 – 0.1μ	0.1 – 1.0μ	1.0–10μ
	(%)	(%)	(%)
0°	2%	6%	25%
20°	2%	5%	27%
60°	1%	9%	35%
110°	3%	15%	32%
164°	4%	9%	43%
180°	4%	16%	46%

In between these "defined" values the piecewise fitting errors must be added in proportion to the distance from the defined angle. These errors have been discussed in one of the previous paragraphs, and since no attempt has been made to assess them, statistically they will not be combined with the above table to produce a grand model error table. For the (0.01-0.1μ) size range the "in-between" errors are of the order of 10% at maximum. For the (0.1-1.0μ) range the maximum fitting error is roughly 50%, and for the (1.0-10μ) range it is approximately 100%. A graphical display of the error sources is shown in Figure 3.3-6.

3.3.4 Models of the Extinction, Scattering and Absorption Cross Sections

The cross sections were modeled by applying the regression procedure described above for the phase functions. Since the cross sections for absorption and scattering sum to the extinction cross section, only two of the three cross sections need be modeled in each case. Thus the two with the smallest variances were chosen from each set of three models and used to produce the third by algebraic combination. The errors for these quantities are listed in Table 3.3-VI.

TABLE 3.3-VI

CROSS-SECTION ERRORS

	0.01-0.1μ		0.1-1.0μ		1.0-10μ	
	σ(%)	Max(%) Error	σ(%)	Max(%) Error	σ(%)	Max(%) Error
σ_a (absorption)	3	10	2	5	2	9
σ_s (scattering)	0.3	1	-	-	-	-
σ_e (extinction)	-	-	10	34	18	52

The standard errors for the unlisted cross sections can be determined if the correlations are known, however, since these errors were not used explicitly in the inversion procedure the correlations were not computed.

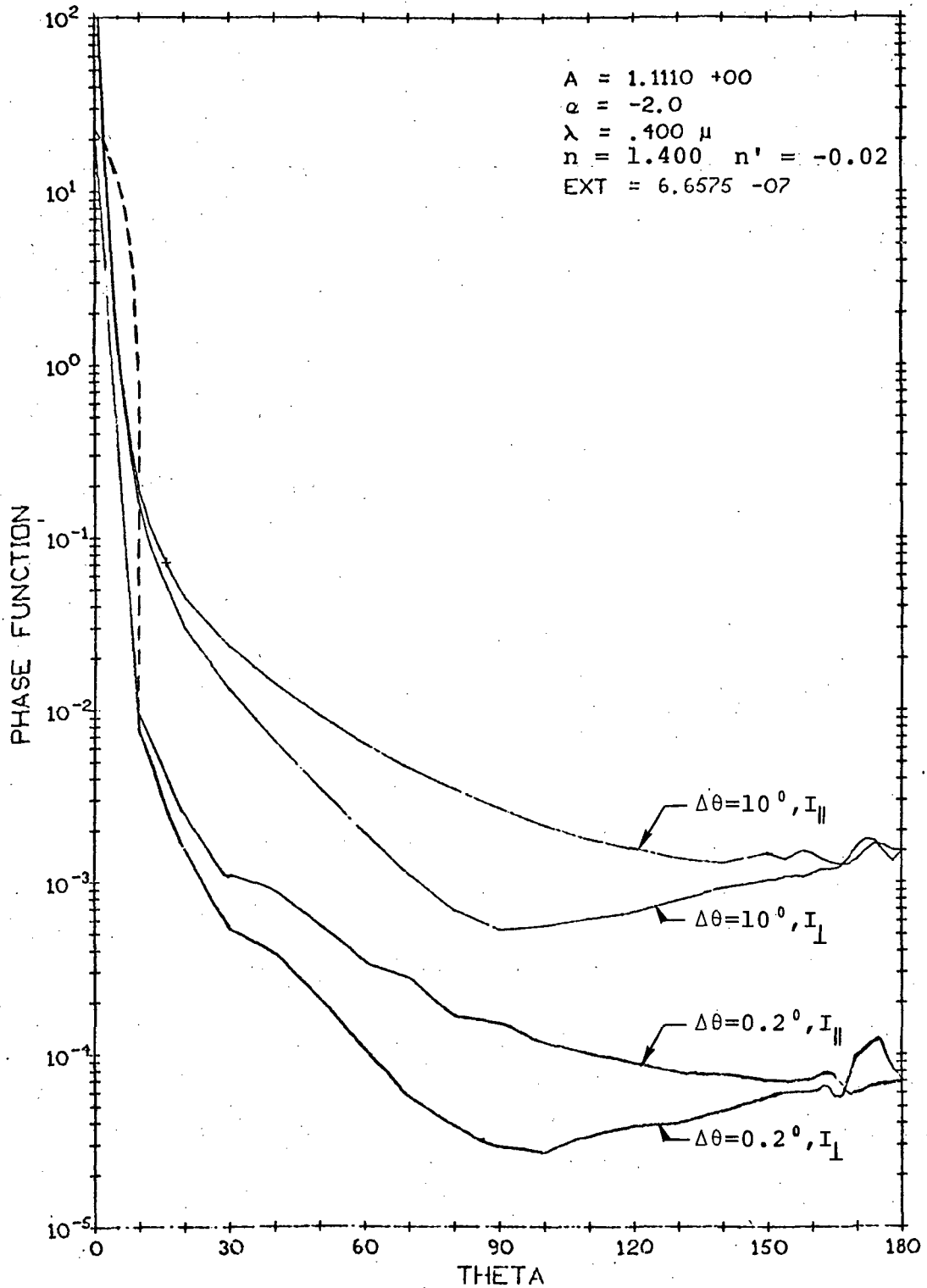

Fig. 3.3-1 Dependence of Normalization Adjustment Upon Δθ Sample Size.

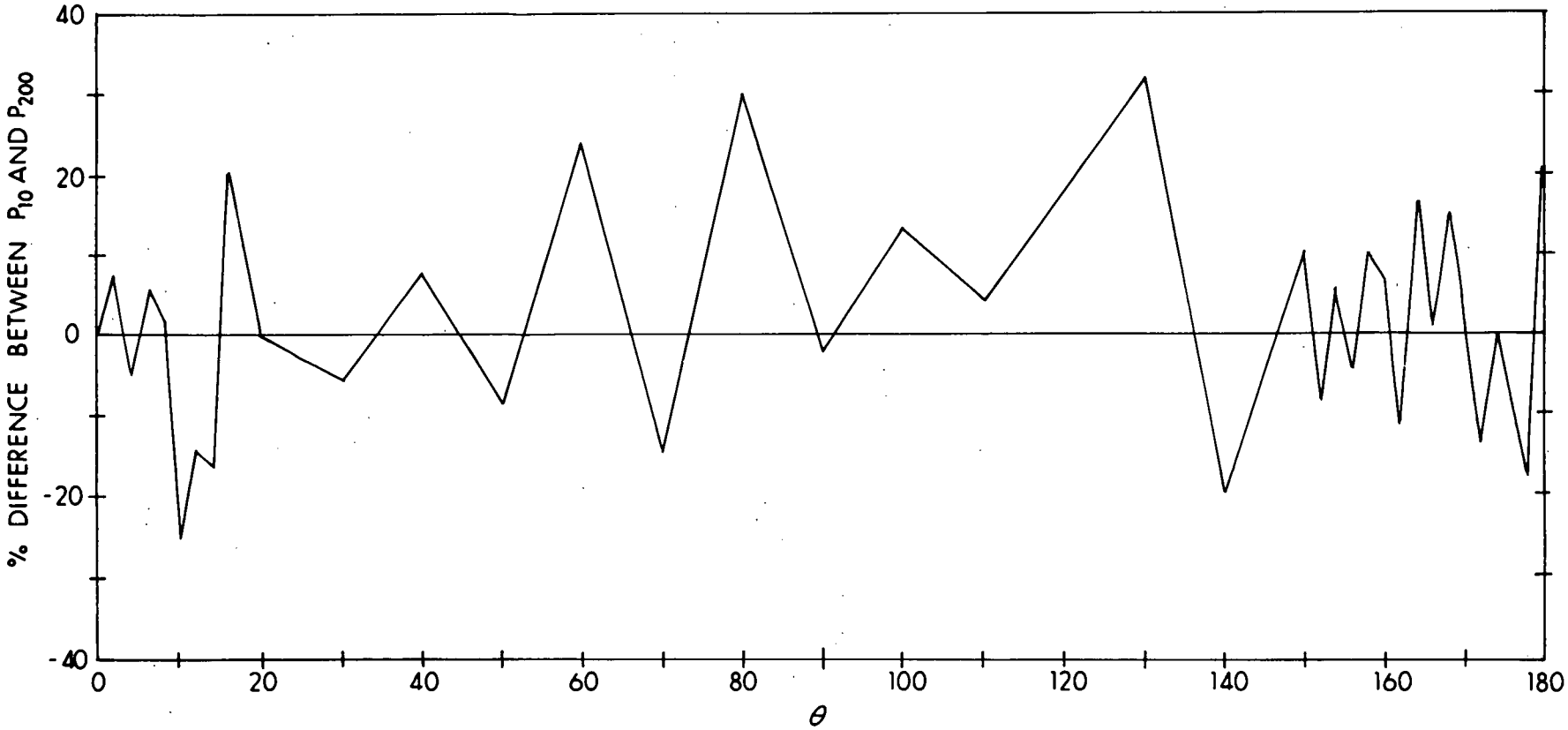

Fig. 3.3-2 Percent errors due to size distribution sample intervals using 10 and 200 steps, (1-10μ) aerosol size range

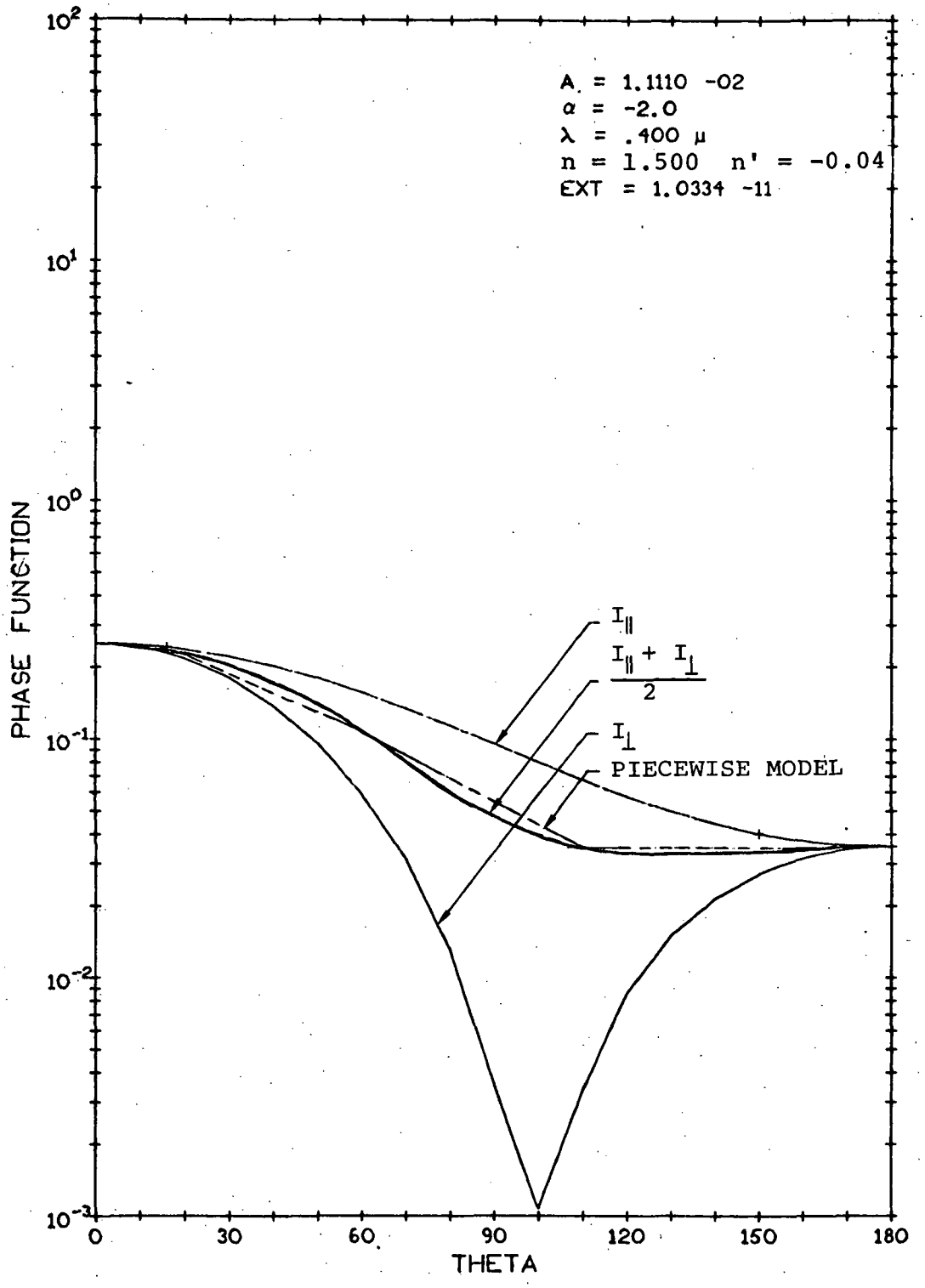

Fig. 3.3-3 Worst Case Fitting Errors, 0.01-0.1μ Range

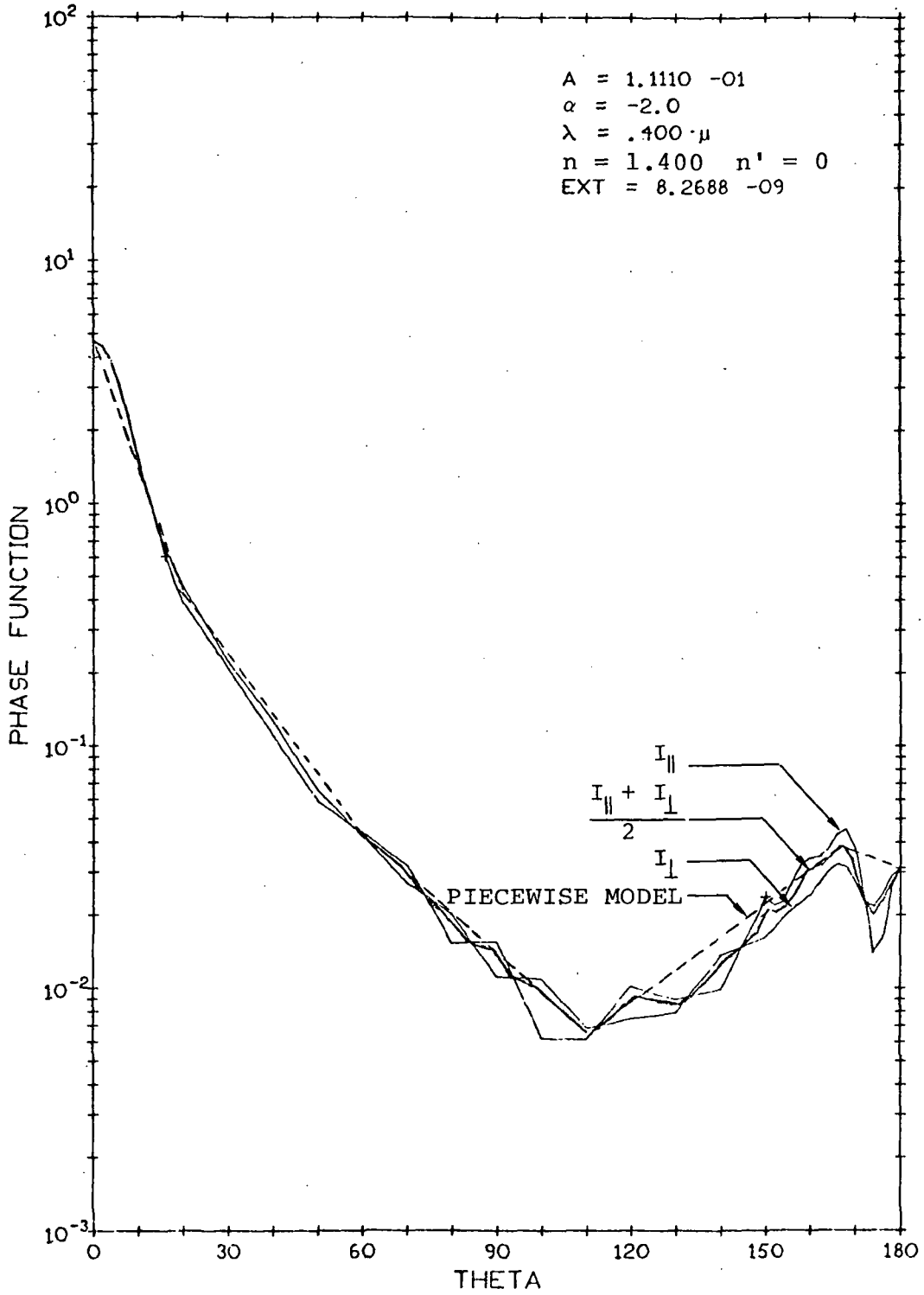

Fig. 3.3-4 Worst Case Fitting Errors,
0.1-1.0μ Size Range

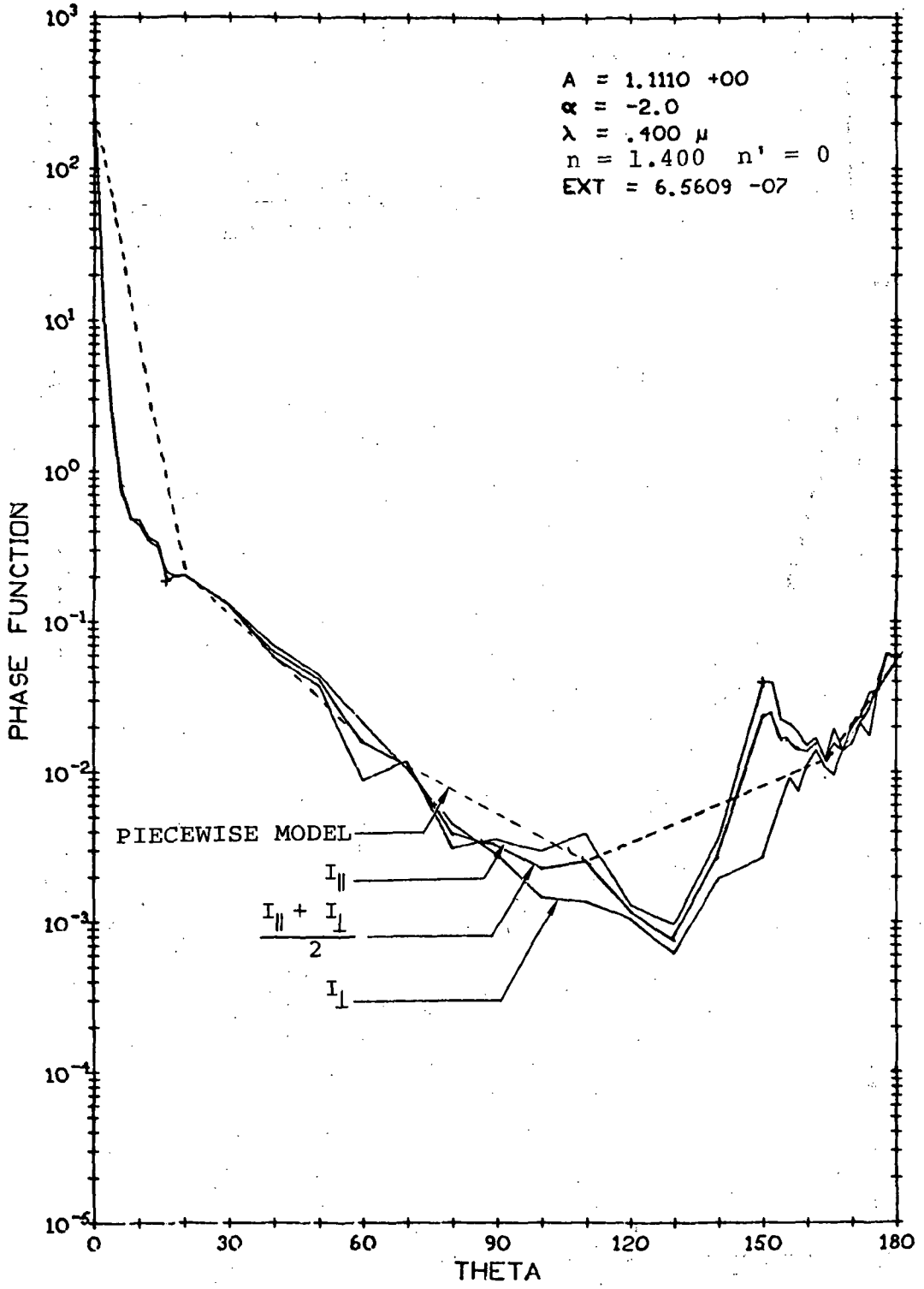

Fig. 3.3-5 Worst Case Fitting Errors, 1.0-10μ Size Range

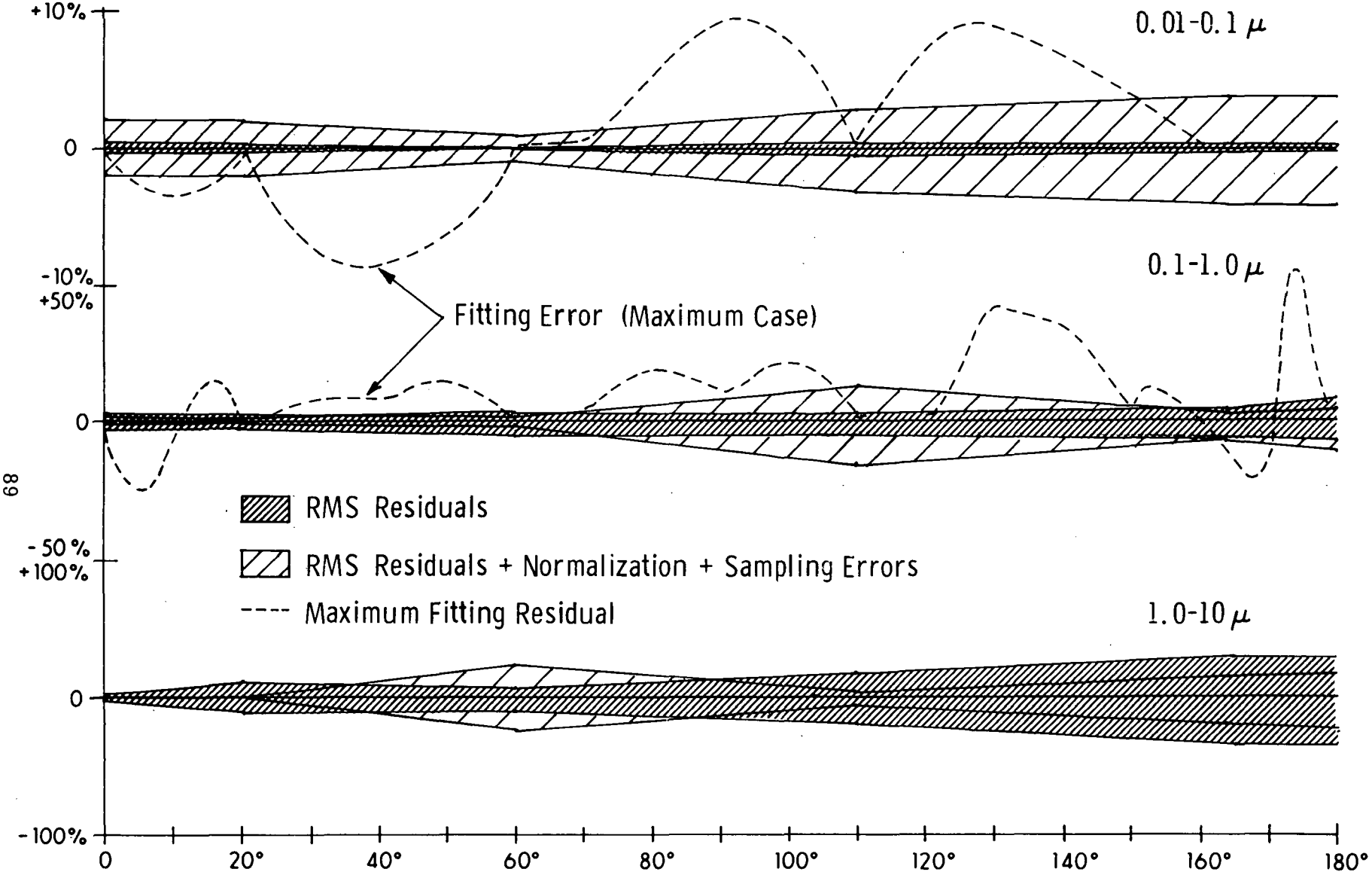

Fig. 3.3-6 Phase function error sources

REFERENCES

SECTION 3

1) Anderson, G.P., "The Vertical Distribution of Ozone between 35 and 55 Km as Determined from Satellite Ultraviolet Measurements", Thesis for Master of Science, Department of Astro Geophysics, University of Colorado, 1969.

2) Collins, D., and M. Wells, "Flash, A Monte Carlo Procedure for Use in Calculating Light Scattering in a Spherical Shell Atmosphere", AFCRL Report No. 70-0206, 1970.

3) Hayes, P.B., and R.D. Roble, "Stellar Spectra and Atmospheric Composition", J. Atm. Sci., 25, 1141-1153, November, 1968.

4) Hunt, G.E., "A Review of Computational Techniques for Analyzing the Transfer of Radiation Through a Model Cloudy Atmosphere", J. Quant. Spectrosc. Radiat. Transfer, 11, 655-690, 1971.

5) Kahng, S.W., "Best Lp Approximation", Mathematics of Computation, 26, 505-508, 1972.

6) Newell, R.E., and C.R. Gray, "Meteorological and Ecological Monitoring of the Stratosphere and Mesosphere", NASA Contractor Report, NASA CR-2094, August, 1972.

7) Var, R.E., "A Hybrid Algorithm for Computing Scattered Sunlight Horizon Profiles", MIT Aeronomy Program Internal Report No. AER 7-3, June, 1971.

8) Whitney, C.K., "Implications of a Quadratic Stream Definition in Radiative Transfer Theory", J. Atm. Sci., 29, 1520-1530, November, 1972.

4.0 SUMMARY

4.1 CONCLUSIONS — AEROSOL PHYSICAL PROPERTIES

The vertical distribution of aerosols from approximately 10 km upwards to 100 km can be determined globally by a satellite horizon inversion technique. Additionally, information such as the number density, the size distribution, and the complex parts of the index of refraction can be obtained.

Three particle size ranges (0.01-0.1μ, 0.1-1.0μ, 1.0-10μ) were considered in the simulations, and the results show that the quality of the physical characteristic information is size range dependent, i.e., that the relative observability of the physical characteristics changes from one size range to the next. For the smallest size range (0.01-0.1μ) the number density (ρ) and the size distribution parameter (α) are observable, but the indices of refraction are not. However this result rests partly upon the assumption that the initial uncertainties of the four modeled physical parameters are as follows: $\sigma_{\rho o} = \pm 300\%$, $\sigma_{\alpha o} = \pm 1$, $\sigma_{n'o} = \pm 0.005$, $\sigma_{no} = \pm 0.05$. Reductions in $\sigma_{\rho o}$ and $\sigma_{\alpha o}$ have the effect of increasing the observability of (n'). A simple covariance propagation case in this size range, using four kilometer horizon sample intervals and five wavelength channels, reduces the initial variances as follows: $\sigma_{\rho o}(\pm 300\%) \rightarrow \sigma_{\rho} = \pm 150\%$, $\sigma_{\alpha o}(\pm 1) \rightarrow \sigma_{\alpha} = \pm 0.1$, $\sigma_{n} \rightarrow \sigma_{no}$, $\sigma_{n'} \rightarrow \sigma_{n'o}$.

For the medium sized particles (0.1-1.0μ), using the same initial covariances, the simulations show that the complex part of the index of refraction becomes generally observable. The peak sensitivity of (n') jumps from a value of ≈ 0.01 to ≈ 0.4 which is in the highly observable range. A simple covariance propagationcase, using four kilometer horizon sample intervals and three wavelengths showed initial covariance reductions as follows:

$$\sigma_{\rho o}(\pm 300\%) \rightarrow \sigma_{\rho} = \pm 60\%, \qquad \sigma_{\alpha o}(\pm 1) \rightarrow \sigma_{\alpha} = \pm 0.2,$$

$$\sigma_{n'o}(\pm 0.005) \rightarrow \sigma_{n'} = \pm 0.001, \; \sigma_{no}(\pm 0.05) \rightarrow \sigma_{n} = \pm 0.05.$$

All four physical parameters are found to be observable for the large particle (1.0-10μ) size range. However the observability of the index of refraction is strongly dependent upon the scattering angle, i.e. the sun azimuth and zenith angles. For a scattering angle in the forward region ($\approx 50^{o}$), (n) is found to be unobservable. In the side-scattering region of the phase function(n') is unobservable and the observabilities of (n) and (α) are considerably reduced. However in the backscattering directions all four aerosol parameters are observable.

An estimate of the state errors resulting from errors in the models was made based upon the filter gain and computed horizon intensity deviations. The calculations show that the aerosol modeling errors induce physical parameter estimation errors that are generally smaller than the final variances resulting from a covariance matrix propagation. However the error analysis also shows that a deviation of the albedo of 0.5 from the assumed value can cause large uncertainties in the state vector elements. Thus the albedo should be included as an element of the state vector.

4.2 RESEARCH EXTENSION

The results obtained in study show how well one can determine the parameters of a specific aerosol model. For example the inchoate model developed for this research uses a single parameter, power law size distribution. If the real aerosol size distribution is of some other functional form, then the results of applying the chosen model in an inversion would be to obtain a best power law fit to the real function. If the best power law fit to the real function can be closely related to the real distribution, then the results are useful for aerosol research. To this end, then, it is important to attempt to generate the most realistic aerosol models possible. A first step in this direction is to insure that the ranges of the chosen variables cover the real physical range. This has been done in the model used here in every respect except the aerosol size range. Hence one of the next steps in a continuation of aerosol model development would be to reconstruct the model with variable particle radius limits. This would

increase the size of the state vector by two elements, however, the present model could be used to optimize the selection of wavelength channels. By fixing wavelength, the dimension of the model could be reduced by one element for a net increase of one dimension in the model.

To insure that fitting errors are minimized in extended aerosol models, a procedure should be constructed which determines a minimum set of phase function defining angles consistent with accuracy goals. The models should also make maximum use of the analytical relationships derived from ray optics (Van de Hulst, 1957) and information theory (Whitney, 1972).

The design of the filter algorithm should be further extended to include the additional states resulting from improvements in the aerosol model and from the inclusion of polarization measurements. The effects of model type error sources such as approximation errors in the radiative transfer simulation, fitting errors in the aerosol models, and relative fluctuations in the solar power output should be explicitly included in the filter formulation. As the aerosol models become more complex, additional sources of information will be required besides the measurements at different wavelengths. Two possible sources are measurements at different solar angles and measurements of polarization. The present radiative transfer simulation for a curved atmosphere includes the necessary polarization calculations, however, these simulations would have to be checked against other results to insure their accuracy. Accurate inclusion of cloud scattering effects at low sun angles ($<10^{o}$) would require modifications of the existing code as well as simulations of the transfer problem within a cloud.

REFERENCES

SECTION 4

1) Van de Hulst, H. C., Light Scattering by Small Particles, John Wiley & Sons, Inc., New York, 1957.

2) Whitney, C. K., "Stream Transformation and Phase-Function Integrals in Radiative Transfer Theory", MIT Aeronomy Program Internal Report No. AER 22-3, January, 1972.

5.0 APPENDICES

5.1 THEORETICAL HORIZON PROFILES

This appendix contains the theoretical multiple scattering horizon profiles discussed in Section 2.3. The profiles illustrating the effects of changes in various measurement parameters are arranged as follows.

Figure Numbers	Variable Measurement Parameter(s)
5.1-1 to 5.1-12	Season; for 12 combinations of latitude and wavelength.
5.1-13 to 5.1-28	Wavelength; for 16 combinations of cloud cover, ground cover and zenith angle.
5.1-29 to 5.1-64	Zenith angle; for 36 combinations of azimuth angle, wavelength, and ground albedo.
5.1-65 to 5.1-72	Ground albedo; for 8 combinations of zenith angle and wavelength.

The units of solar irradiance (SUN PWR) are in μwatts/cm^{2}A.

Figures 5.1-73 to 5.1-84 show the vertical distributions of neutral and ozone densities for 12 combinations of season and latitude. These figures illustrate the mean and one sigma standard deviation values about the mean.

Neutral density data was obtained from Valley, 1965 and from the data compiled by Groves, 1970. The designations winter, spring, summer, and fall refer to the months January, April, July, and October. The ozone density data was generated from the modified Fermi distribution function developed by Wu, 1970 and the peculiar appearance of the ozone density distribution for the minus one sigma curve is due to the fact that the one sigma values are equal to or greater than 100 per cent of the mean value below approximately 10 km and again above approximately 50 km. Aerosol extinction data was compiled from a variety of sources by Malchow, 1971 and the composite model illustrated in Figure 5.1-85 was constructed.

Latitudinal variations in the aerosol extinction data were accounted for on the basis of data gathered by Salah, 1971 as illustrated in Figure 5.1-86. Due to a lack of sufficient seasonal distribution, this aerosol extinction data was used to represent the four seasons.

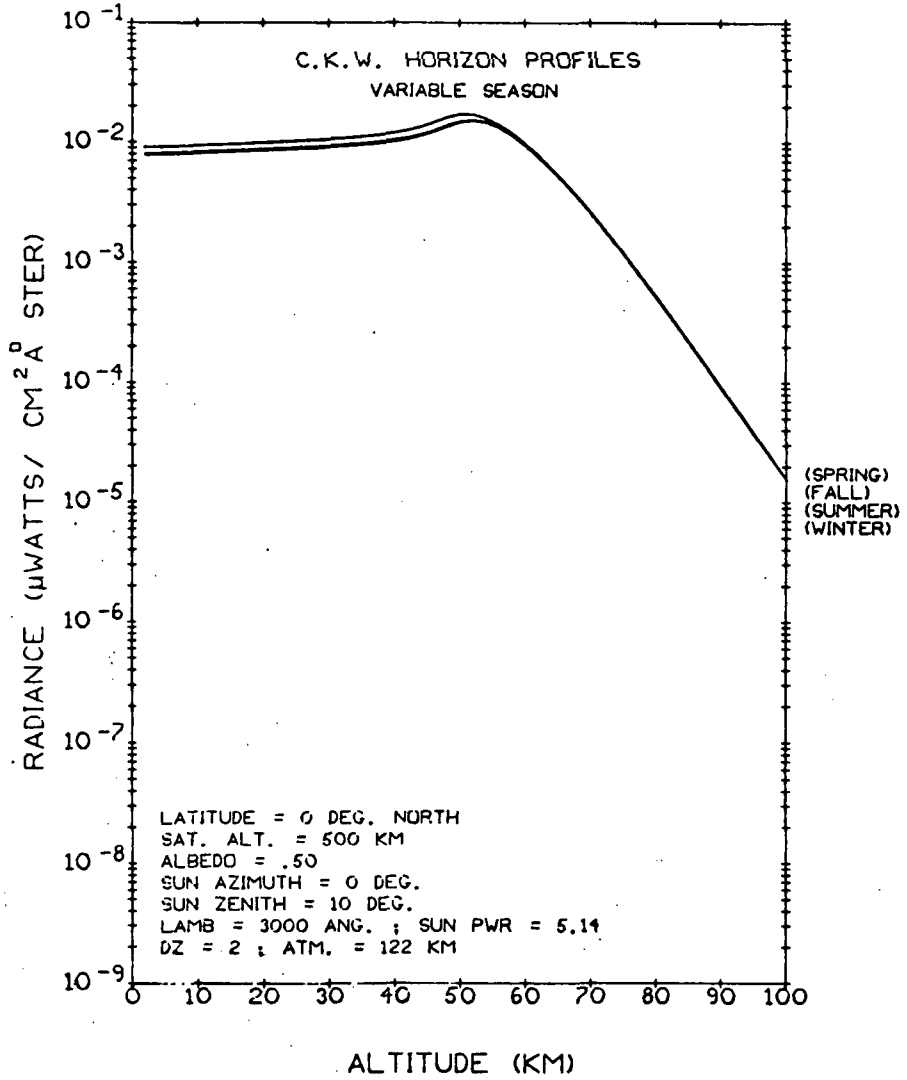

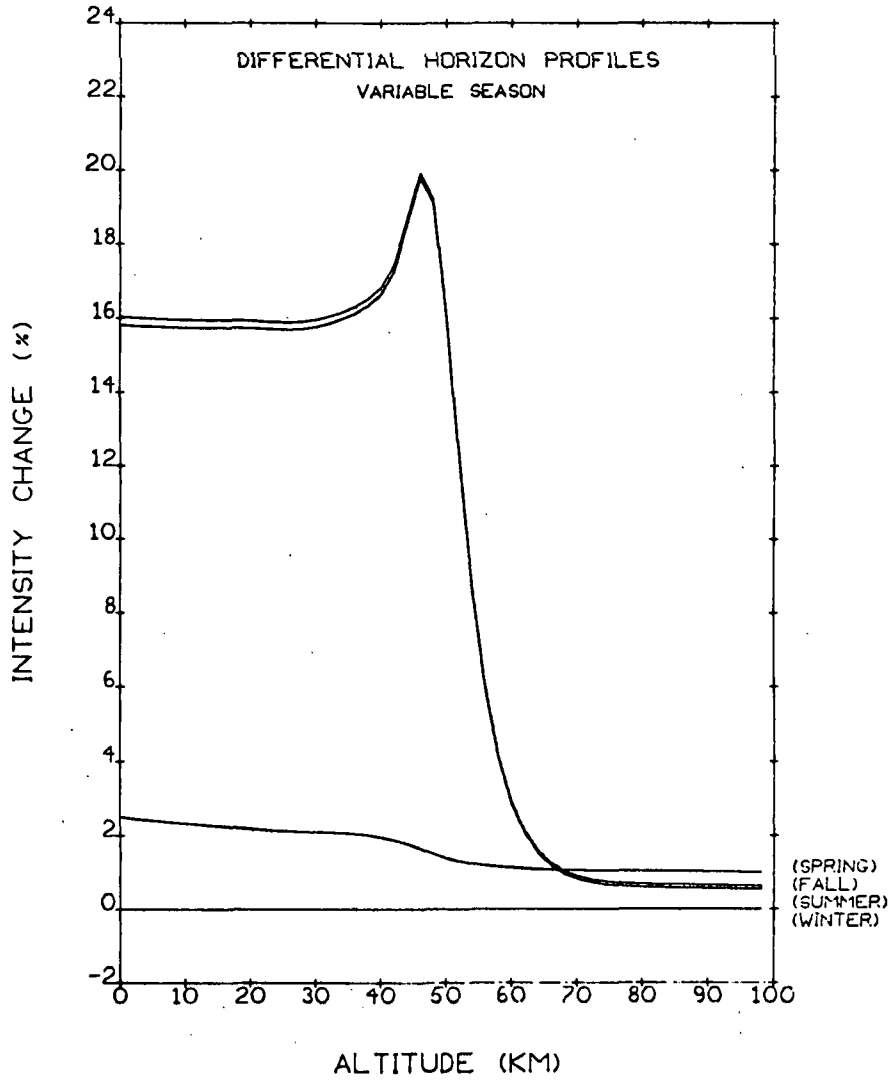

Fig. 5.1-1 Variable Season Horizon Profiles (λ=3000 Å, LAT.=0°N)

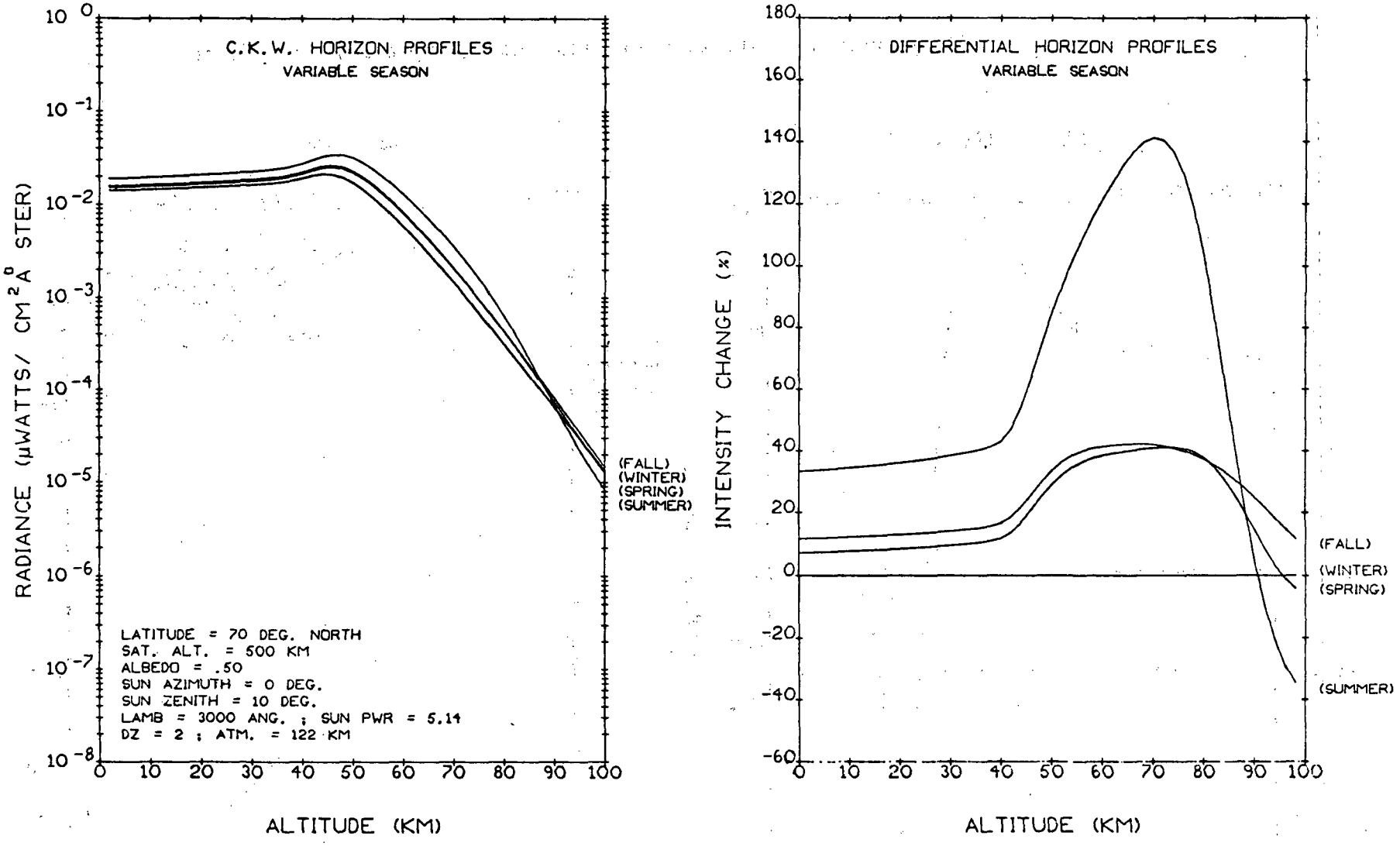

Fig. 5.1-3 Variable Season Horizon Profiles (λ=3000 Å, LAT.=70°N)

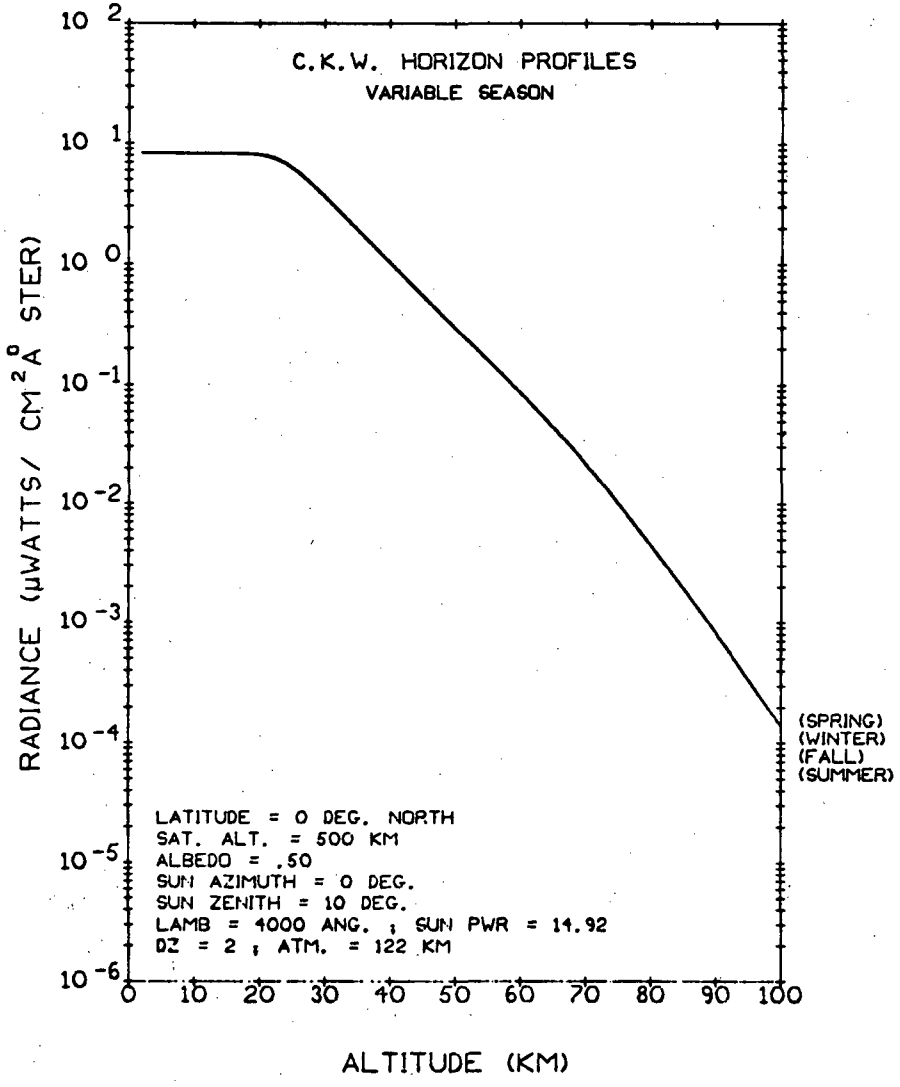

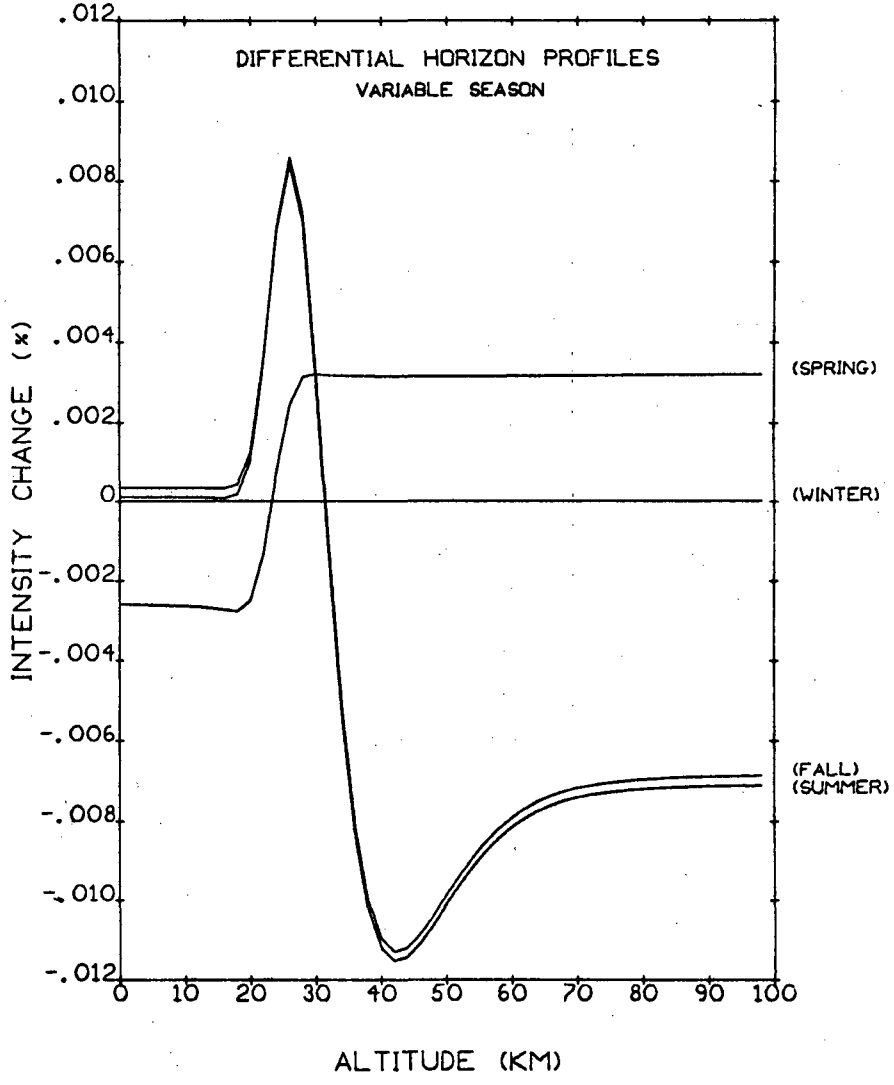

Fig. 5.1-4 Variable Season Horizon Profiles (λ=4000 Å, LAT.=0°N)

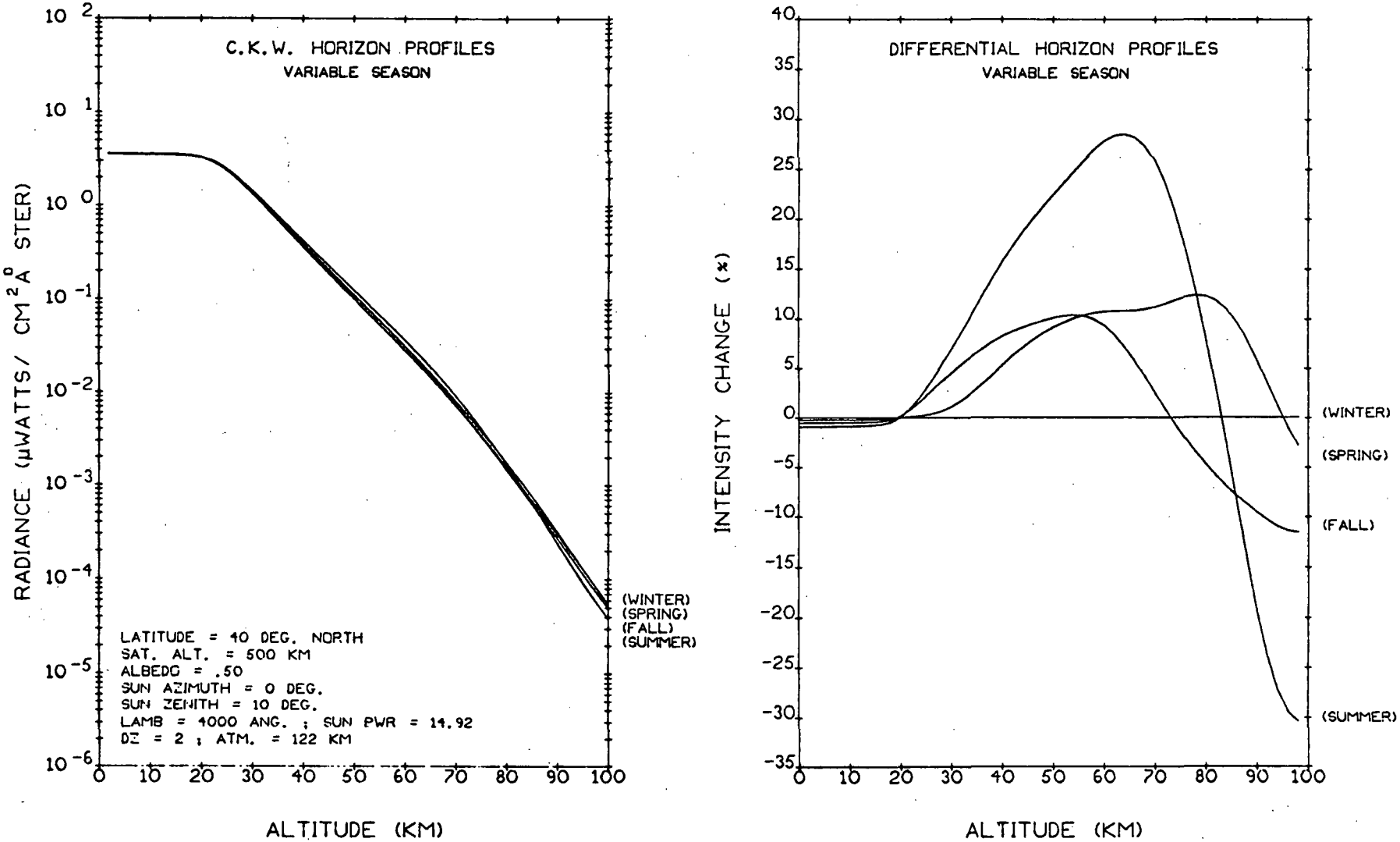

Fig. 5.1-5 Variable Season Horizon Profiles (λ=4000 Å, LAT.=40°N)

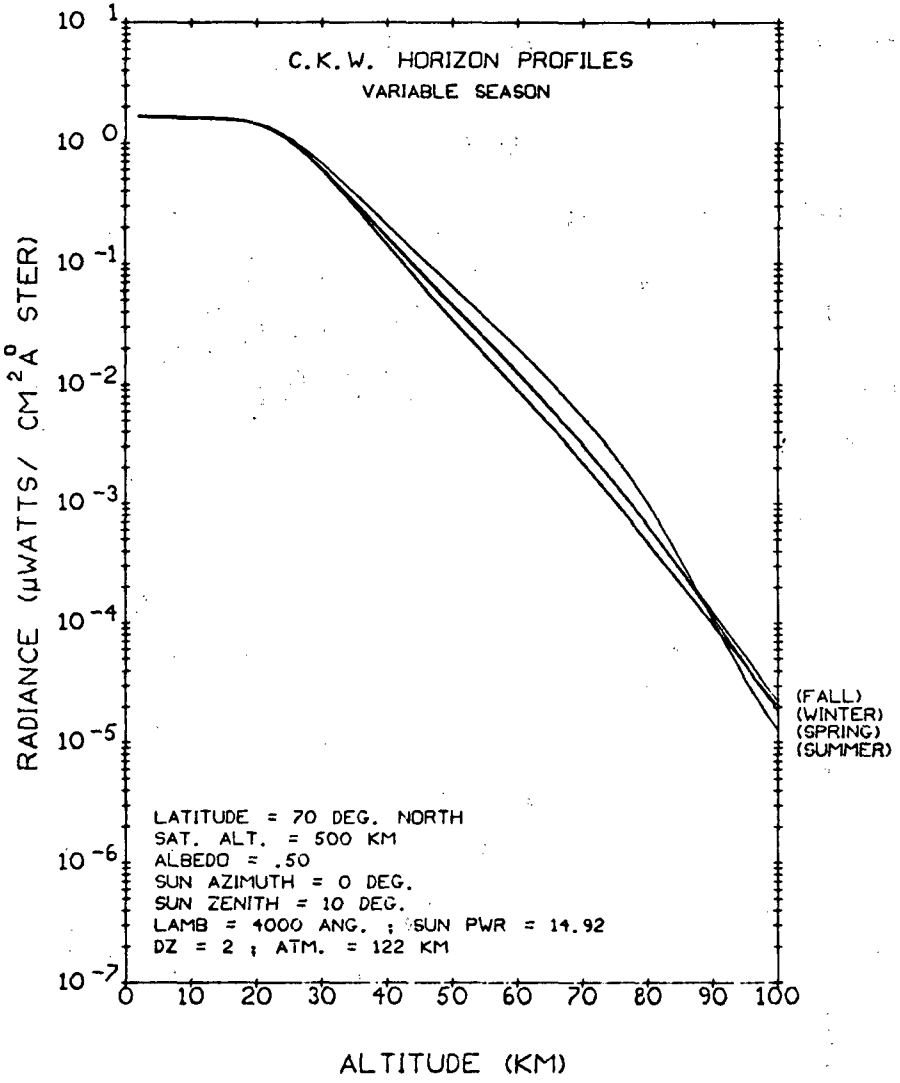

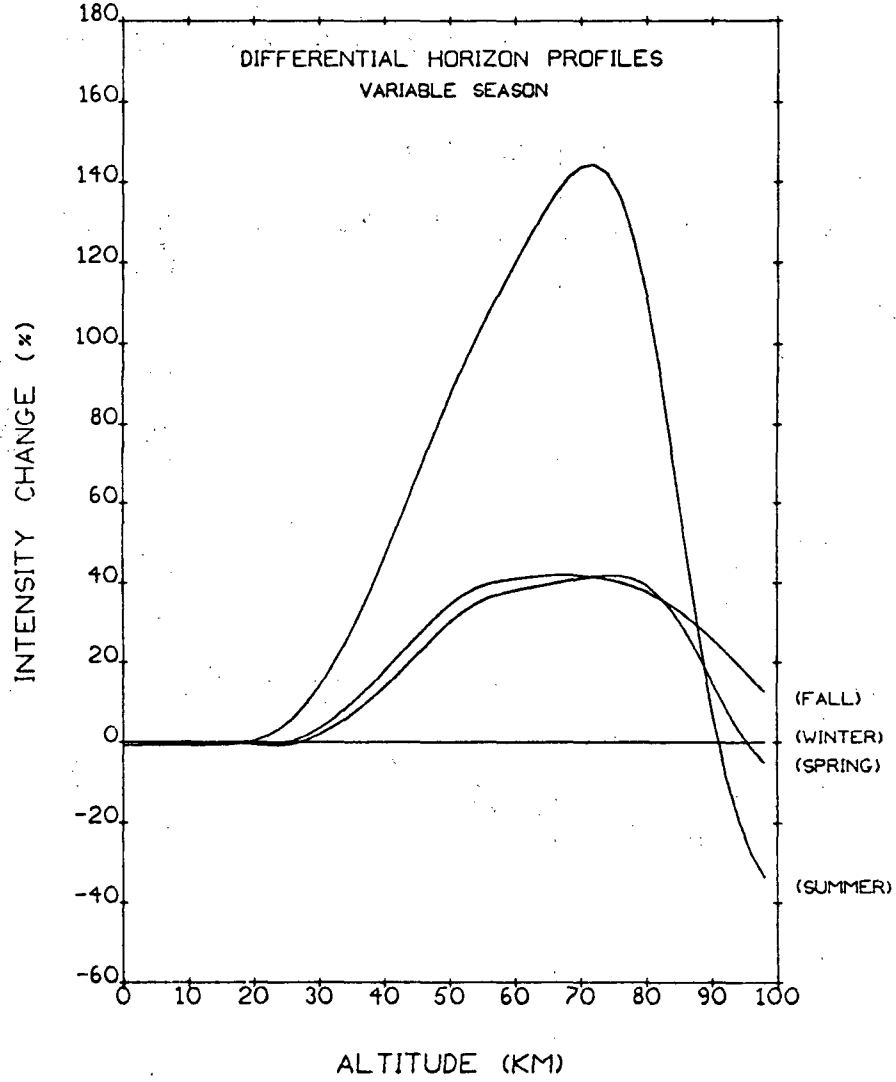

Fig. 5.1-6 Variable Season Horizon Profiles (λ=4000 Å, LAT.=70^{o}N)

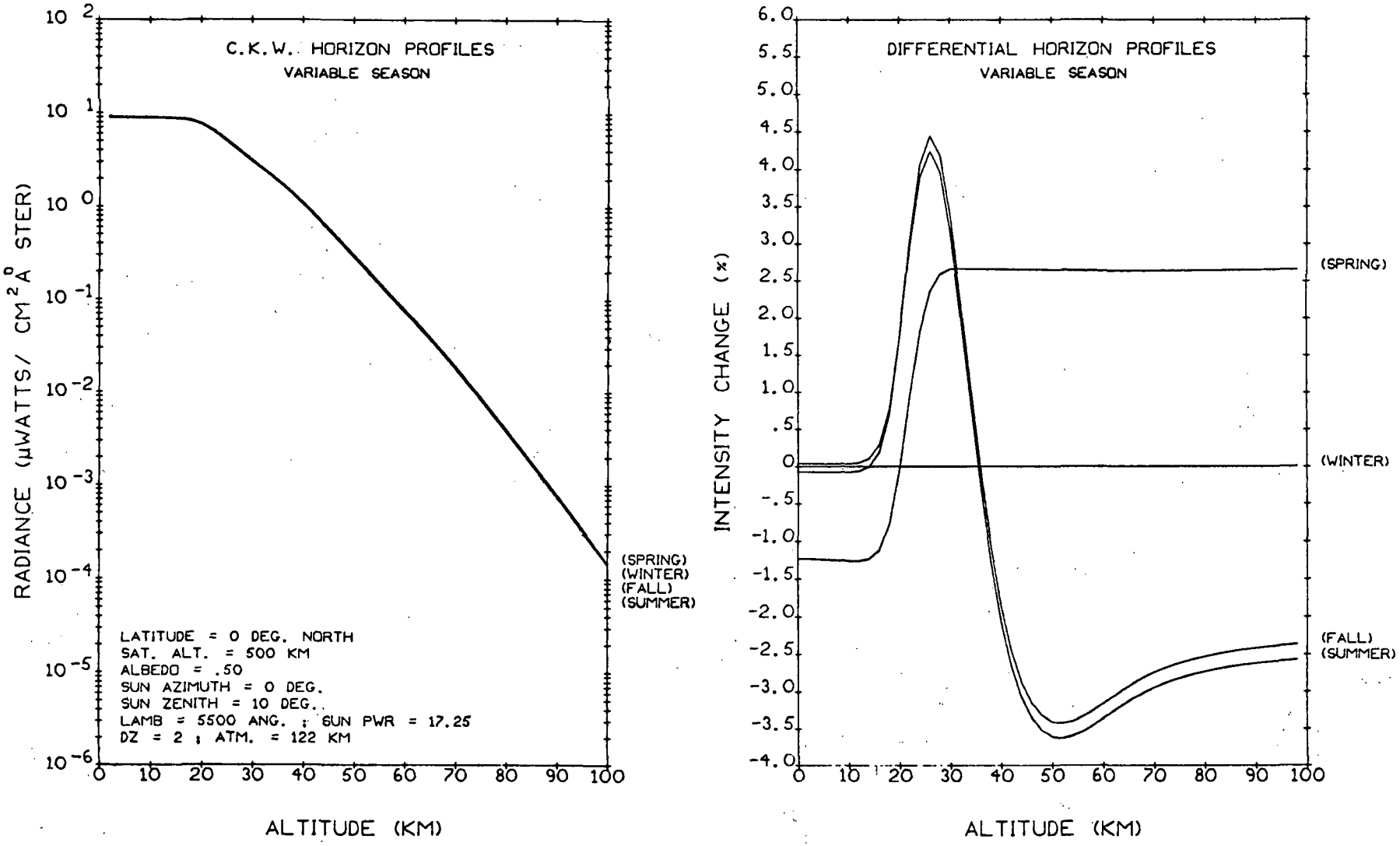

Fig. 5.1-7 Variable Season Horizon Profiles (λ=5500 Å, LAT.=0°N)

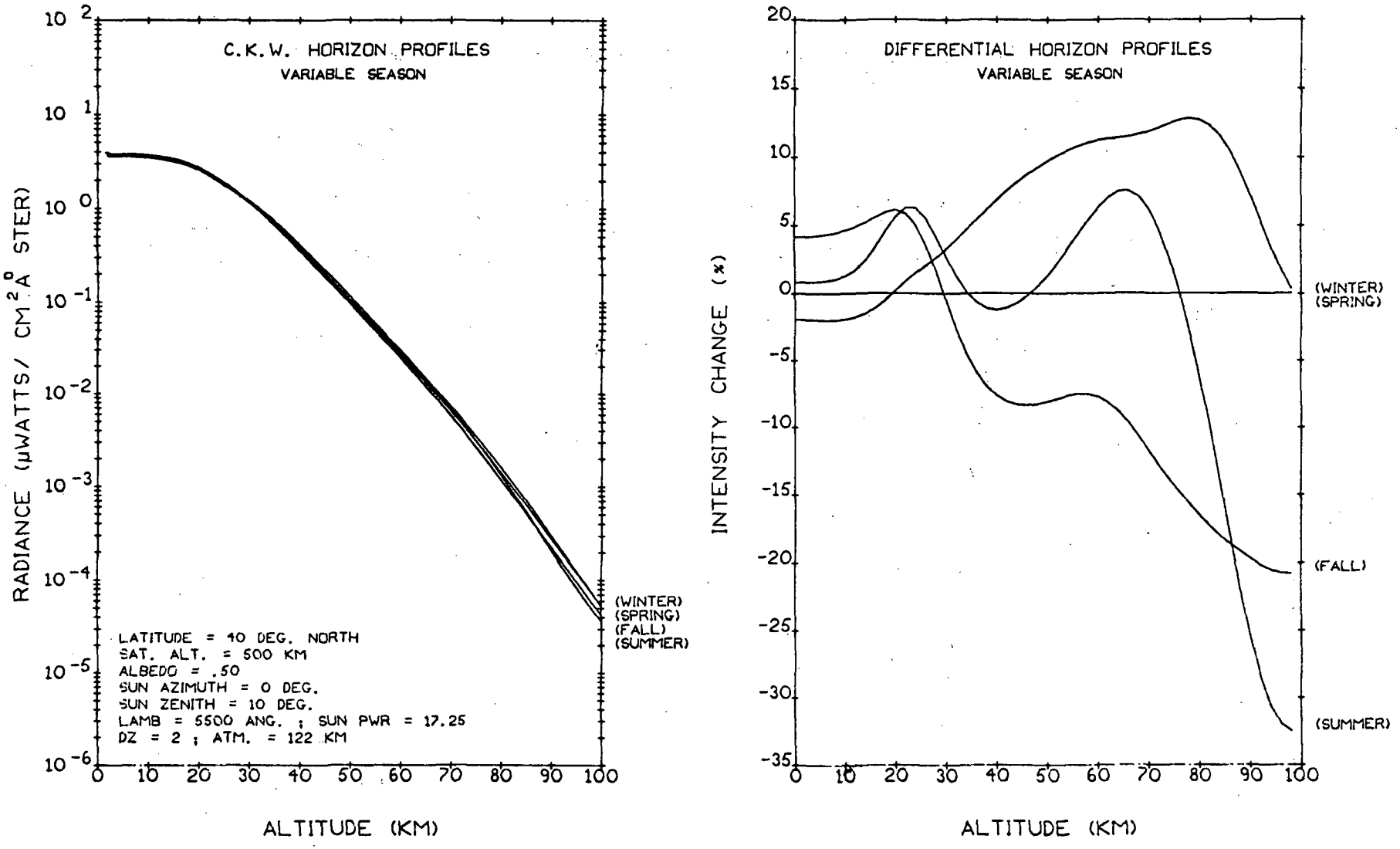

Fig. 5.1-8 Variable Season Horizon Profiles (λ=5500 Å, LAT.=40°N)

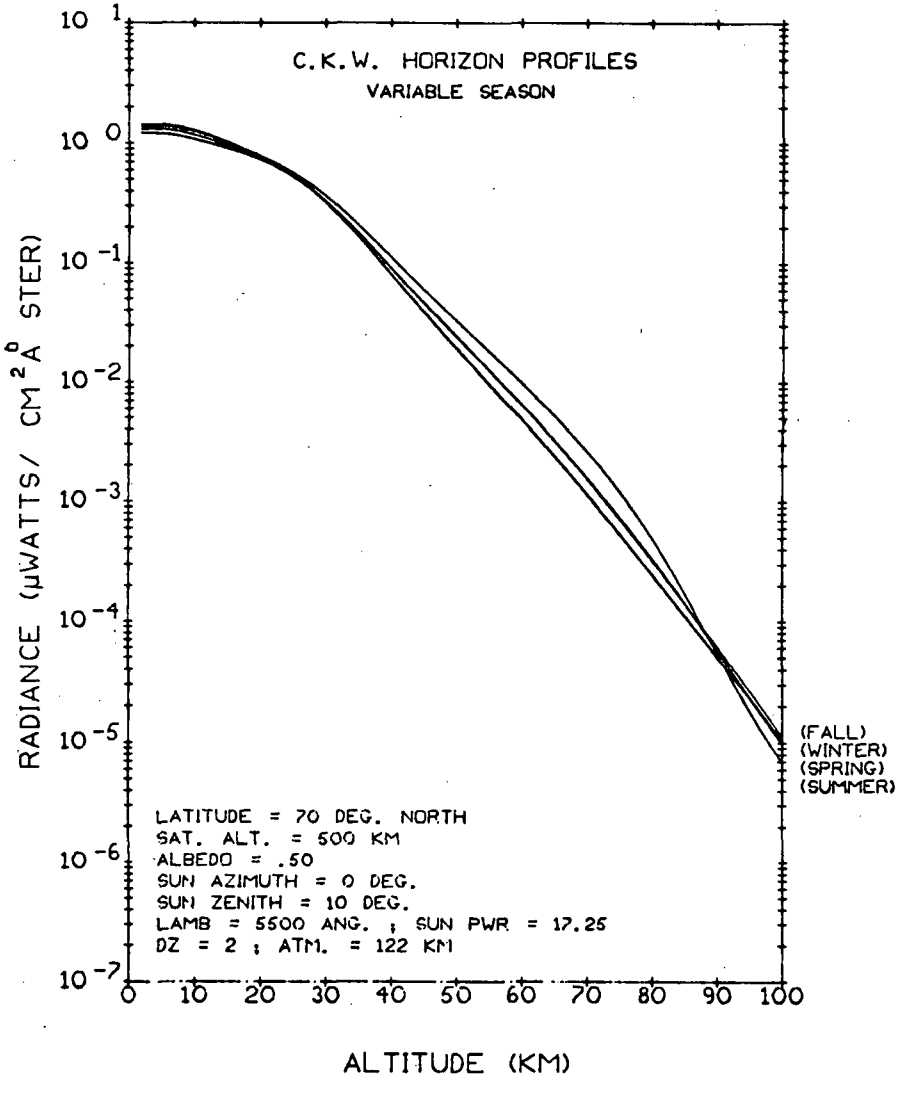

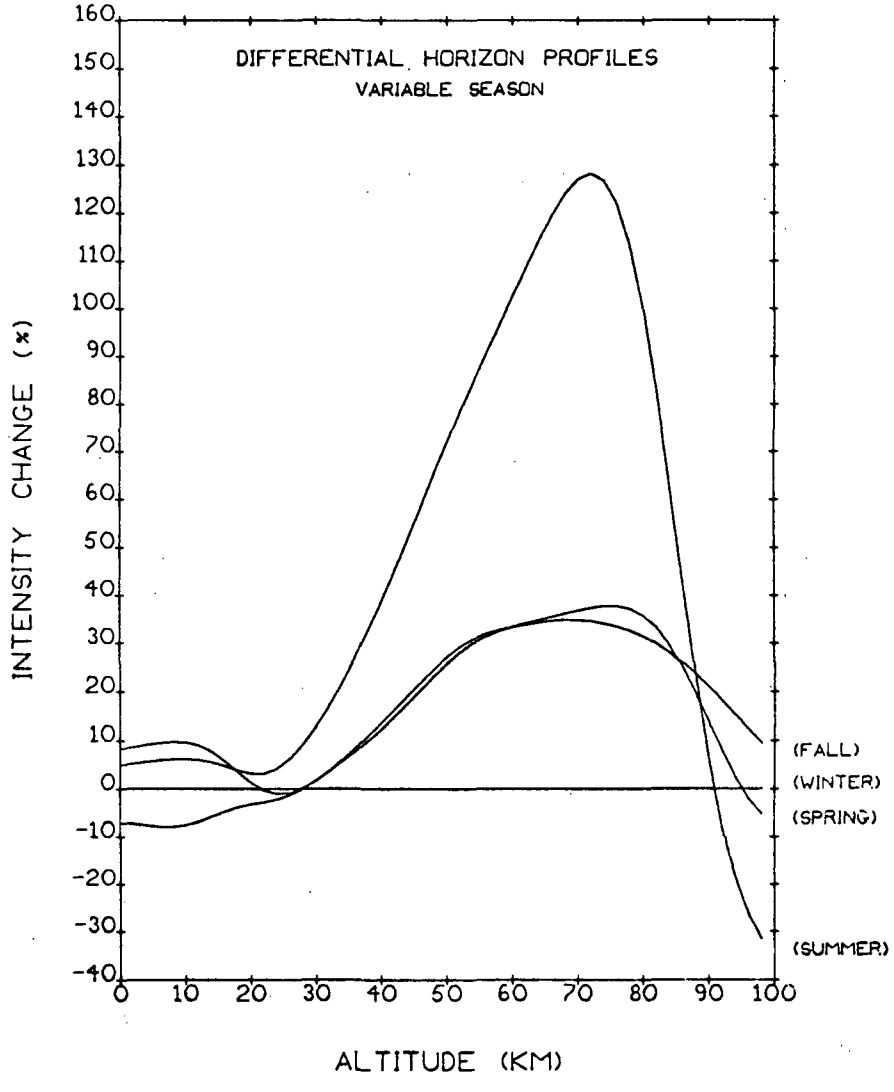

Fig. 5.1-9 Variable Season Horizon Profiles (λ=5500 Å, LAT.=70°N)

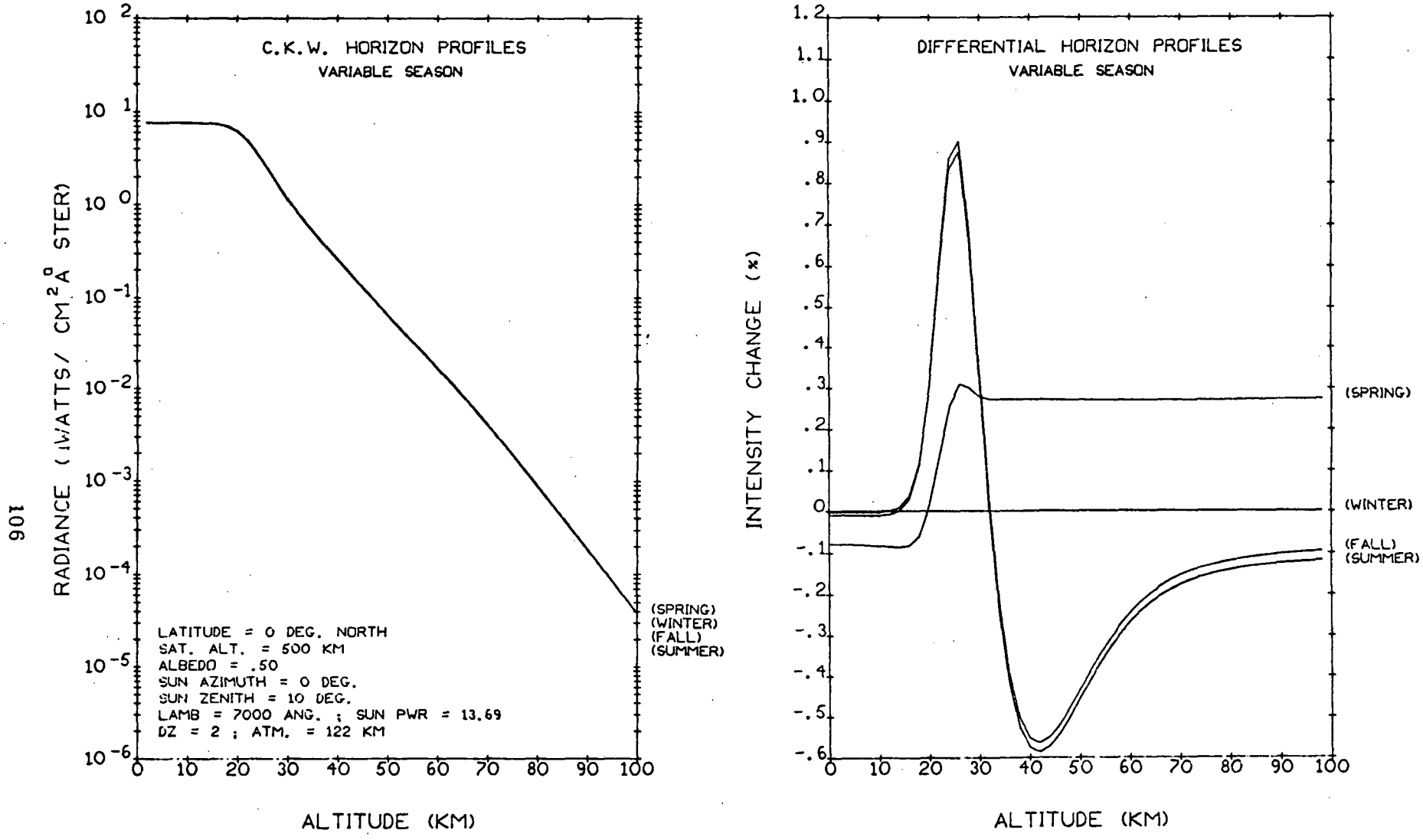

Fig. 5.1-10 Variable Season Horizon Profiles (λ=7000 Å, LAT.=0°N)

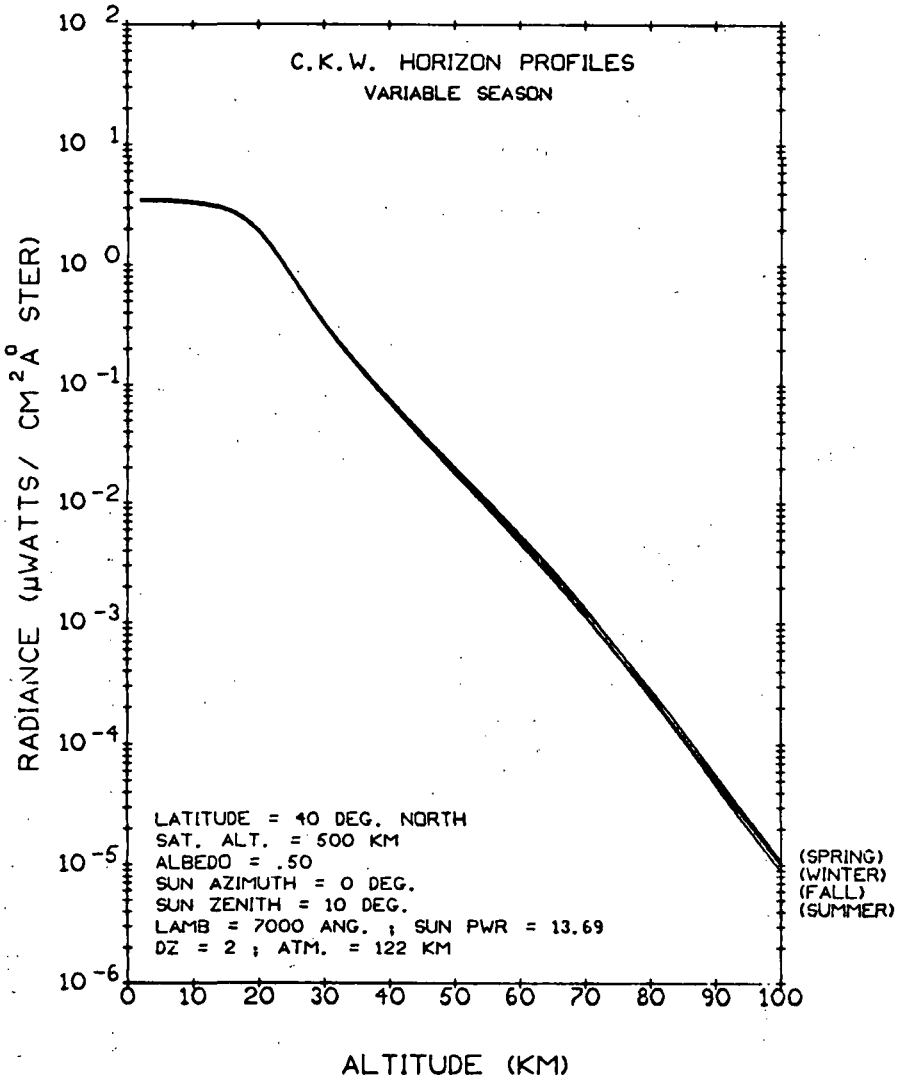

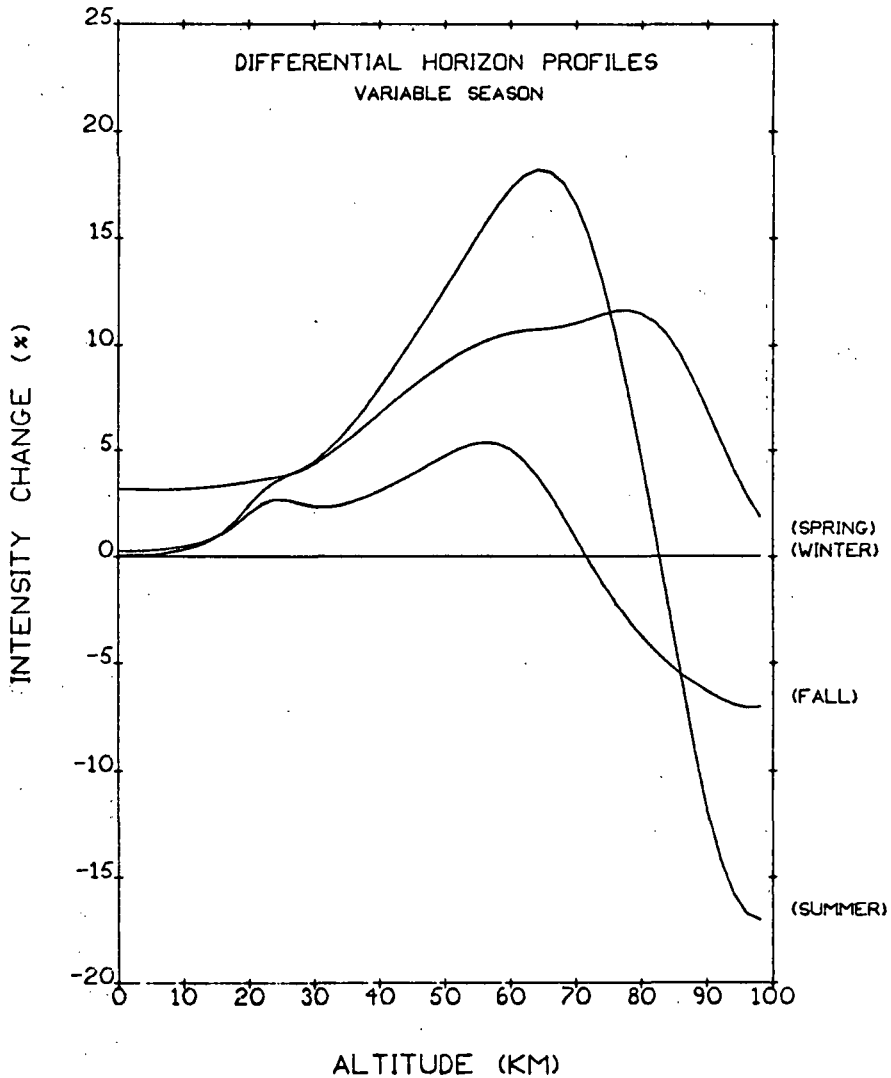

Fig. 5.1-11 Variable Season Horizon Profiles (λ=7000 Å, LAT.=40^{o}N)

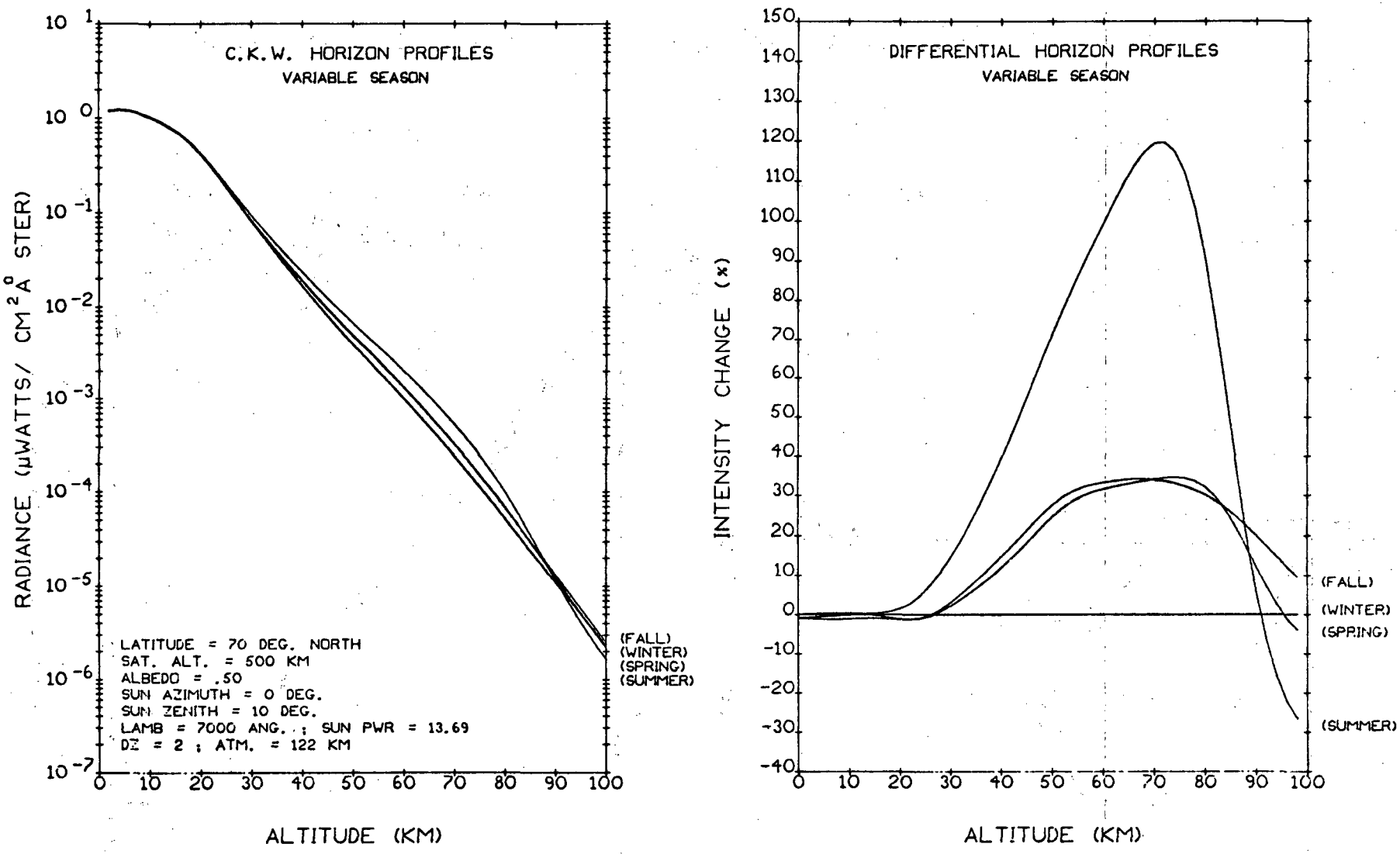

Fig. 5.1-12 Variable Season Horizon Profiles (λ=7000 Å, LAT.=70°N)

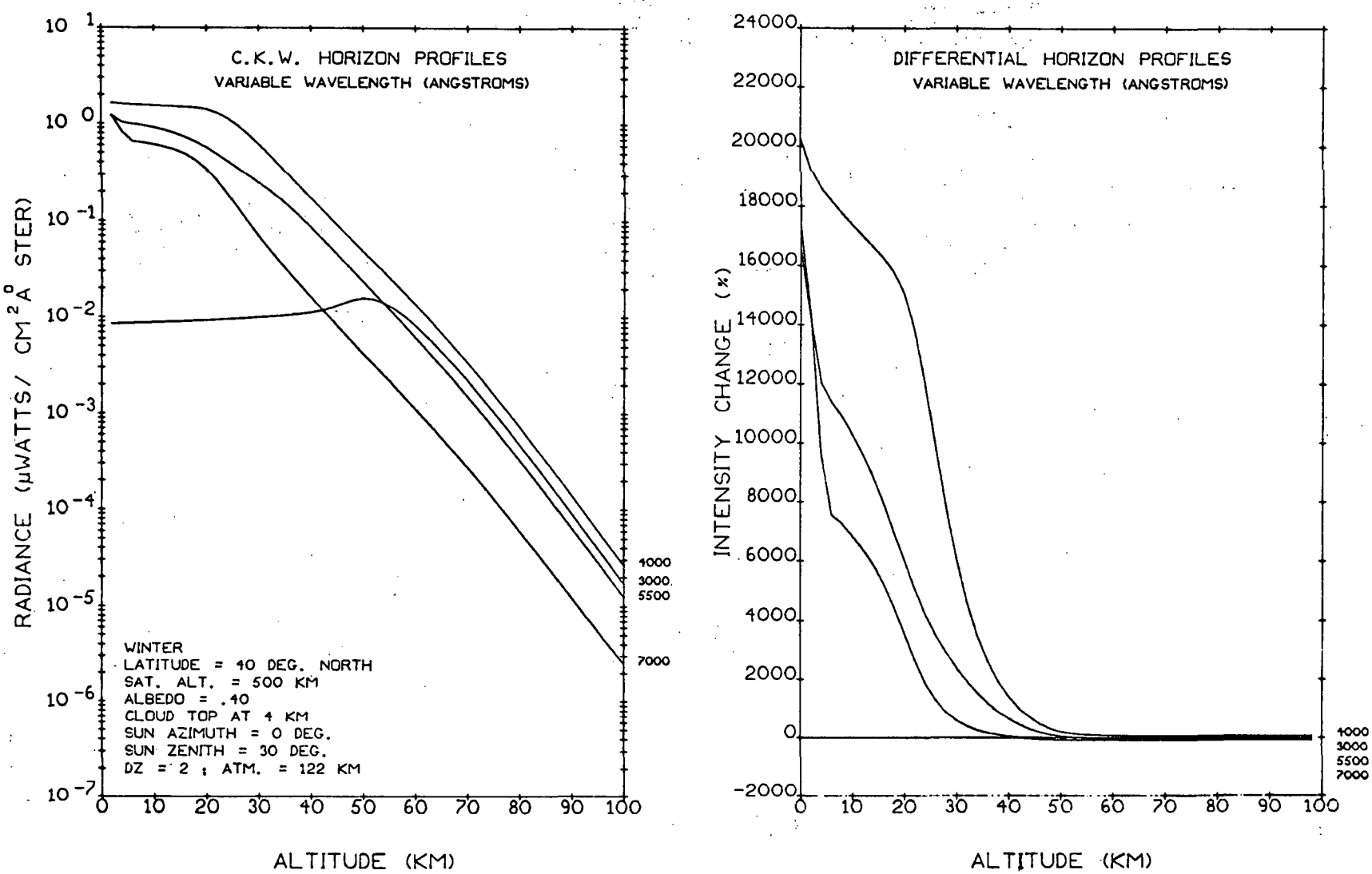

Fig. 5.1-13 Variable Wavelength Horizon Profiles
(Zenith=30°, Cloud Top at 4 km, Albedo=.4)

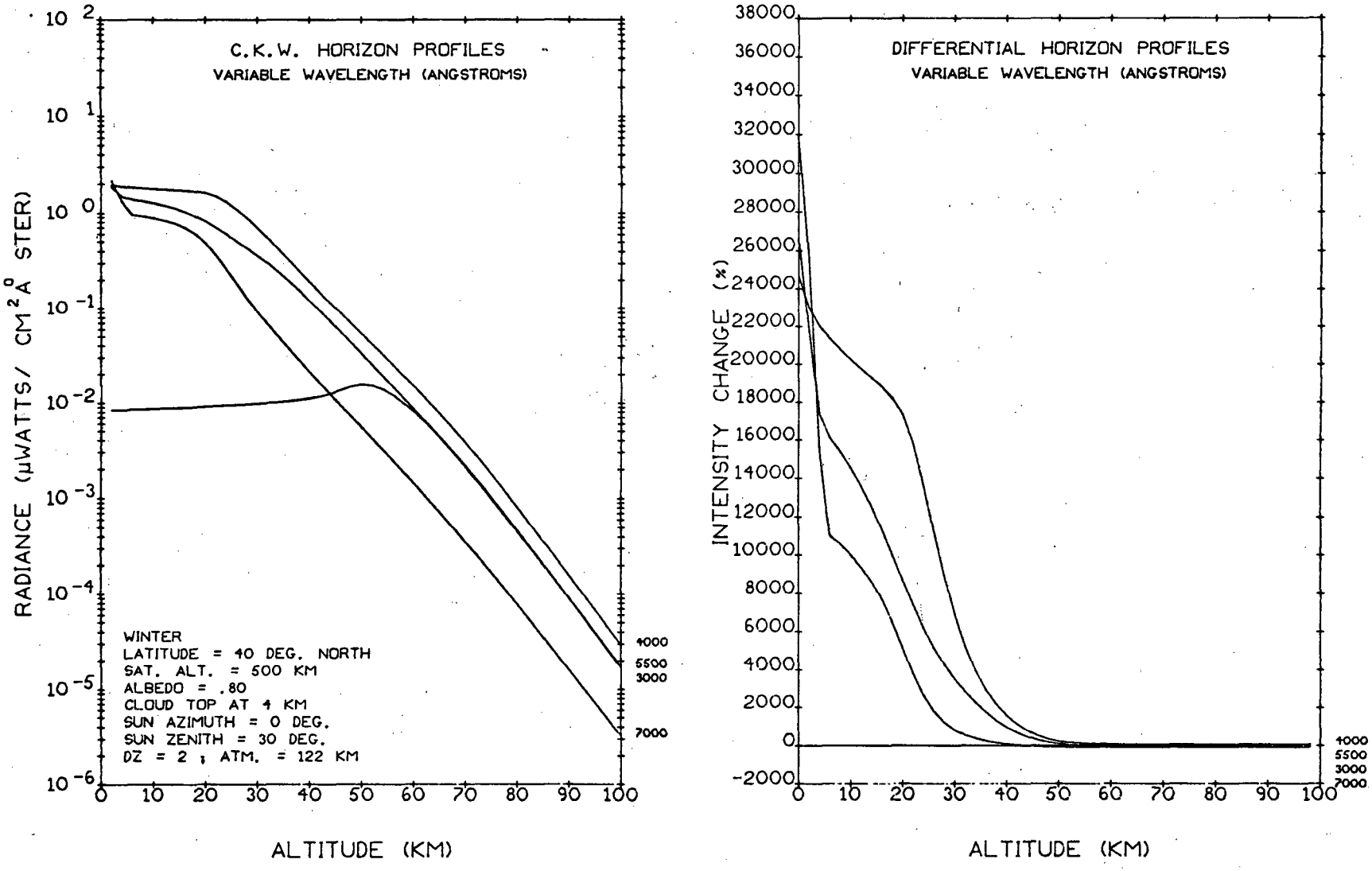

Fig. 5.1-14 Variable Wavelength Horizon Profiles
(Zenith=30°, Cloud Top at 4 km, Albedo=.8)

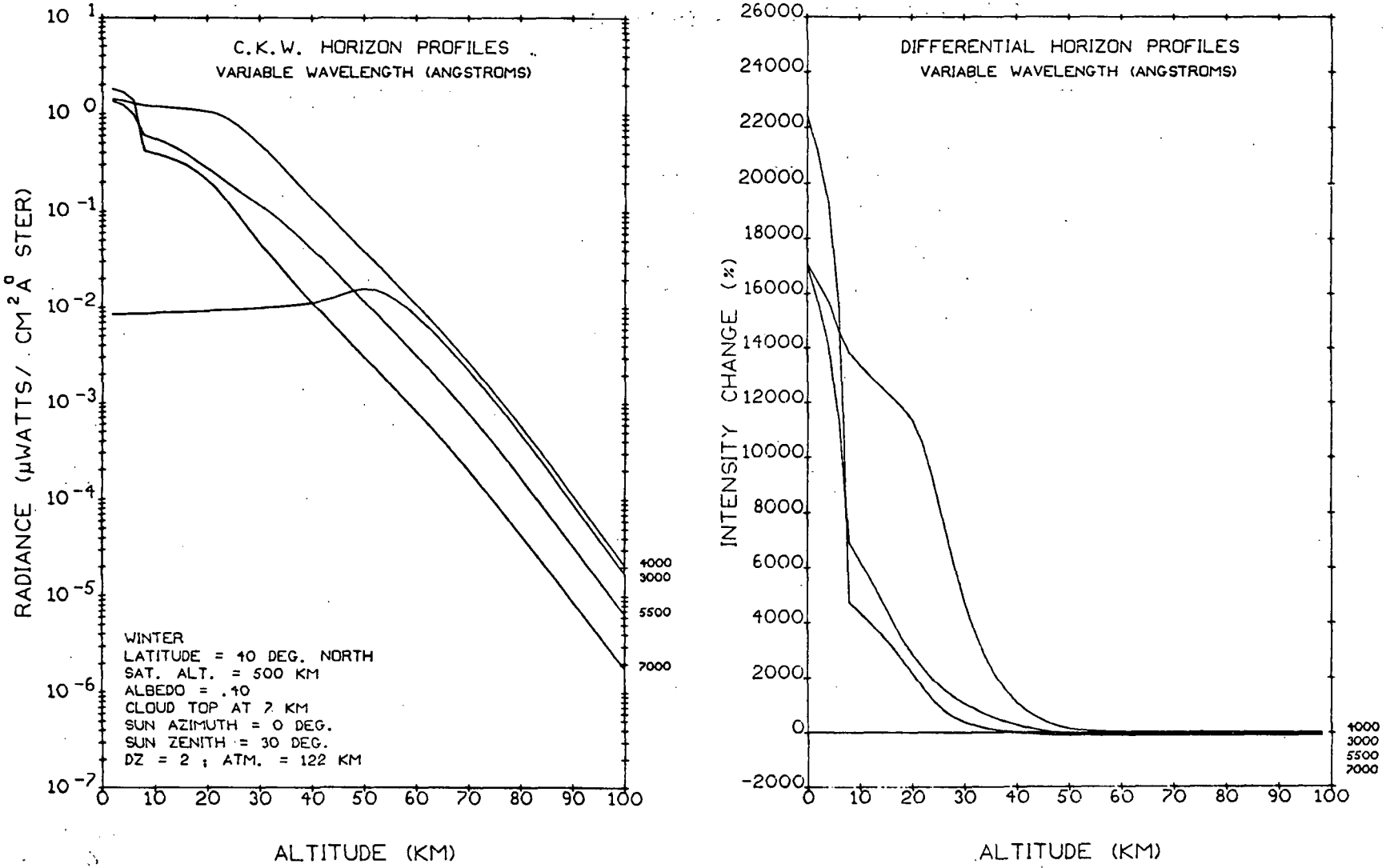

Fig. 5.1-15 Variable Wavelength Horizon Profiles
(Zenith=30°, Cloud Top at 7 km, Albedo=.4)

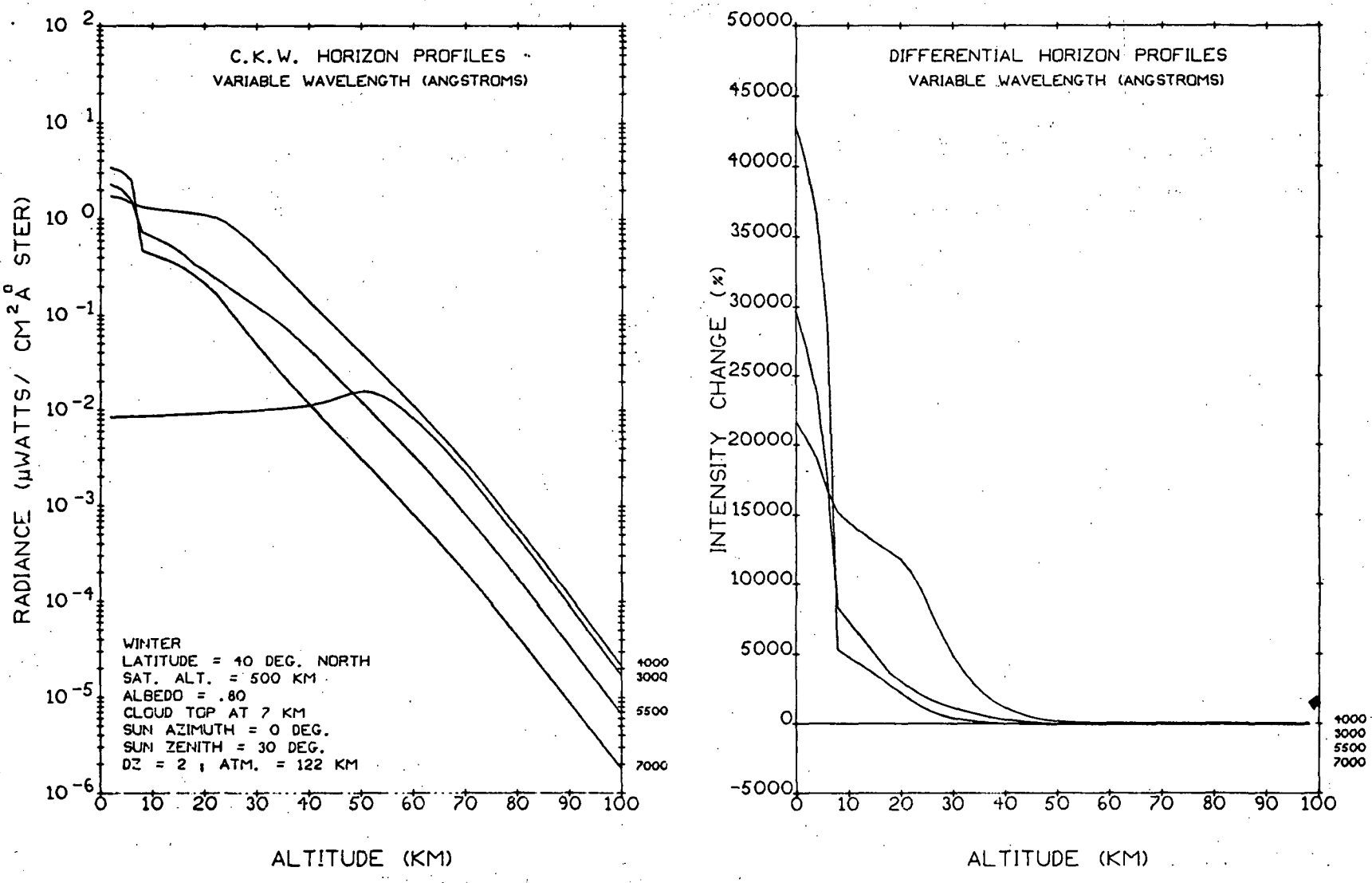

Fig. 5.1-16 Variable Wavelength Horizon Profiles
(Zenith=30°, Cloud Top at 7 km, Albedo=.8)

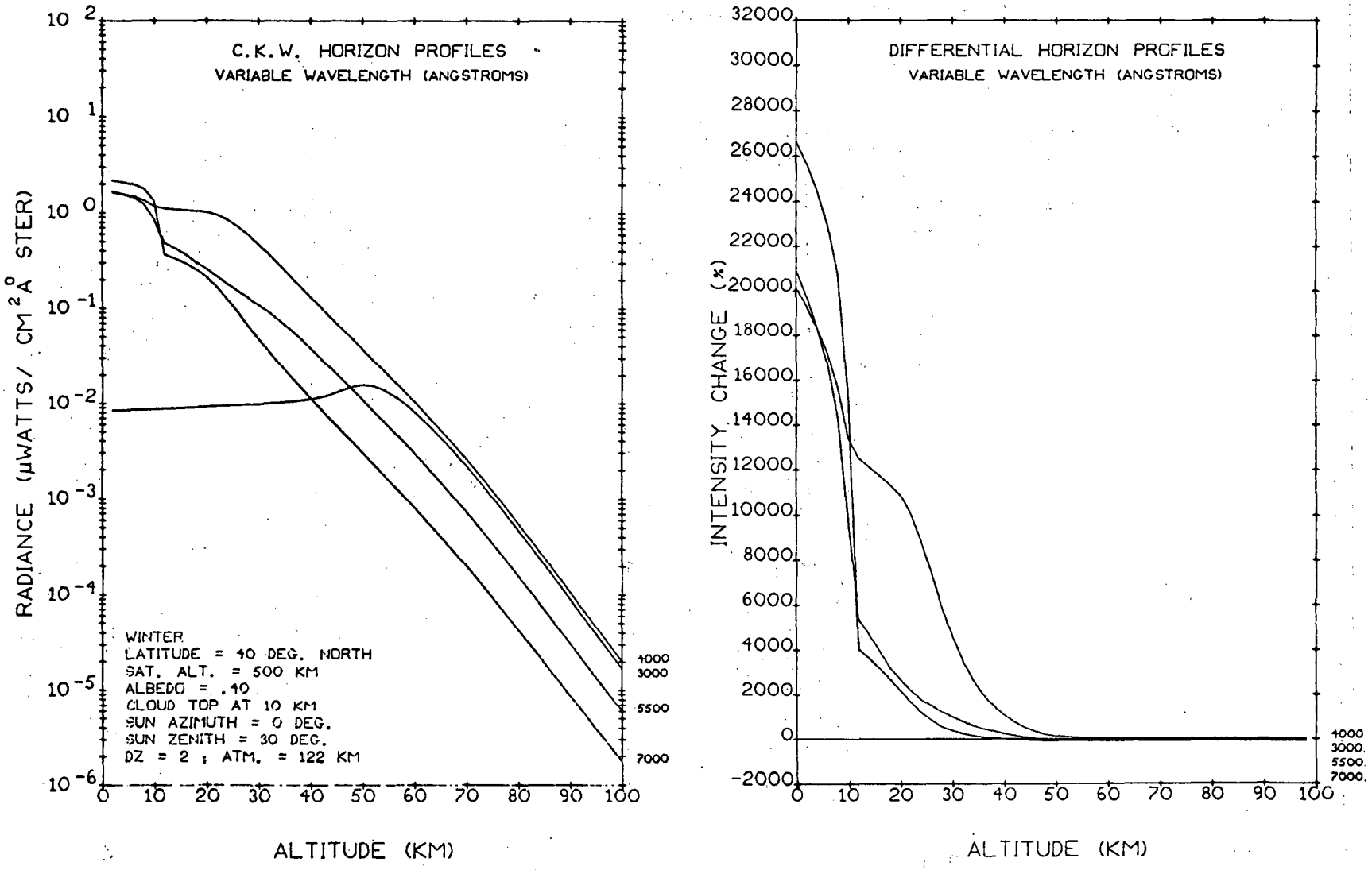

Fig. 5.1-17 Variable Wavelength Horizon Profiles
(Zenith=30°, Cloud Top at 10 km, Albedo=.4)

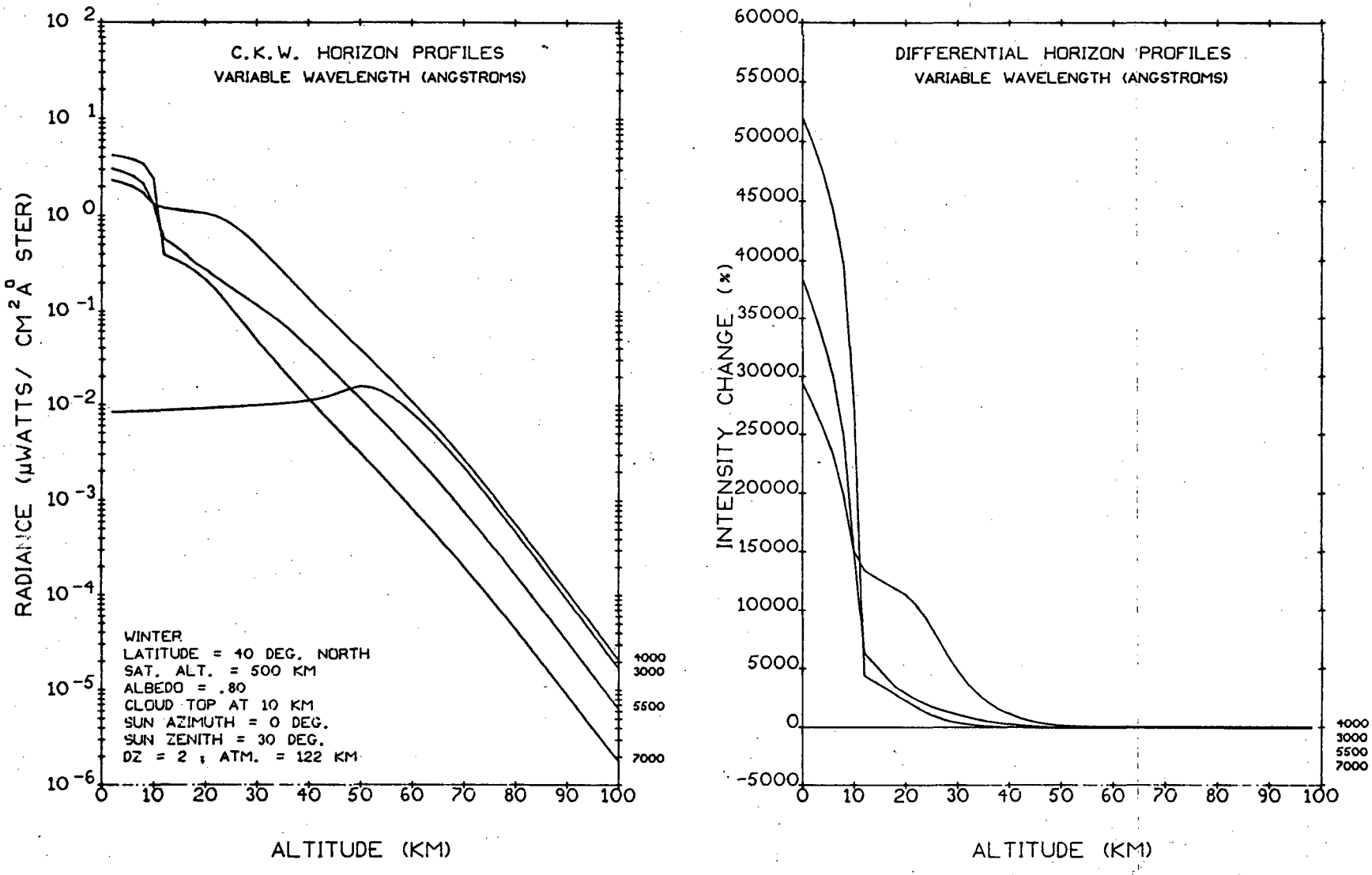

Fig. 5.1-18 Variable Wavelength Horizon Profiles
(Zenith=30°, Cloud Top at 10 km, Albedo=.8)

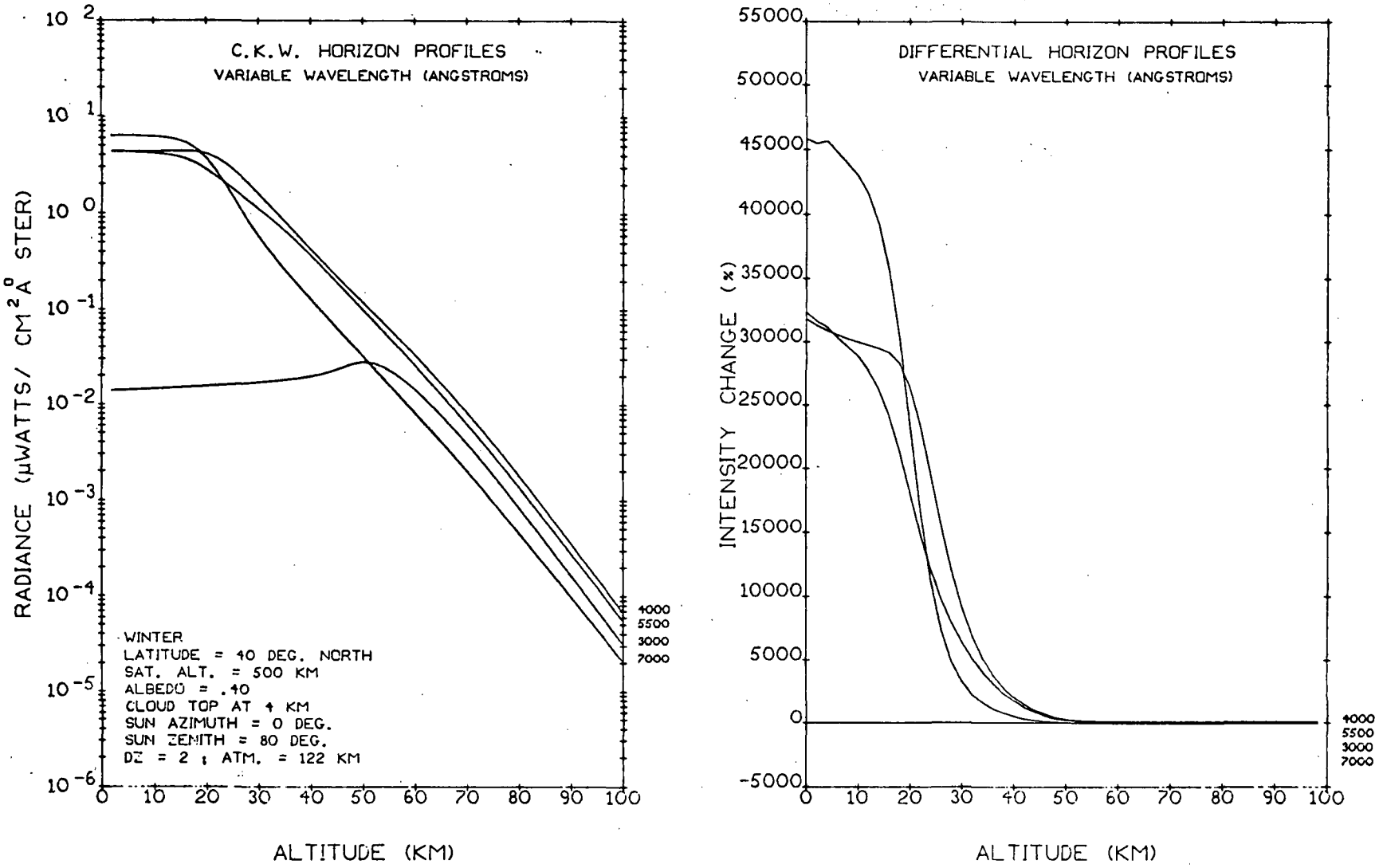

Fig. 5.1-19 Variable Wavelength Horizon Profiles
(Zenith=80°, Cloud Top at 4 km, Albedo=.4)

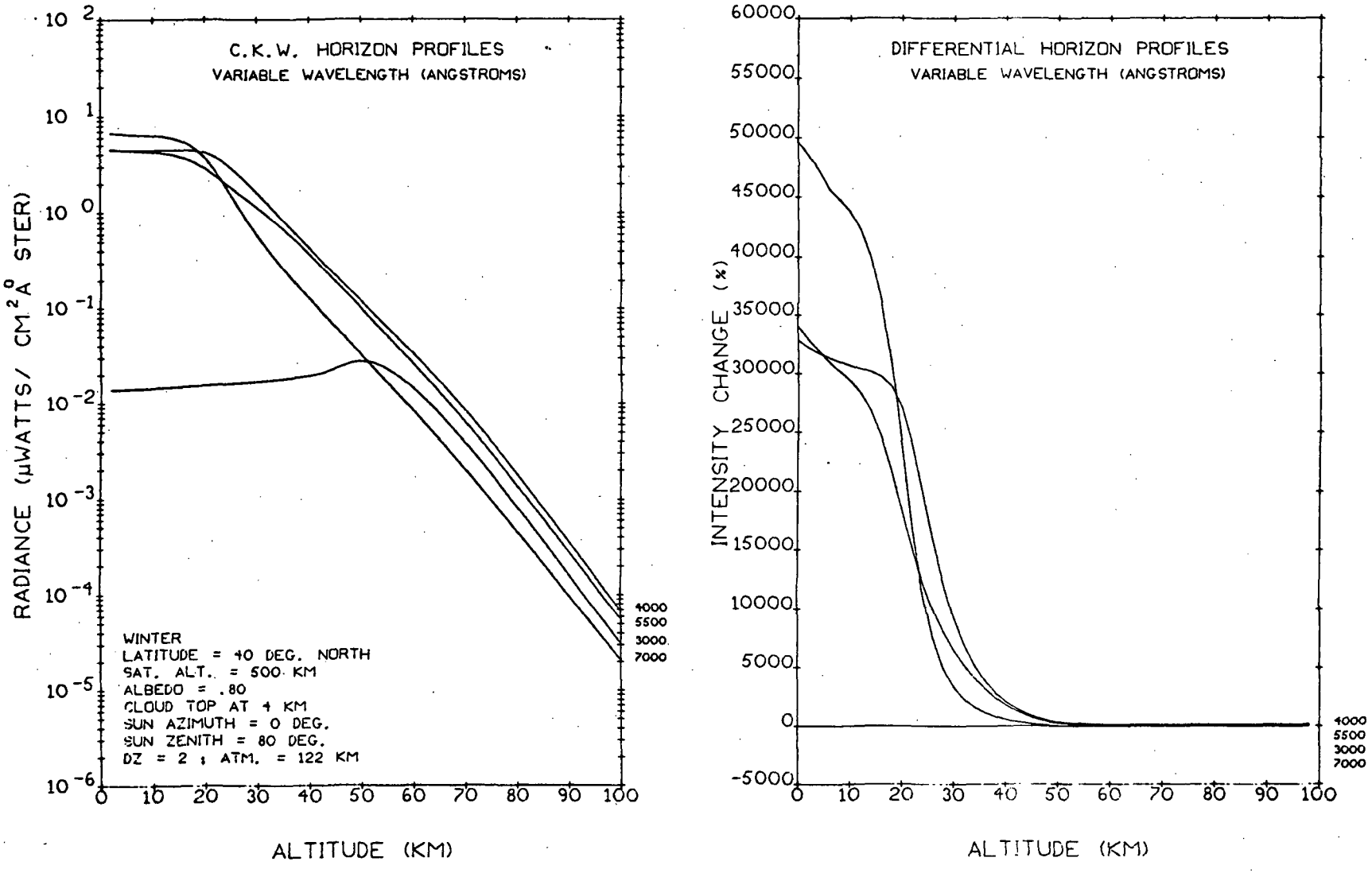

Fig. 5.1-20 Variable Wavelength Horizon Profiles
(Zenith=80°, Cloud Top at 4 km, Albedo=.8)

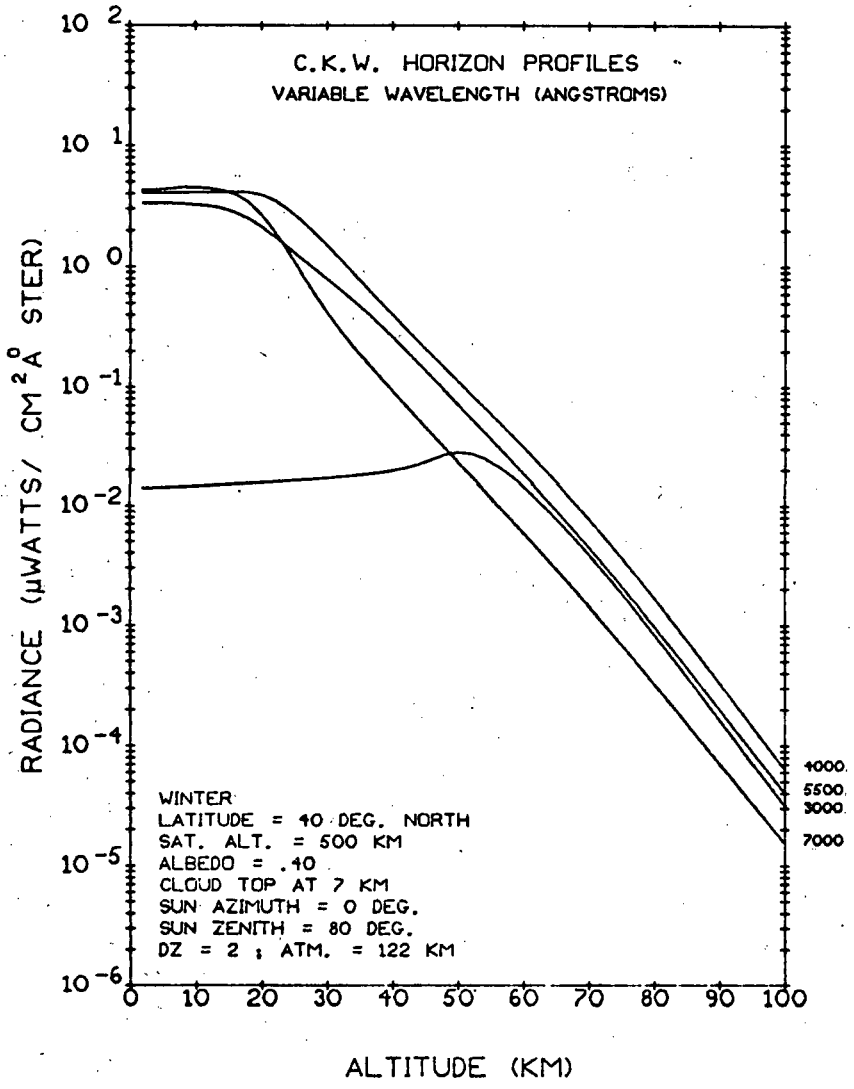

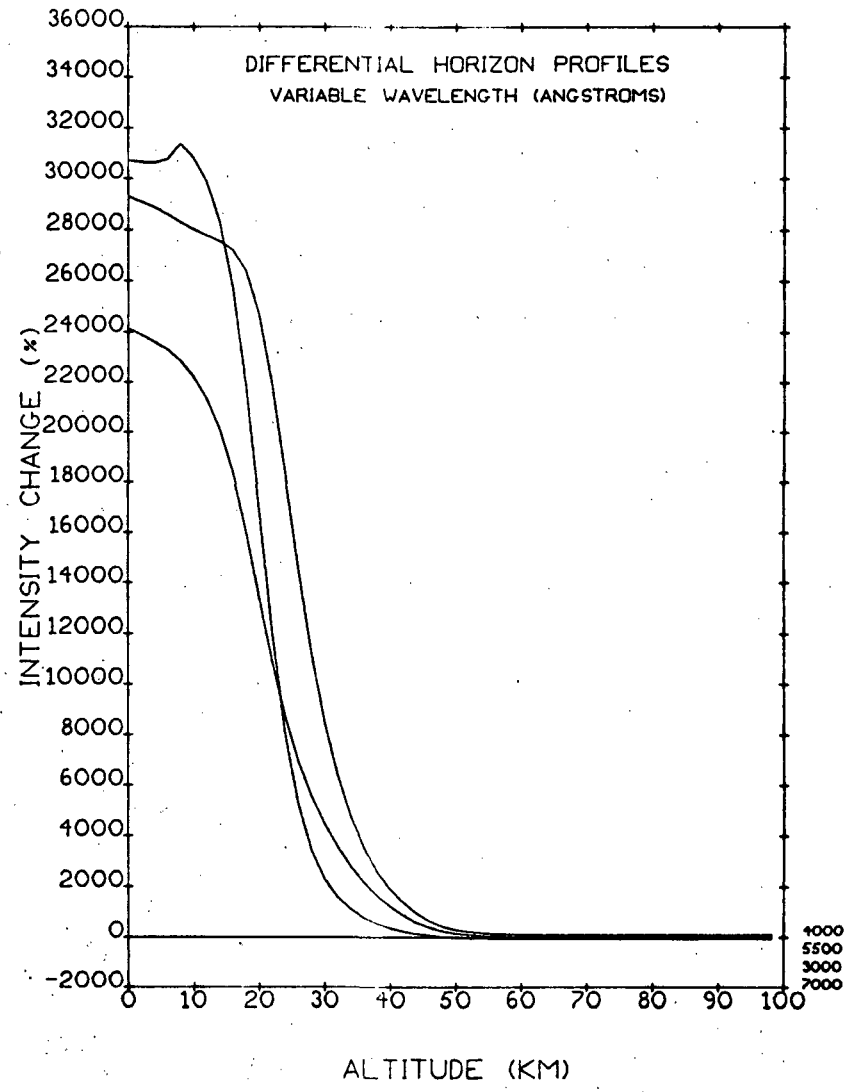

Fig. 5.1-21 Variable Wavelength Horizon Profiles
(Zenith=80°, Cloud Top at 7 km, Albedo=.4)

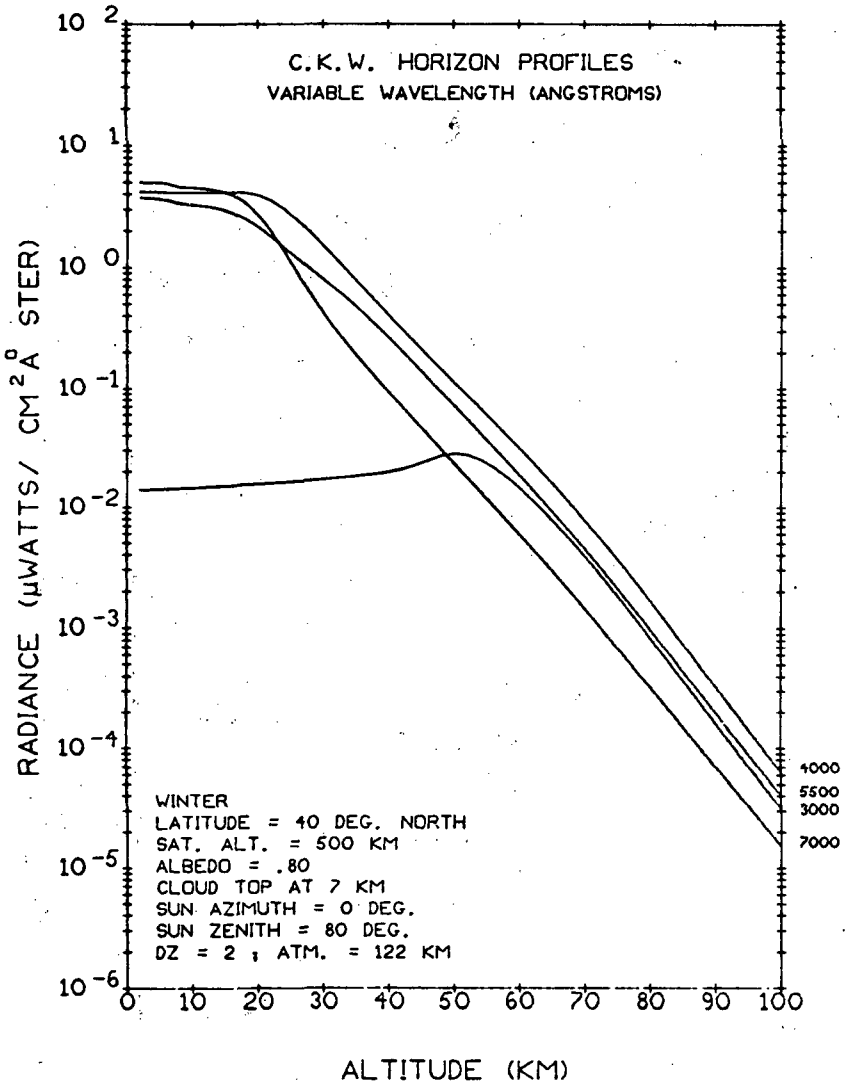

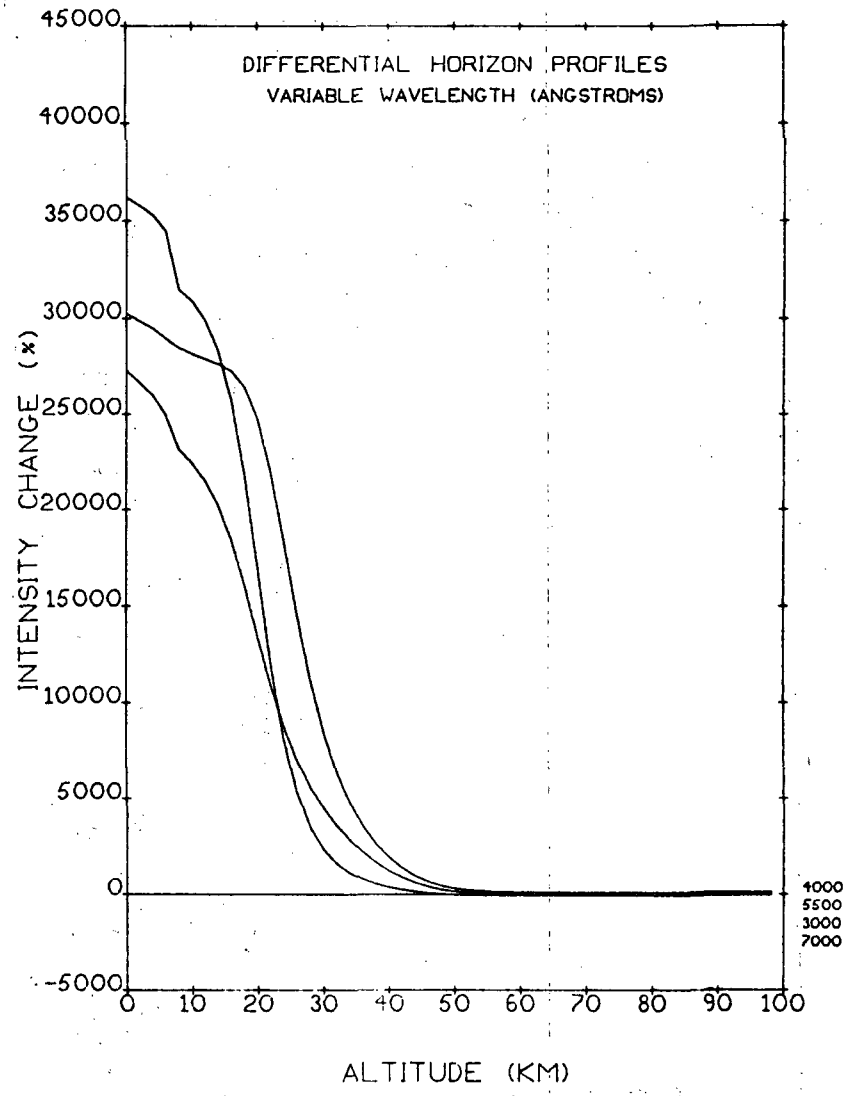

Fig. 5.1-22 Variable Wavelength Horizon Profiles
(Zenith=80^o, Cloud Top at 7 km, Albedo=.8)

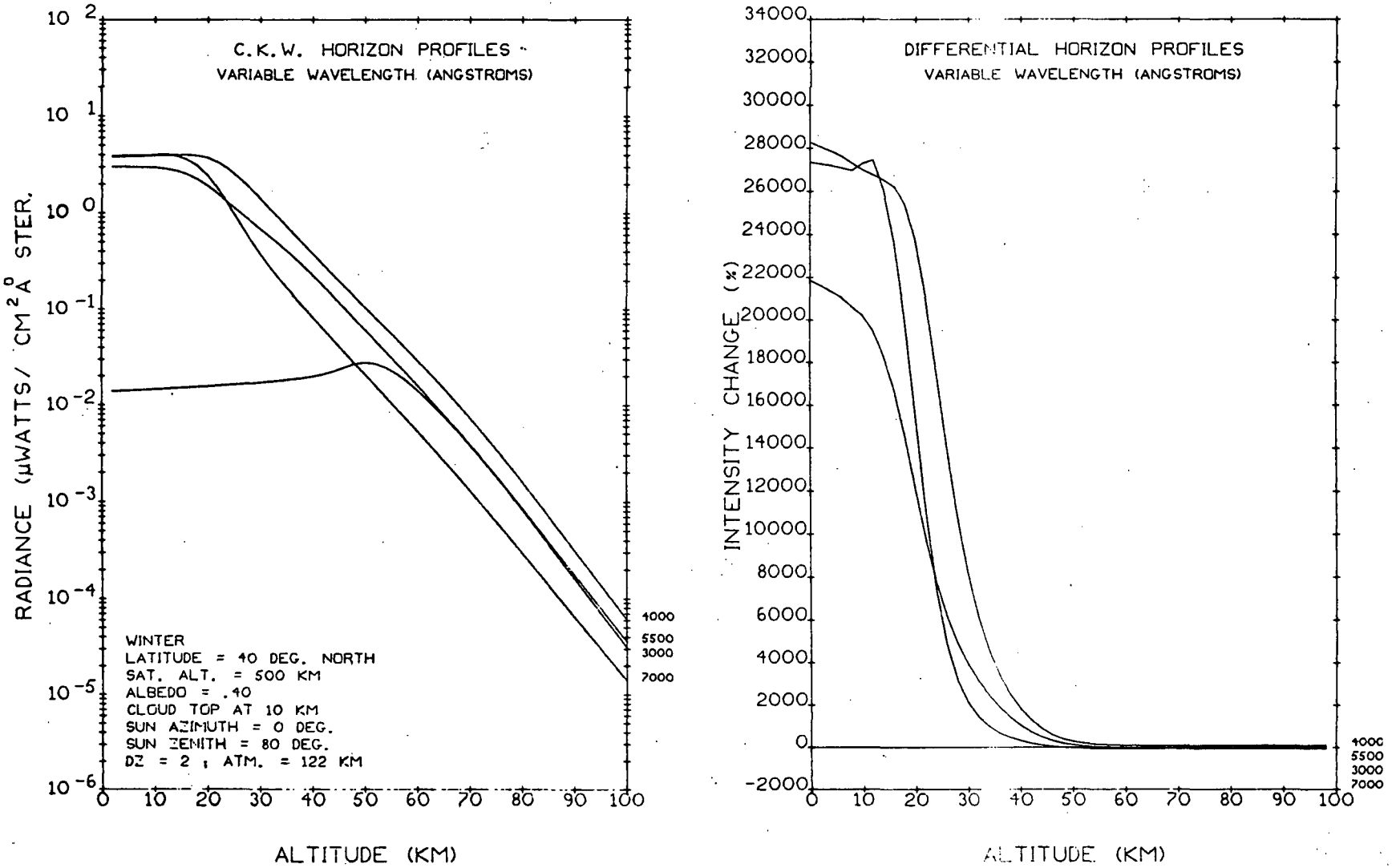

Fig. 5.1-23 Variable Wavelength Horizon Profiles
(Zenith=80°, Cloud Top at 10 km, Albedo=.4)

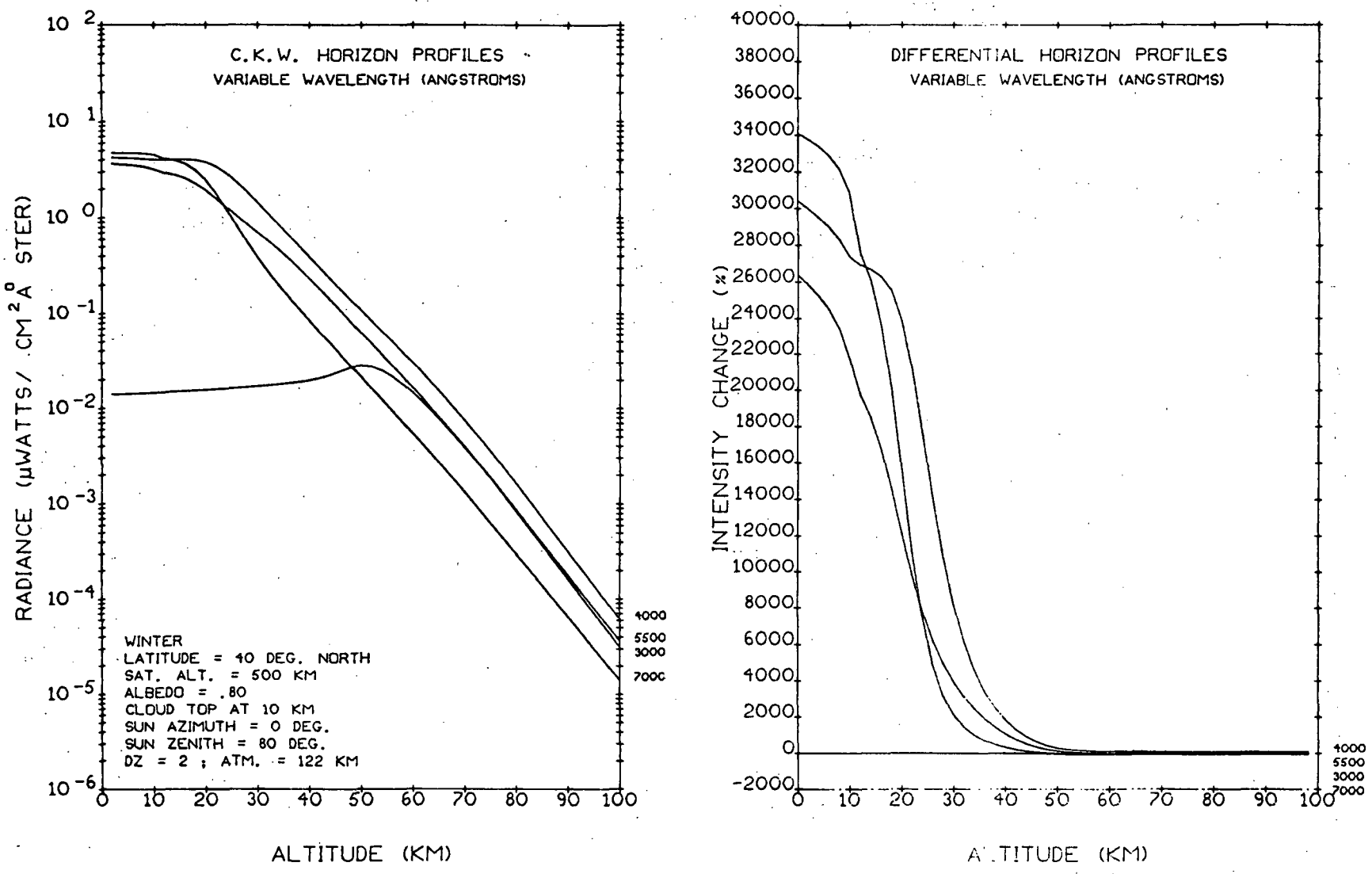

Fig. 5.1-24 Variable Wavelength Horizon Profiles
(Zenith=80°, Cloud Top at 10 km, Albedo=.8)

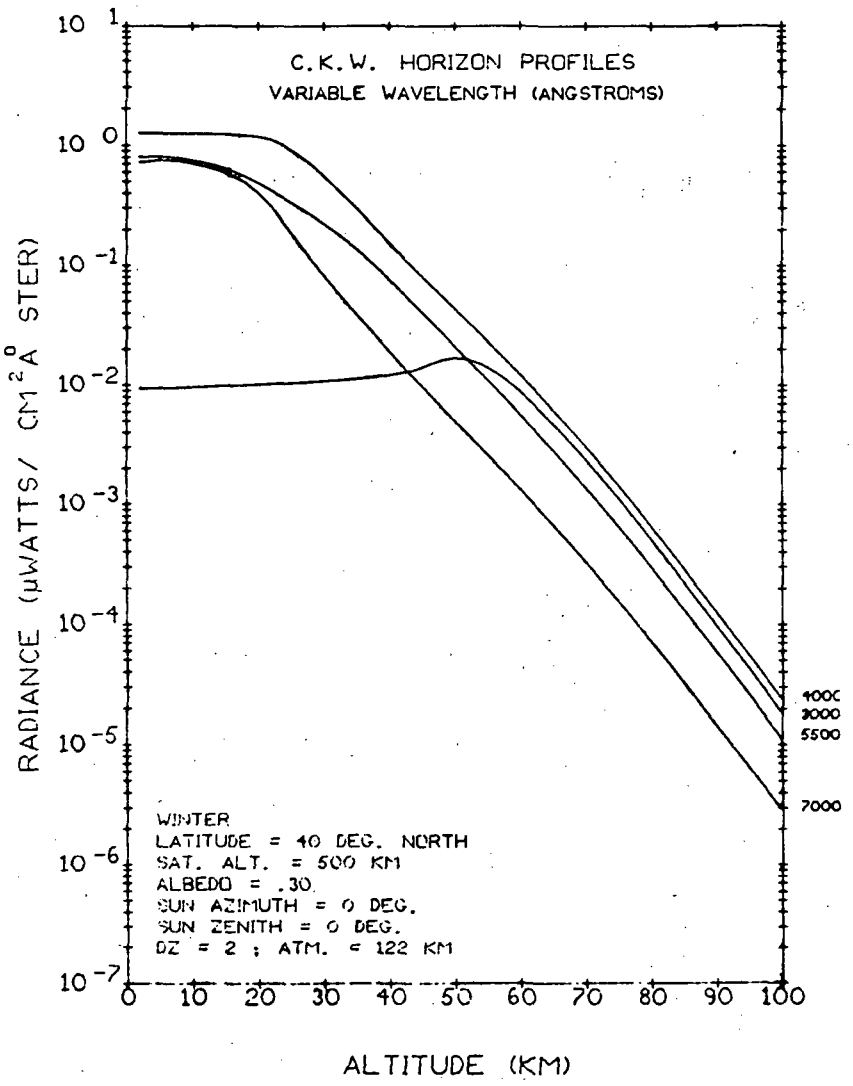

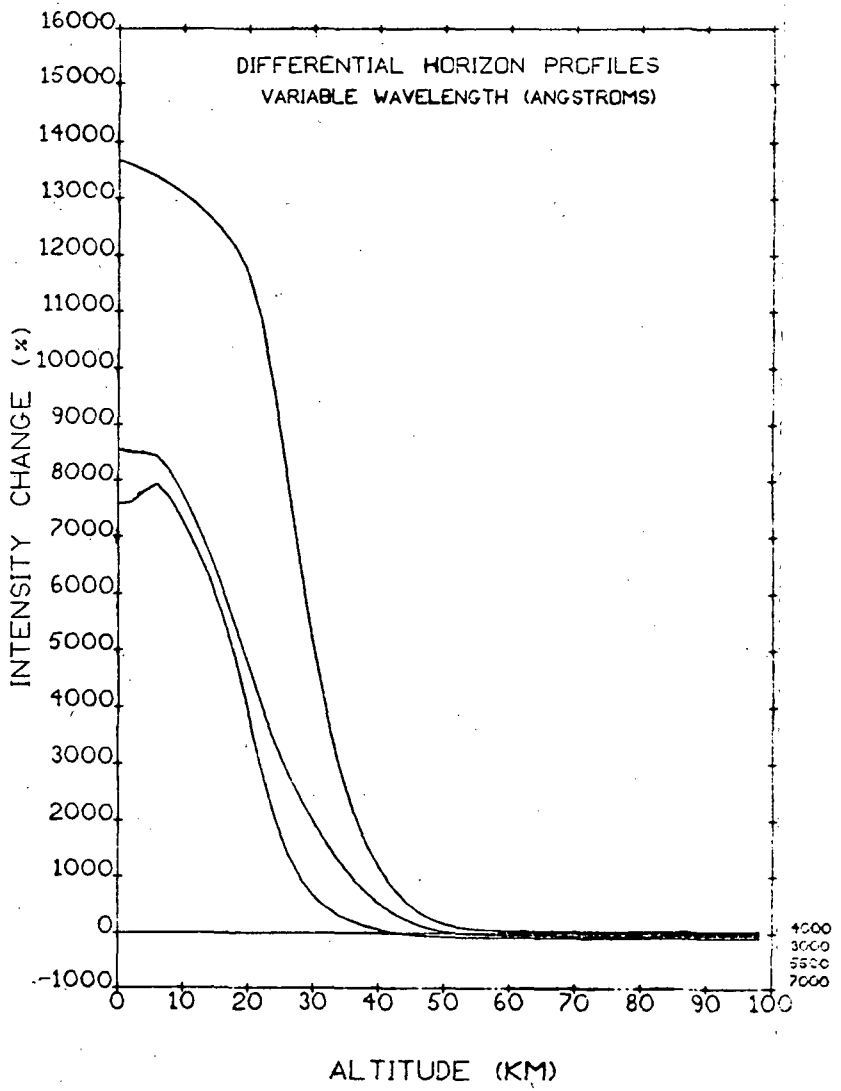

Fig. 5.1-25 Variable Wavelength Horizon Profiles
(Zenith=0^o, Cloud Top at 0 km, Albedo=.3)

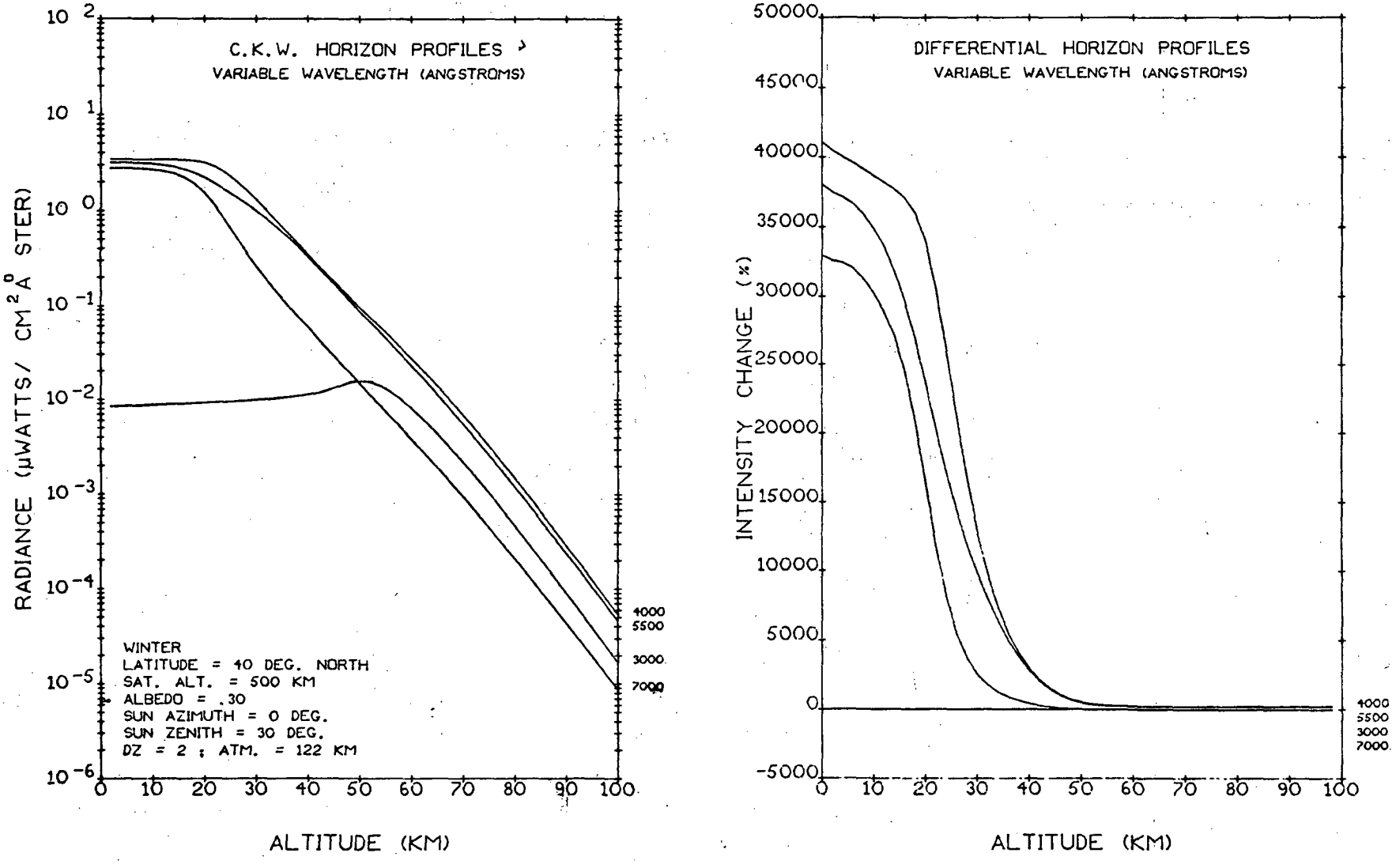

Fig. 5.1-26 Variable Wavelength Horizon Profiles
(Zenith=30^o, Cloud Top at 0 km, Albedo=.3)

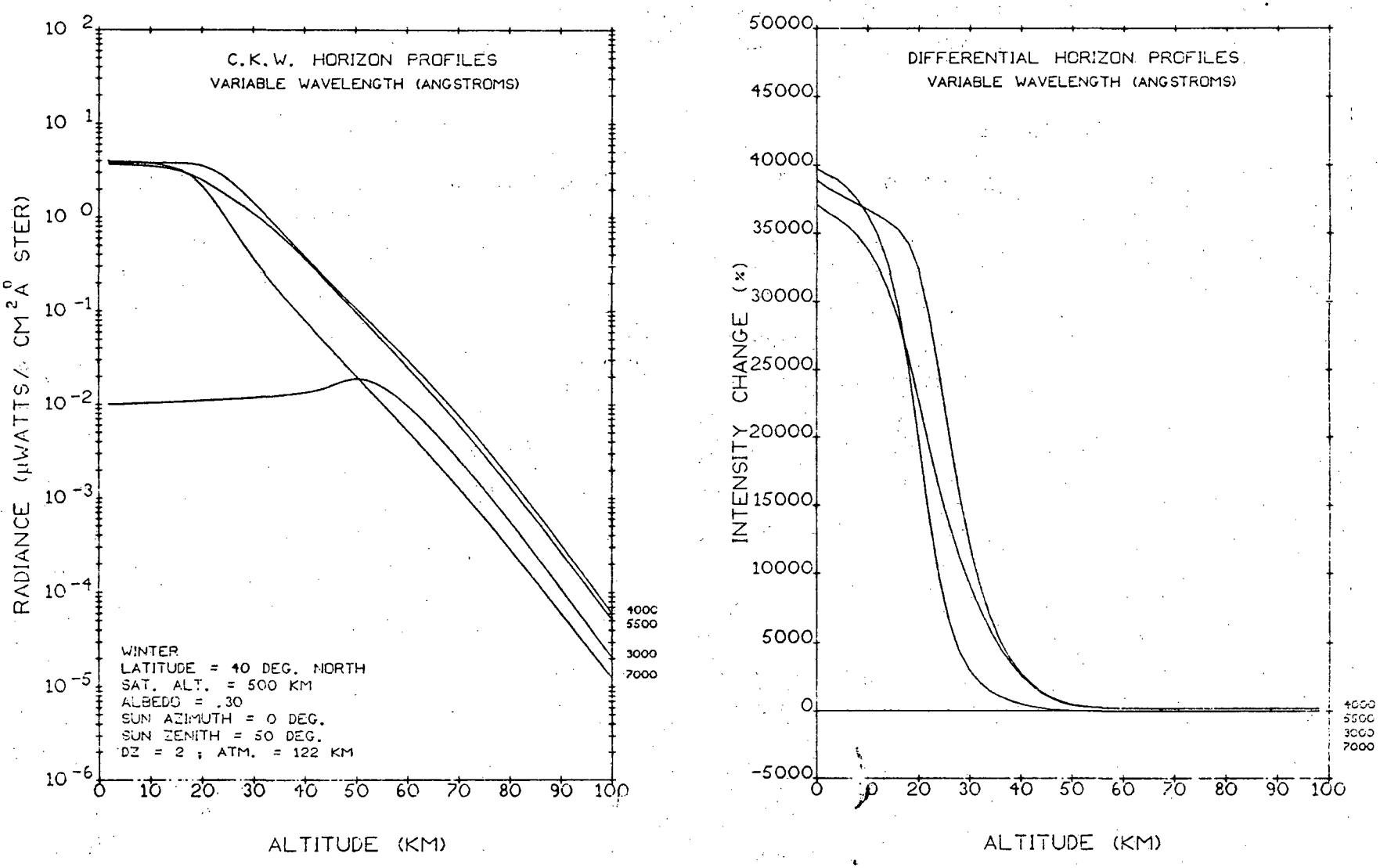

Fig. 5.1-27 Variable Wavelength Horizon Profiles
(Zenith=50°, Cloud Top at 0 km, Albedo=.3)

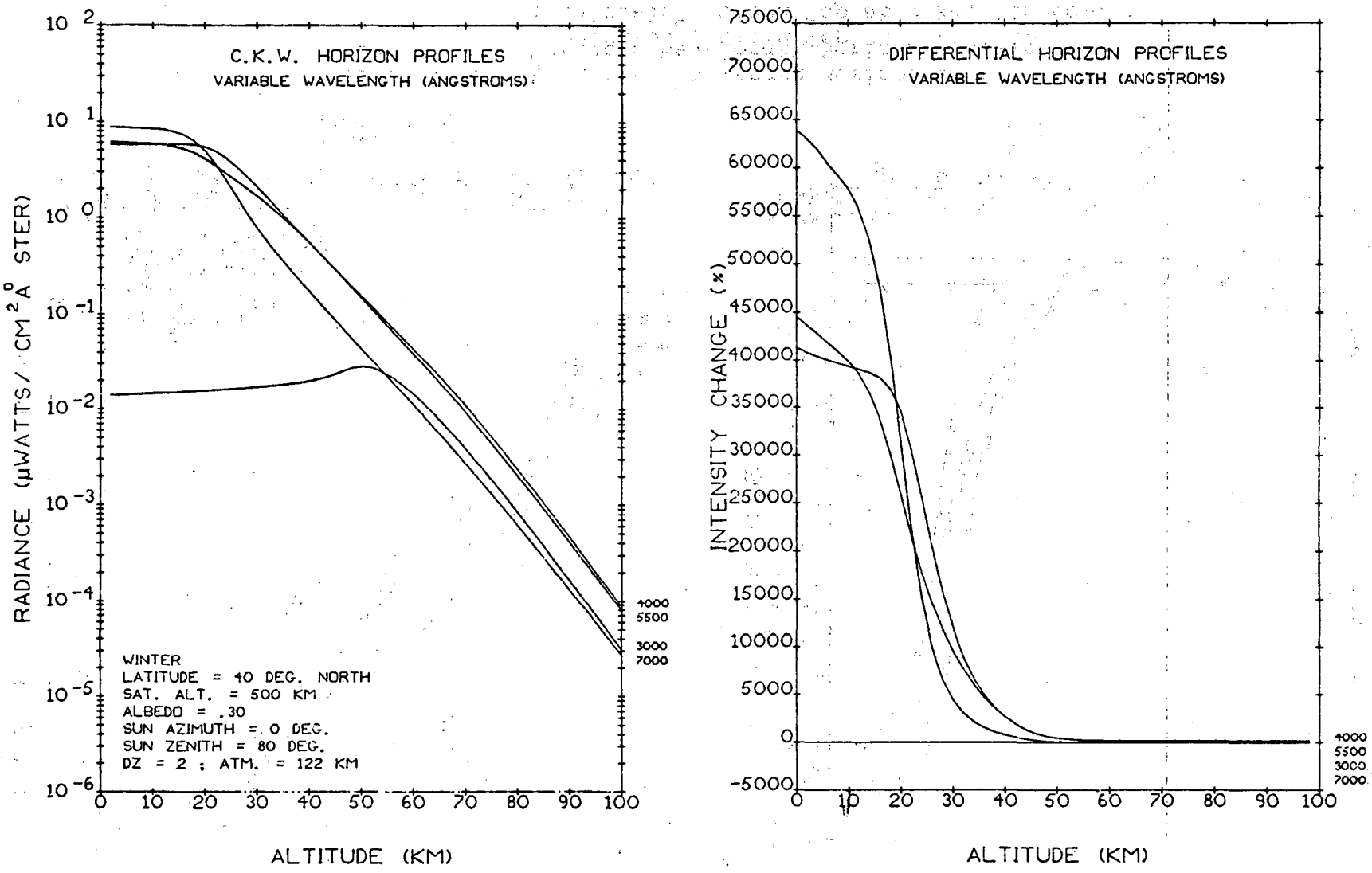

Fig. 5.1-28 Variable Wavelength Horizon Profiles
(Zenith=80^o, Cloud Top at 0 km, Albedo=.3)

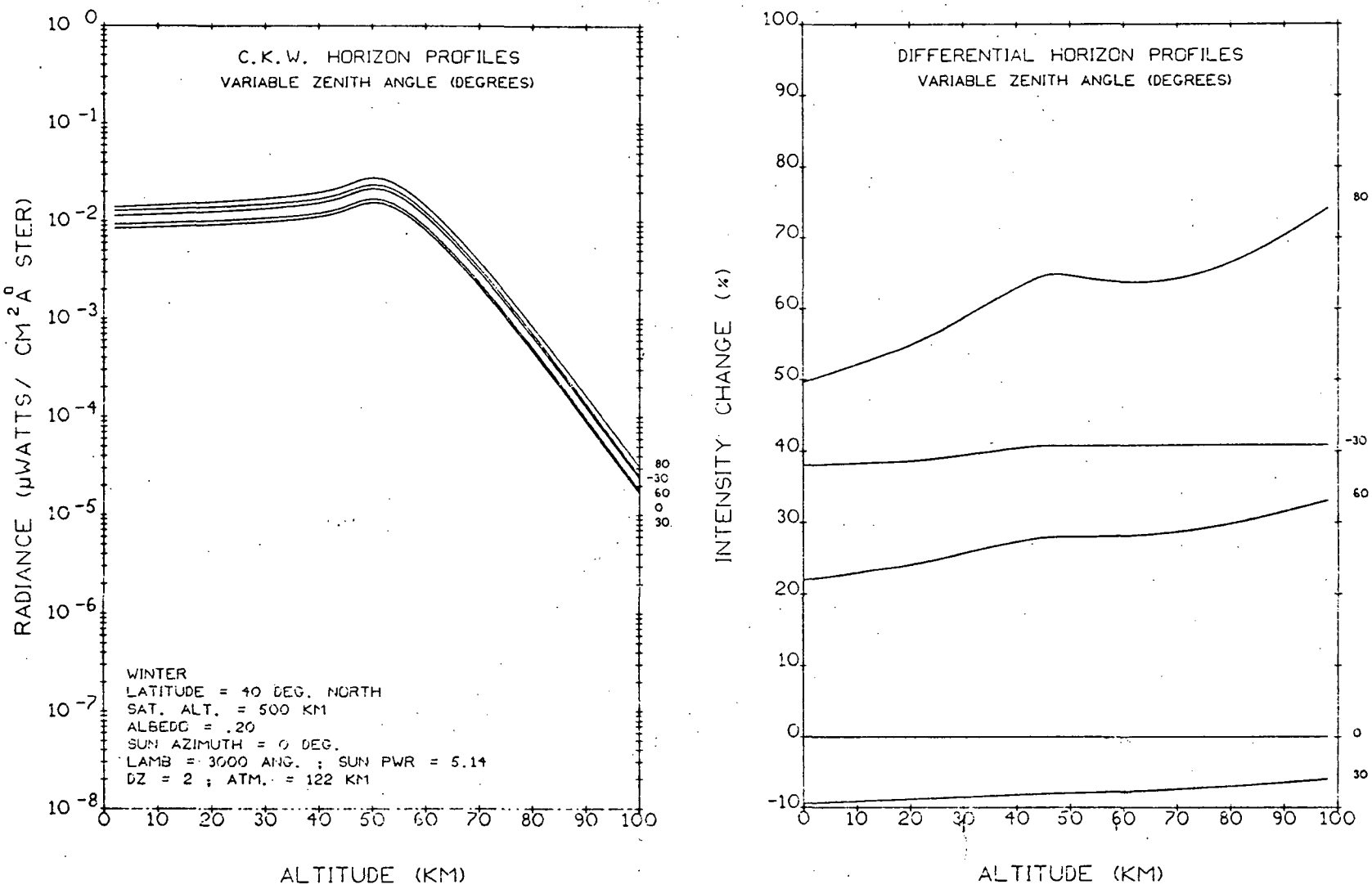

Fig. 5.1-29 Variable Zenith Angle Horizon Profiles
(Azimuth=0°, λ=3000 Å, Albedo=.2)

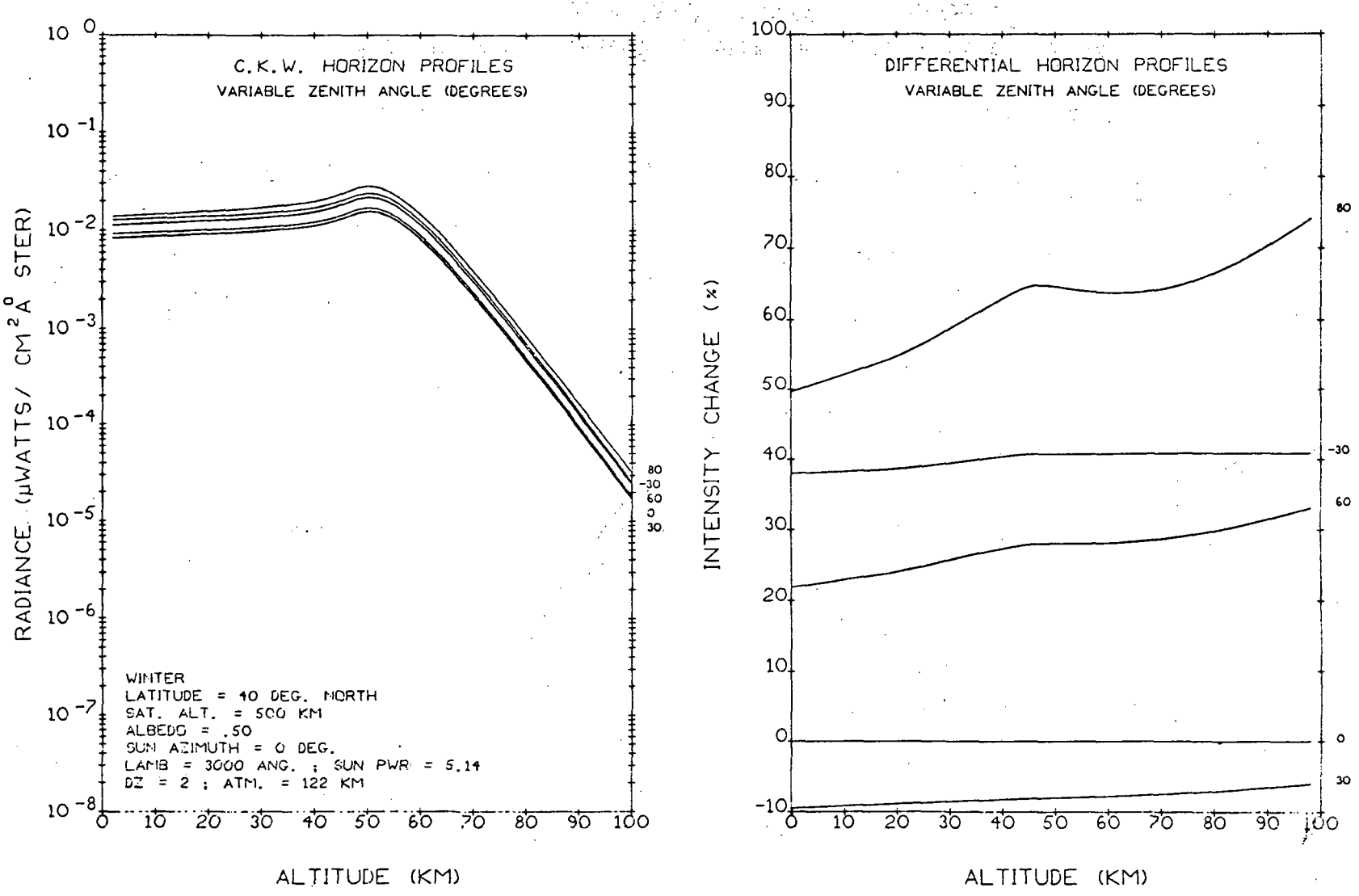

Fig. 5.1-10 Variable Zenith Angle Horizon Profiles
(Azimuth=0°, λ=3000 Å, Albedo=.5)

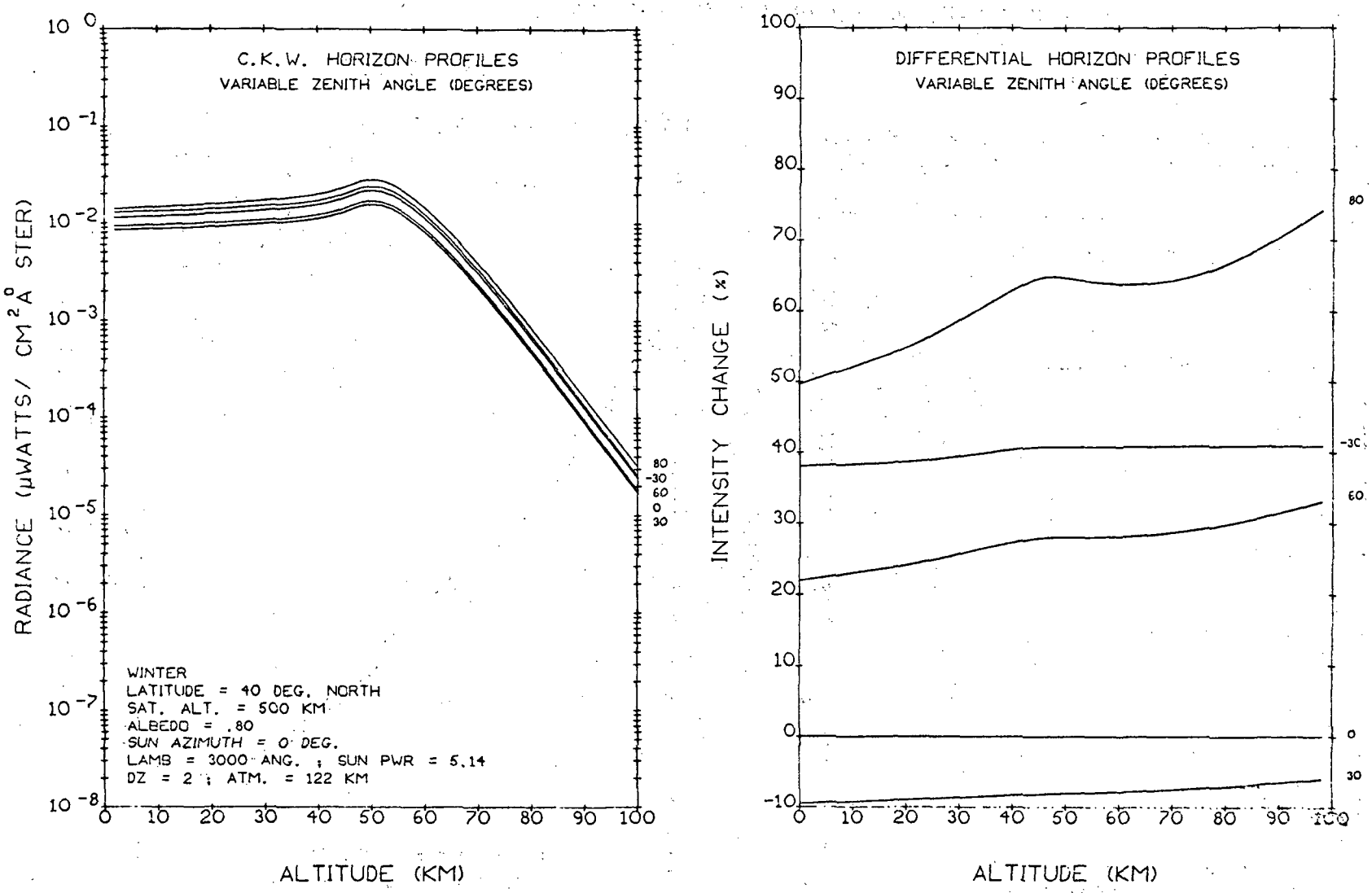

Fig. 5.1-31 Variable Zenith Angle Horizon Profiles
(Azimuth=0°, λ=3000 Å, Albedo=.8)

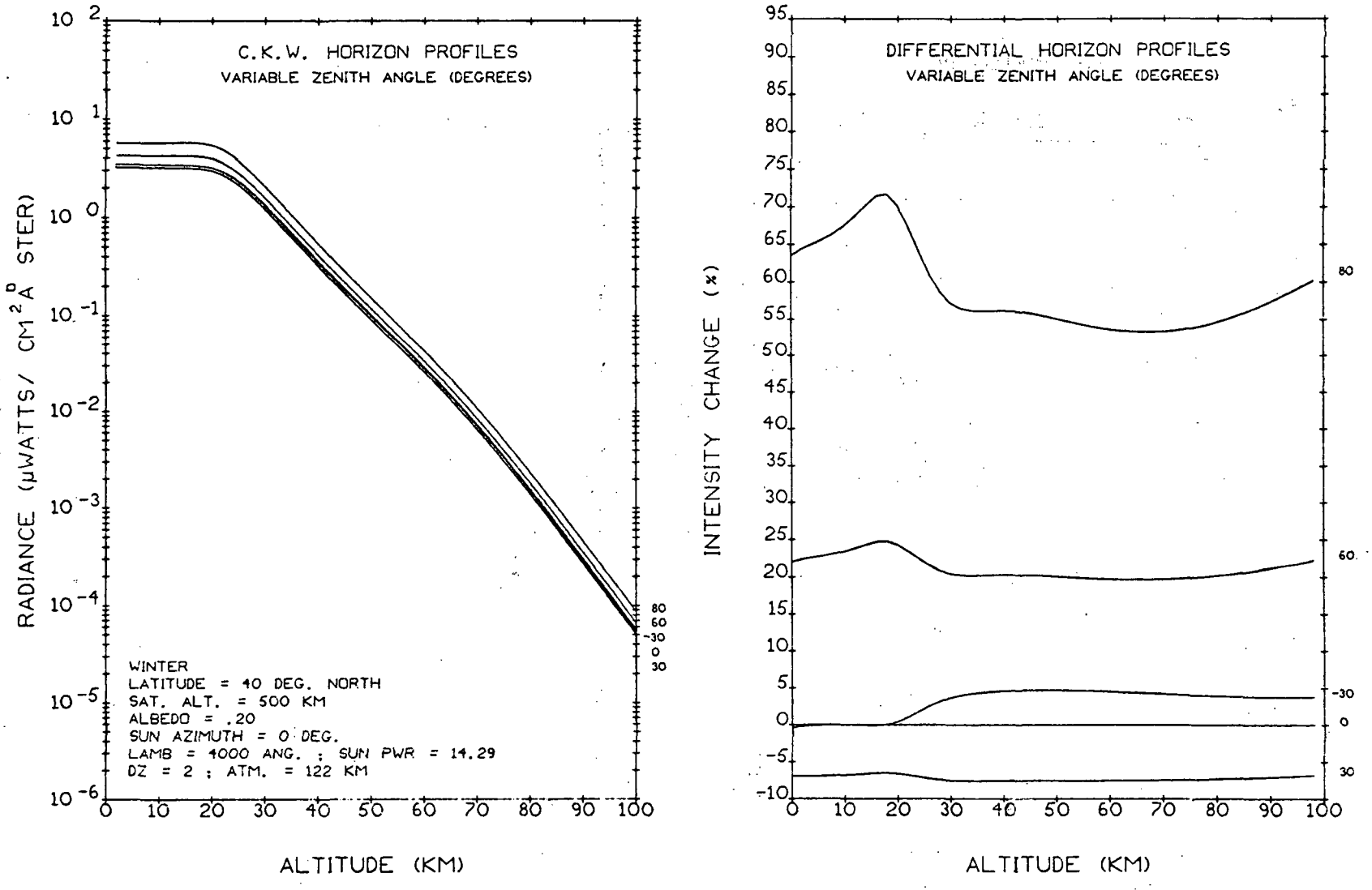

Fig. 5.1-32 Variable Zenith Angle Horizon Profiles
(Azimuth=0°, λ=4000 $\mathring{A}$, Albedo=.2)

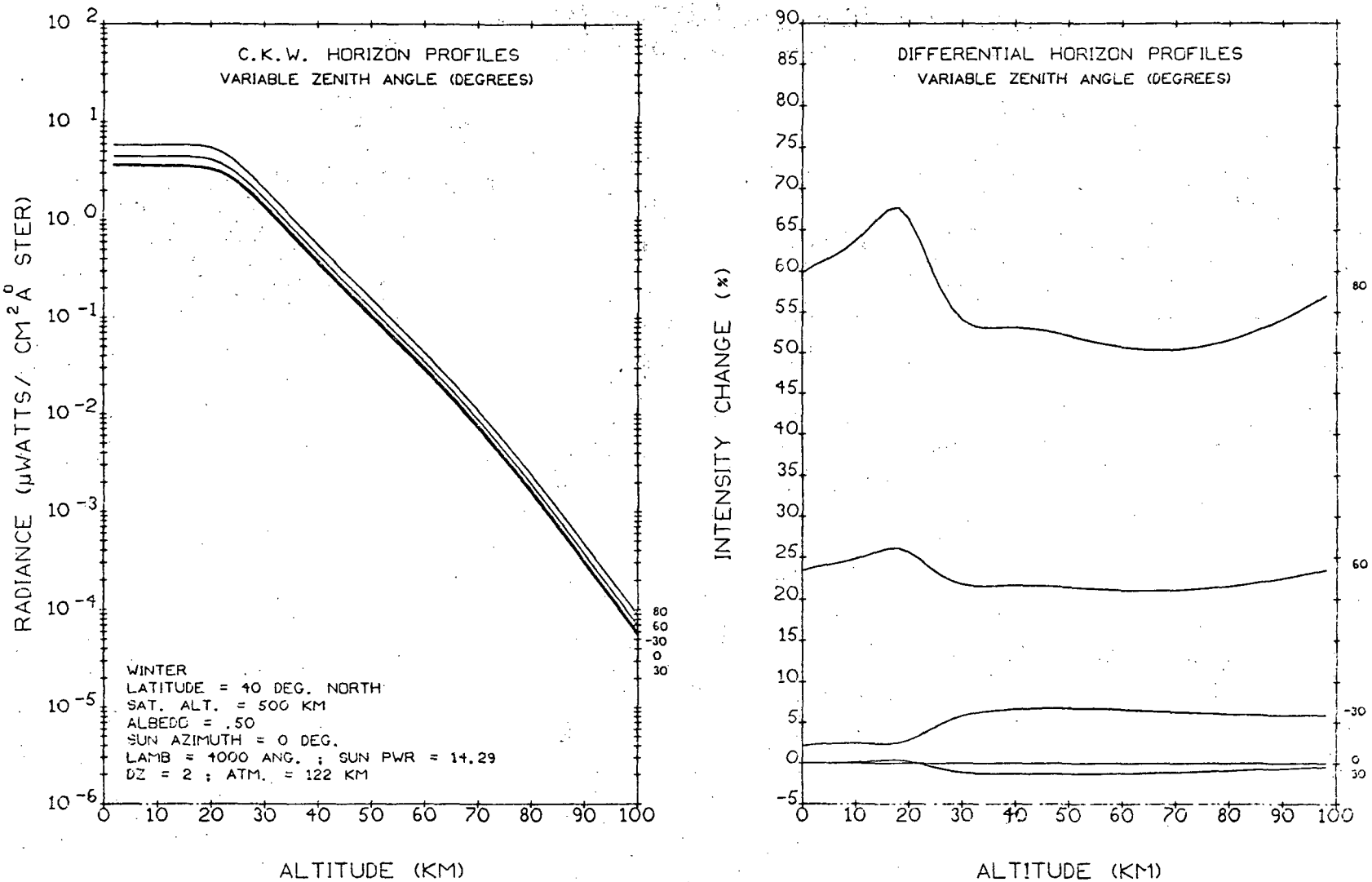

Fig. 5.1-33 Variable Zenith Angle Horizon Profiles
(Azimuth=0°, λ=4000 Å, Albedo=.5)

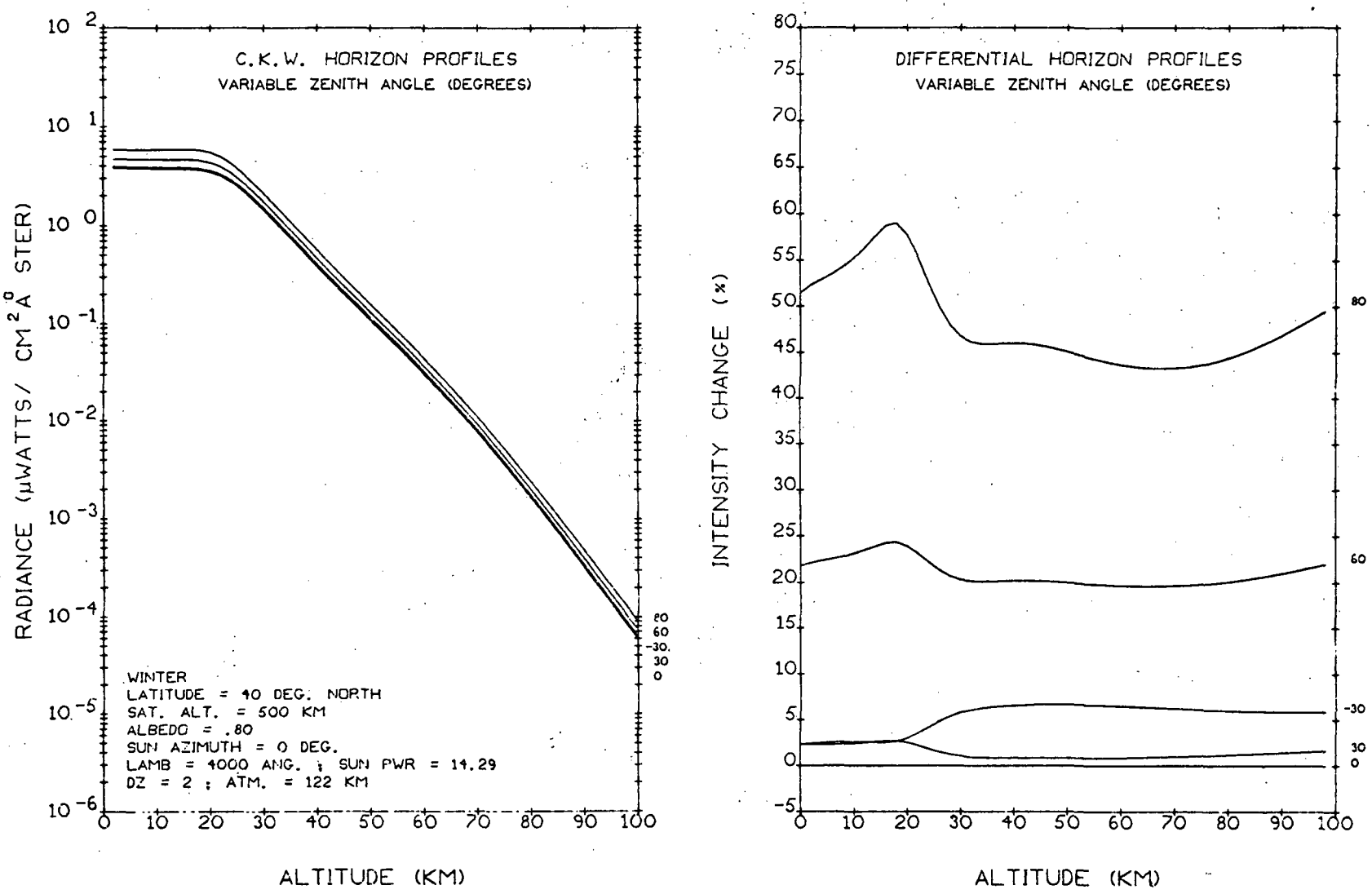

Fig. 5.1-34 Variable Zenith Angle Horizon Profiles
(Azimuth=0°, λ=4000 Å, Albedo=.8)

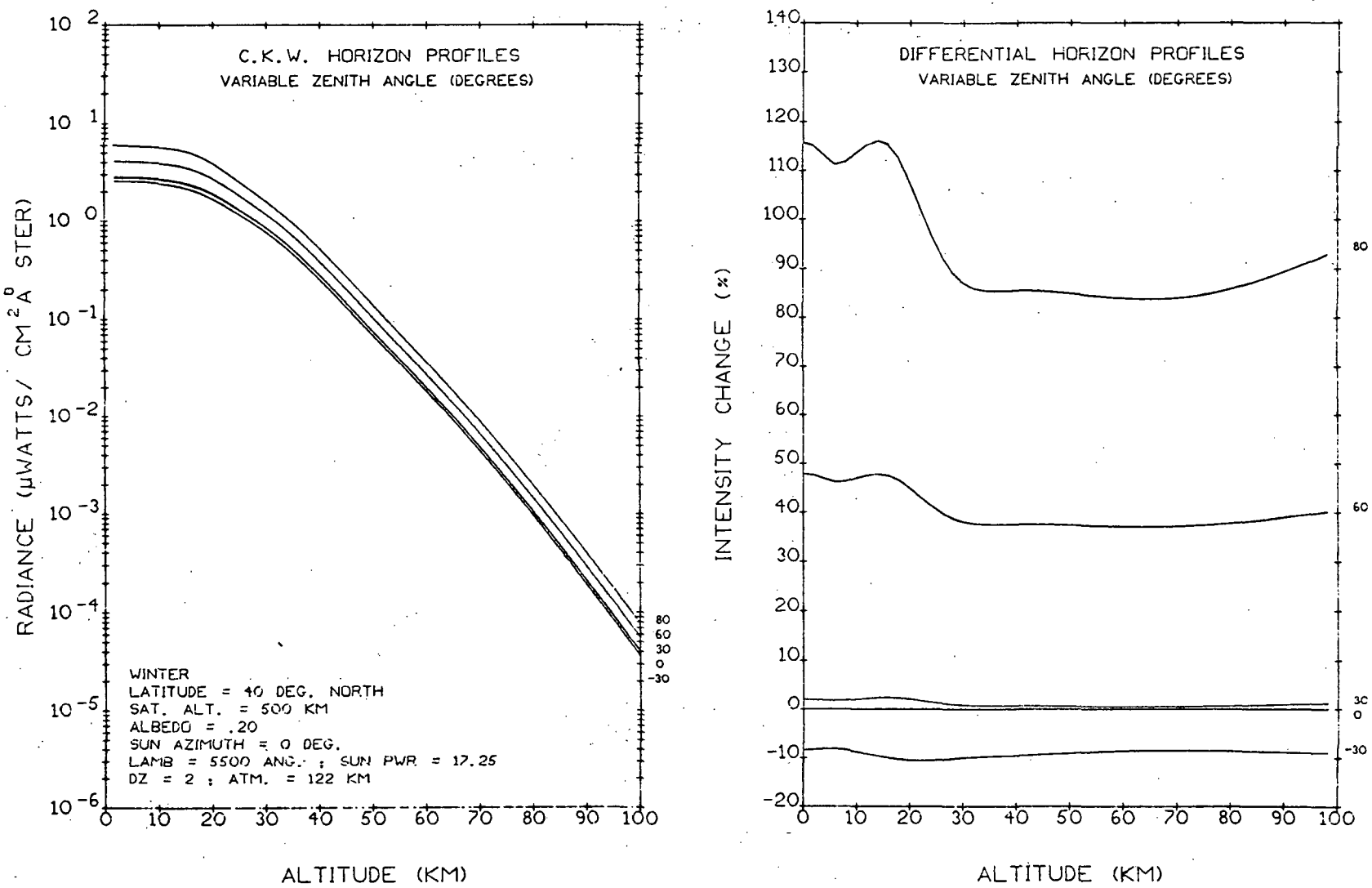

Fig. 5.1-35 Variable Zenith Angle Horizon Profiles
(Azimuth=0°, λ=5500 Å, Albedo=.2)

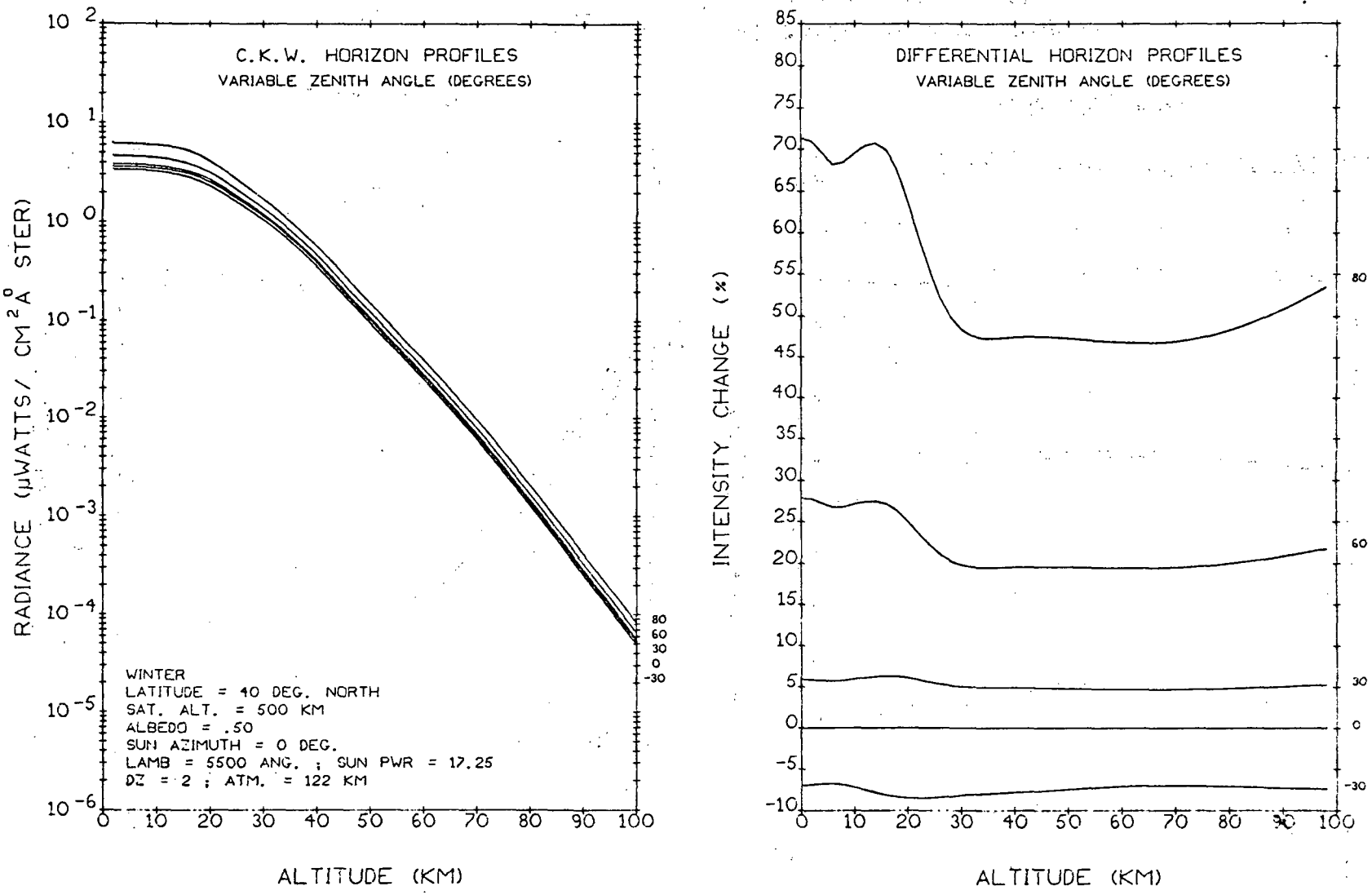

Fig. 5.1-36 Variable Zenith Angle Horizon Profiles
(Azimuth=0°, λ=5500 Å, Albedo=.5)

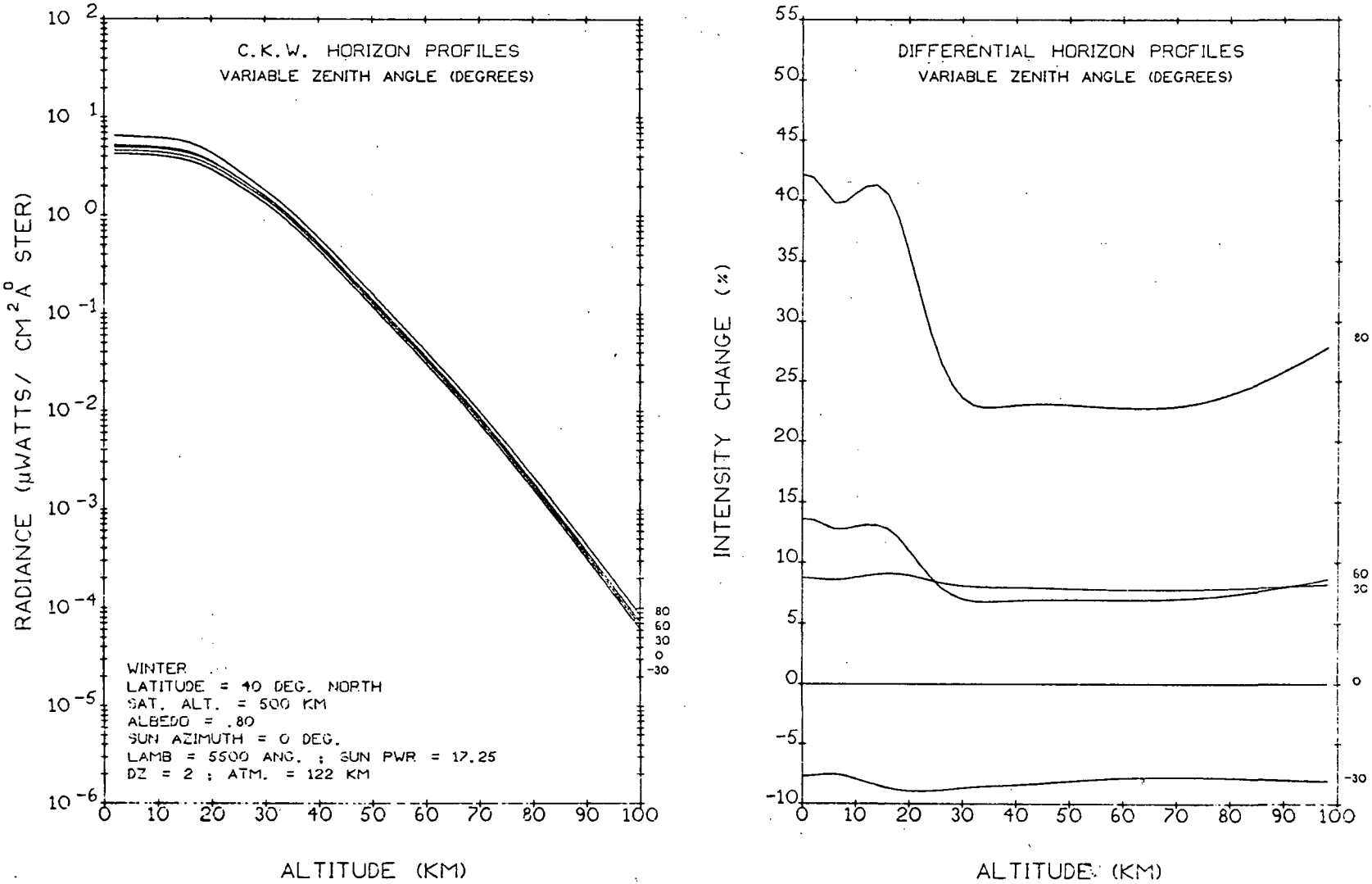

Fig. 5.1-37 Variable Zenith Angle Horizon Profiles
(Azimuth=0°, λ=5500 Å, Albedo=.8)

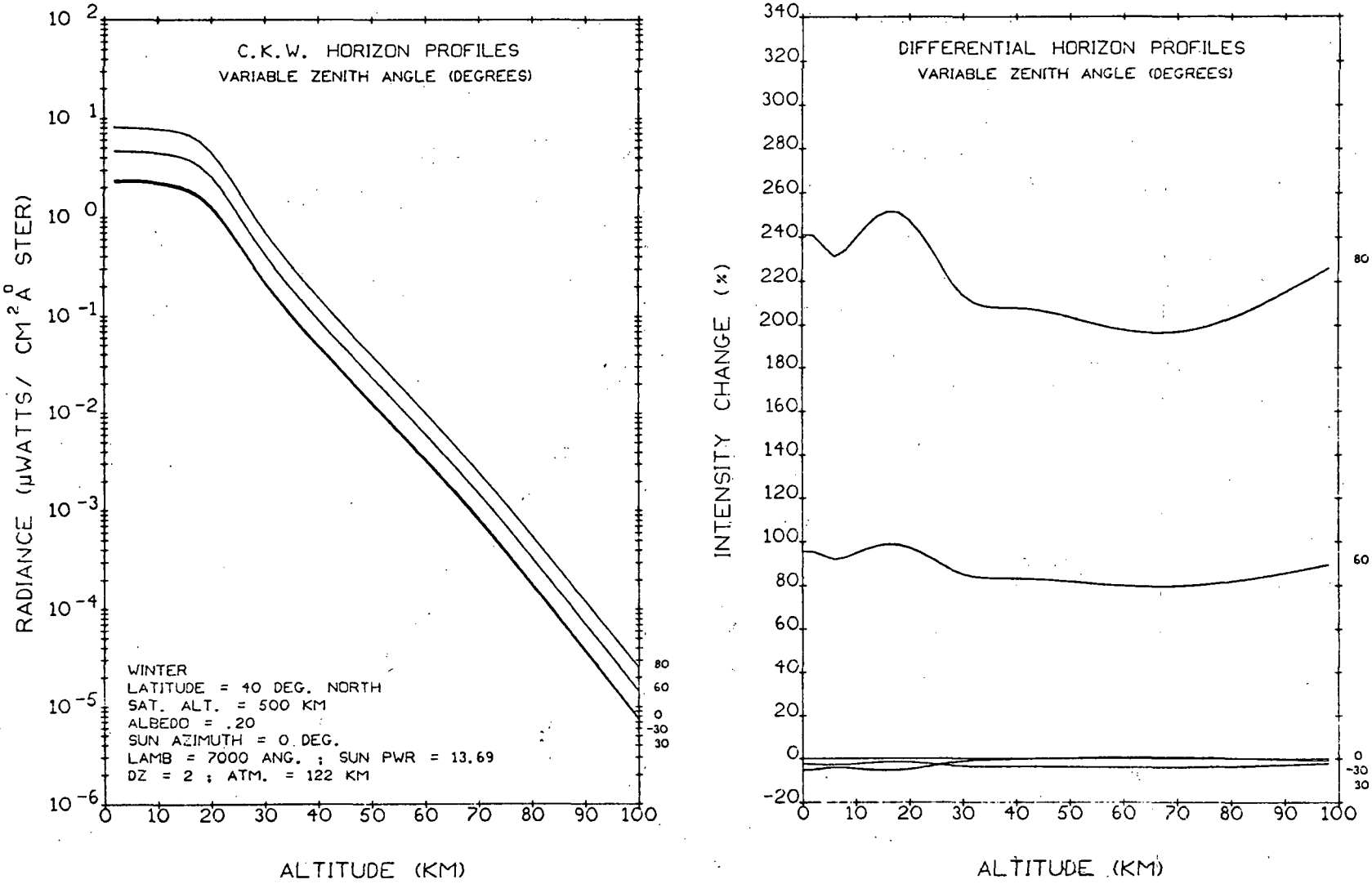

Fig. 5.1-38 Variable Zenith Angle Horizon Profiles
(Azimuth=0^o, λ=7000 Å, Albedo=.2)

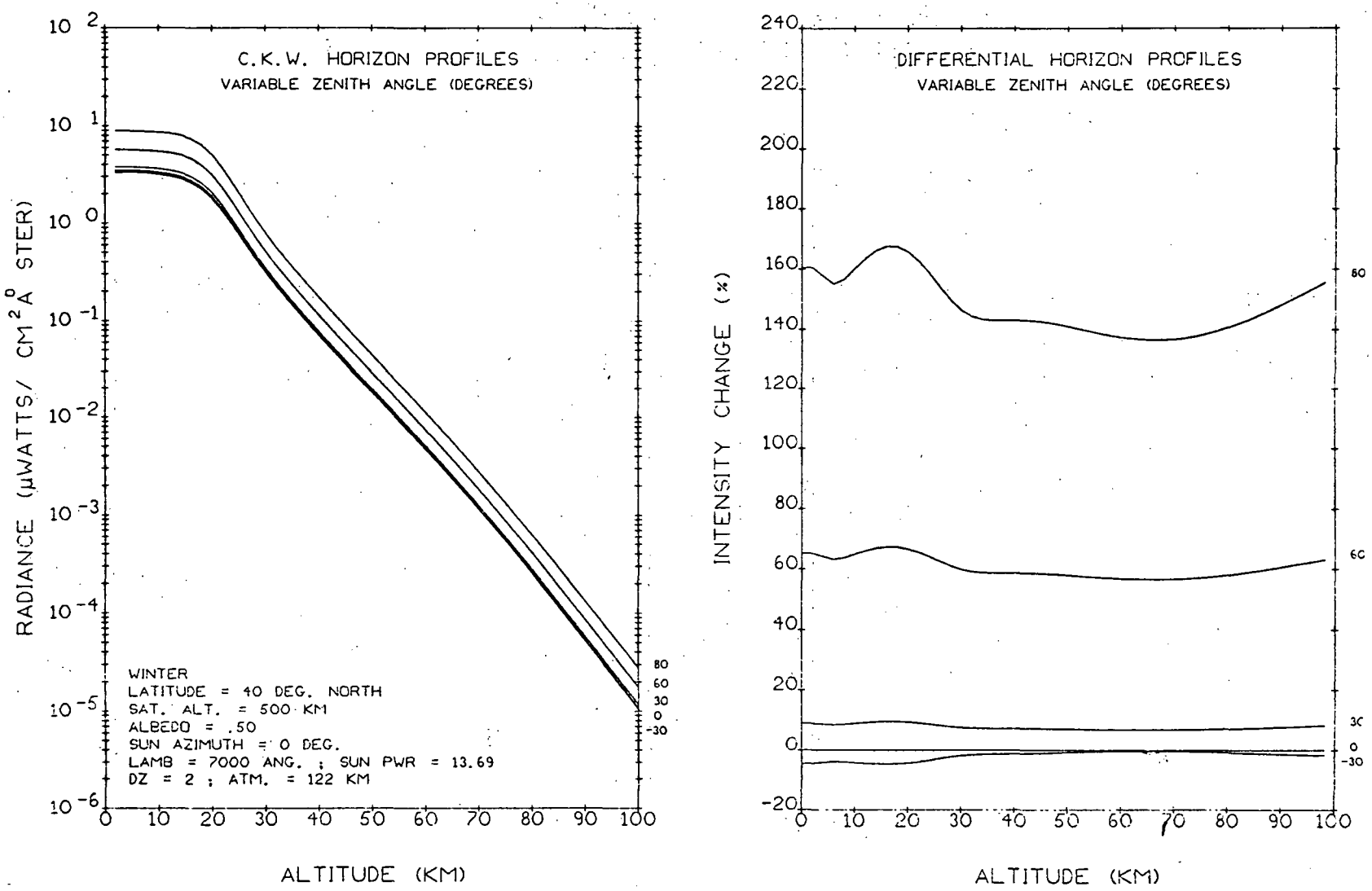

Fig. 5.1-39 Variable Zenith Angle Horizon Profiles
(Azimuth=0°, λ=7000 Å, Albedo=.5)

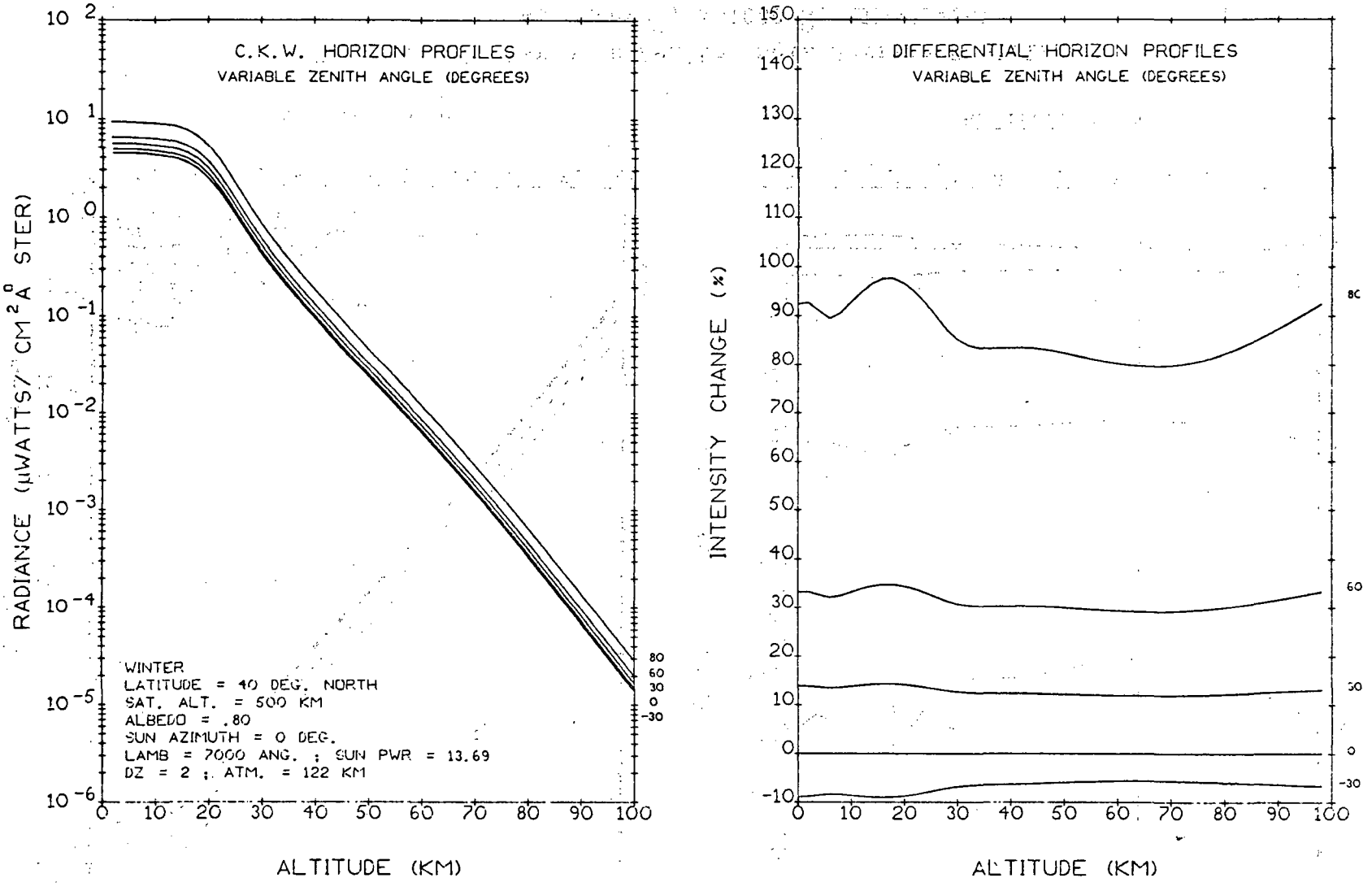

Fig. 5.1-40 Variable Zenith Angle Horizon Profiles
(Azimuth=0°, λ=7000 Å, Albedo=.8)

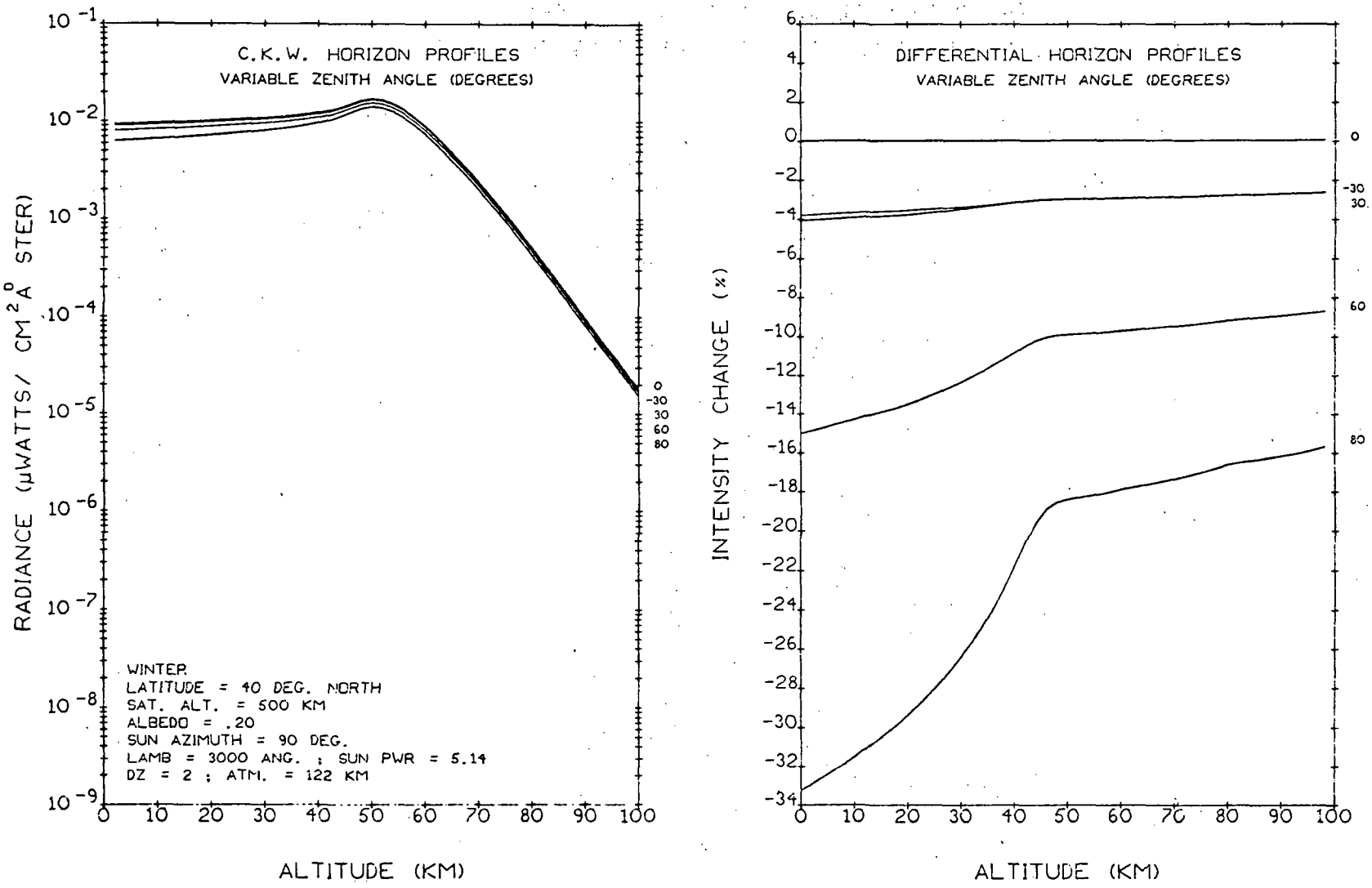

Fig. 5.1-41 Variable Zenith Angle Horizon Profiles
(Azimuth=90°, λ=3000 Å, Albedo=.2)

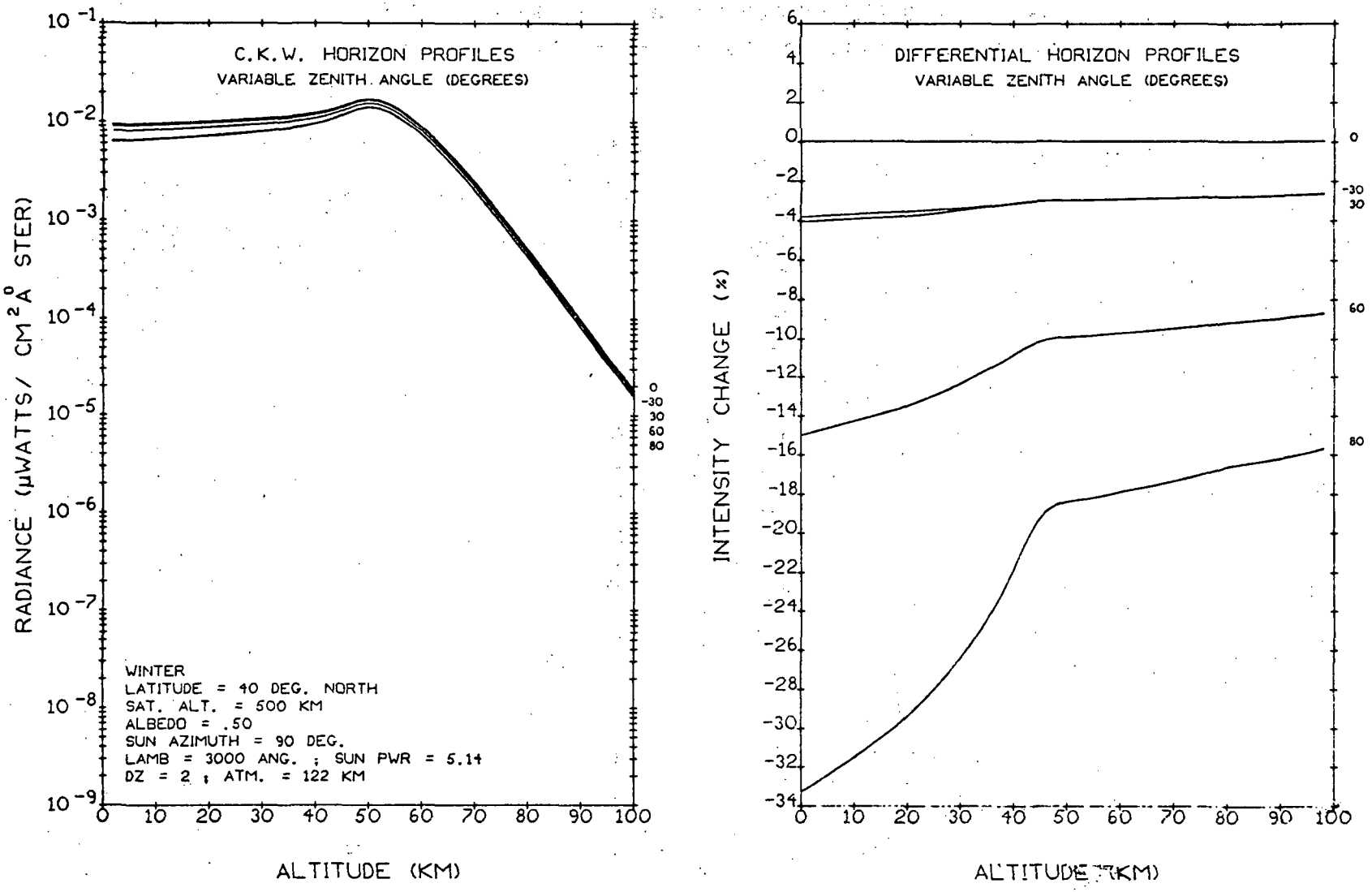

Fig. 5.1-42 Variable Zenith Angle Horizon Profiles-
(Azimuth=90°, λ=3000 Å, Albedo=.5)

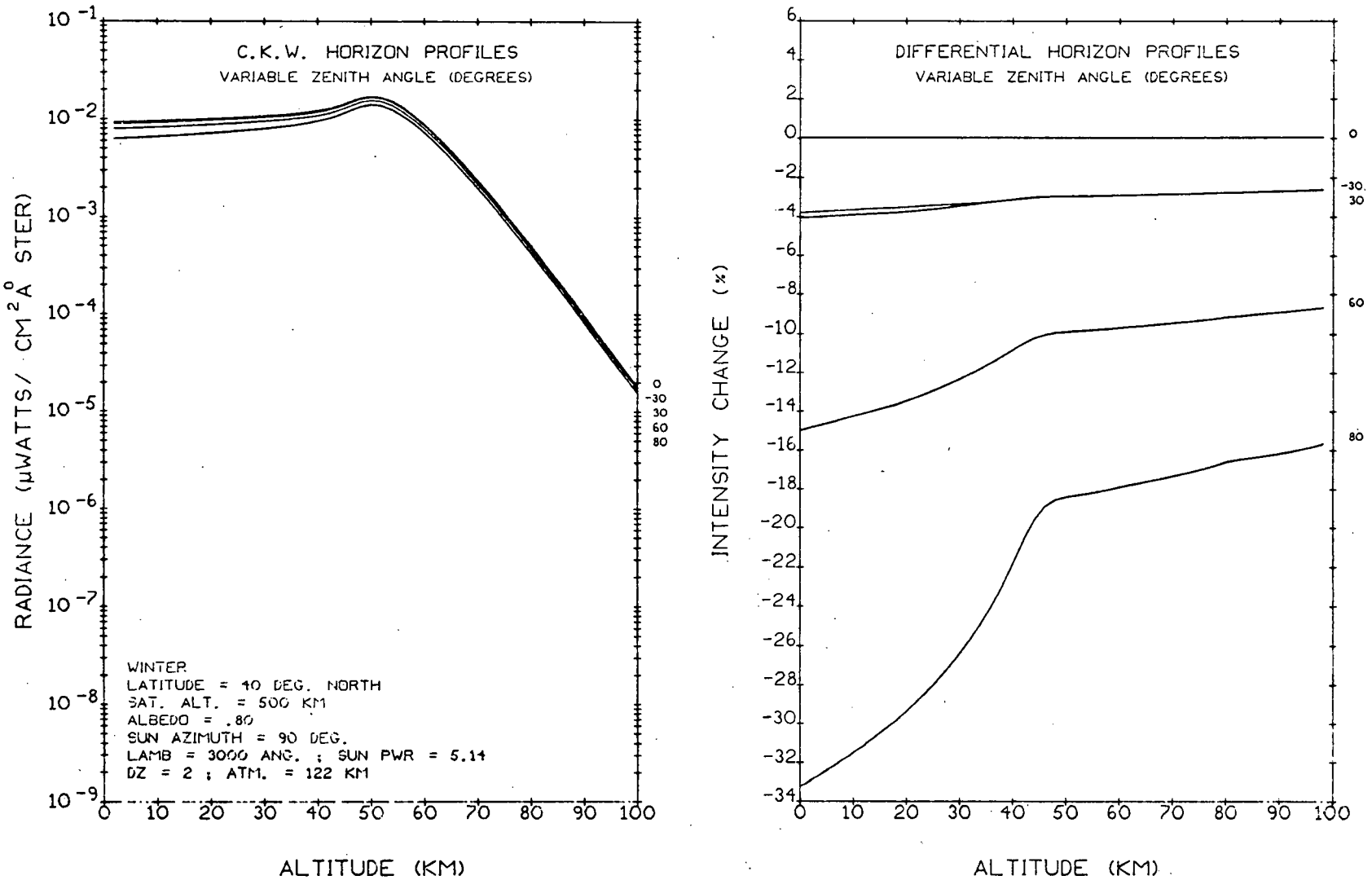

Fig. 5.1-43 Variable Zenith Angle Horizon Profiles
(Azimuth=90^o, λ=3000 Å, Albedo=.8)

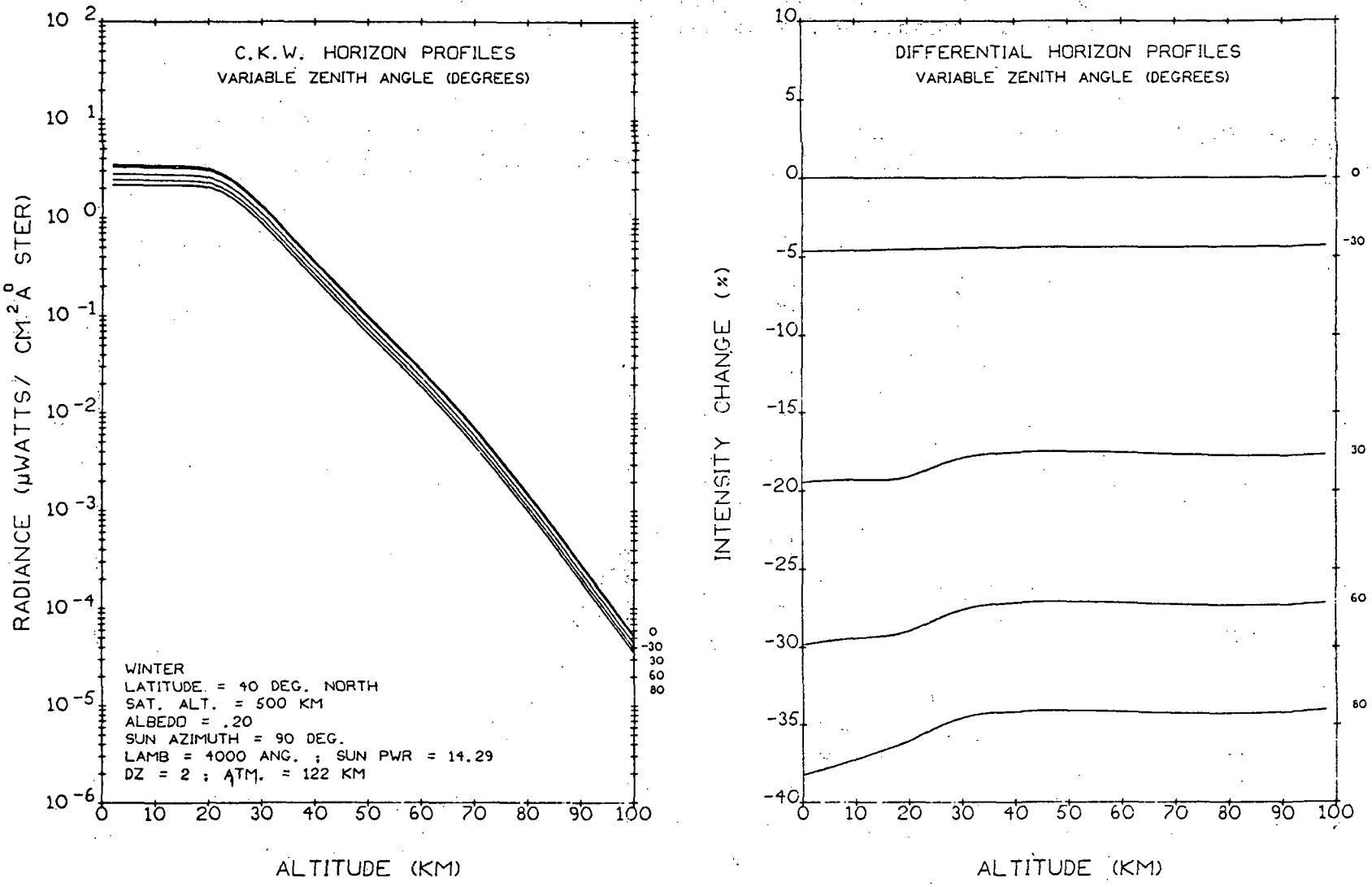

Fig. 5.1-44 Variable Zenith Angle Horizon Profiles
(Azimuth=90^o, λ=4000 $\mathring{A}$, Albedo=.2)

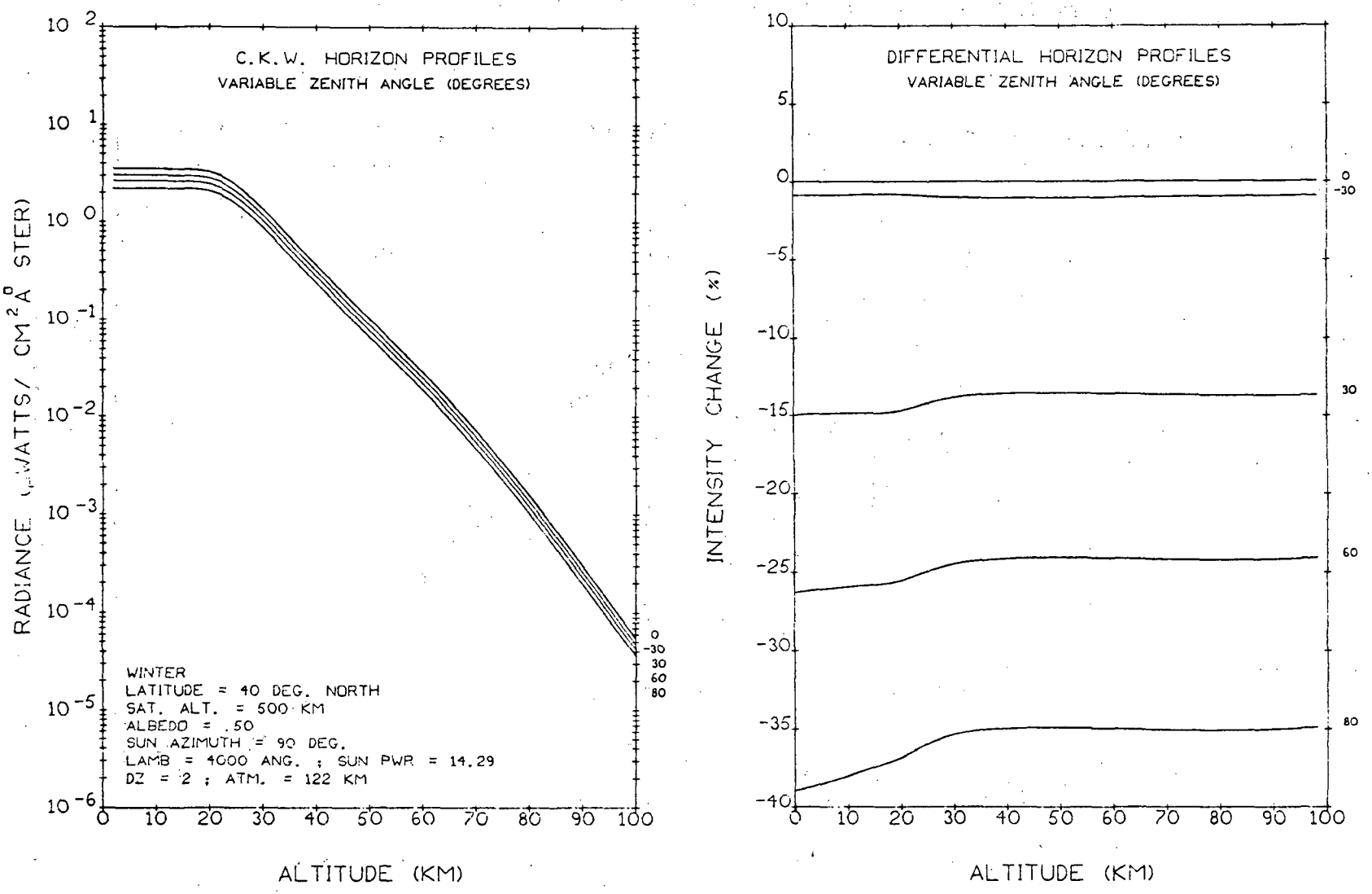

Fig. 5.1-45 Variable Zenith Angle Horizon Profiles
(Azimuth=90°, λ=4000 Å, Albedo=.5)

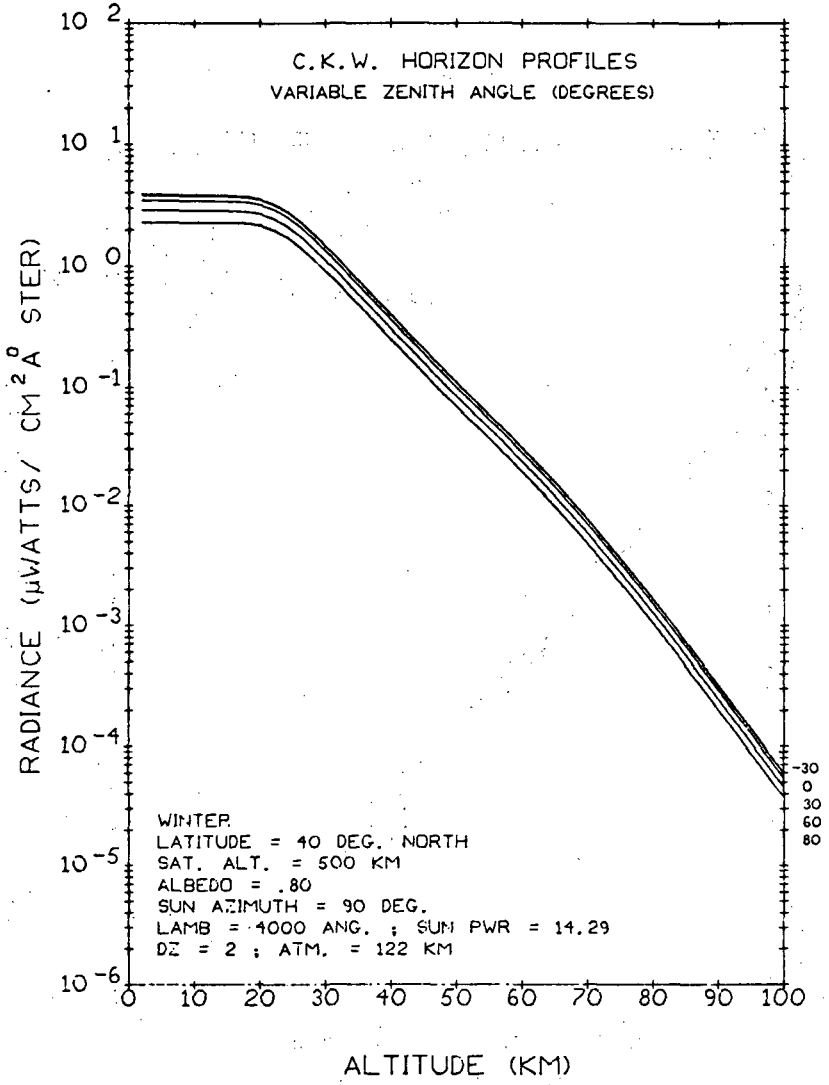

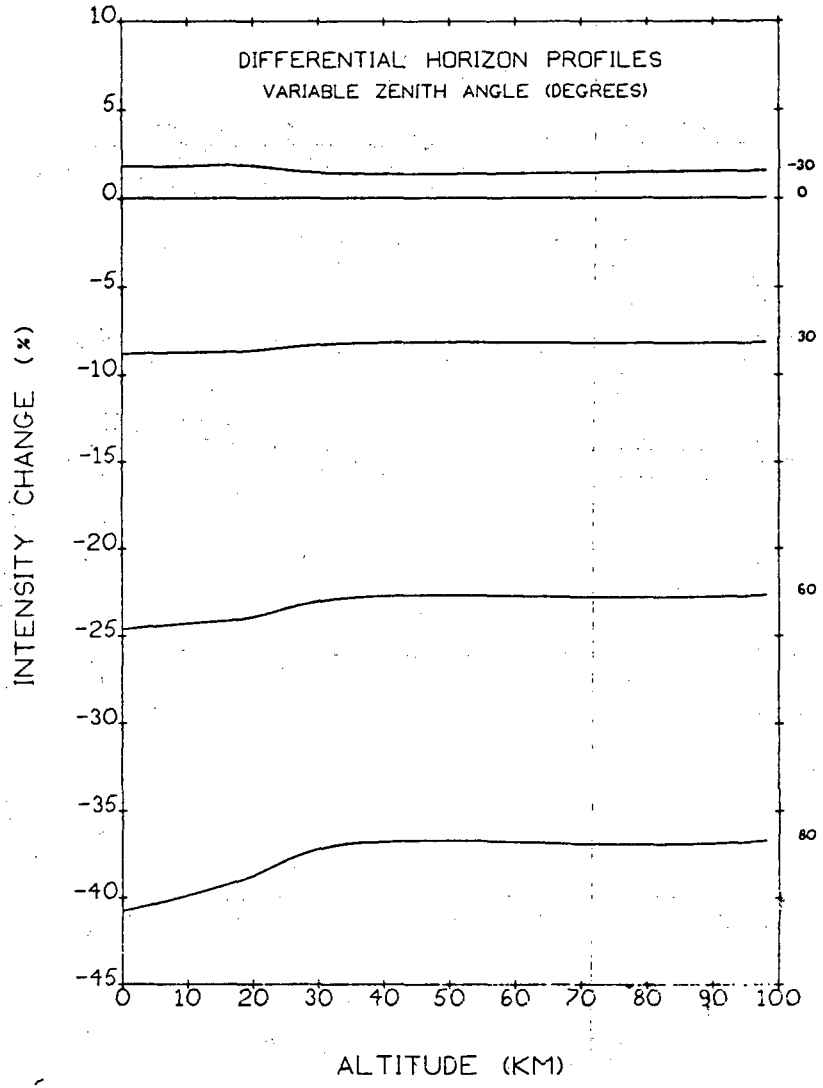

Fig. 5.1-46 Variable Zenith Angle Horizon Profiles
(Azimuth=90°, λ=4000 Å, Albedo=.8)

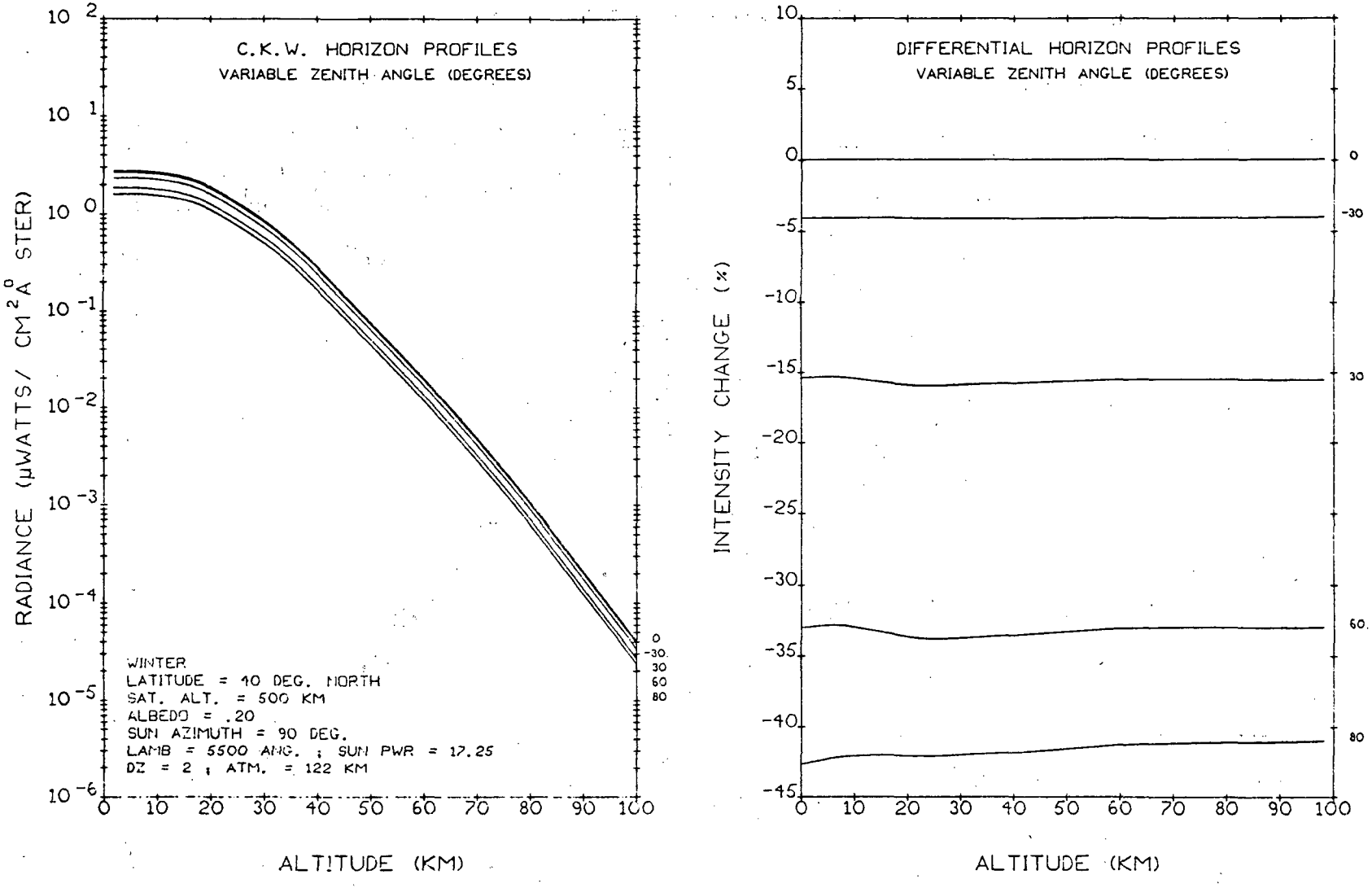

Fig. 5.1-47 Variable Zenith Angle Horizon Profiles
(Azimuth=90°, λ=5500 Å, Albedo=.2)

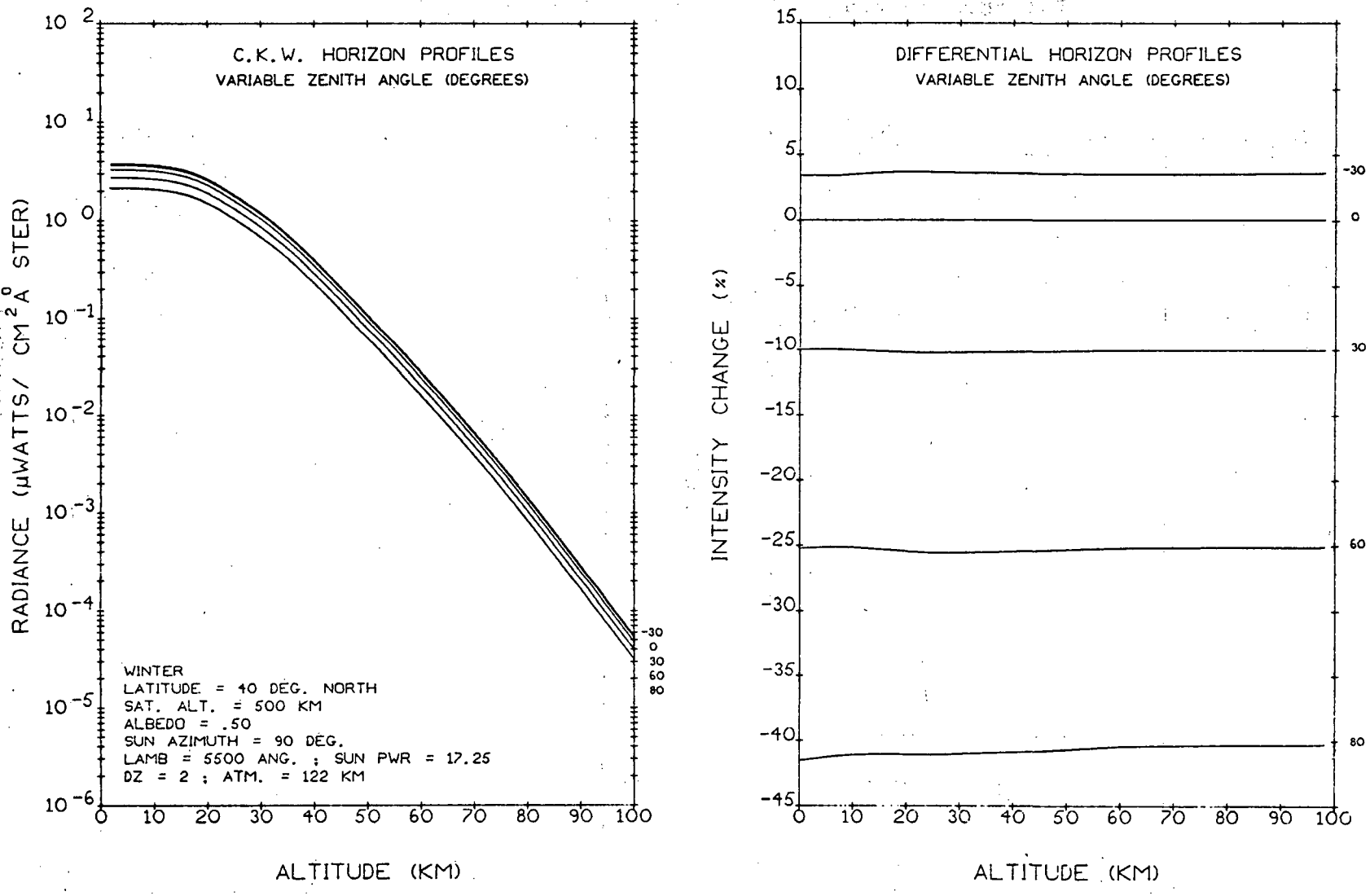

Fig. 5.1-48 Variable Zenith Angle Horizon Profiles
(Azimuth=90°, λ=5500 Å, Albedo=.5)

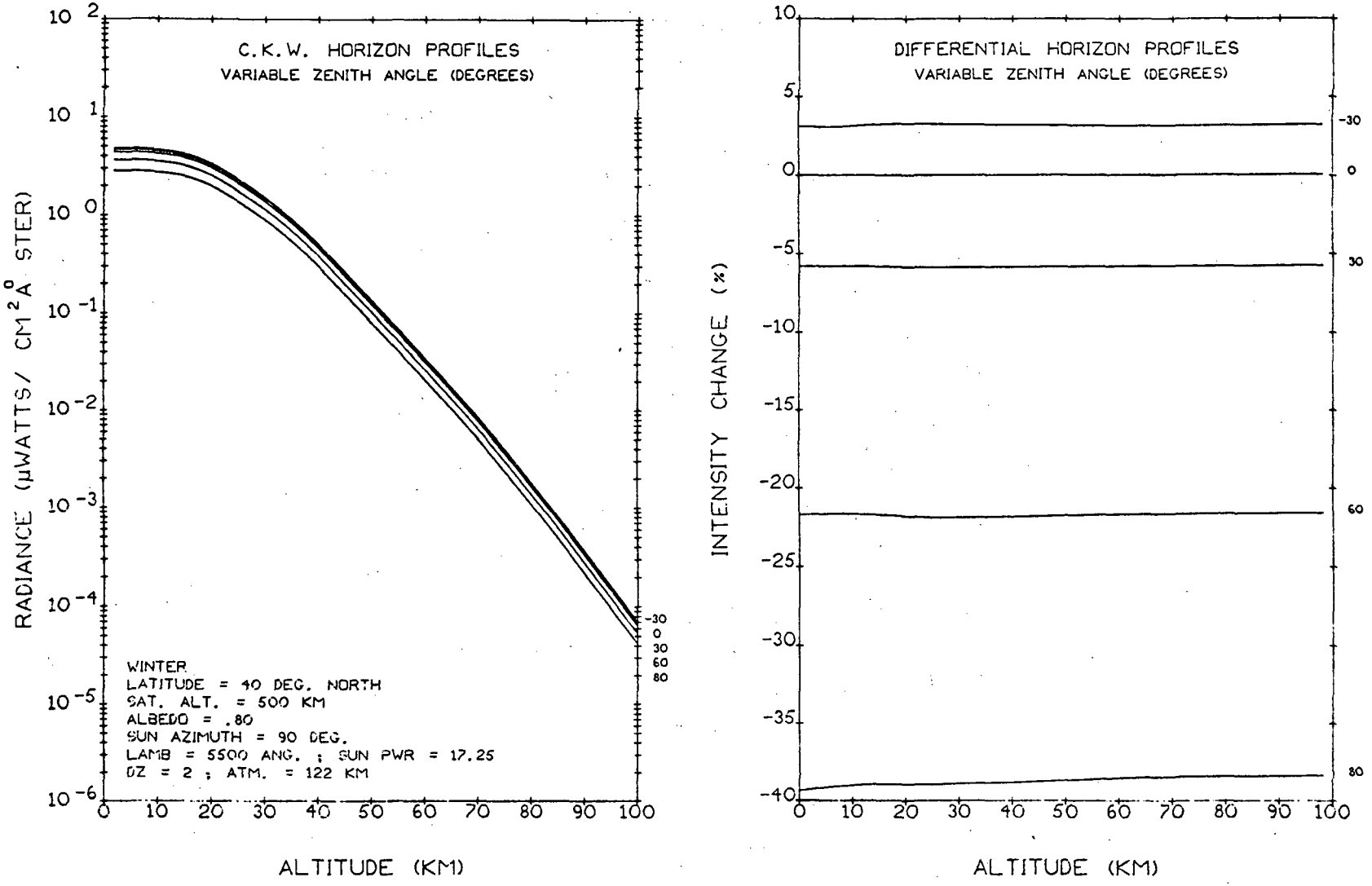

Fig. 5.1-49 Variable Zenith Angle Horizon Profiles
(Azimuth=90°, λ=5500 Å, Albedo=.8)

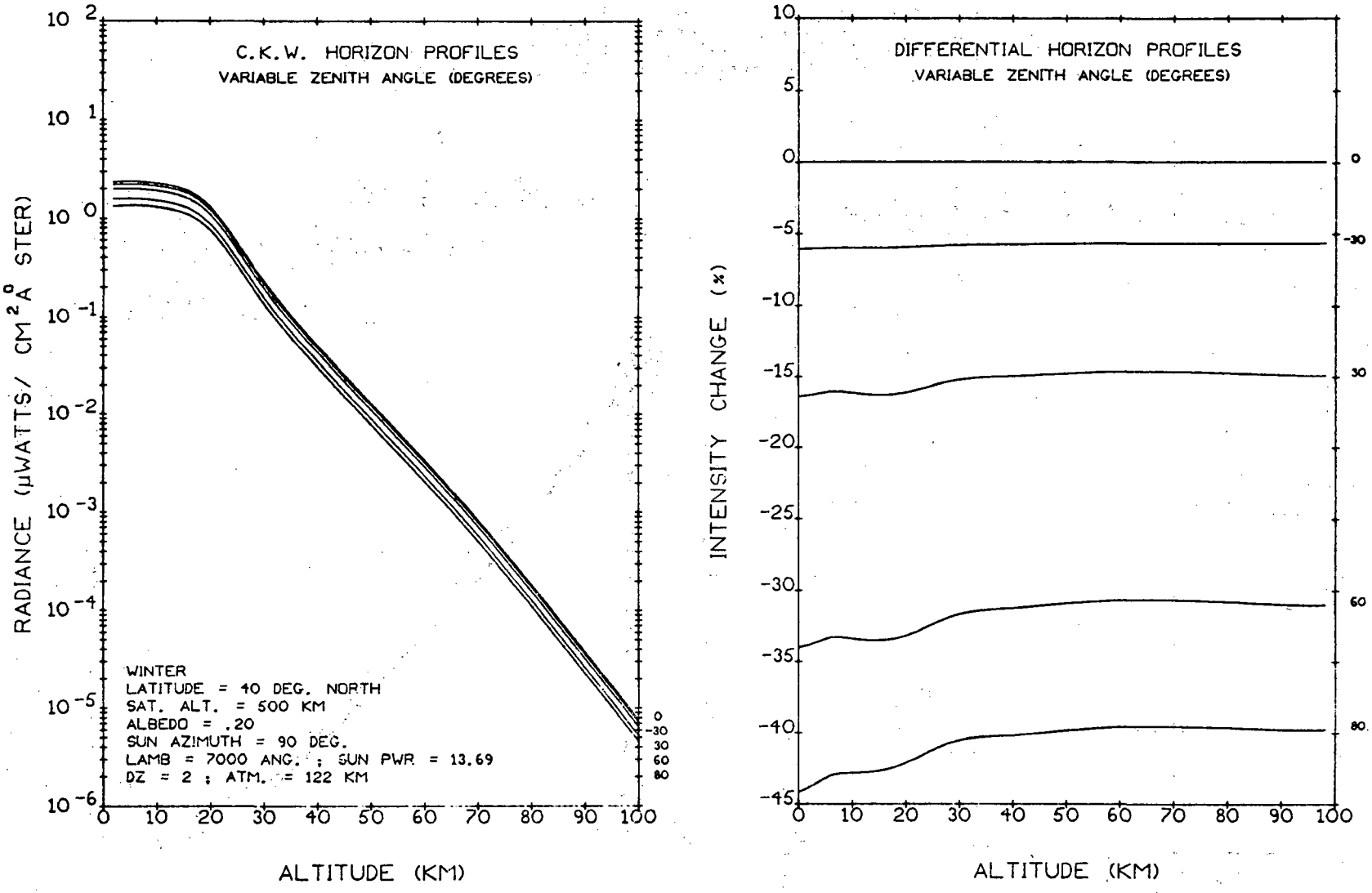

Fig. 5.1-50 Variable Zenith Angle Horizon Profiles
(Azimuth=90°, λ=7000 Å, Albedo=.2)

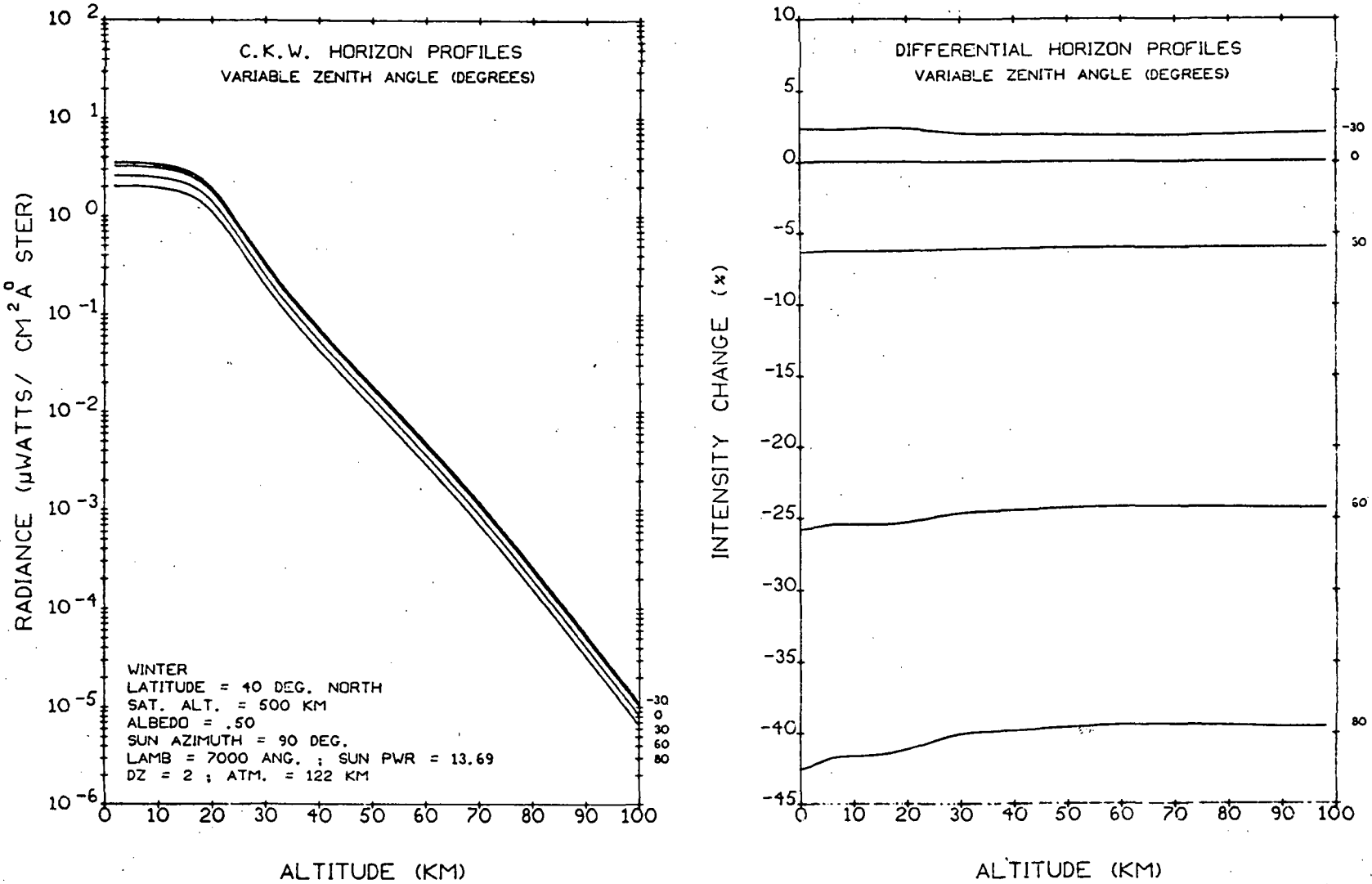

Fig. 5.1-51 Variable Zenith Angle Horizon Profiles
(Azimuth=90°, λ=7000 Å, Albedo=.5)

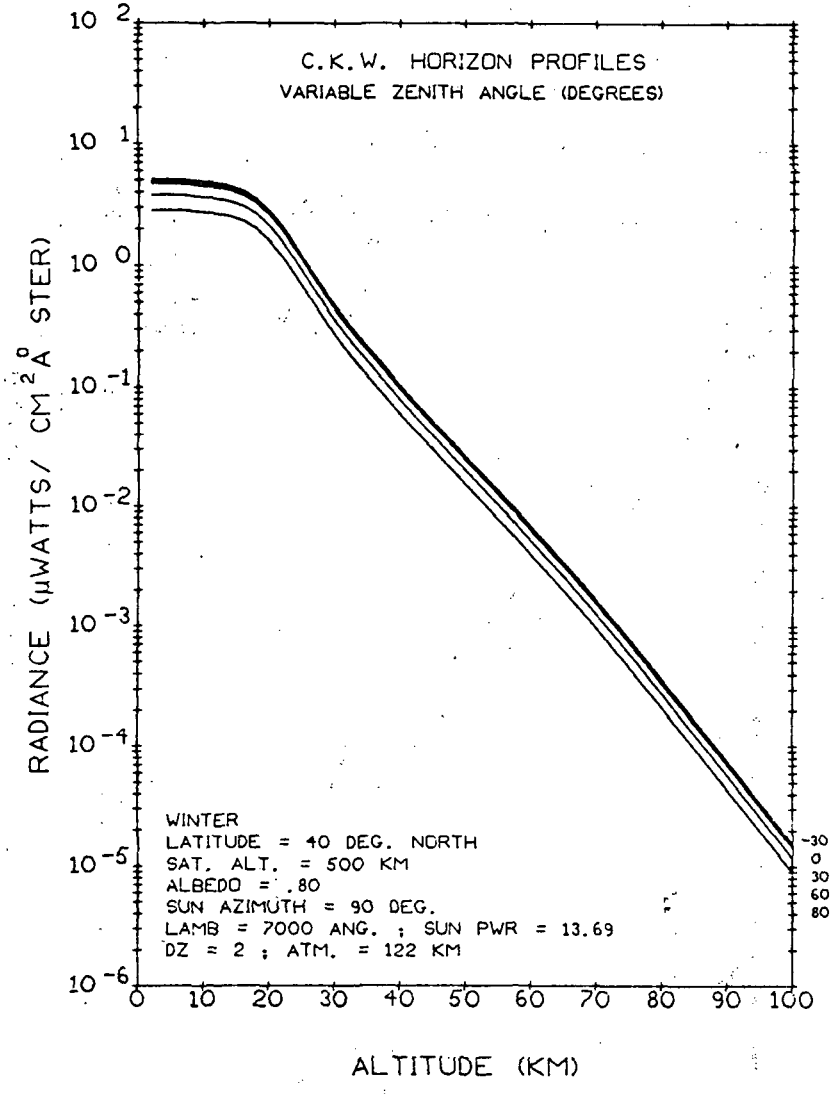

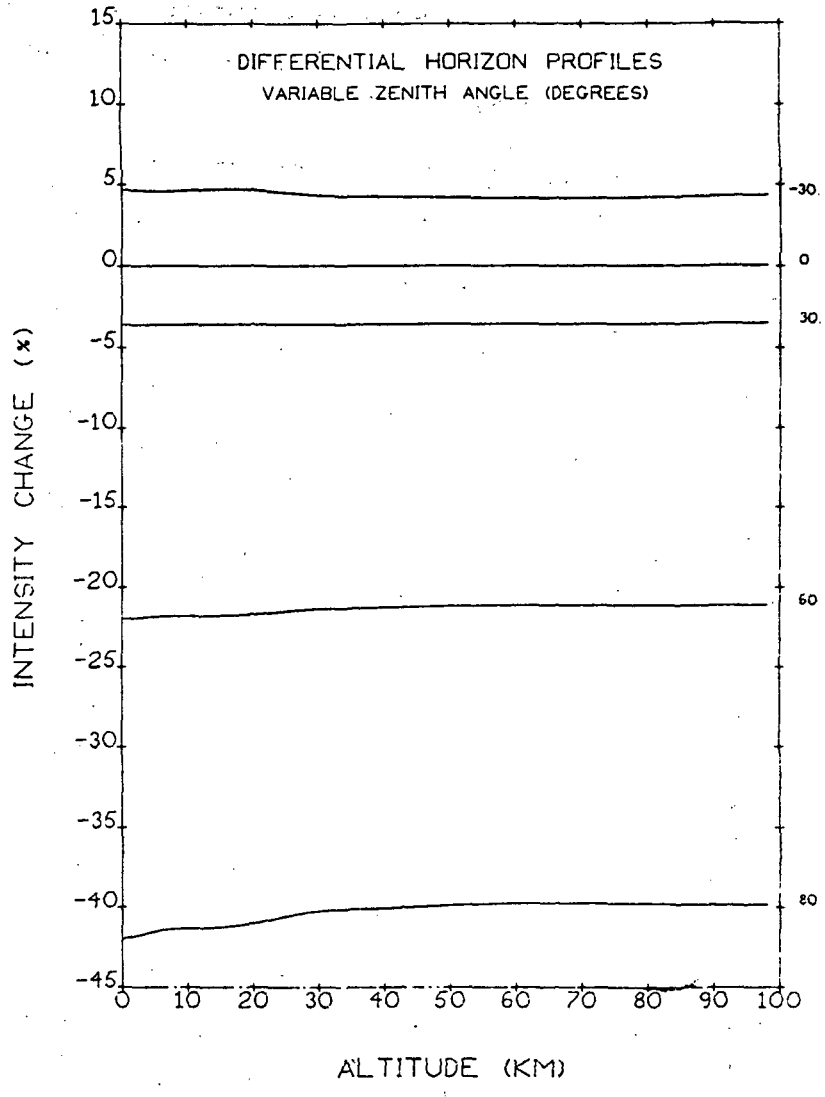

Fig. 5.1-52 Variable Zenith Angle Horizon Profiles
(Azimuth=90°, λ=7000 Å, Albedo=.8)

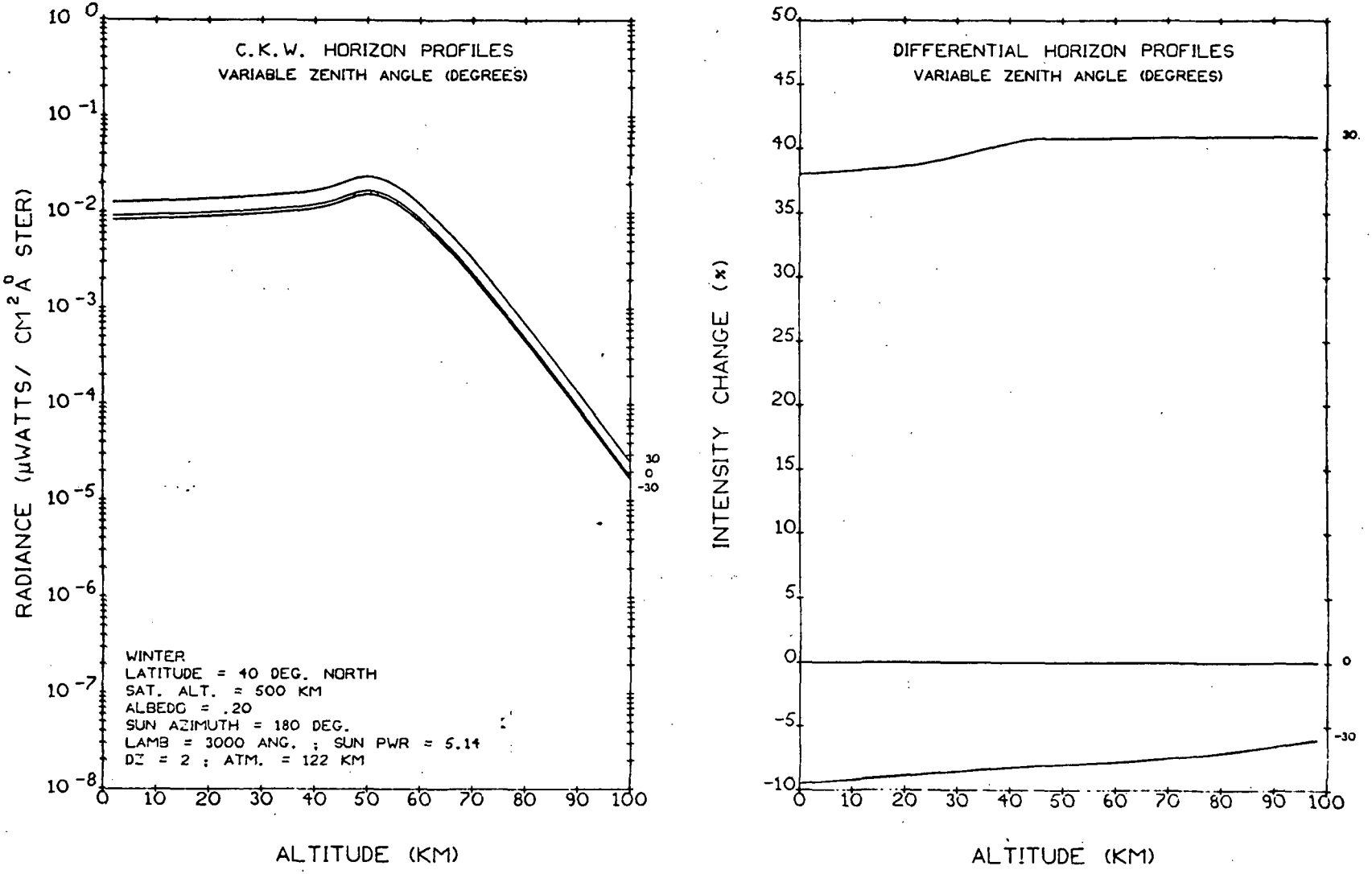

Fig. 5.1-53 Variable Zenith Angle Horizon Profiles
(Azimuth=180°, λ=3000 Å, Albedo=.2)

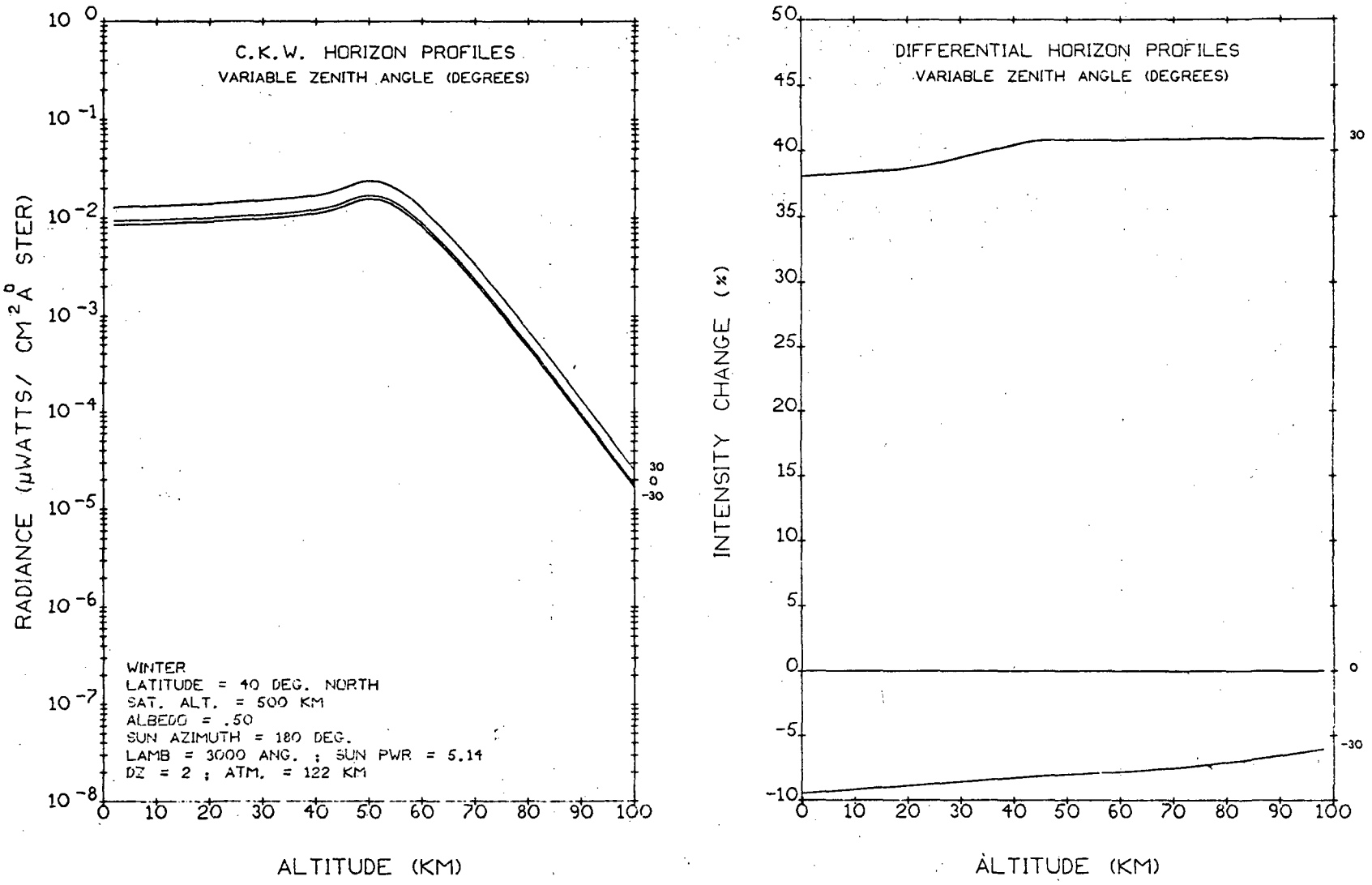

Fig. 5.1-54 Variable Zenith Angle Horizon Profiles
(Azimuth=180°, λ=3000 Å, Albedo=.5)

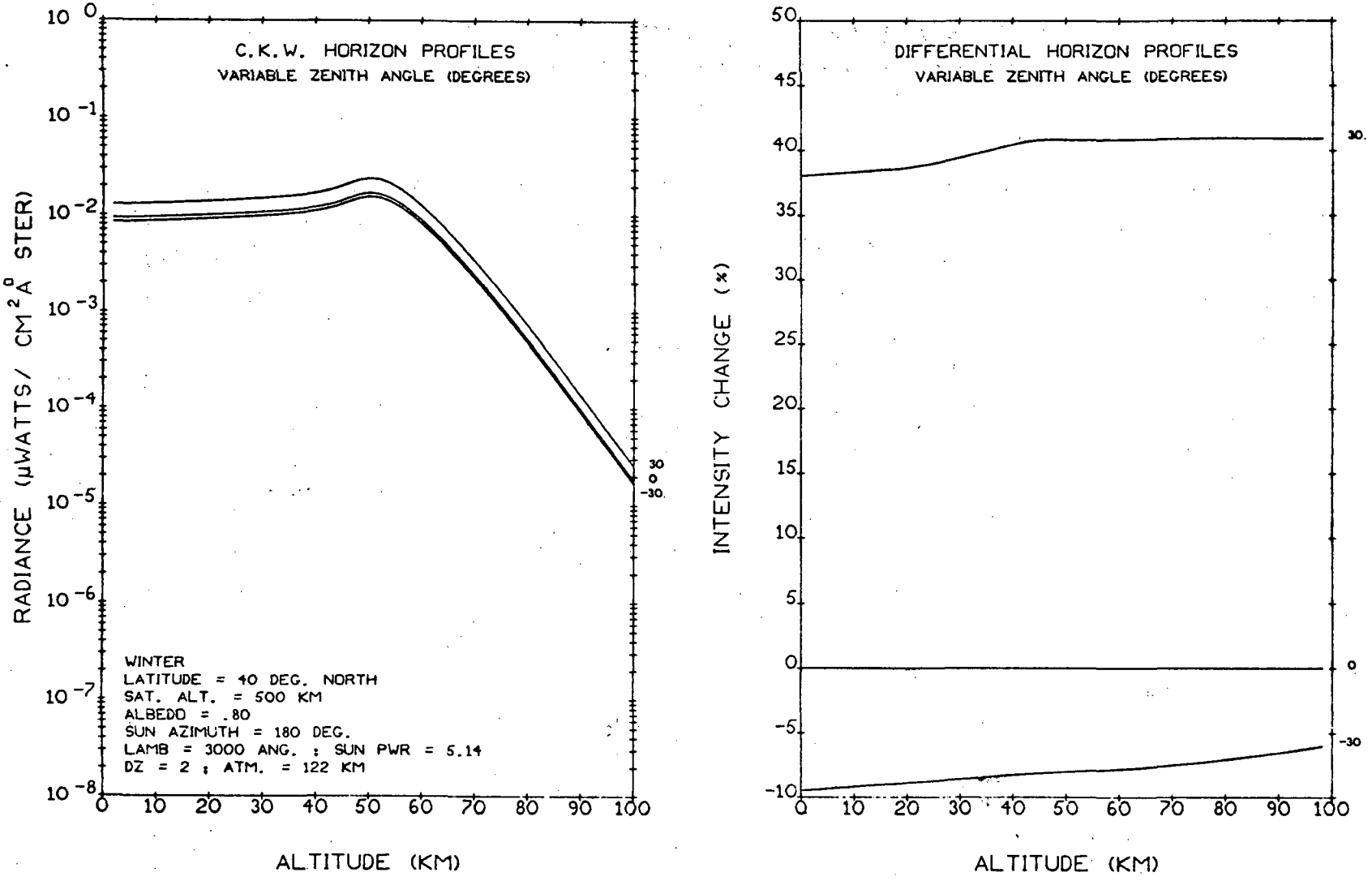

Fig. 5.1-55 Variable Zenith Angle Horizon Profiles
(Azimuth=180°, λ=3000 Å, Albedo=.8)

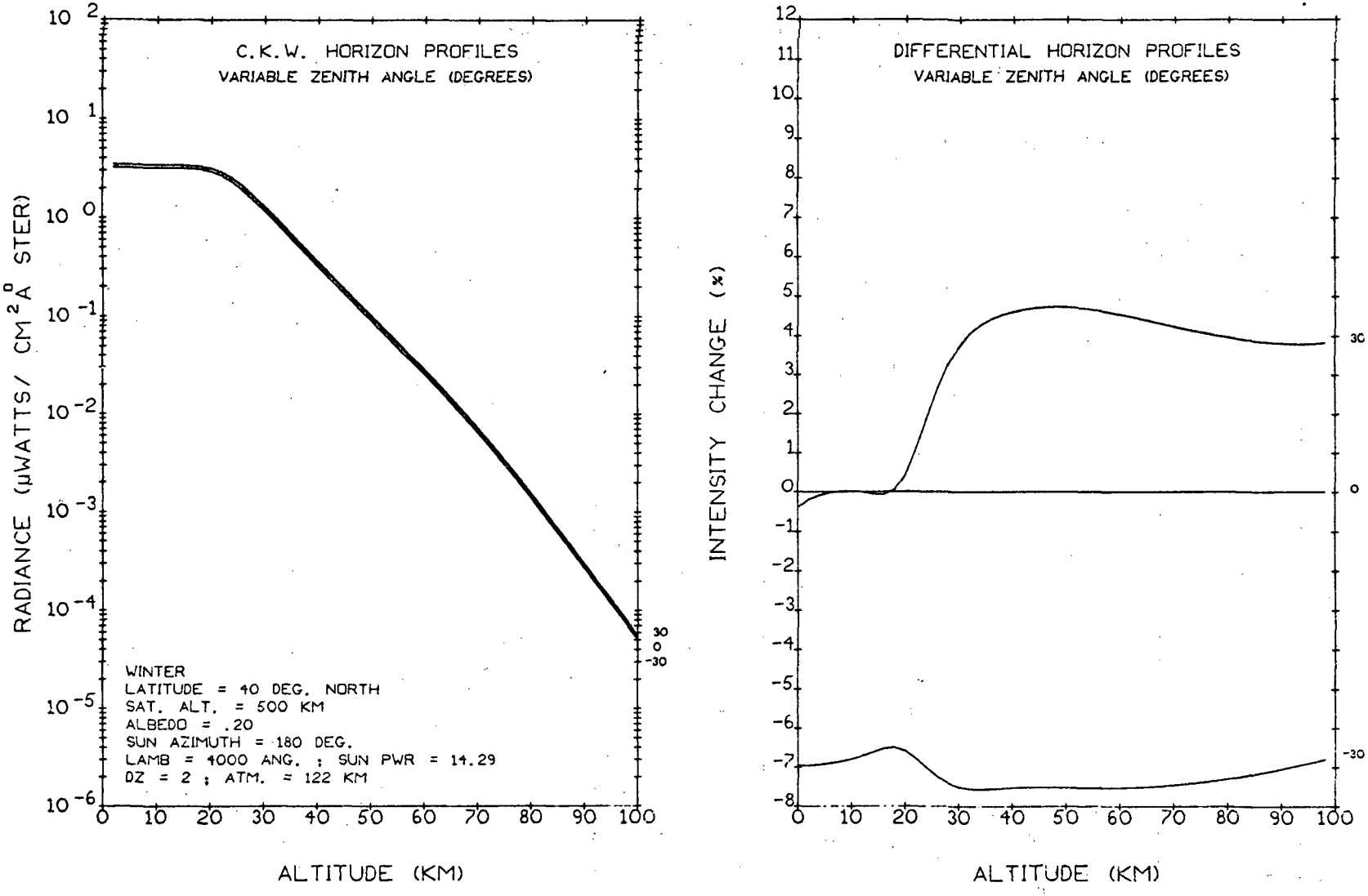

Fig. 5.1-56 Variable Zenith Angle Horizon Profiles
(Azimuth=180°, λ=4000 Å, Albedo=.2)

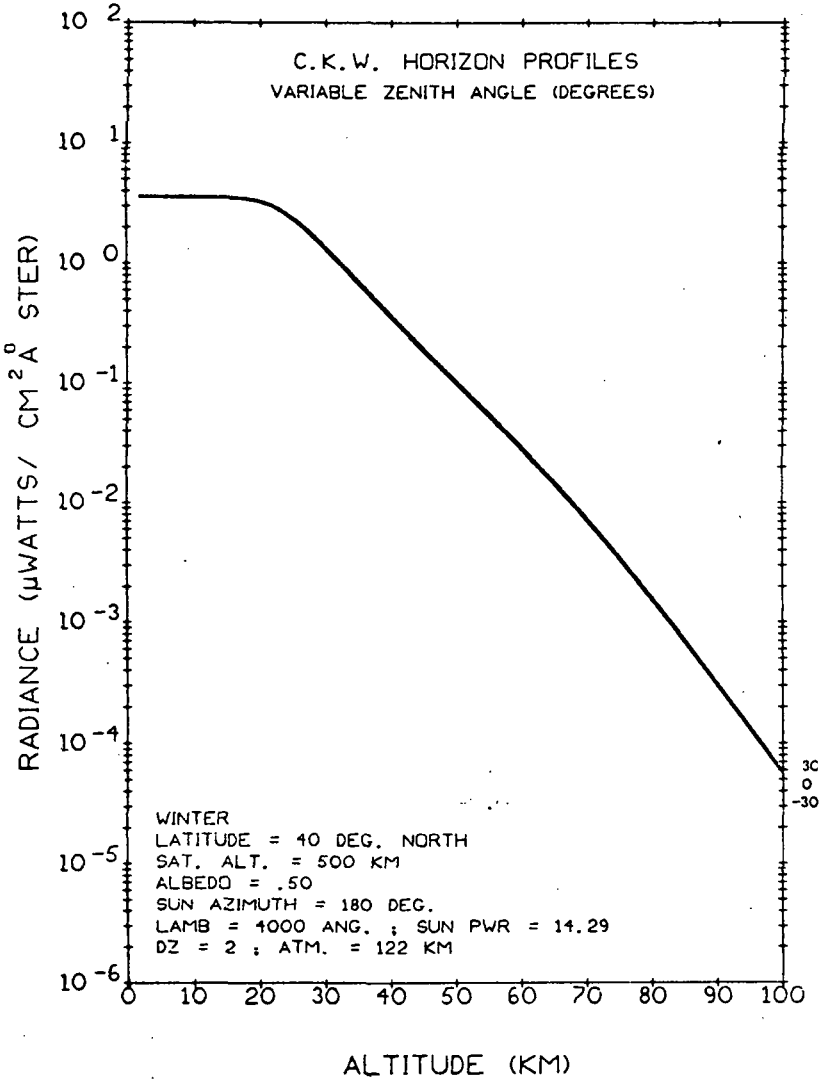

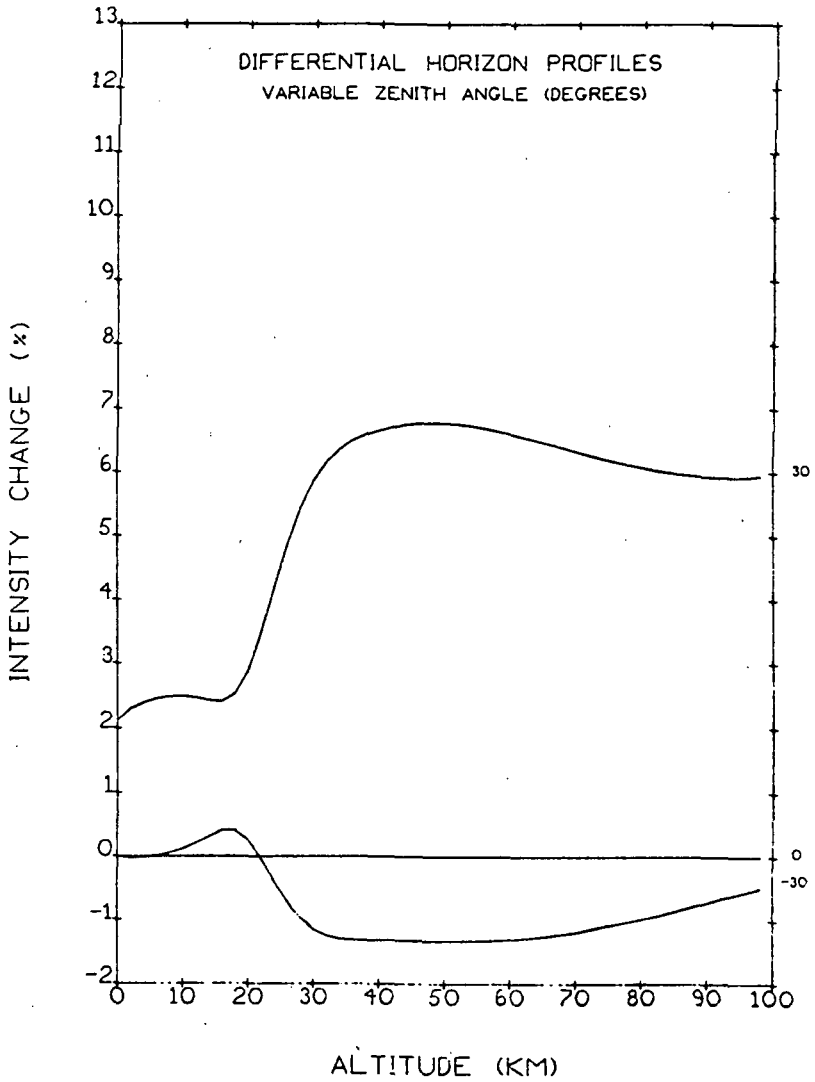

Fig. 5.1-57 Variable Zenith Angle Horizon Profiles
(Azimuth=180°, λ=4000 Å, Albedo=.5)

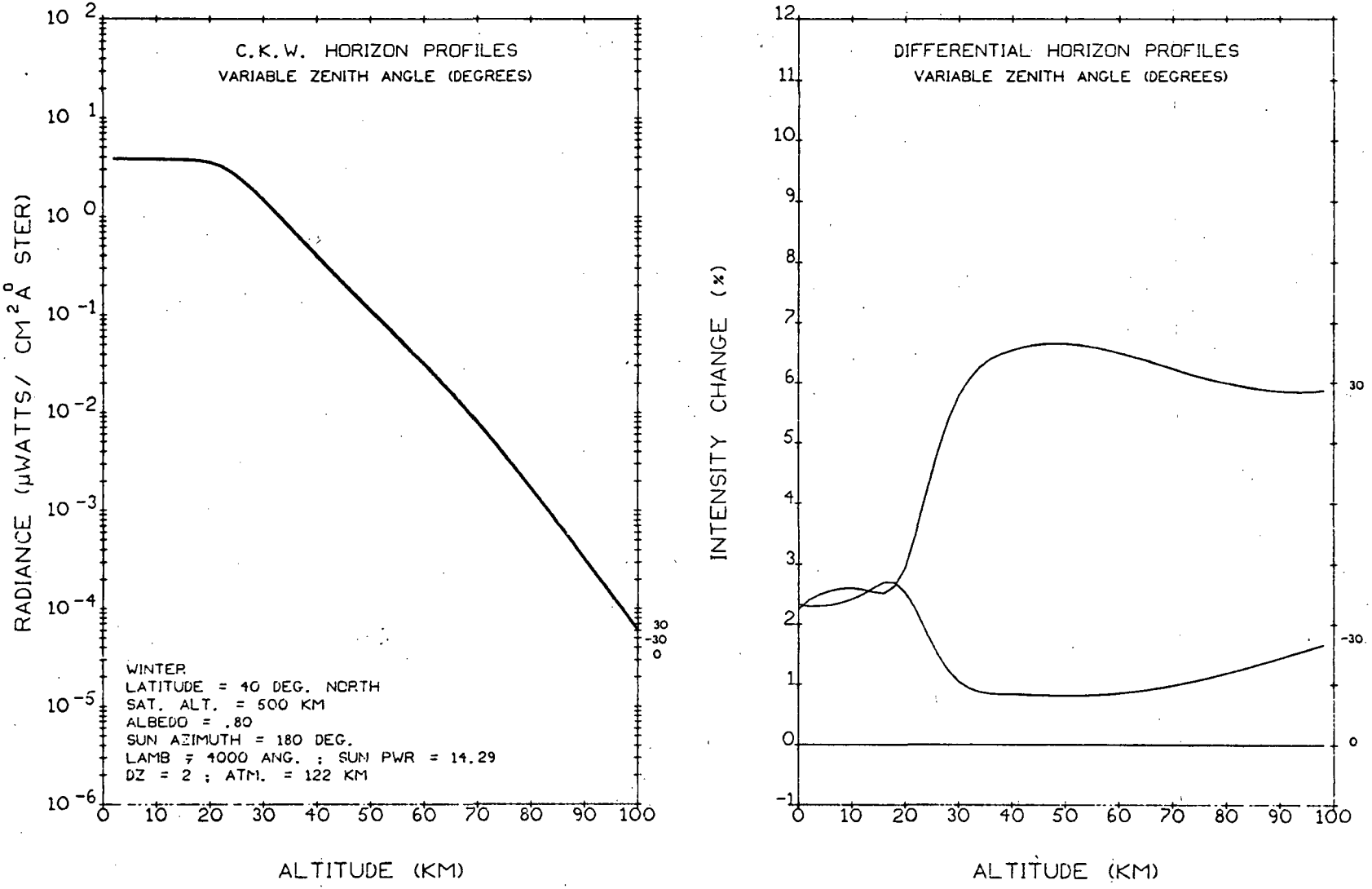

Fig 5.1-58 Variable Zenith Angle Horizon Profiles
(Azimuth=180°, λ=4000 Å, Albedo=.8)

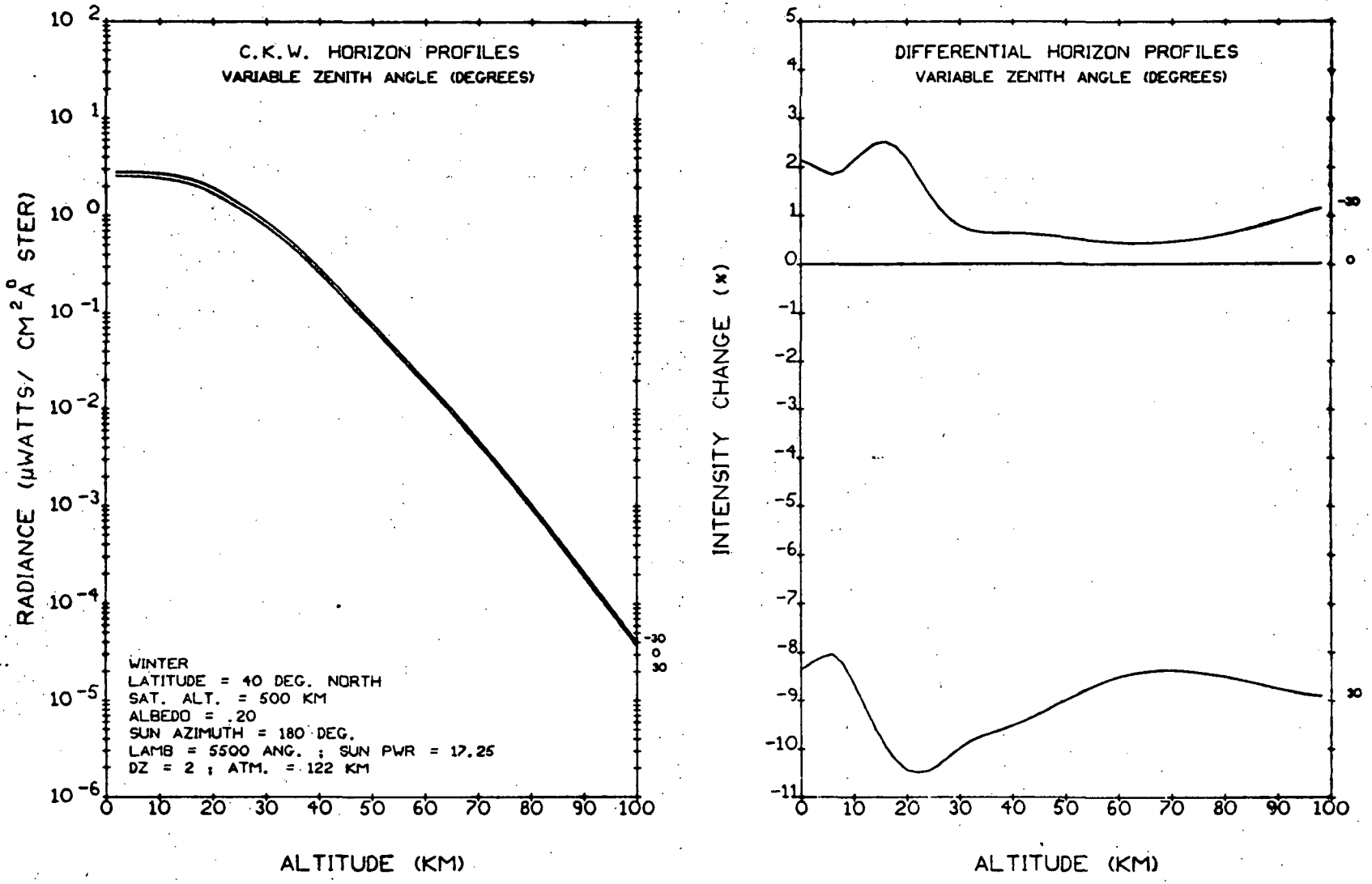

Fig. 5.1-59 Variable Zenith Angle Horizon Profiles
(Azimuth=180°, λ=5500 Å, Albedo=.2)

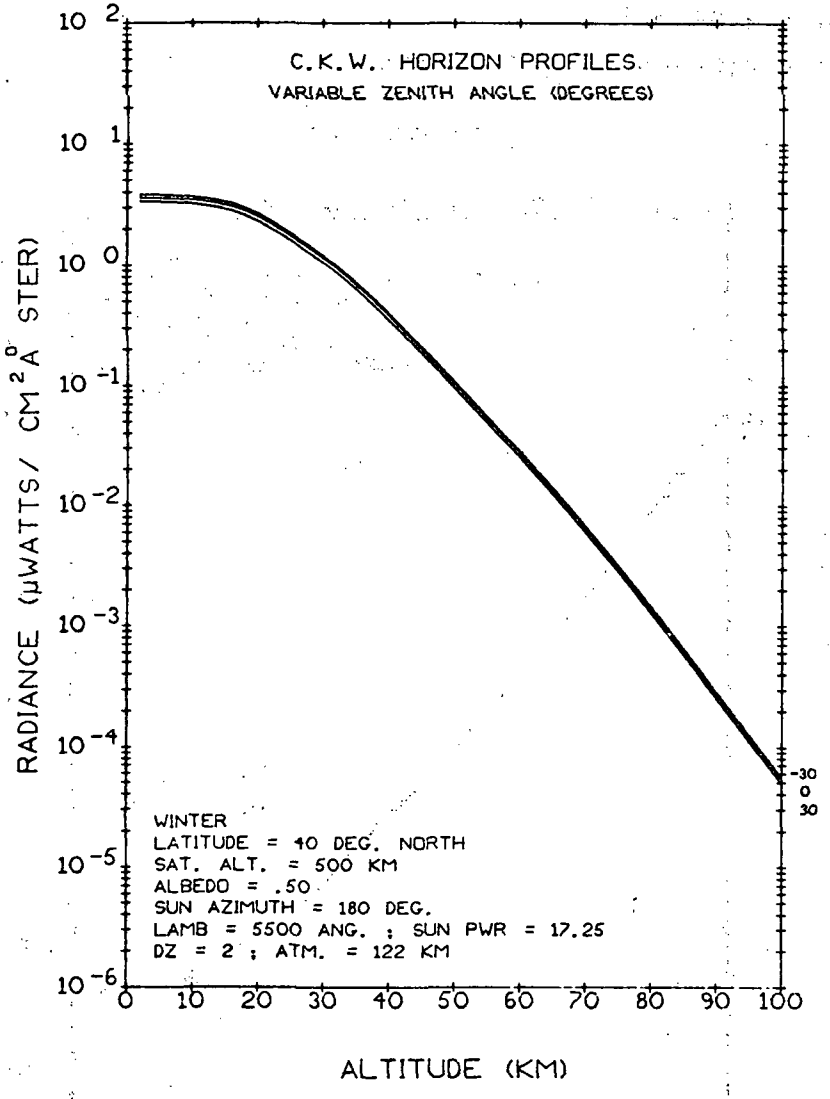

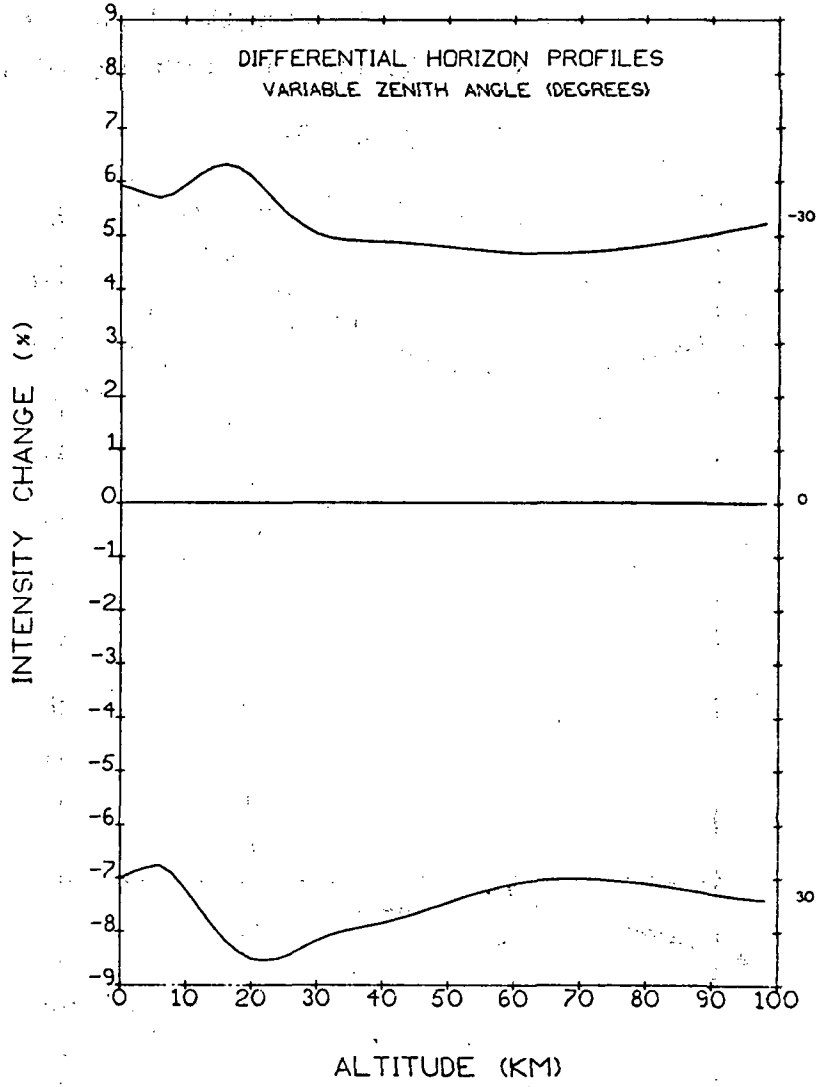

Fig. 5.1-60 Variable Zenith Angle Horizon Profiles
(Azimuth=180°, λ=5500 Å, Albedo=.5)

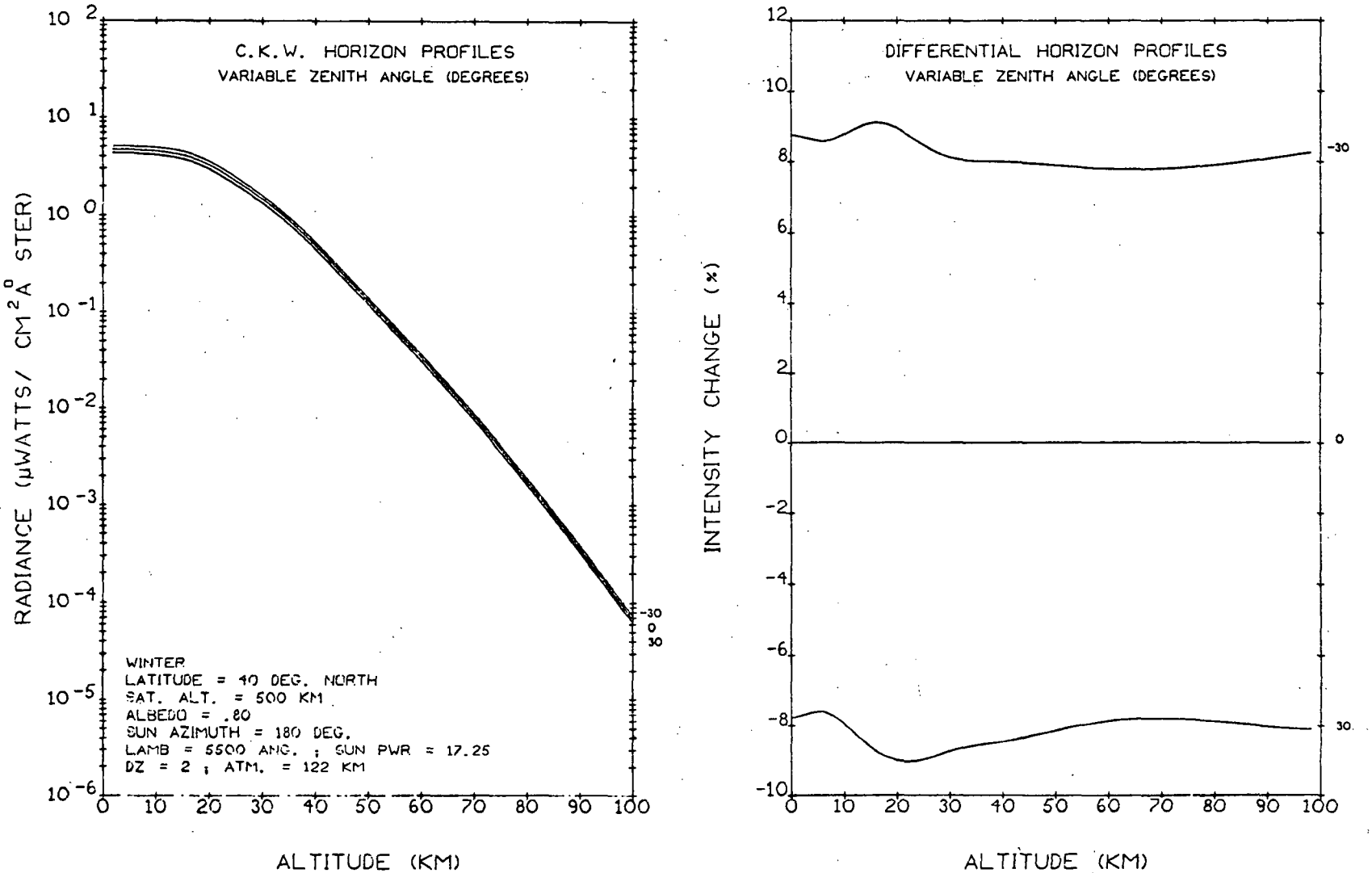

Fig. 5.1-61 Variable Zenith Angle Horizon Profiles
(Azimuth=180°, λ=5500 Å, Albedo=.8)

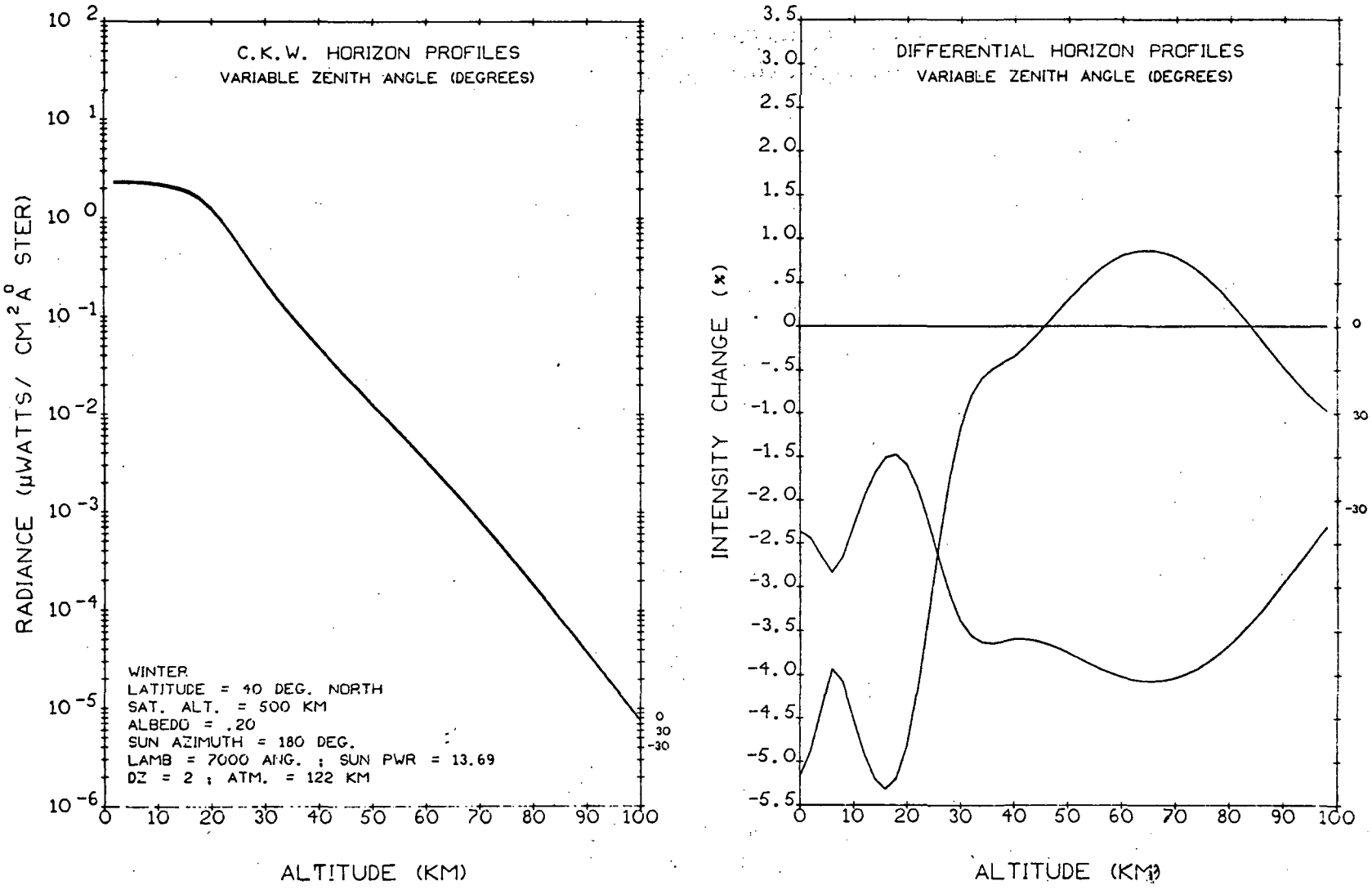

Fig. 5.1-62 Variable Zenith Angle Horizon Profiles
(Azimuth=180°, λ=7000 Å, Albedo=.2)

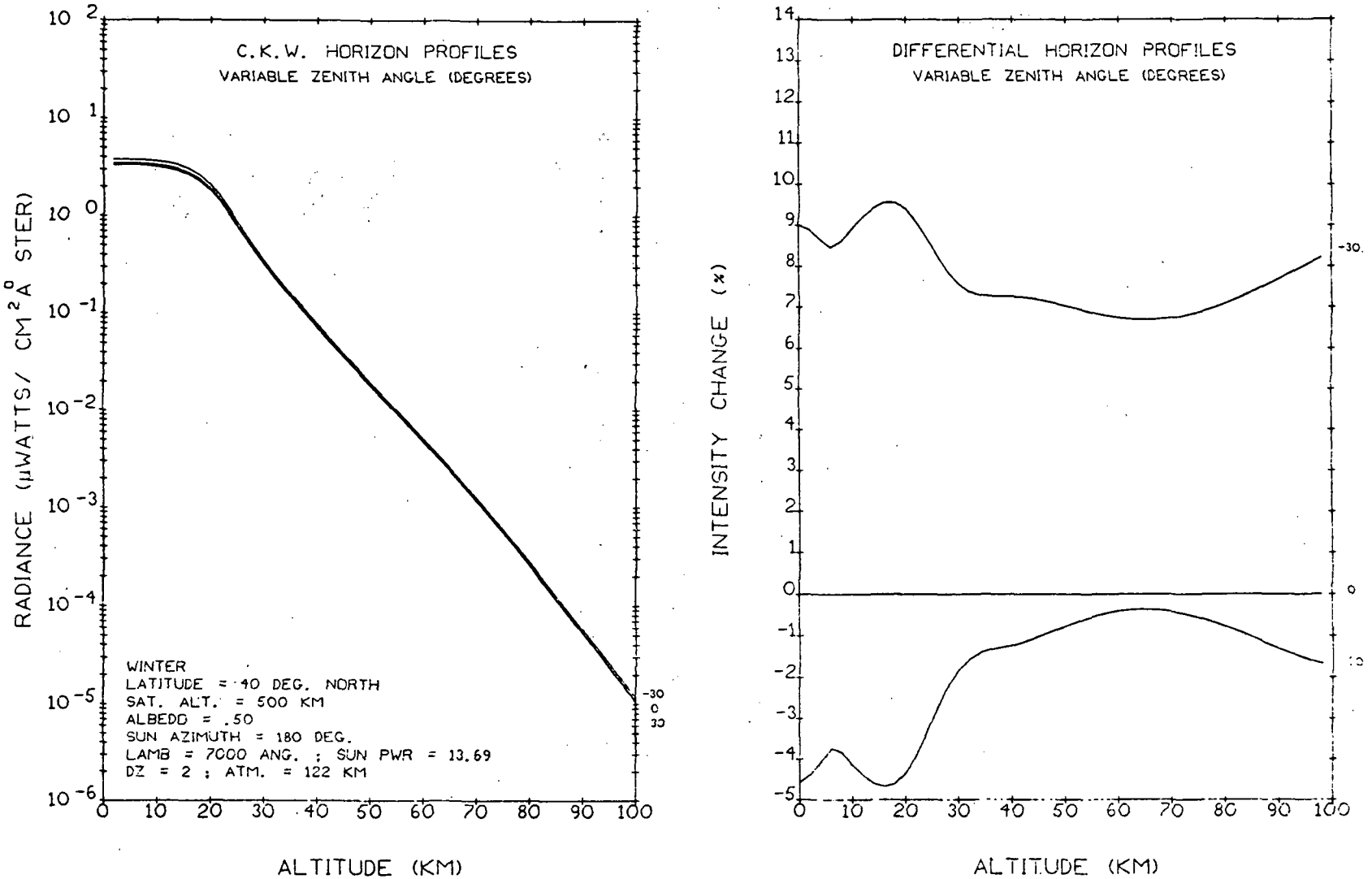

Fig. 5.1-63 Variable Zenith Angle Horizon Profiles
(Azimuth=180°, λ=7000 Å, Albedo=.5)

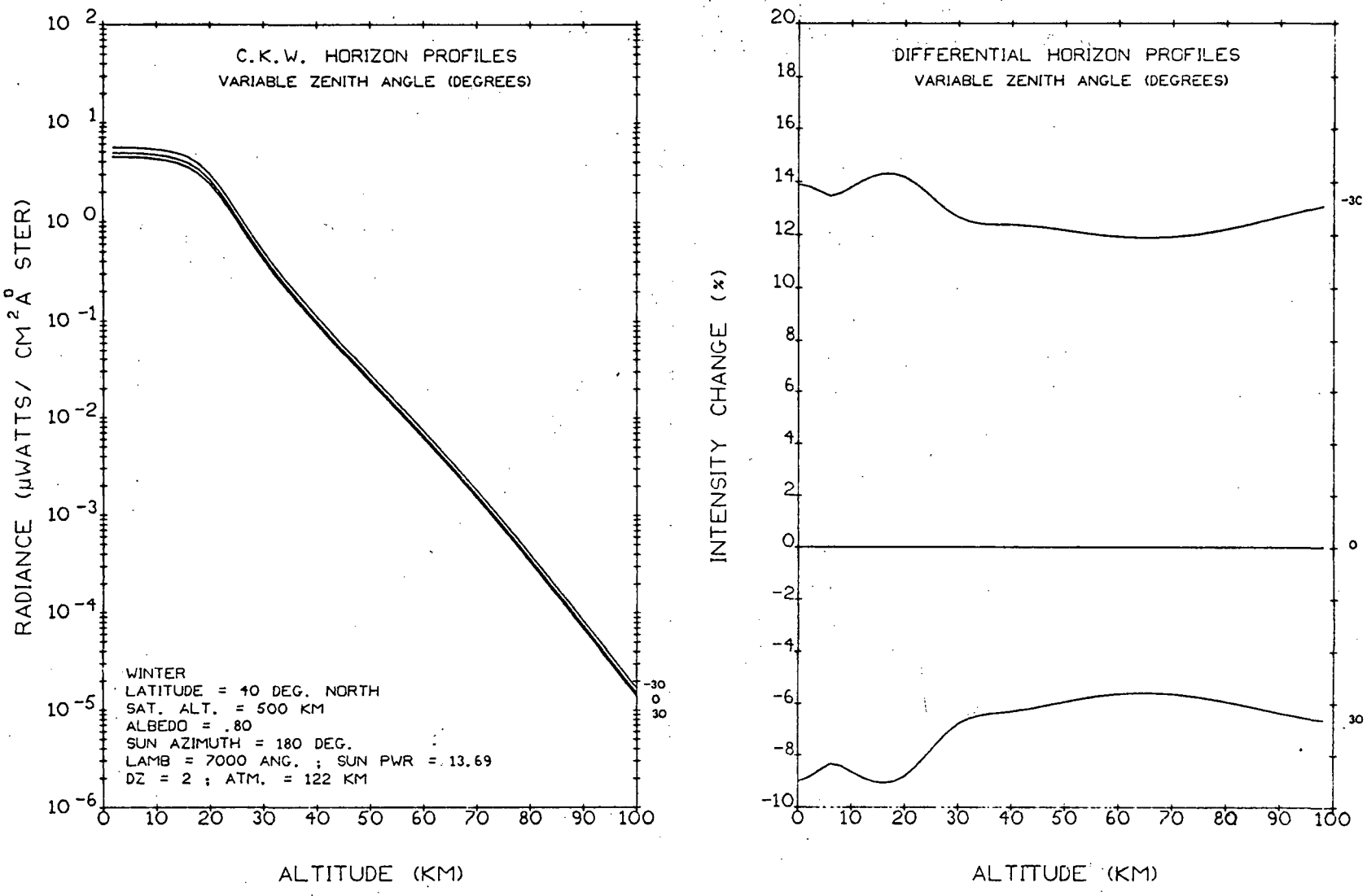

Fig. 5.1-64 Variable Zenith Angle Horizon Profiles
(Azimuth=180^o, λ=7000 $\mathring{A}$, Albedo=.8)

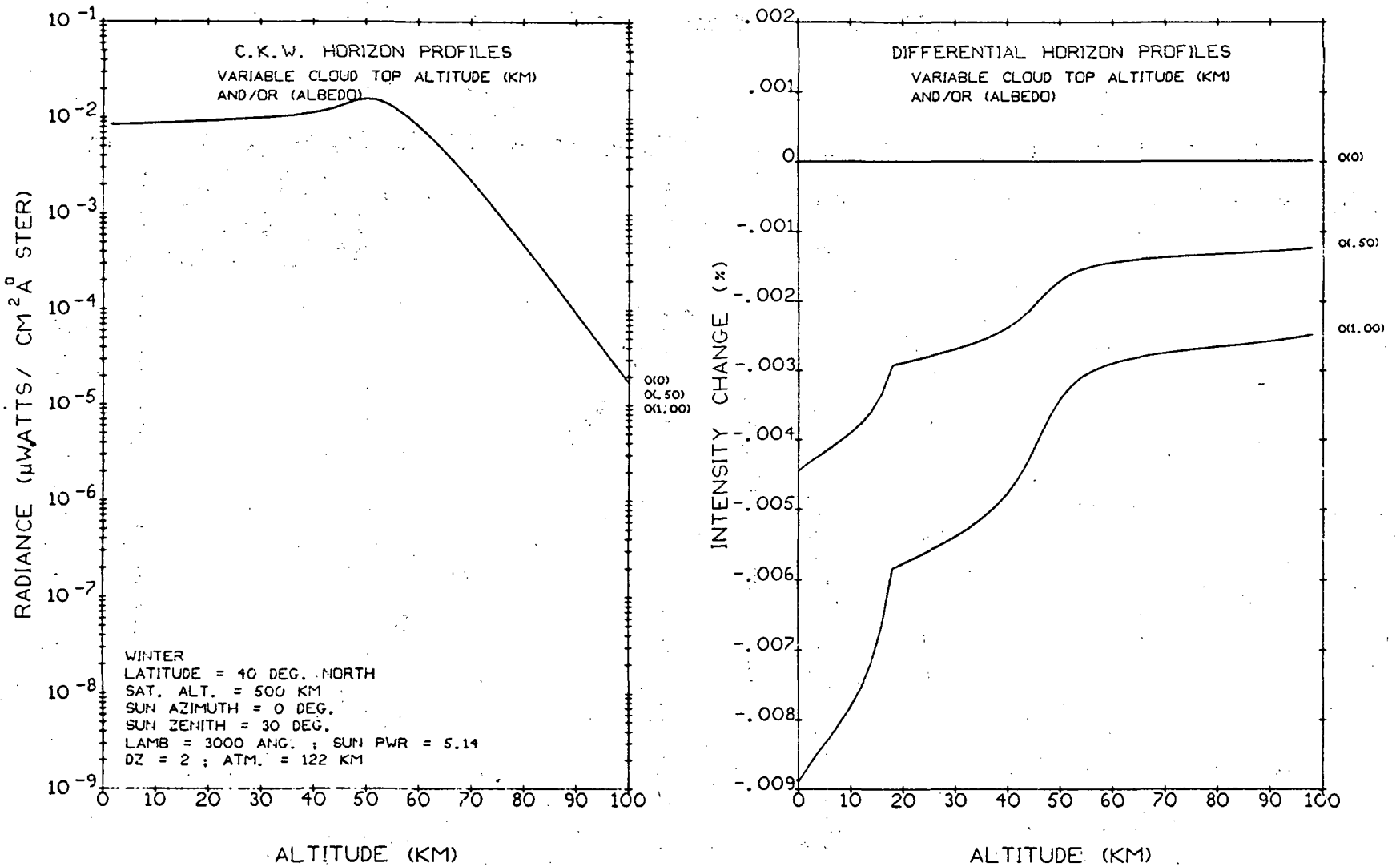

Fig. 5.1-65 Variable Albedo Horizon Profiles
(Zenith Angle = 30°, λ=3000 Å)

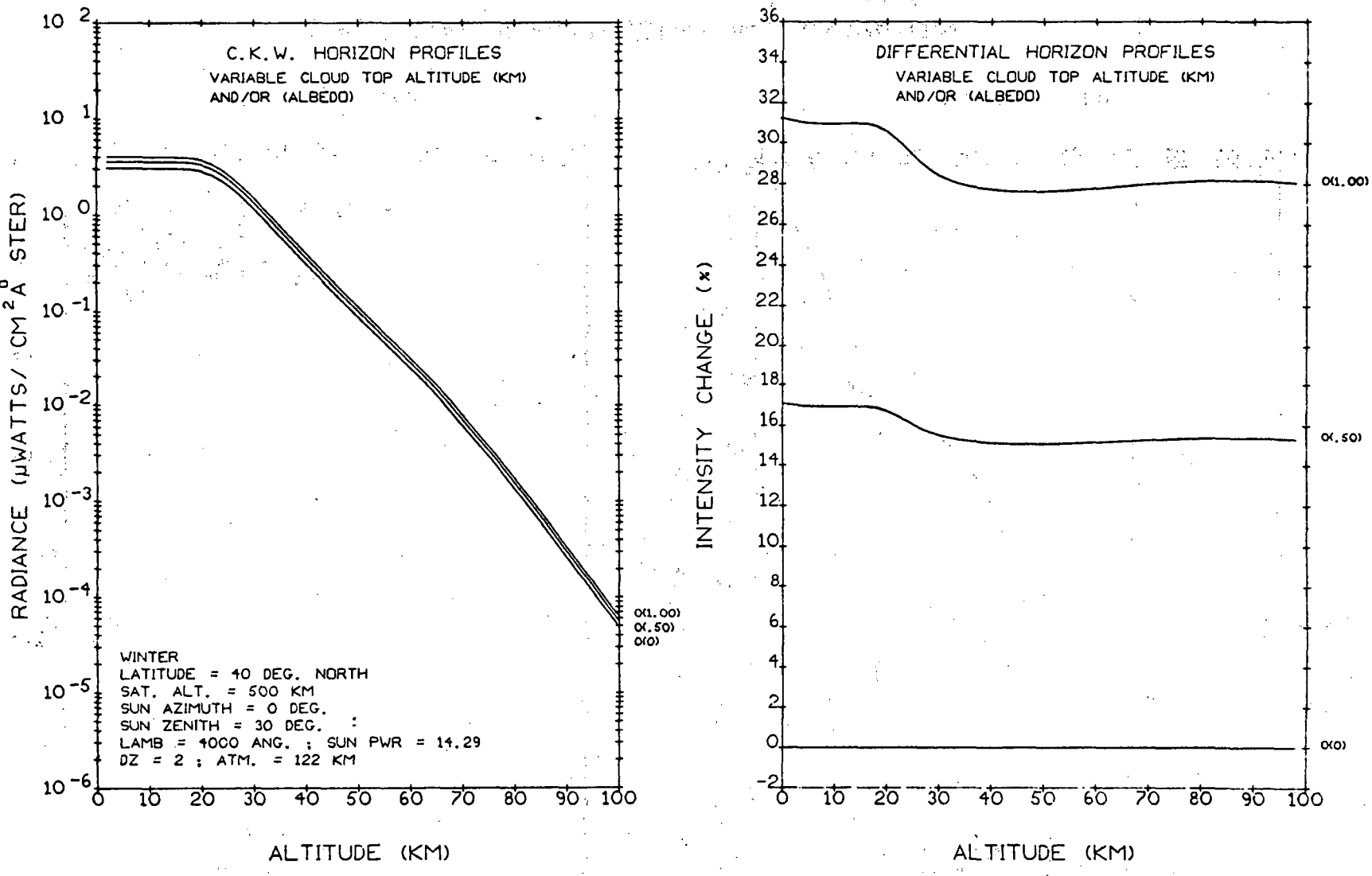

Fig. 5.1-66 Variable Albedo Horizon Profiles
(Zenith Angle = 30^{o}, λ=4000 Å)

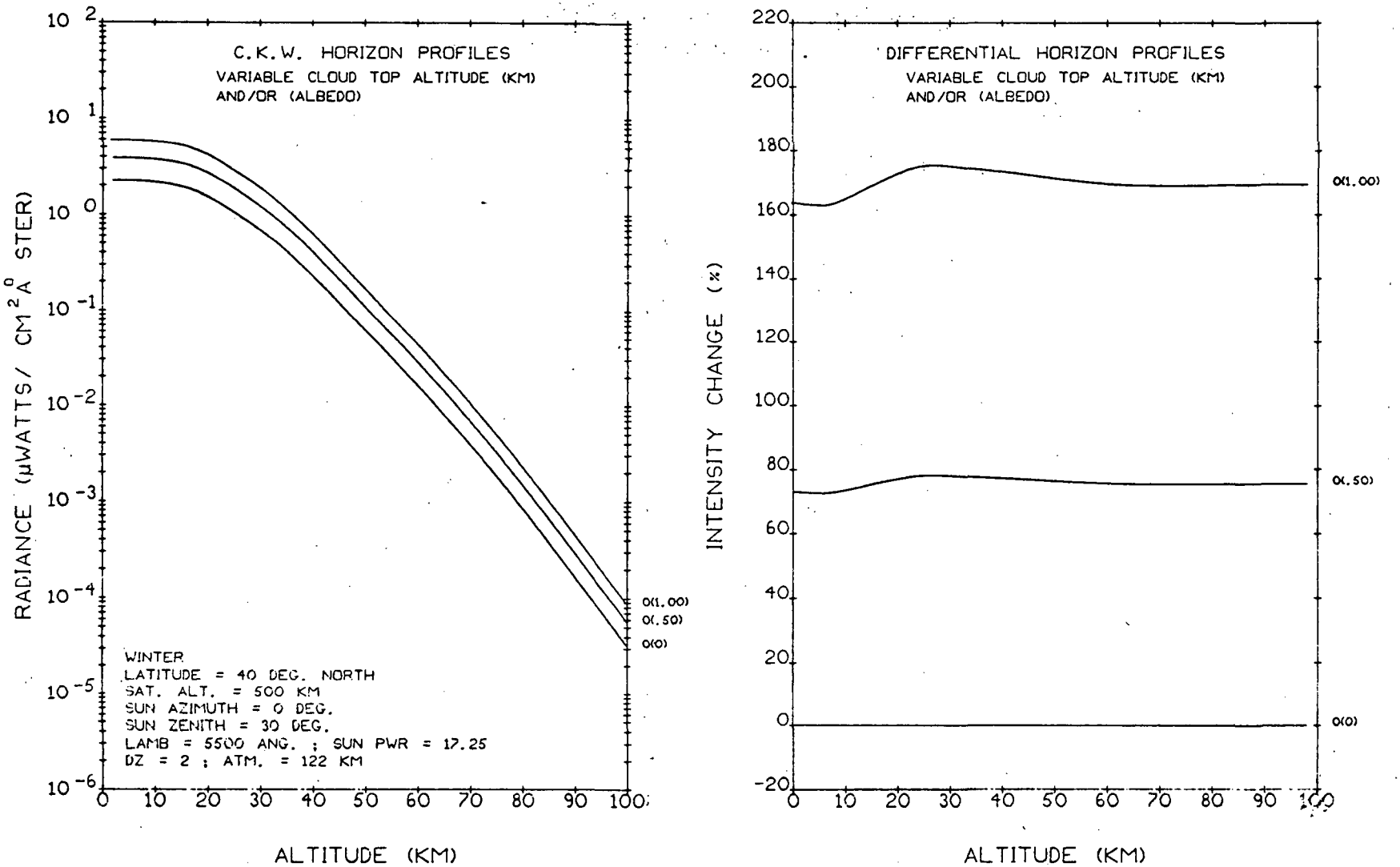

Fig. 5.1-67 Variable Albedo Horizon Profiles
(Zenith Angle = 30°, λ=5500 Å)

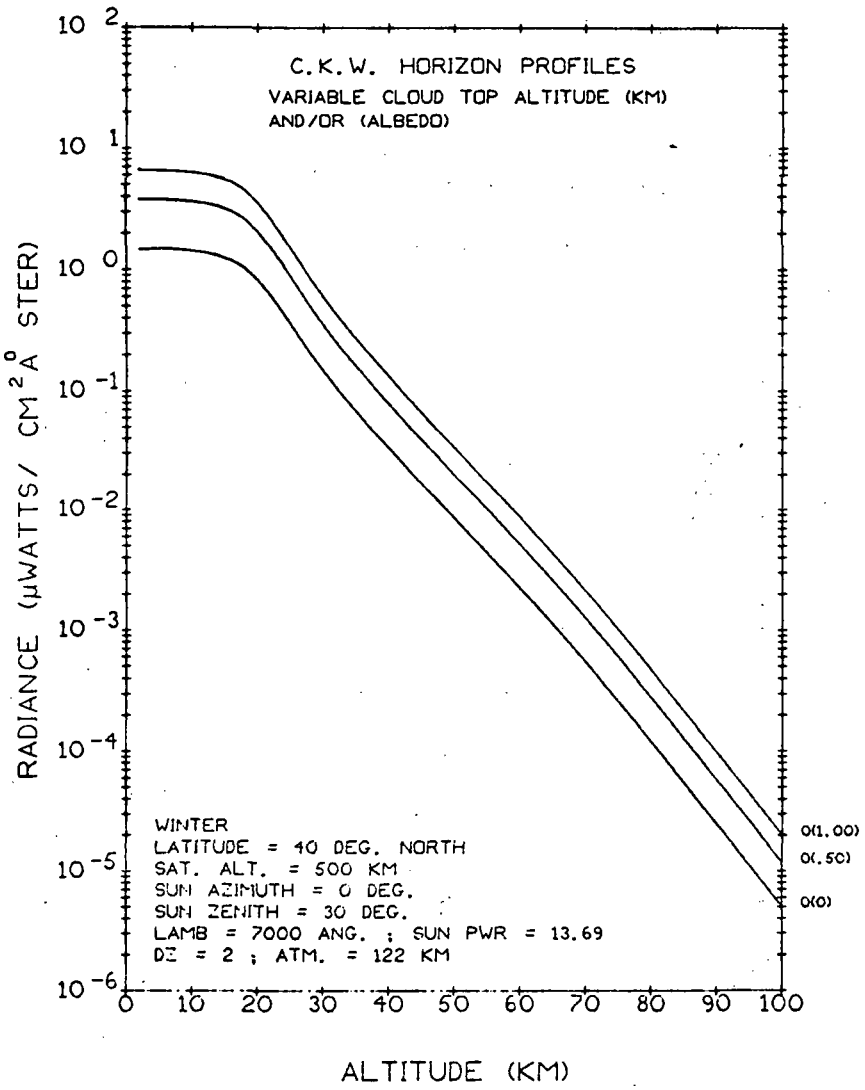

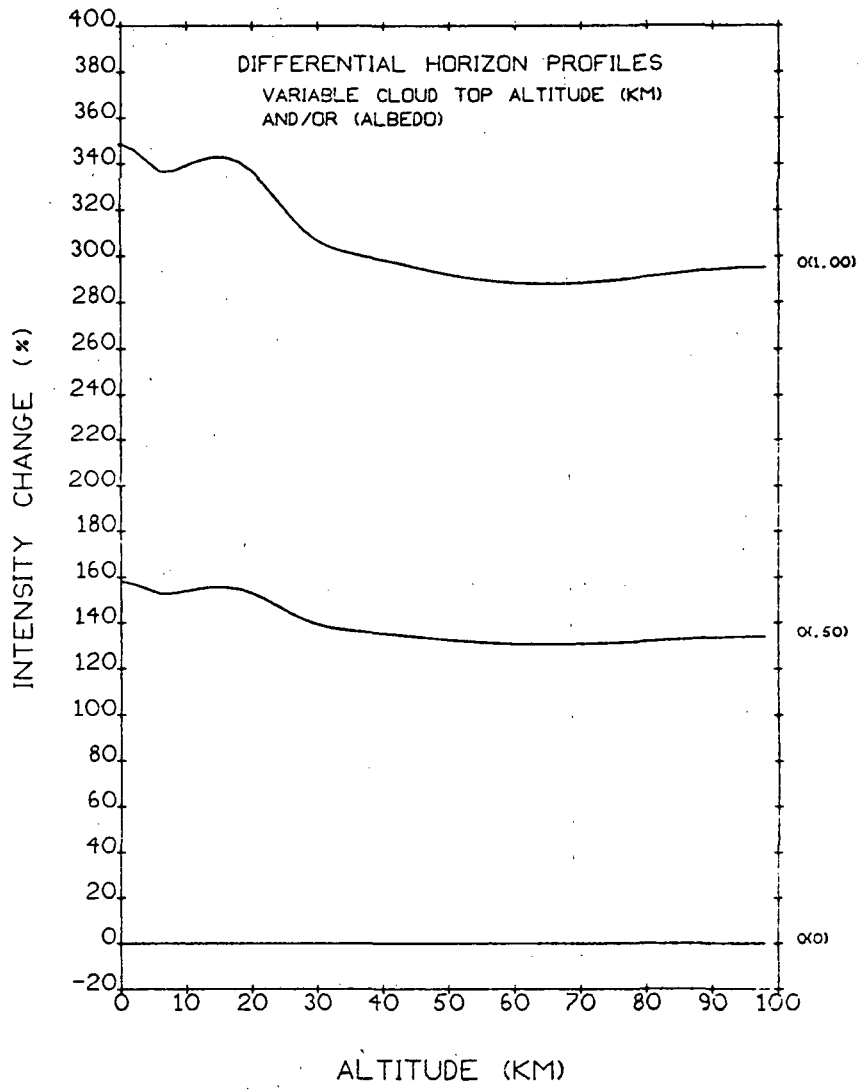

Fig. 5.1-68 Variable Albedo Horizon Profiles
(Zenith Angle = 30°, λ=7000 Å)

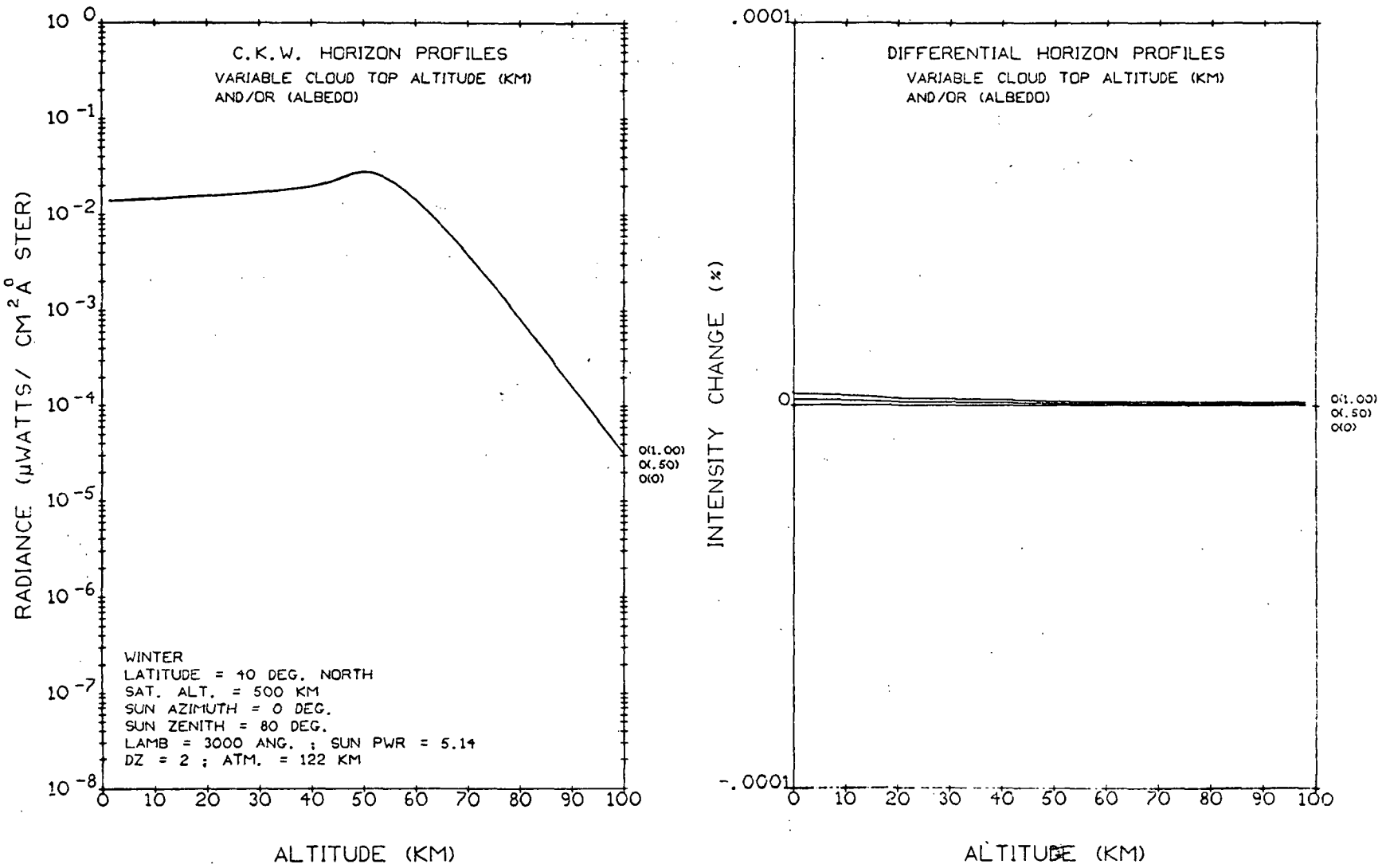

Fig. 5.1-69 Variable Albedo Horizon Profiles
(Zenith Angle = 80°, λ=3000 Å)

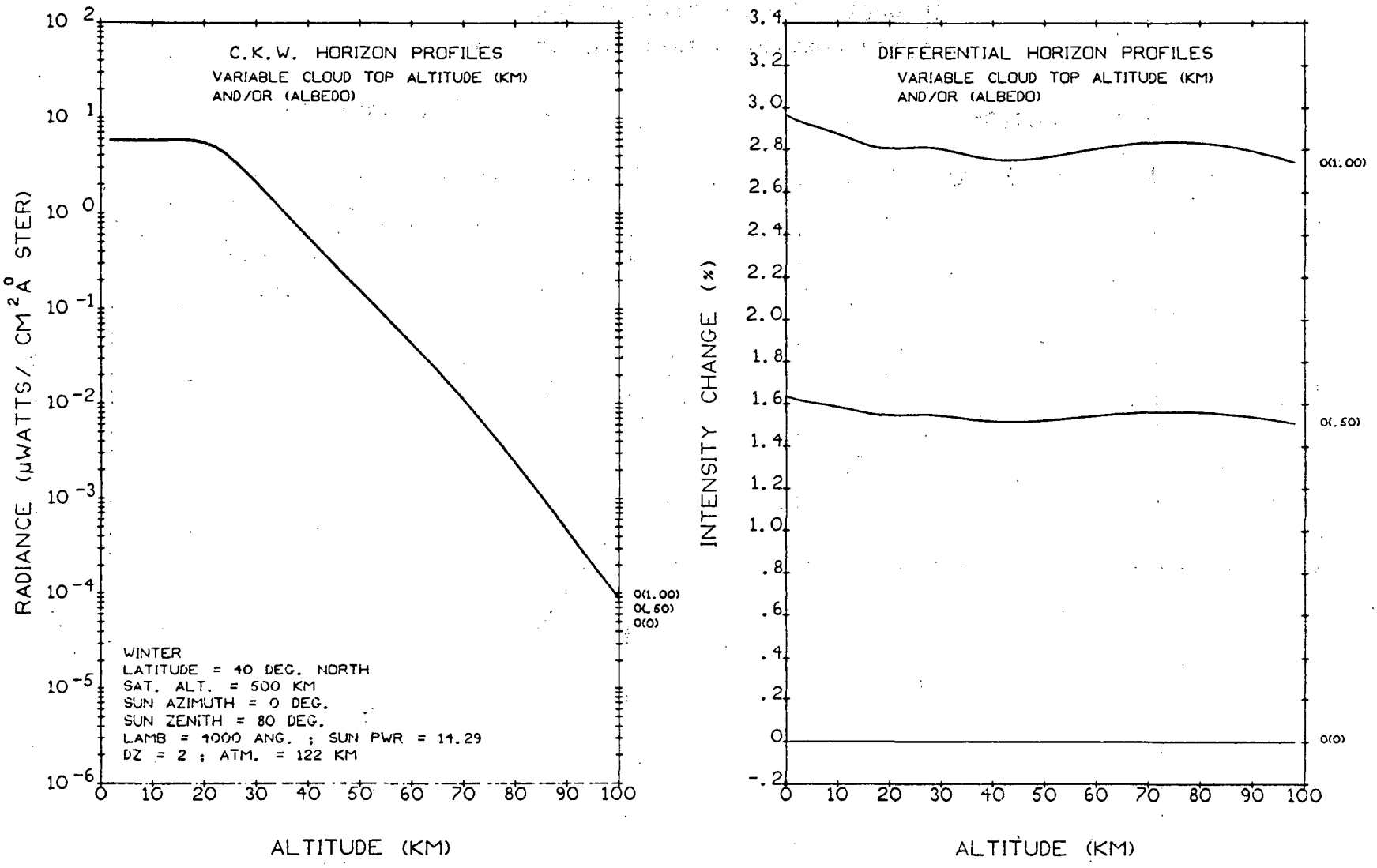

Fig. 5.1-70 Variable Albedo Horizon Profiles
(Zenith Angle = 80°, λ=4000 Å)

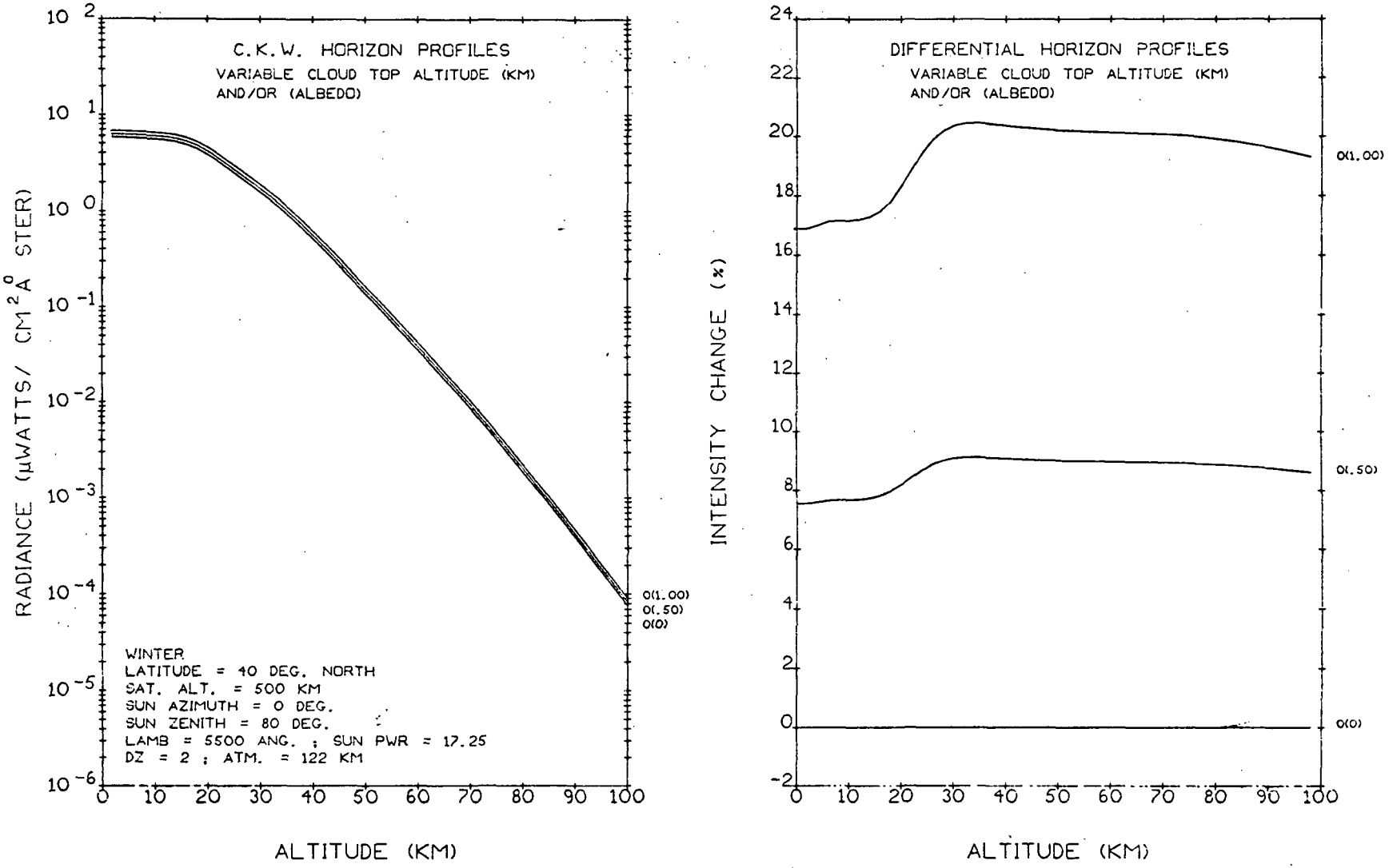

Fig. 5.1-71 Variable Albedo Horizon Profiles
(Zenith Angle = 80^{o}, λ=5500 Å)

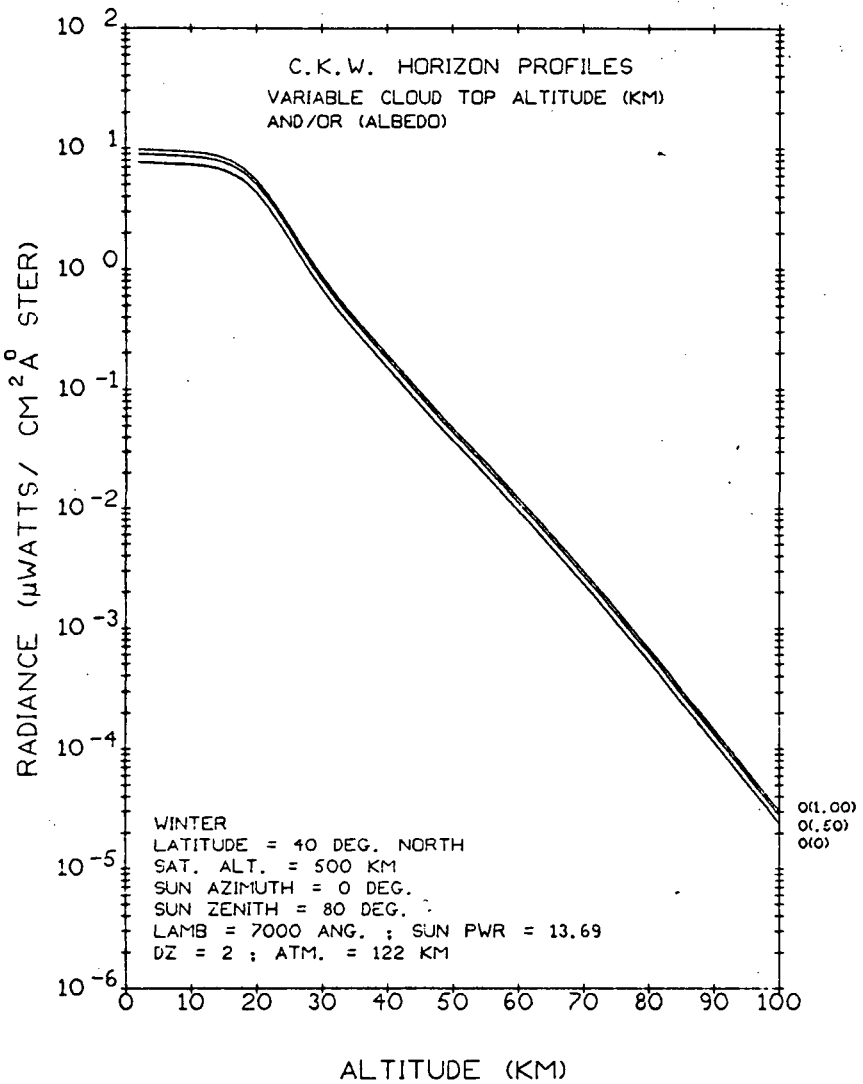

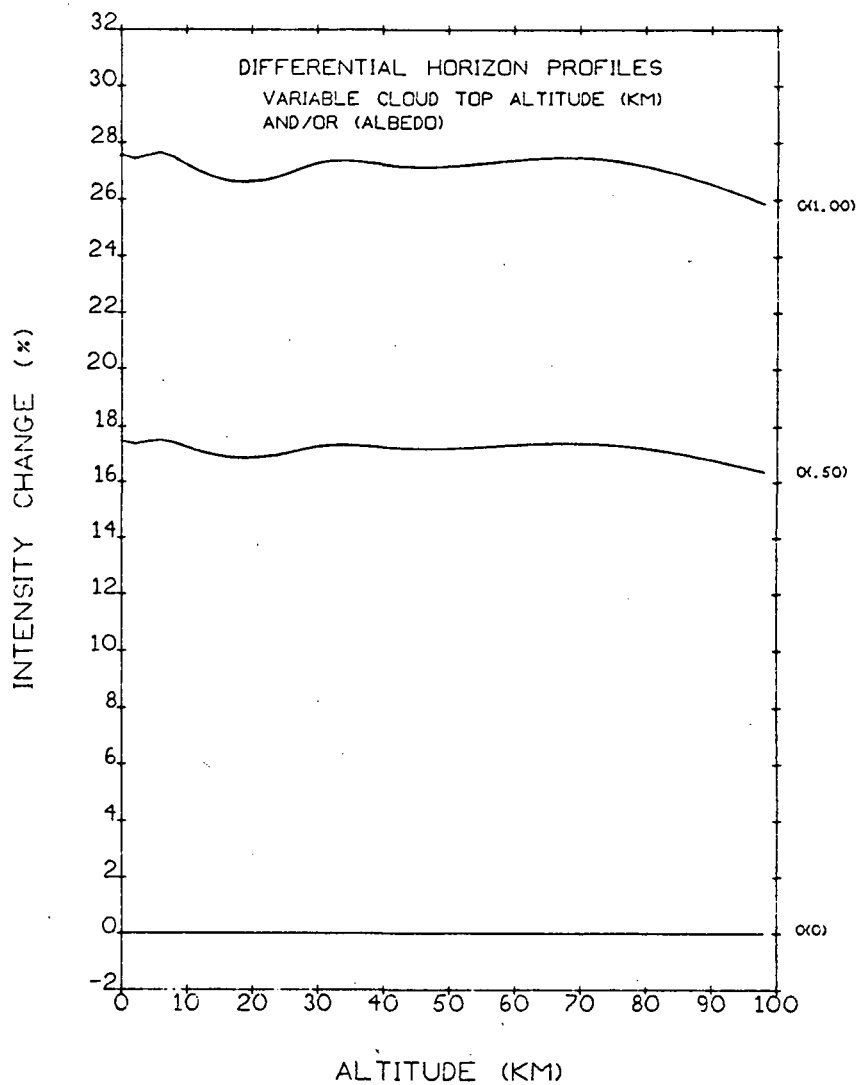

Fig. 5.1-72 Variable Albedo Horizon Profiles
(Zenith Angle = 80°, λ=7000 Å)

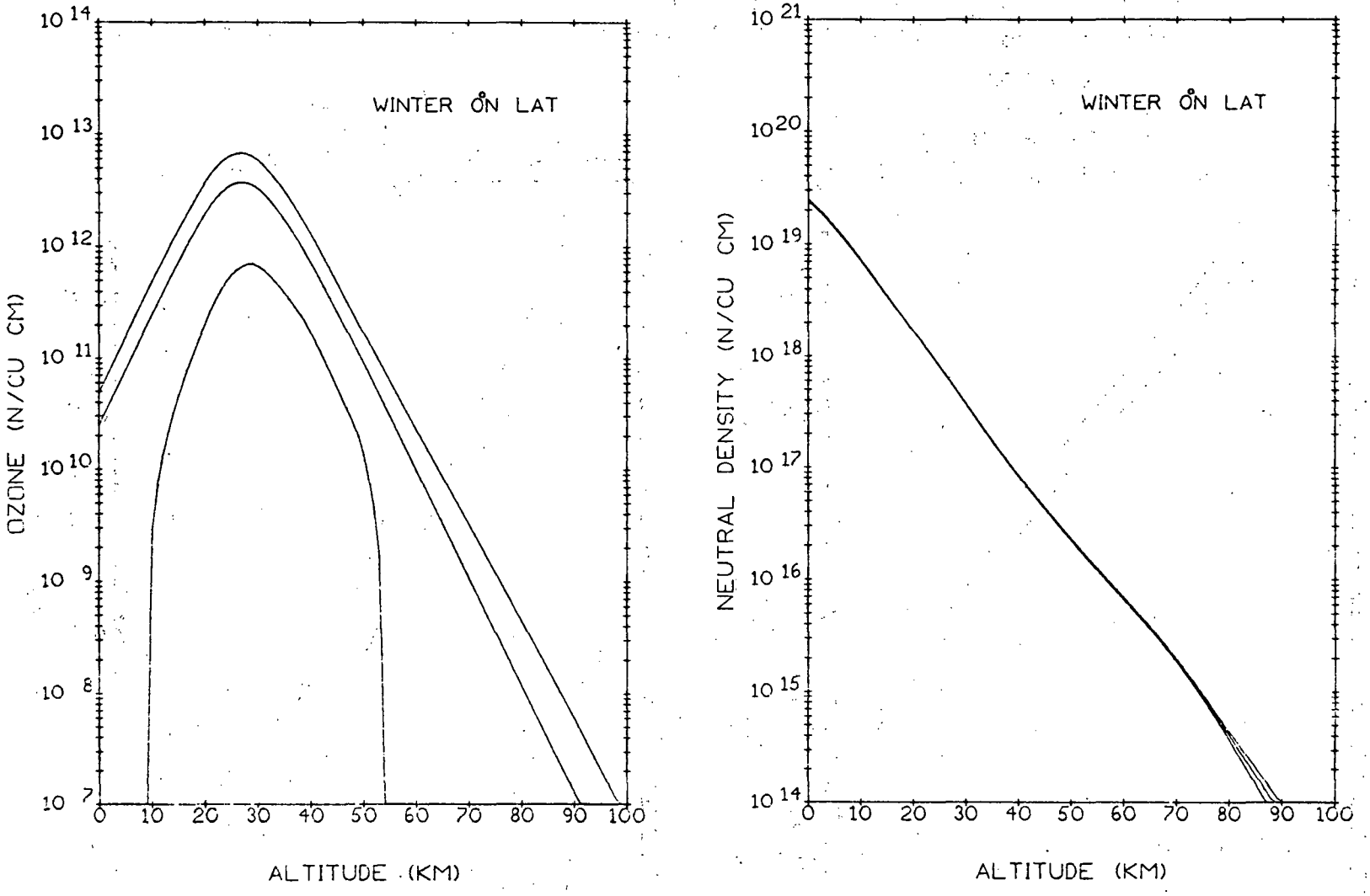

Fig. 5.1-73 Neutral and Ozone Density Profiles (Winter, 0^{o}N. LATITUDE) for mean and ± 1σ values

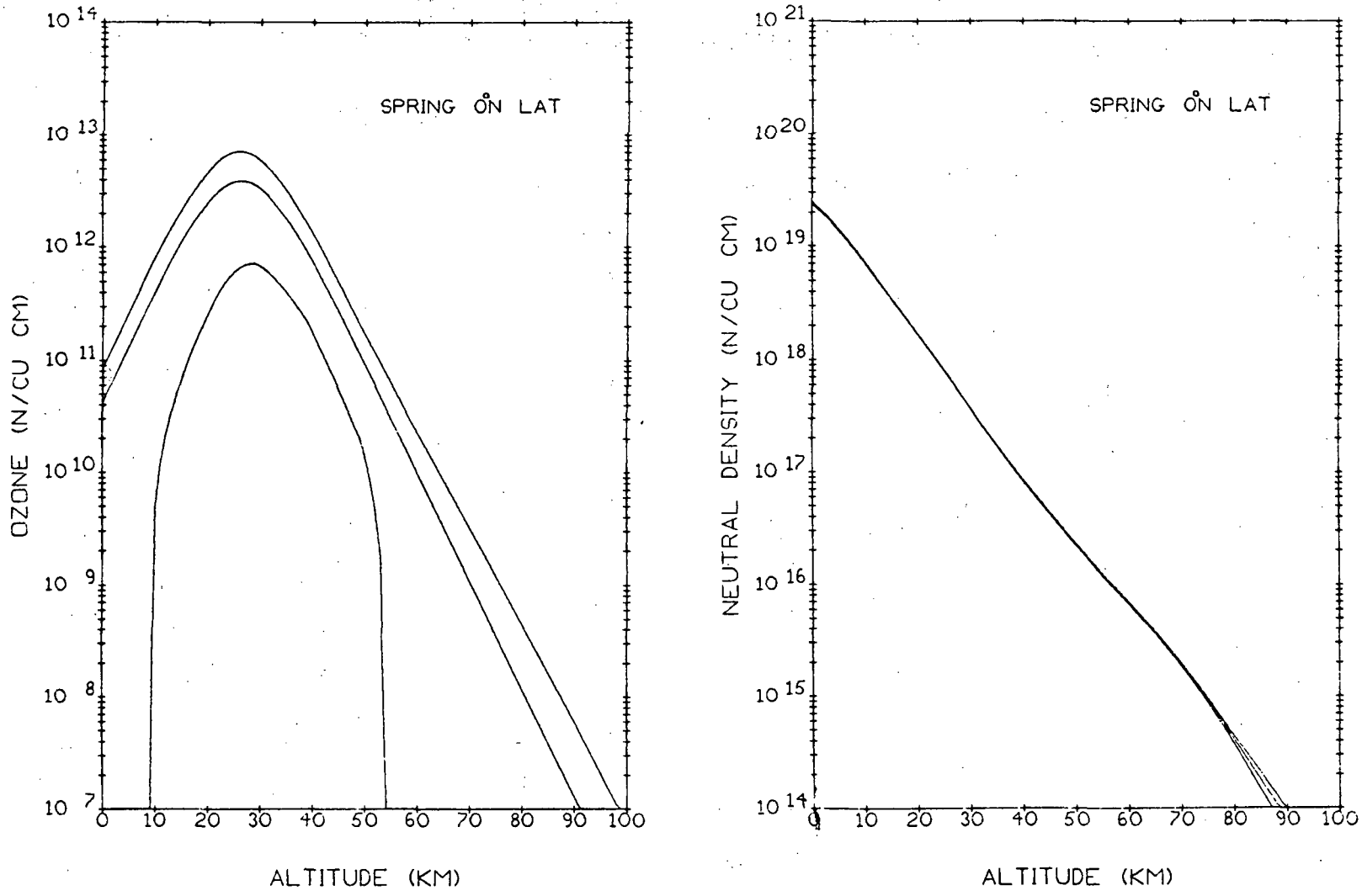

Fig. 5.1-74 Neutral and Ozone Density Profiles (Spring, 0^{o}N. LATITUDE) for mean and ± 1σ values

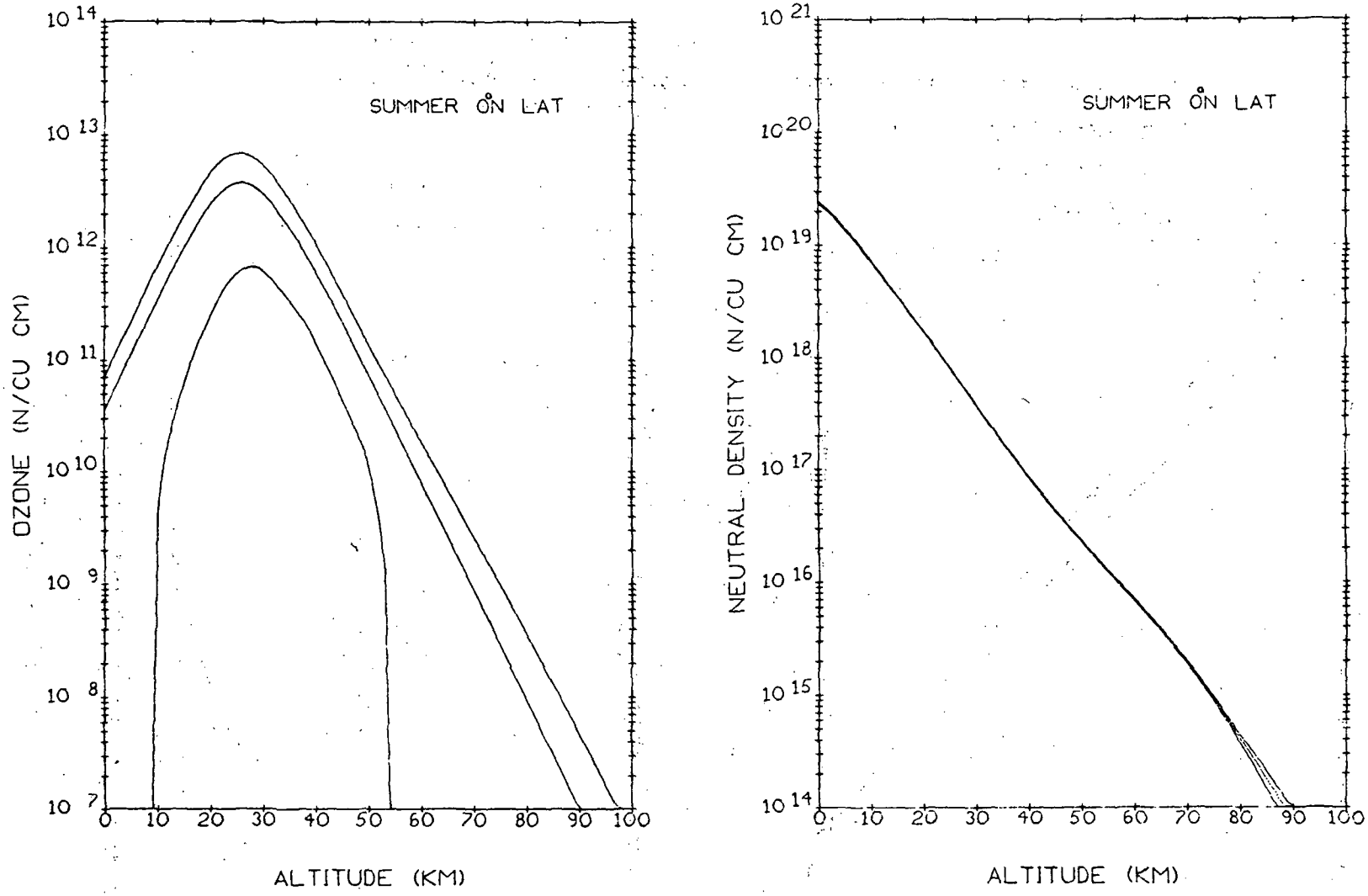

Fig. 5.1-75 Neutral and Ozone Density Profiles (Wummer, 0°N. LATITUDE) for mean and ± 1σ values

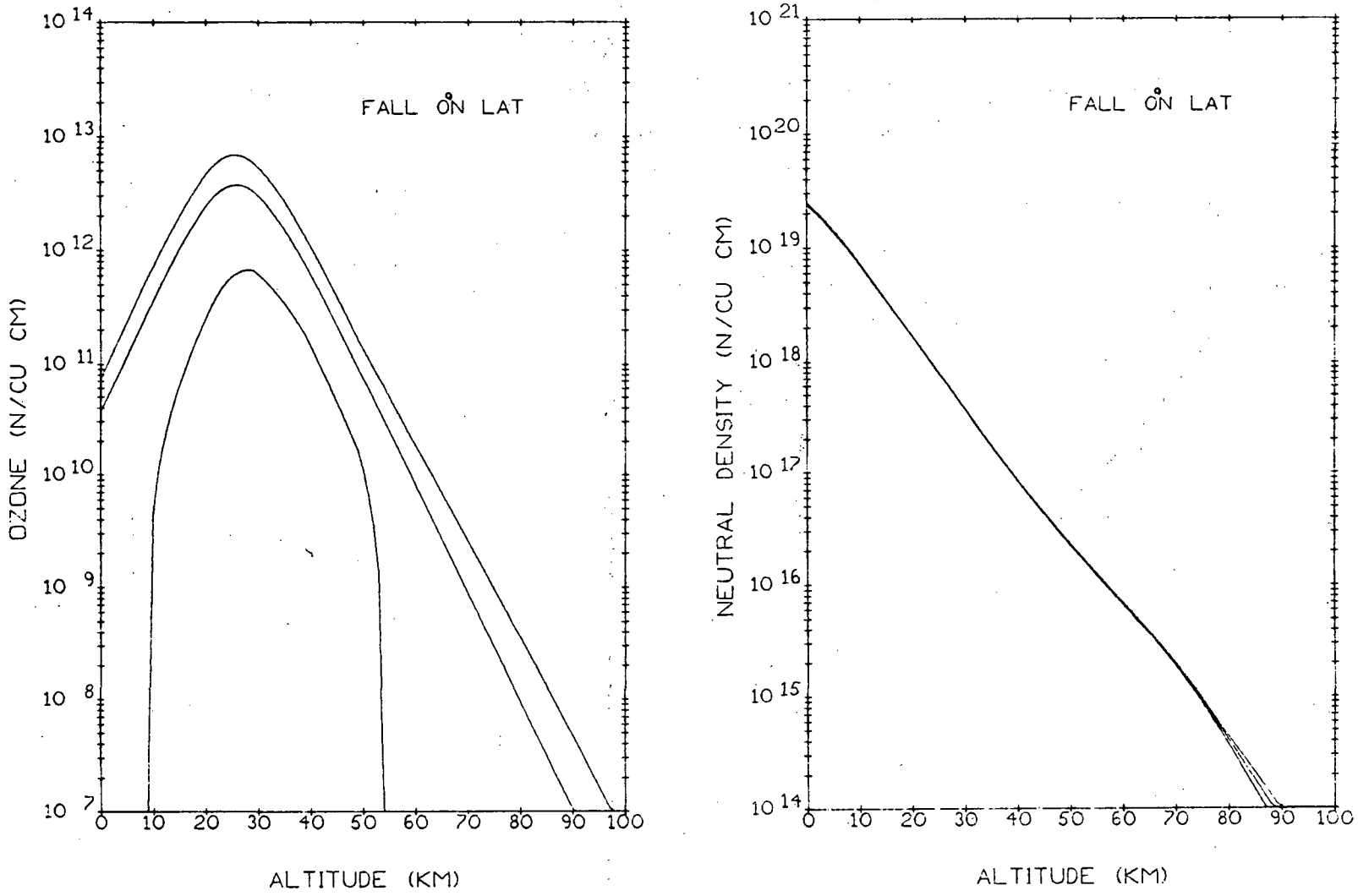

Fig. 5.1-76 Neutral and Ozone Density Profiles (Fall, 0^{o}N. LATITUDE) for mean and ± 1σ values

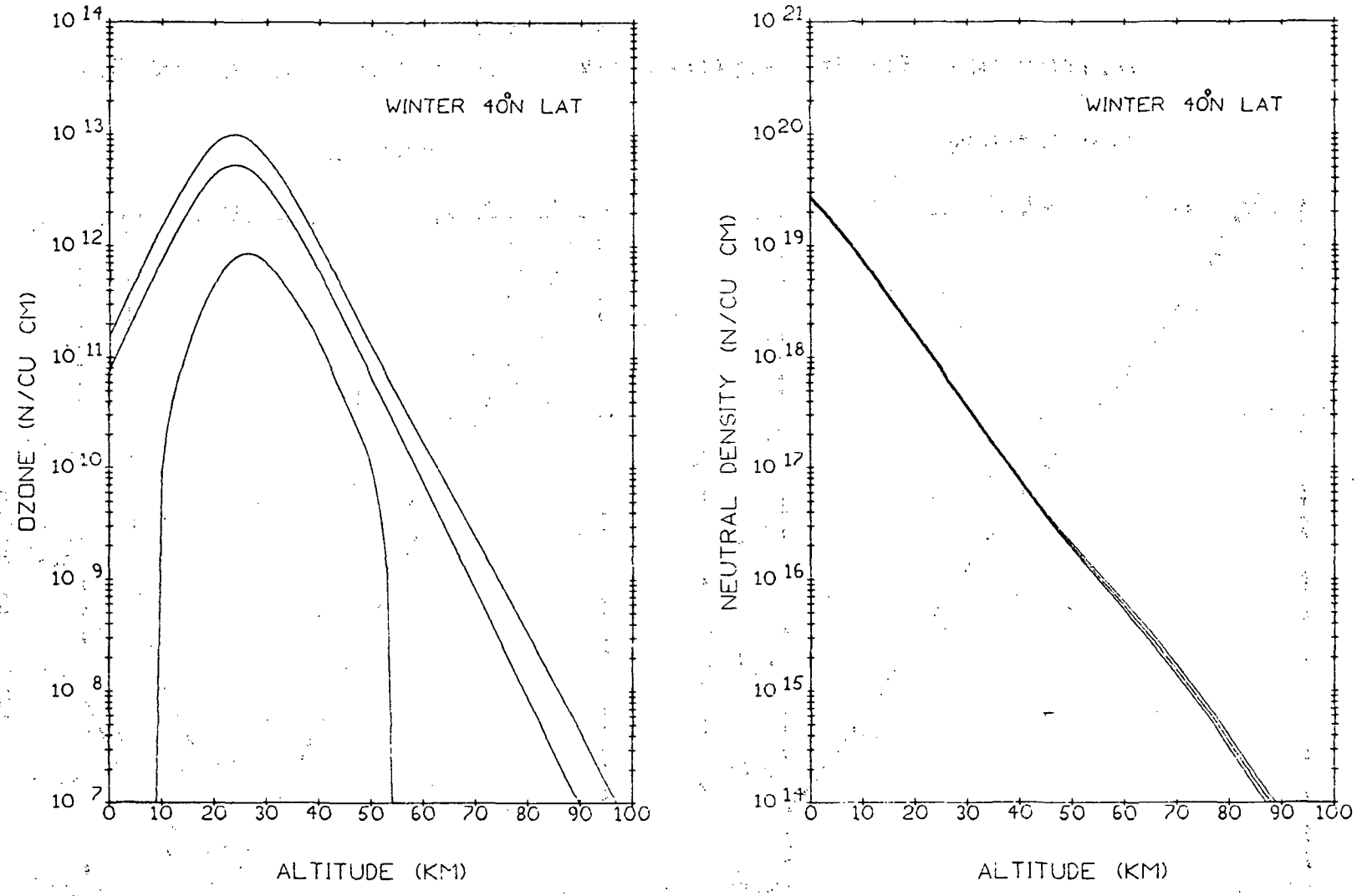

Fig. 5.1-77 Neutral and Ozone Density Profiles (Winter, 40°N. LATITUDE) for mean and ± 1σ values

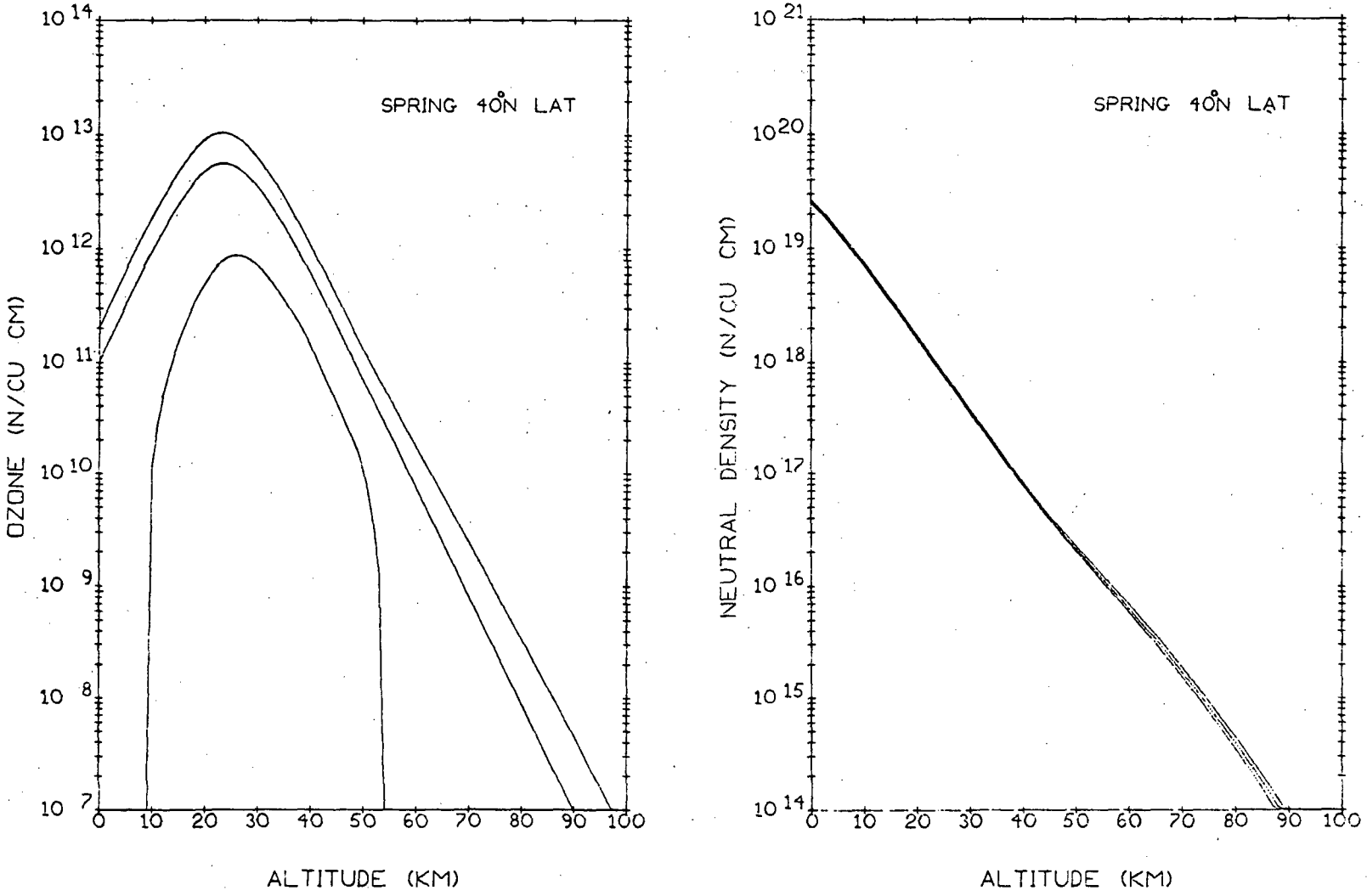

Fig. 5.1-78 Neutral and Ozone Density Profiles (Spring 40°N. LATITUDE) for mean and ± 1σ values

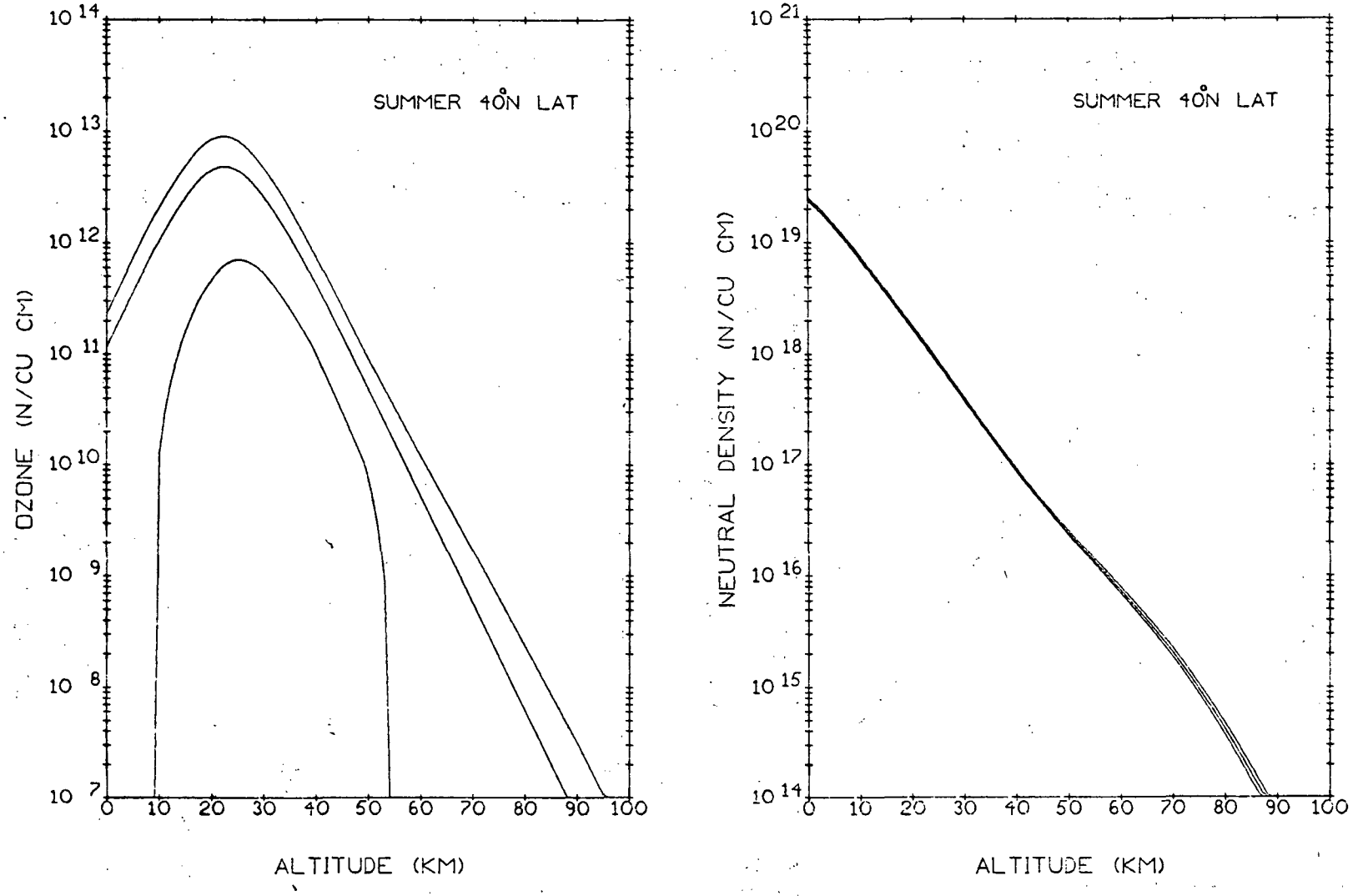

Fig. 5.1-79 Neutral and Ozone Density Profiles (Summer, 40°N. LATITUDE) for mean and ± 1σ values

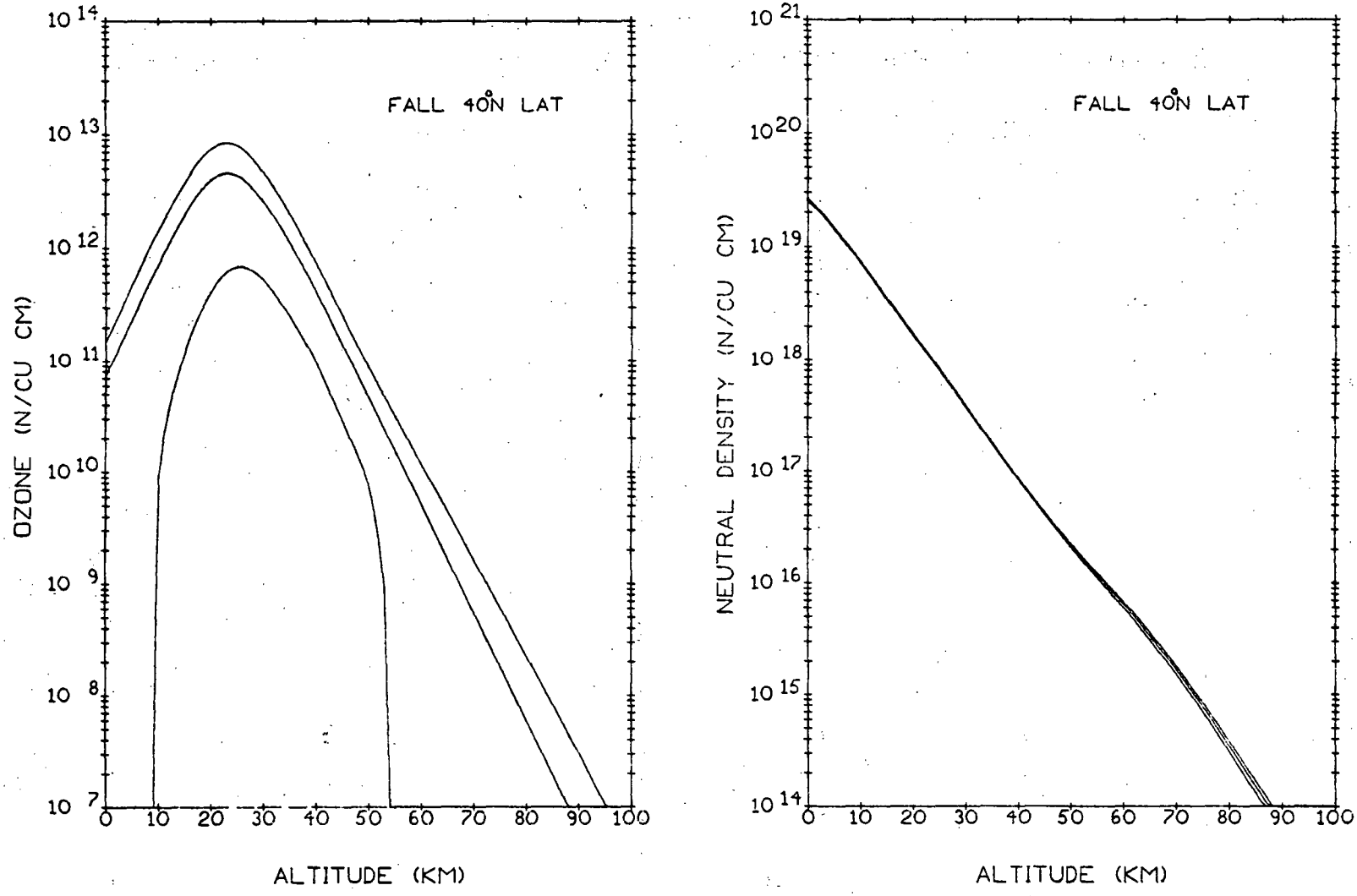

Fig. 5.1-80 Neutral and Ozone Density Profiles (Fall, 40°N. LATITUDE) for mean and ± 1σ values

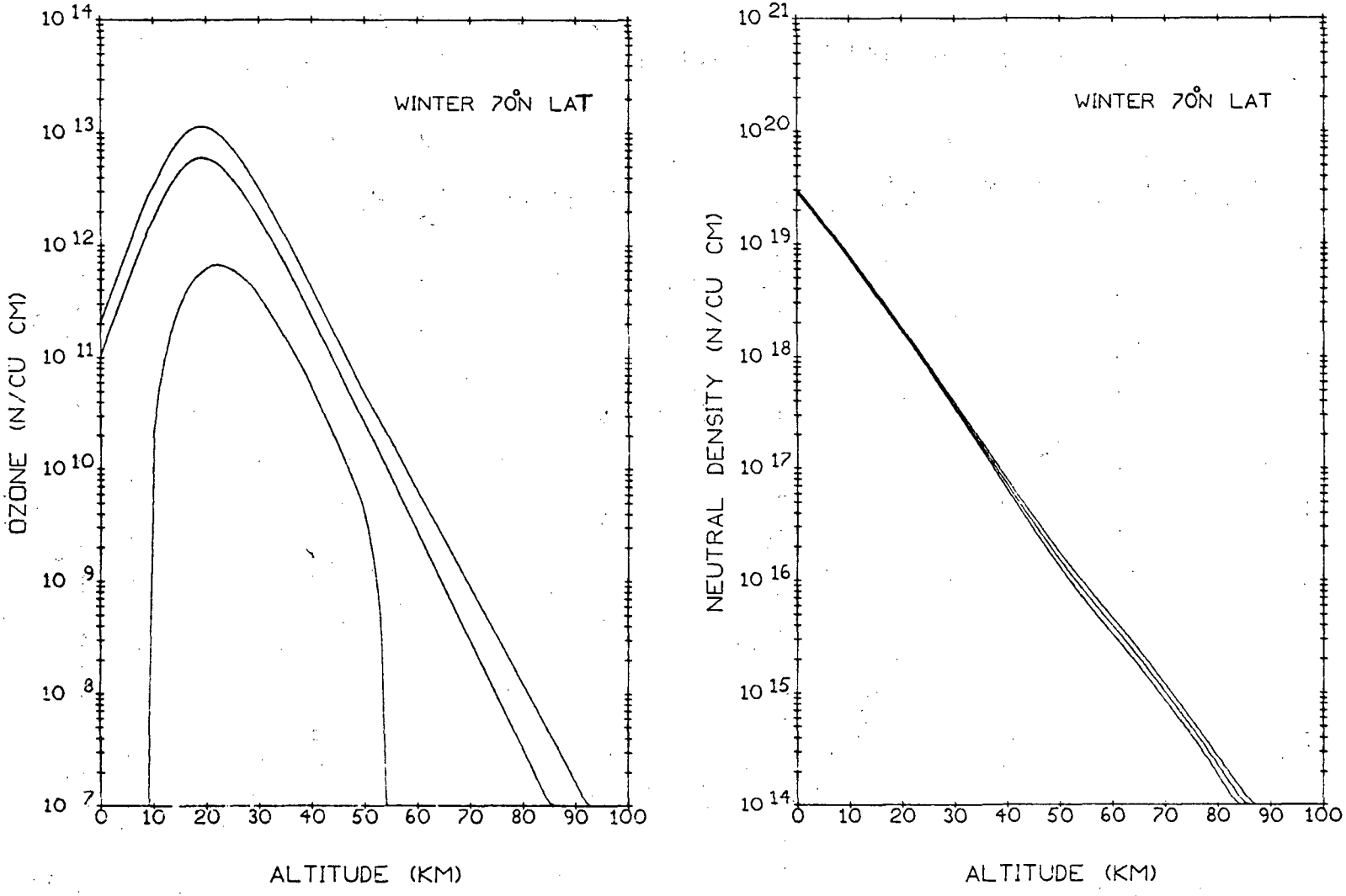

Fig. 5.1-81 Neutral and Ozone Density Profiles (Winter, 70°N. LATITUDE) for mean and ± 1σ values

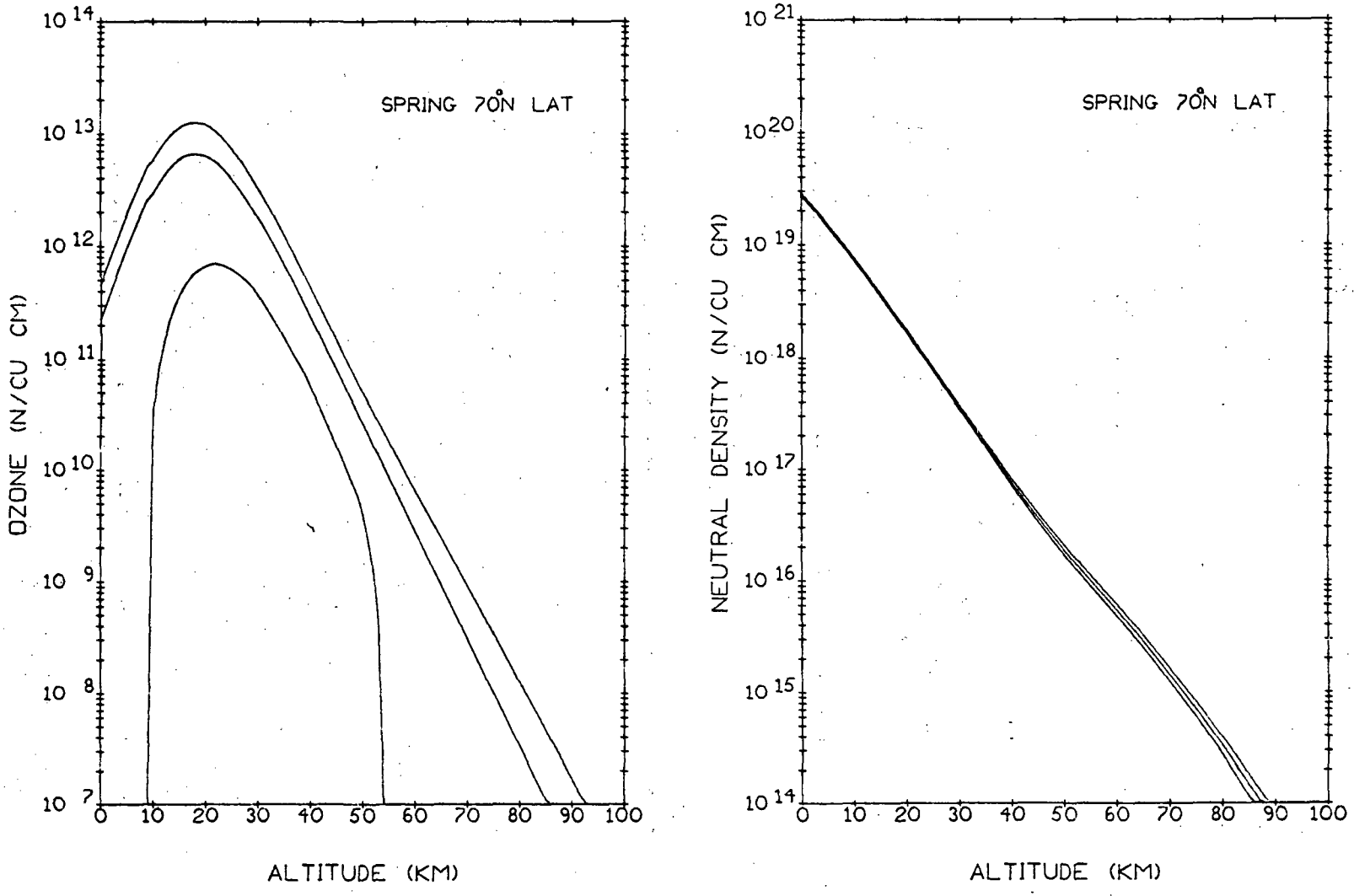

Fig. 5.1-82 Neutral and Ozone Density Profiles (Spring, 70°N. LATITUDE) for mean and ± 1σ values

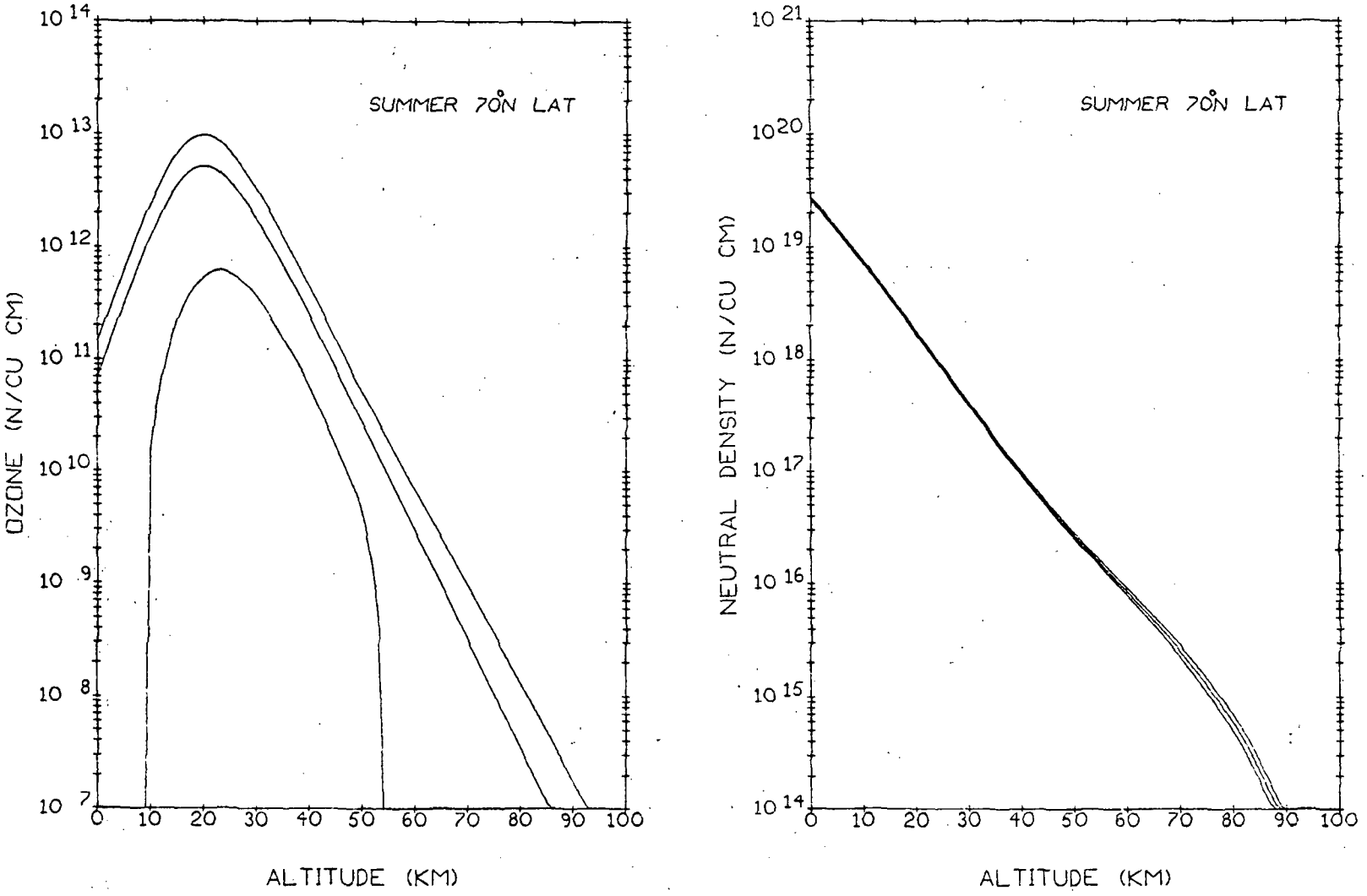

Fig. 5.1-83 Neutral and Ozone Density Profiles (Summer, 70°N, LATITUDE) for mean and ± 1σ values

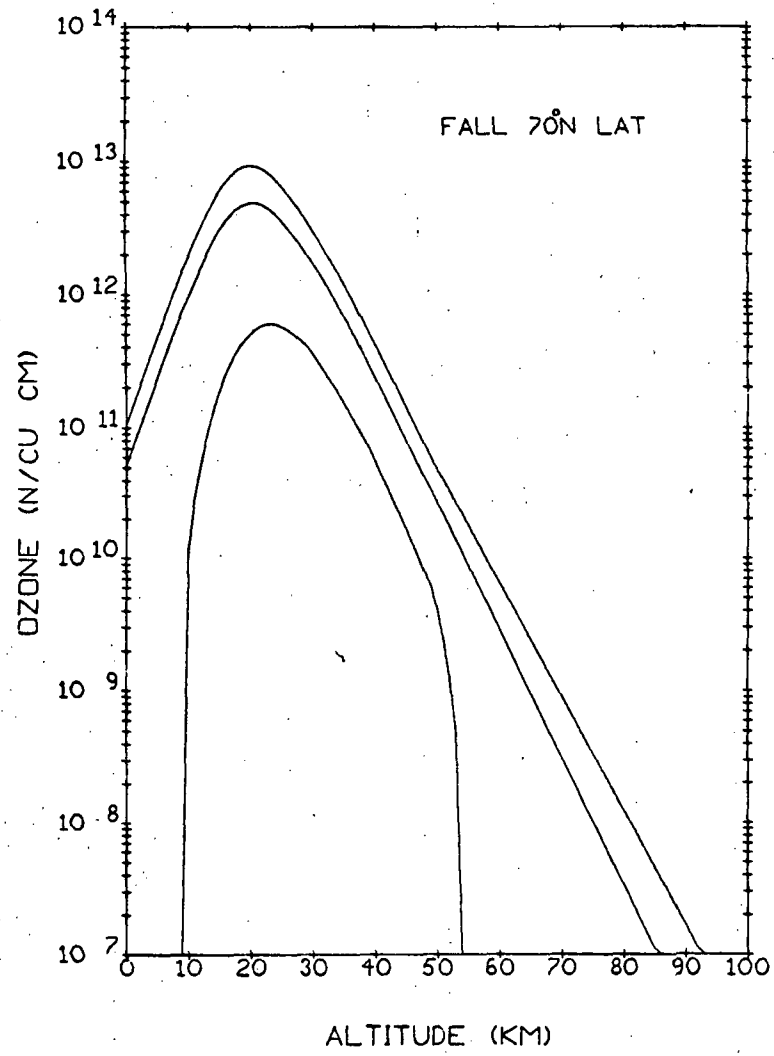

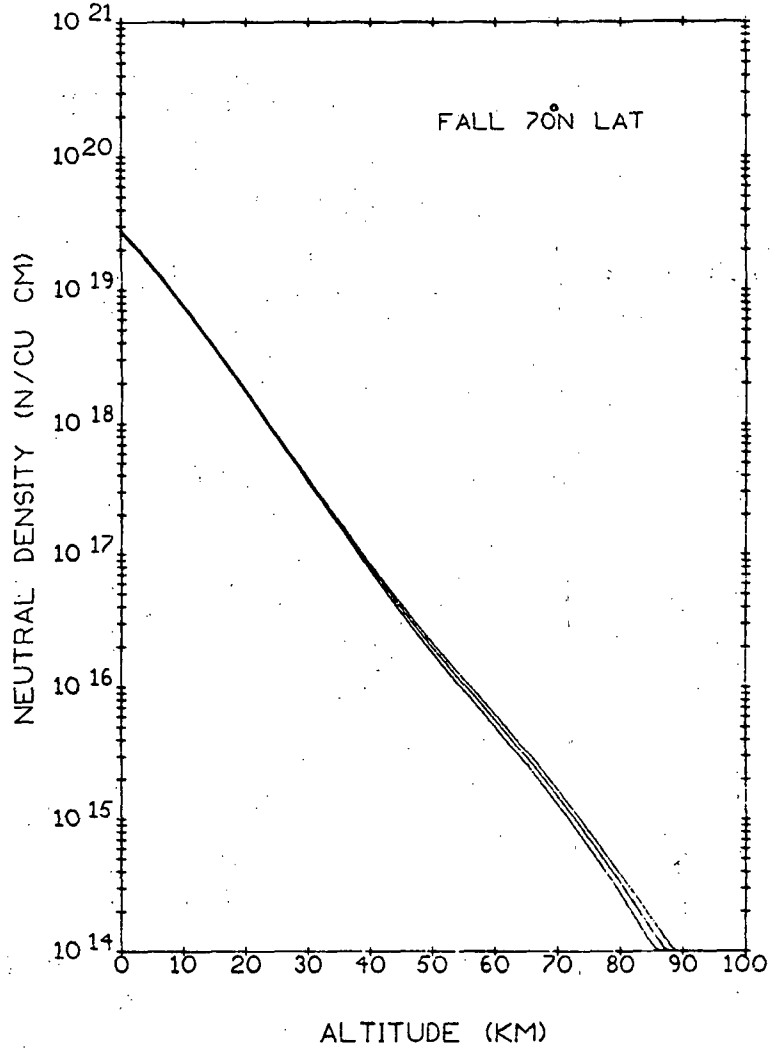

Fig. 5.1-84 Neutral and Ozone Density Profiles (Fall, 70°N. LATITUDE) for mean and ± 1σ values

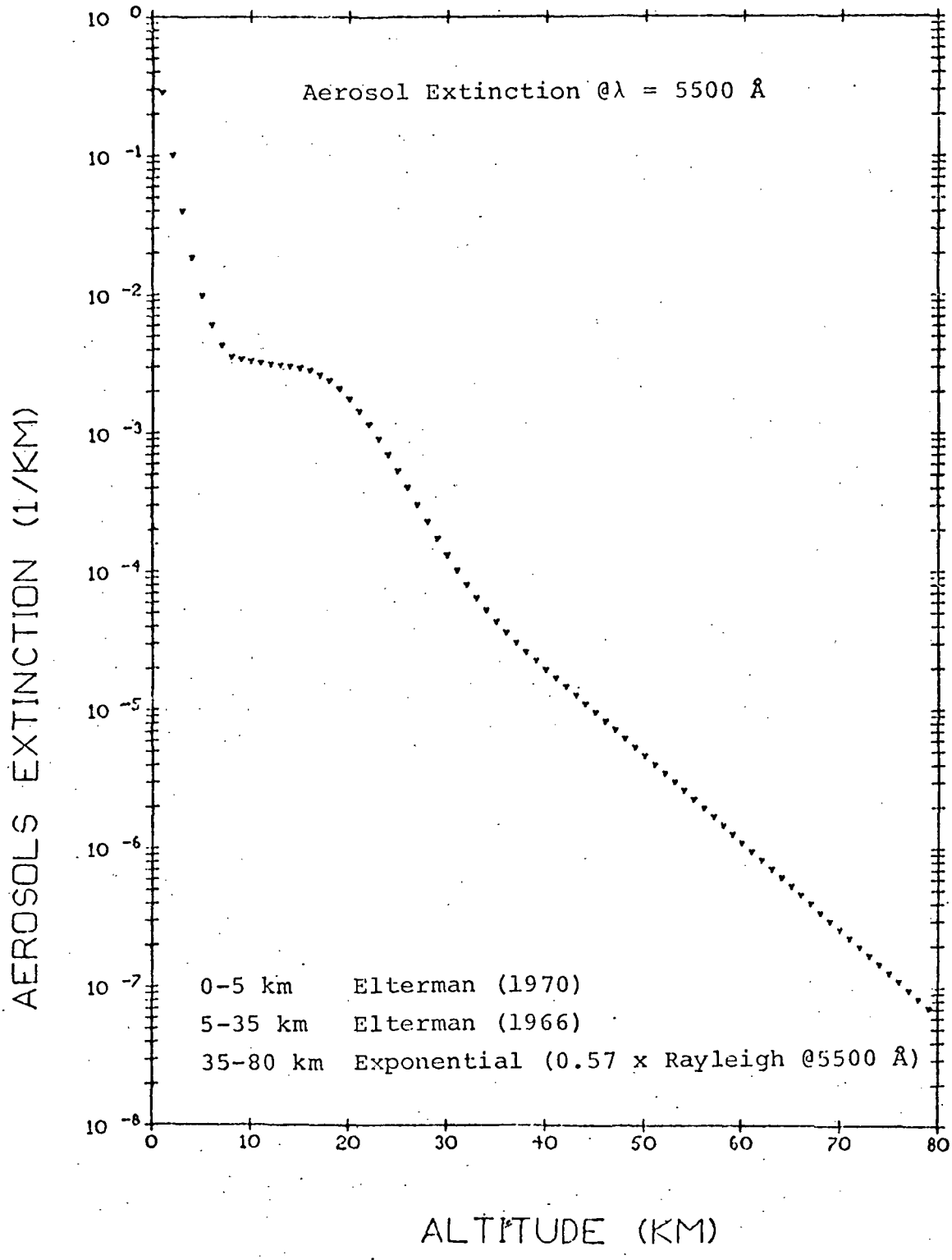

Figure 5.1-85 Aerosol Extinction Profile

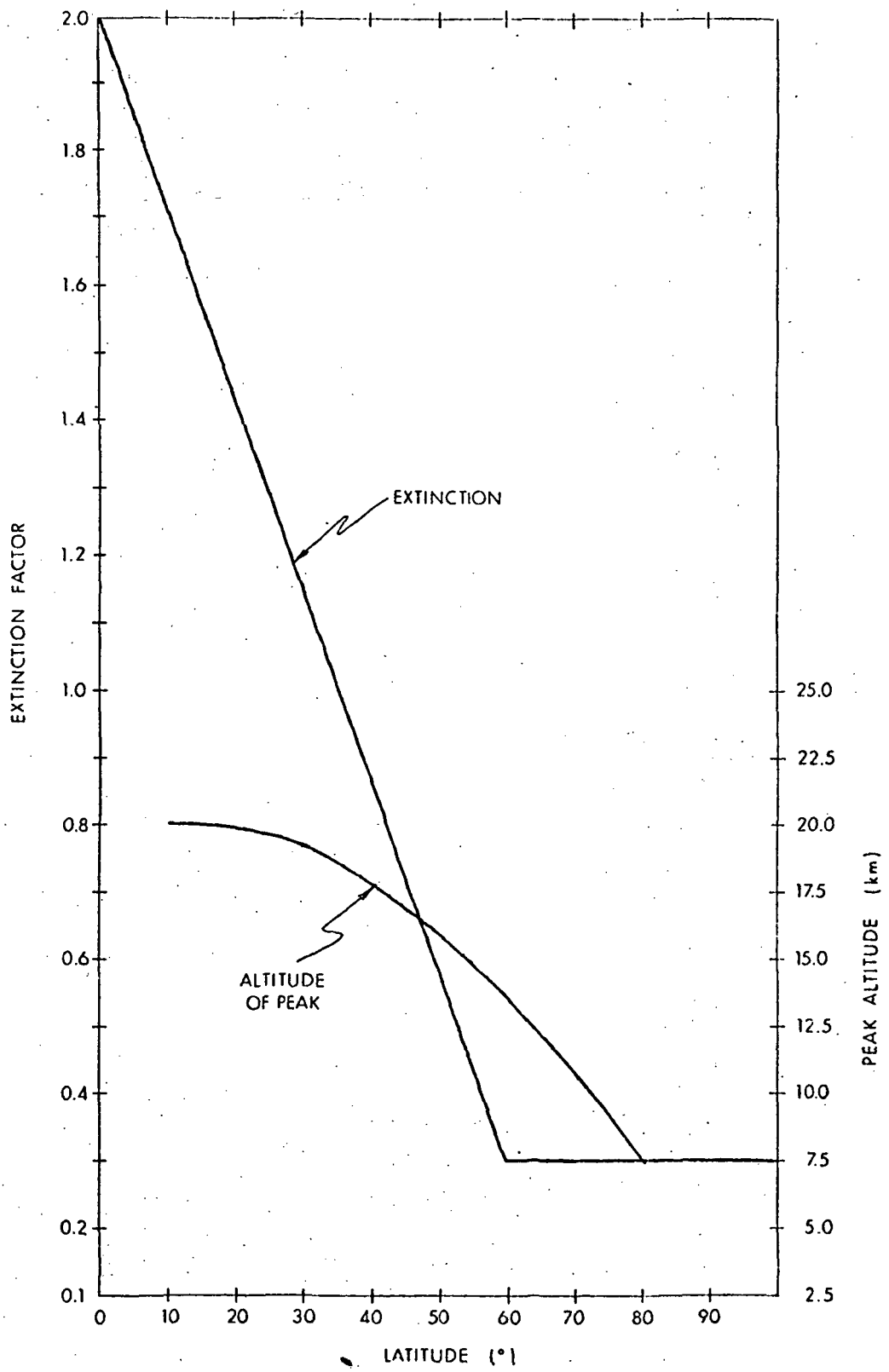

Figure 5.1-86 Stratospheric Aerosol Latitude Factors

5.2 MODELED AEROSOL FUNCTIONS

This appendix gives the analytic expressions obtained (by a multivariate regression procedure discussed in Section 3.3 for scattering phase-functions $P(\theta_i; \alpha, \lambda, n, n')$ at $\theta_i = 0^o$, 20^o, 60^o, 110^o, 164^o and 180^o, the total cross-section $\sigma_t(\alpha, \lambda, n, n')$ and either the absorption cross-section $\sigma_a(\alpha, \lambda, n, n')$ or the scattering cross-section $\sigma_s(\alpha, \lambda, n, n')$. These expressions are grouped according to the particle size ranges (0.01-0.1μ, 0.1-1.0μ, and 1.0-10μ).

In the 0.01 to 0.1μ range we have:

$$P(0^o) = \exp(-2.937E\text{-}2 + 5.234E\text{-}2\ \alpha\lambda - 4.747\ \lambda - 5.812E\text{-}2\ \alpha\lambda^2 - 3.388E\text{-}2\ \alpha^2 + 3.259\ \lambda^2 + 6.963E\text{-}2\ \alpha^2\lambda + 1.195E\text{-}1\ n^2 - 3.961E\text{-}2\ \alpha^2\lambda^2 - 3.744E\text{-}1\ n\lambda)$$

$$P(20^o) = \exp(-2.396E\text{-}1 + 4.447E\text{-}2\ \alpha\lambda - 4.687\ \lambda - 4.803E\text{-}2\ \alpha\lambda^2 - 3.229E\text{-}2\ \alpha^2 + 3.069\ \lambda^2 + 6.728E\text{-}2\ \alpha^2\lambda + 1.295E\text{-}1\ n^2 - 3.887E\text{-}2\ \alpha^2\lambda^2 - 1.451E\text{-}1\ n^2\lambda)$$

$$P(60^o) = \exp(-1.776 + 6.964E\text{-}2\ \alpha\lambda - 1.906\ \lambda - 9.225E\text{-}2\ \alpha\lambda^2 - 1.402E\text{-}2\ \alpha^2 + 1.388\ \lambda^2 + 2.051E\text{-}2\ \alpha^2\lambda + 9.914E\text{-}2\ n^2 - 2.343E\text{-}1\ n\lambda - 4.050E\text{-}3\ n\alpha^2\lambda^2)$$

$$P(110^o) = \exp(-4.482 + 4.928\ \lambda + 3.946E\text{-}2\ \alpha^2 - 3.747\ \lambda^2 - 1.013E\text{-}1\ \alpha^2\lambda - 2.372E\text{-}1\ n^2 + 6.485E\text{-}2\ \alpha^2\lambda^2 + 2.946E\text{-}1\ n\lambda + 1.534\ E\text{-}1\ n^2\lambda + 1.100E\text{-}2\ n^2\lambda^2\alpha)$$

$$P(164^{\circ}) = \exp(-6.612 - 1.685\,\alpha\lambda + 1.227E{+}1\,\lambda + 1.166\,\alpha\lambda^2 - 8.577\,\lambda^2 - 3.798E{-}1\,n^2 - 7.140E{-}3\,\alpha^2\lambda^2 + 4.126E{-}1\,n^2\lambda + 5.990E{-}1\,\alpha + 5.850E{-}3\,n\alpha^2)$$

$$P(180^{\circ}) = \exp(-6.686 - 1.711\,\alpha\lambda + 1.249E{+}1\,\lambda + 1.179\,\alpha\lambda^2 - 8.693\,\lambda^2 - 3.715E{-}1\,n^2 - 6.800E{-}3\,\alpha^2\lambda^2 + 4.027E{-}1\,n^2\lambda + 6.117E{-}1\,\alpha + 5.800E{-}3\,n\alpha^2)$$

$$\sigma_s = \exp(1.511E{+}1 - 1.779E{-}1\,\alpha\lambda + 1.189E{-}2\,n\alpha\lambda^2 + 3.959\,\lambda^2 - 1.604\,\alpha - 9.541\,n^{-1} - 1.043E{+}1\,\lambda + 2.689E{-}2\,\alpha^2)$$

$$\sigma_a = .007259 + 77.895\,n'\{(2.58(\alpha/2)^{2.35} - .79\alpha)(\lambda/.4)^{1.3}\}^{-1} \{1 + .0208\,\lambda(\alpha-2)(7-\alpha)\{|(n-1.234)|/.066\}^{-(\lambda/.4)^{.585}} - \{.1667(\alpha-2)(\alpha-4)(n/1.3)^{5.75}(.06-n')\}\{1+7.5(\lambda-.4)(\lambda-.6)\}\}$$

In the 0.1 to 1μ range we have:

$$P(0^{\circ}) = \exp(6.415E{-}1 + 2.302\,n\alpha\lambda + 1.992E{-}1\,n\lambda^2\alpha + 5.082\,n\lambda^2 + 1.841E{-}1\,\alpha^2\lambda^2 + 9.519E{-}1\,n\alpha - 1.404E{-}1\,n\alpha^2 + 9.720\,nn' - 1.533\,nn'\alpha\lambda - 1.560E{+}1\,n\lambda + 1.679E{-}1\,(n\alpha)^2 + 2.865E{-}1\,nn'(\alpha\lambda)^2 - 2.336\,\alpha\lambda^2 + 3.003\,n^2 - 1.569\,n^2\alpha + 9.547\,\lambda - 2.570E{-}1\,n\alpha^2\lambda + 3.095E{-}1\,n^2\alpha\lambda - 6.137\,nn'\lambda^2 - 9.415E{-}1\,nn')$$

$$P(20^{\circ}) = \exp(-3.668 - 9.038E{-}3\,(n\alpha)^2 + 2.348E{-}1\,n\alpha\lambda - 3.470E{-}3\,(n\alpha)^2 + 2.986\,n^{-1} - 8.749\,\alpha^2\lambda + 4.534E{-}2\,(n\alpha\lambda)^2 - 4.293\,\lambda^2 + 1.473E{-}1\,n\alpha - 3.111E{-}1\,(n\lambda)^2\alpha + 7.388\,n\lambda^2 + 1.166E{+}1\,\lambda n'n^2 - 2.672E{+}1\,n'\lambda - 1.666E{-}1\,n'(\lambda n\alpha)^2 - 2.416\,(n\lambda)^2 + 2.292E{-}1\,n'(\lambda\alpha)^2 + 8.322E{-}2\,\alpha + 2.412E{+}1\,\lambda^2 n' + 1.235E{-}1\,n'n^2\alpha - 9.250(\lambda n)^2 n')$$

$$P(60^{\circ}) = \exp(-5.344 - 1.100E\text{-}2\, n^2\alpha + 3.714\, n^3\lambda + 1.168E\text{-}1\, n^{(\alpha\lambda)} - 2.729E\text{-}2\, (n\alpha\lambda)^2 - 4.697\, n^2\lambda + 2.213E\text{-}1\, (n)^{n^2}\alpha + 2.068E+1\, n'\lambda/\alpha - 1.715\, \lambda^n + 2.363\, n\alpha\lambda - 1.429\, n^2\alpha\lambda - 4.949E\text{-}1\, n^{n^3} + 3.470\, n^2/\{(1+5n')\alpha\} - 2.016E+1\, n^2\alpha^{-3} + 5.328E\text{-}1\, (n')^{.5} + 9.547\, n^2\alpha^{-2} - 3.757E\text{-}1\, n^2(1+5n')^{-2} - 2.719\, n' + 1.058E\text{-}1 \exp(-10\, n'\alpha) - 4.793E\text{-}3\, (n\alpha)^2\lambda - 2.276E\text{-}1\, n^2 + 2.996E+1\, (n'\lambda/\alpha)^2 + 4.266E\text{-}2\, n^2(1+5n')^{-1})$$

$$P(110^{\circ}) = \exp(4.751 - 4.099\, n^2\alpha\lambda - 8.511\, n + 3.866\, \alpha\lambda + 9.015E\text{-}2\, (n\alpha\lambda)^2 - 3.342E+1\, n' + 8.520\, \lambda n'\alpha - 3.278E\text{-}12\, n\alpha^{12}/\lambda + 6.585E\text{-}1\, \alpha^2\lambda + 2.164\, n^2\alpha - 5.439\, \alpha\lambda^2 - 3.228E+1\, n\lambda^2 - 9.783E\text{-}2\, nn'(\alpha\lambda)^2 - 7.001E\text{-}1\, (\alpha\lambda)^2 + 4.486E+1\, n\lambda + 3.729E+1\, \lambda^2 - 1.196E\text{-}1\, n\alpha^2 - 5.399E+1\, \lambda + 1.259E+1\, nn' - 3.436\, nn'\alpha\lambda^2 - 5.098\, n'(n\alpha)^2 + 1.143E+2\, \lambda(n')^2 + 6.578\, n\alpha\lambda^2 - 2.303\, n\alpha - 2.545E+1\, \alpha(n'\lambda)^2)$$

$$P(164^{\circ}) = \exp(2.472E+1 + 7.151E\text{-}1\, (\alpha-2)(\alpha-4)(\lambda-.4)(\lambda/.6)^{-1.08} + 2.546\, (n-1.35)|\alpha-7|(n/1.4)^{-3.88} - 4.058E+1\, nn' + 7.673E\text{-}1\, nn'(\alpha\lambda)^2 - 1.056\, \alpha^2 - 5.101E+1\, \lambda^2 - 1.843\, \alpha^2\lambda + 7.514E\text{-}1\, nn'\alpha^2\lambda - 1.471\, \alpha + 1.769E+1\, \alpha\lambda - 7.267E\text{-}1\, (1+50\, n')/\alpha + 2.921\, n\alpha^2 + 5.524E\text{-}1\, \lambda(n\alpha)^2 + 7.434\, (n\alpha\lambda)^2 - 1.854\, n(\alpha\lambda)^2 - 2.226\, \lambda/(1+50\, n') + 4.555E+2\, n(n')^2 + 3.278E+1\, n\lambda^2 - 7.245\, \alpha\lambda n^2 - 1.336E+1\, n\alpha - 1.815E+1\, n + 9.171\, n^2\alpha - 1.379\, (n\alpha)^2 + 1.352\, (\alpha\lambda)^2 + 2.562E\text{-}1\, \alpha(n\lambda)^2)$$

$$P(180^{\circ}) = \exp(1.340 + 5.193E\text{-}2\, \ln\{(\alpha-2/\lambda)^{(2/n^2)}(1+50\, n')^{-1/\lambda}\} - 2.180E+1\, n - 1.070\, nn'(\alpha\lambda)^2 - 1.092E\text{-}1\, (n\alpha)^2 - 1.379E\text{-}1\, n\alpha^2 + 3.134E\text{-}1\, \lambda\alpha^2 + 3.732\, nn'\alpha\lambda^2 + 5.469E\text{-}1\, (n\alpha\lambda)^2$$

$$- 3.927E+1\ nn' + 8.804\ n'\alpha\lambda - 8.464\ n^2\alpha\lambda + 1.187E+1\ \lambda^2$$
$$- 3.627E+1\ n\lambda^2 + 3.261\ \alpha\lambda - 1.255\ (\alpha\lambda)^2 + 1.495E-1$$
$$n'(n\alpha)^2 + 1.427\ n' + 3.153\ n\alpha\lambda^2 + 3.236E-1\ (\alpha-2/\lambda)^2$$
$$+ 4.157E+1\ n(n')^2 + 3.377\ \alpha\lambda^2 + 8.490\ n\lambda + 3.580\ \alpha n^2$$
$$- 5.849E+1\ \lambda)$$

$$\sigma_T = \exp\{2.3\{\lambda \sum_{j=0}^{4} A_j\alpha^j - \exp(\sum_{j=0}^{4} B_j\alpha^j)\}\{1+.036\alpha(n-1.4)\}^{-1}\}$$

where $A_0 = -8.896\ E-1$ $\quad A_1 = 1.288$

$A_2 = -5.316\ E-1$ $\quad A_3 = 6.727\ E-2$

$A_4 = -2.855\ E-3$

$B_0 = 1.948$ $\quad B_1 = 1.159\ E-1$

$B_2 = -2.551\ E-2$ $\quad B_3 = 2.491\ E-3$

$B_4 = -8.889\ E-5$

$$\sigma_a = -1.518E-3 + FX\ \{1 +12.5(\lambda-.6)(\lambda-.8)(.215 + DX + .5(n-1.3)$$
$$CX + (n-1.3)(n-1.4)\ BX\} + 25(\lambda-.4)(\lambda-.8)(.25-.03(7-\alpha)$$
$$- .7(n-1.3)) - 12.5(\lambda-.4)(\lambda-.6)(.47 - .032(7-\alpha) - .7(n-1.3)$$
$$EX - .2(n-1.3)(\alpha-4)(\alpha-2)/15)\}(1.61(\alpha/2)^{2.32} - .61)^{-1}$$

where $FX = 1.372\ (n'/.02)^{AX}$

$AX = .585 + 2.5(\lambda-.4)(.138 - .0163(\alpha-2)) + .0644(\alpha-2)$

$CX = |(\alpha-2)|\alpha^{-\alpha/8}$

$BX = \alpha^2\ CX/8$

$DX = |(n-1.3)|(n/1.4)^{-10.21}$

$EX = |(\alpha-7)|\alpha/12$

In the 1 to 10μ range we have:

$$P(0^{o}) = \exp(8.457 - 1.357\,\alpha + 6.576\,\lambda + 9.534E{+}1\,n' - 6.383\,\alpha^{2} - 2.374E{+}4\,(n')^{2} - 8.454\,\lambda^{2} - 1.596E{+}1\,\lambda n'\alpha^{2} + 2.076E{+}3\,\lambda(n'\alpha)^{2} - 7.498E{-}1\,\alpha\lambda^{2} - 1.161E{+}1\,(\alpha\lambda)^{2} + 9.258\,n\alpha^{2} + 8.853\,\lambda(n\alpha)^{2} - 3.303\,(n\alpha)^{2} - 3.573E{+}1\,nn' + 1.211E{+}2\,\lambda n'\alpha + 1.375\,\lambda n'n^{2} - 6.465E{+}1\,\lambda\alpha(n')^{2} - 3.425E{+}3\,\lambda n(n')^{2} - 9.796E{+}1\,(\lambda\alpha n')^{2} - 3.656E{+}1\,\alpha n' + 1.262\,n^{2} + 5.706E{+}1\,n\alpha(\lambda n')^{2} + 4.348\,n'\alpha^{2} + 5.356E{+}2\,\alpha(\lambda n')^{2} + 2.365E{+}3\,n(\lambda n')^{2} + 1.036E{+}3\,\lambda(n\alpha n')^{2} - 7.508\,n'(\lambda n\alpha)^{2} - 6.004\,(n\alpha\lambda)^{2} + 1.221\,\alpha\lambda + 1.677E{+}1\,n(\alpha\lambda)^{2} - 2.909E{+}3\,n\lambda(\alpha n')^{2} - 1.155E{+}4\,(nn')^{2} + 3.359E{+}4\,n(n')^{2} - 1.199E{+}2\,\alpha n'\lambda^{2} + 9.740\,n\lambda^{2} + 1.736E{-}3\,nn'\alpha^{2} - 1.195E{+}1\,n\lambda - 2.378E{+}1\,n\lambda\alpha^{2} + 1.717E{+}1\,\lambda\alpha^{2} + 2.148\,nn'(\alpha\lambda)^{2})$$

$$P(20^{o}) = \exp(-6.551 - 5.221E{+}1\,nn' - 6.469E{+}2\,n\alpha\lambda(n')^{2} + 6.866E{+}1\,n(\alpha\lambda n')^{2} + 3.327E{+}2\,nn'(\alpha\lambda)^{2} - 8.600E{+}4\,(nn')^{2} + 3.156E{+}3\,\alpha\lambda n' - 1.193E{+}2\,n'(\alpha n\lambda)^{2} - 2.377E{+}2\,n'(\alpha\lambda)^{2} + 7.901/n + 2.525\,n^{2} - 5.764E{+}1\,n' - 1.585E{+}3\,\lambda^{2} + 5.231E{+}2\,\lambda n^{2} + 9.972E{-}2\,(n\alpha)^{2} - 1.822E{+}1\,\lambda\alpha^{2} + 2.823E{+}1\,(\alpha\lambda)^{2} - 8.998\,\lambda(n\alpha)^{2} + 2.520E{+}1\,n\lambda\alpha^{2} + 2.304E{+}3\,n\lambda^{2} - 8.260E{+}2\,(n\alpha)^{2} - 1.941E{-}2\,n\alpha^{2} + 2.430E{+}5\,n(n')^{2} - 1.689E{+}5\,(n')^{2} - 3.983E{+}1\,n'\lambda^{2} - 1.402E{+}1\,n\alpha n' + 9.910\,\alpha(n\lambda)^{2} + 1.379E{+}1\,(n\alpha\lambda)^{2} - 4.360\,n\alpha\lambda + 1.000E{+}3\,\lambda - 3.913E{+}1\,n(\alpha\lambda)^{2} - 1.560\,n\alpha + 1.587E{+}3\,\lambda\alpha n'n^{2} - 4.434E{+}3\,nn'\alpha\lambda - 1.463E{+}3\,n\lambda - 1.903E{+}1\,n\alpha\lambda^{2} + 1.422E{+}1\,\alpha\lambda + 6.747\,\alpha n'n^{2})$$

$$P(60^{\circ}) = \exp(-2.065E+2 - 1.942E+3\ n' + 1.348E-1\ \alpha\lambda n^2 + 3.908\ (\alpha\lambda)^2 + 5.889E+2\ \alpha n'\lambda^2 - 2.647E+1\ (n')^2 + 3.968E+2\ \alpha(\lambda n')^2 + 1.789E+2\ n^{-1} + 3.761E+1\ n^2 + 3.453\ \alpha\lambda n' + 2.123E+2\ n\lambda - 3.399E+2\ n\alpha(n')^2 - 2.754E+1\ \alpha n^2 - 1.225E-2\ \alpha^2 - 8.192E+1\ \lambda n^2 - 1.354E+2\ \lambda + 5.389\ \lambda\alpha^2 - 4.490E+2\ n\alpha(\lambda n')^2 - 1.054E+3\ n'n^2 + 7.534E+1\ n\alpha + 1.800\ (n\alpha\lambda)^2 + 1.274E+3\ (nn')^2 + 3.513E+2\ \alpha n'(n\lambda)^2 - 2.453\ n'(\lambda n\alpha)^2 + 3.865E+1\ n(\alpha\lambda n')^2 + 1.520\ \alpha n'n^2 - 4.816\ \alpha\lambda^2 - 5.124E+1\ \alpha - 5.320\ n(\alpha\lambda)^2 + 2.786\ E+3\ nn' - 9.080E+2\ nn'\alpha\lambda^2 - 5.976E+2\ \lambda(nn')^2 + 1.106E+1\ (\alpha nn')^2 - 7.938\ n\lambda\alpha^2 + 2.916\ \lambda(n\alpha)^2 + 3.193\ n\alpha\lambda^2)$$

$$P(110^{\circ}) = \exp(2.558E+2 + 5.608E+1\ \alpha(n\lambda)^2 + 1.412E+4\ n' - 2.236E+4\ nn' + 8.719E+3\ n'n^2 + 9.753E+3\ (n')^2 - 2.447E+2/n - 4.403E+1\ n^2 - 1.587E+2\ n\alpha\lambda^2 + 2.201\ \alpha(nn')^2 - 1.782E+1\ \alpha\lambda - 1.075\ \alpha n^2 - 1.409E+4\ n'\lambda^2 + 1.440E+4\ \lambda(nn')^2 + 1.113E+2\ \alpha\lambda^2 - 4.937E+3\ \lambda n'n^2 - 1.838E+1\ \alpha n'n^2 - 2.539E+2\ \alpha\lambda n' + 7.063\ nn'\lambda + 1.474E+4\ nn'\lambda^2 - 3.422E+3\ n'(n\lambda)^2 + 1.419\ (\alpha nn')^2 - 5.161\ \lambda n'\alpha^2 - 5.923\ n'(n\alpha)^2 - 4.134E-3\ (n\alpha)^2 - 2.600E+3\ \alpha n'\lambda^2 - 5.367E-1\ \lambda(\alpha nn')^2 - 3.557E+3\ (nn')^2 - 2.589E+4\ n\lambda(n')^2 - 7.125\ \alpha\lambda n^2 + 2.336E+1\ n\alpha\lambda + 6.357E-3\ \alpha + 1.431\ n\alpha + 5.565E+3\ (\lambda n')^2 - 1.618E+3\ \alpha n'(n\lambda)^2 + 4.130E+3\ \alpha nn'\lambda^2 + 1.549E+2\ \alpha\lambda n'n^2 + 1.079\ nn'\alpha^2)$$

$$P(164^{\circ}) = \exp(2.689E+2 + 1.618E+4\ n' + 8.978E-2\ \alpha(n\lambda)^2 - 2.602E+2/n - 2.900E+4\ (n')^2 - 3.299E+3\ \alpha n'\lambda^2 - 3.436E+4\ \alpha n(n'\lambda)^2 + 6.153E+3\ n'n^2 - 2.036E+4\ nn' - 4.332\ n'(\alpha\lambda)^2 + 1.493\ \alpha\lambda + 1.669E+4\ (nn')^2 + 2.443E-2\ n\alpha^2 + 2.274E+3\ nn'\alpha\lambda^2$$

$$+ 4.619E+1\ \alpha n'(n\lambda)^2 - 5.877E+1\ n\alpha - 1.269\ E-1\ (\alpha\lambda)^2$$
$$- 1.429\ \lambda n^2 - 9.151E+3\ \alpha\lambda(nn')^2 + 7.659E+1\ \lambda(\alpha n')^2$$
$$- 1.297E+3\ \alpha\lambda n'n^2 - 8.899E+4\ n(\lambda n')^2 - 5.749E+3\ \lambda n'$$
$$- 4.313E+1\ n^2 - 8.996E+3\ \alpha(nn')^2 + 2.629E+3\ \alpha\lambda n'$$
$$+ 1.798E+4\ \alpha(n')^2 - 1.885E+3\ \alpha n' + 1.339E+3\ \alpha nn'$$
$$- 1.059E+5\ \alpha\lambda(n')^2 + 5.003E+4\ \alpha(\lambda n')^2 + 8.643E+4\ \alpha\lambda(n')^2$$
$$+ 4.100E+1\ \alpha + 1.062E+1\ \alpha n^2 + 4.159E+3\ \lambda nn' + 1.225E+5$$
$$(\lambda n')^2)$$

$$P(180^\circ) = \exp(1.759E+2 + 1.334E+2\ n' + 3.142E+4\ \alpha\lambda(nn')^2 - 2.056E+3$$
$$\lambda(\alpha n')^2 - 3.018E+1\ n^2 - 1.074E+3\ \lambda n'\alpha^2 + 4.978E+3\ (n')^2$$
$$+ 5.162E+2\ \alpha\lambda n'n^2 - 2.187E+1\ (\alpha\lambda)^2 - 1.068E+1\ (n\alpha\lambda)^2$$
$$+ 6.399E+2\ nn'\lambda\alpha^2 + 2.924E+5\ n\alpha\lambda(n')^2 + 4.239E+1\ \lambda n'(n\alpha)^2$$
$$+ 1.371E+2\ \alpha\lambda + 6.876\ \alpha\lambda n^2 - 9.354E+4\ \alpha(n')^2 + 5.932E+2$$
$$\lambda(nn')^2 - 6.690E+2\ nn'(\alpha\lambda)^2 - 1.508E+3\ \lambda n' - 1.663E+2/n$$
$$- 1.945E+2\ n\alpha\lambda - 6.090\ n'\alpha n^2 + 1.004E+3\ n'(\alpha\lambda)^2 - 9.508E+3$$
$$\alpha(nn')^2 + 8.024E+4\ \alpha n(n')^2 + 1.169E+3\ n'\lambda^2 + 1.629E+5$$
$$n\alpha(\lambda n')^2 - 2.267E+5\ \alpha(\lambda n')^2 + 3.438E+5\ \alpha\lambda(n')^2 + 3.062E+1$$
$$n(\alpha\lambda)^2 - 3.701E+2\ \alpha n'(n\lambda)^2 + 1.939E+2\ n'\alpha^2 - 1.748E+2\ nn'\alpha$$
$$- 8.555E+1\ n'(n\alpha)^2 + 1.618E+3\ n\lambda(\alpha n')^2)$$

$$\sigma_T = \exp(-1.498E+2 - 1.020E+1\ \alpha + 3.730\ \alpha^2 + 8.622E+2\ n\lambda$$
$$- 2.967E+2\ n'(\alpha\lambda)^2 + 1.548\ (n\alpha)^2 - 5.009\ n\alpha^2 - 2.402E+2$$
$$n'(n\alpha\lambda)^2 - 4.761E+2\ n'\lambda\alpha^2 + 1.484E+2\ (n\lambda)^2 + 4.393E+1\ n'\alpha^2$$
$$+ 3.614E+2\ \lambda^2 - 6.377E+2\ \lambda + 2.016E+1\ n^2 - 4.702E+2\ n\lambda^2$$
$$- 2.852\ \lambda n^2 + 5.636E+2\ nn'(\alpha\lambda)^2 + 1.086E+1\ n'(n\alpha)^2$$
$$- 3.906E+1\ nn'\alpha^2 + 1.545E+2/n - 1.476E+2\ \lambda n'(n\alpha)^2$$

$$+ 5.258E+2\ nn'\lambda\alpha^2 + 8.306\ n\alpha + 3.476E+3\ \alpha n'(n\lambda)^2$$
$$- 5.662E+2\ \alpha\lambda n'n^2 - 1.181\ \alpha\lambda^2 + 3.284\ \alpha(n\lambda)^2 + 1.239E+1\ \alpha\lambda$$
$$- 1.423E+1\ n\alpha\lambda + 5.827E+3\ \alpha n'\lambda^2 - 9.137E+3\ nn'\alpha\lambda^2$$
$$+ 9.489E+2\ nn'\alpha\lambda - 8.068E+1\ n'\alpha + 3.763E+1\ n'n^2$$
$$- 1.981E+3\ \lambda n' + 2.406E+3\ nn'\lambda - 1.159E-1\ \lambda(n\alpha)^2$$
$$- 6.879E-1\ (\alpha\lambda)^2 + 8.424E-1\ n\lambda\alpha^2 - 7.663E+2\ \lambda n'n^2$$
$$+ 8.076E+1\ (\lambda n')^2)$$

$$\sigma_a = 1.195E-3 - 2.507E-4\ \alpha + 1.087E+3\ n' + 3.008E+3\ \alpha(n')^2$$
$$+ 2.789E-5\ \alpha^2 - 2.547E+2\ (\alpha n')^2 + 1.191E+1\ n'\alpha^2 - 1.091E+4$$
$$(n')^2 - 1.940E+2\ \alpha n' - 6.414E-4\ \lambda n^2 + 4.157E+3\ \lambda(n')^2$$
$$- 3.911E+2\ \lambda n' - 6.612E+2\ nn' + 1.380\ n\alpha n' - 4.455E+1$$
$$\alpha(\lambda n')^2 + 2.947E-2\ n'(\alpha\lambda)^2 - 2.262\ n'(n\alpha)^2 - 2.715E+2$$
$$n'(n\lambda)^2 + 2.815\ \alpha n'\lambda^2 + 1.853E+2\ n'n^2 + 2.201E+1\ \lambda(\alpha n')^2$$
$$+ 2.609E+2\ nn'\lambda + 5.240\ nn'\alpha^2 - 3.396E+2\ n'\lambda^2 - 2.056E+2$$
$$\alpha\lambda(n')^2 - 5.251\ n\lambda(\alpha n')^2 + 1.317E+3\ n(n')^2 - 1.977E+3$$
$$n\lambda(n')^2$$

5.3 MULTIPLE SCATTERING CODE C.K.W.

5.3.1 Introduction

Because it has not been given more than a cursory description in print, and because its speed makes the model concept potentially valuable to the scientific community as a whole, and because it is the model to be adapted for all our future work we present in this and the following subsections a brief description of the multiple scattering code C.K.W. in its present state of development.

For the program C.K.W. the atmosphere is modeled as a set of concentric spherical layers, each characterized by extinction coefficients for Rayleigh scatterers, aerosols, and ozone, and by an index of refraction, all assumed constant within a given layer. The acceptability of assuming constancy depends on the thickness of layers. Typically, we use 50 to 60 layers of 2 km thickness, and the calculated horizon profile is insensitive to further refinement.

The calculations naturally fall into a hierarchy of increasing difficulty. The simplest problem is single scattering, which is handled in great detail, with the full spherical geometry, exact integrations including refraction, detailed phase function data with polarization, and a Feugelson law for albedo (Kondratyev , 1969). The next case includes some nearly forward scattering on the path from the sun to the site of one major scatter into the detector line of sight. This is done with almost as much refinement as single scattering. The next, more difficult case includes some nearly forward scattering on the path to the detector. For this case, an approximate estimation of coupling between scan lines is introduced. The final case is full multiple scattering, which requires some additional approximations for the geometry. The following sections detail the methods and approximations used to treat each of the successively more difficult cases.

5.3.2 Single Scattering

Basic Geometry

The modeling of the horizon profile requires that we first of all establish a coordinate frame in which all the vectors that occur in the calculation can be expressed unambiguously. For this purpose, we affix a coordinate frame to the detector. The (z) axis is along the local vertical at the detector, the (x) axis is perpendicular to the plane of scan, and the (y) axis lies in the scan plane, pointing roughly in the direction from which the detector seeks light (Figure 5.3-1). This choice of coordinate frame is arbitrary, but convenient on several counts. First, this coordinate frame is independent of the detector altitude. This is useful because one of the applications for horizon profile modeling is in spacecraft navigation, for which the altitude may be unknown. Second, the zenith and azimuth of the sun can be measured directly from the craft, so the vector representing the input sunlight can be defined directly for this frame. Third, in the special but common case that the sun lies in the scan plane, the (x) axis is perpendicular to the scattering plane, so there is a coincidence in regard to the naming of polarization states: both the usual geometric convention and the convention used in scattering theory agree that polarization along (x) corresponds to the same direction in Poincare space.

A second geometric requirement to be met is the specification of the earth and its atmosphere. Thus we introduce the height of the detector, (HDET), and the earth radius (RE), shown in Figure 5.3-1. Also we fix the radii to the bottoms of each of the layers, R_L:

$$R_L = RE + L\ KM \tag{5.3-1}$$

where (KM) is the single-layer thickness and (L) is an integer member of set (NL) defining the number of layers. Next we precalculate geometric quantities that will be used over and over in the horizon profile calculation.

These are the scan path increments through the layers, DX_L for L = 0(1)NL. For the scan path tangent to the earth, the path increment through layer (L) is

$$DX_L \approx \sqrt{2\ RE\ KM}\ (\sqrt{L+1} - \sqrt{L}) \qquad (5.3\text{-}2)$$

Almost these same path increments occur on all the other scan paths too, and so the numbers are saved for use on all the scan paths.

The final item of geometric information to be handled is the location of any cloud. We denote the altitude of a cloud by the variable SOLIDTOP in Figure 5.3-1. If the cloud happens to fall between layers, then it occludes a portion of some layer. This portion is called SOLIDTIP. In the subsequent calculations, any path increment through the partially occluded layer should be adjusted from the appropriate DX_L above. The adjustment factor is

$$SQ = \frac{\sqrt{KM} - \sqrt{SOLIDTIP}}{\sqrt{KM}} \qquad (5.3\text{-}3)$$

Average Attenuation

The attenuation within a path increment (DD) is one of the factors that determine how much radiation is scattered to the detector from (DD). At any point in (DD), the radiation arriving from the sun is damped by passage through a total optical depth denoted by (TTS). Similarly, the radiation scattering to the detector is further attenuated by passage through a total optical depth denoted by (TTD). Thus at a point, the attenuation is

$$e^{-TTS\ -\ TTD}$$

A full contribution to the output from the whole increment (DD) is of the form

$$\int_{DD} e^{-TTS - TTD} \sum_i \sigma_i \, p_i(\psi) \, dx$$

where σ_i and $p_i(\psi)$ are the scattering coefficient and phase function for the i^{th} constituent, and (dx) is a differential increment of length. Assuming constancy of all extinction coefficients in the layer (or at least their local ratios), we split the contribution into two factors:

$$\frac{1}{DD} \int_{DD} e^{-TTS - TTD} \, dx$$

and

$$\sum \sigma_i \, p_i(\psi) \, DD$$

The first factor is the average attenuation, and its evaluation is the subject of this subsection.

To perform the integration in the average attenuation we introduce a change of variables:

$$dx = J \, d(TTS + TTD) \tag{5.3-4}$$

Here (J) is the Jacobian of the transformation,

$$J = 1/(d(TTS + TTD)/dx) \tag{5.3-5}$$

We assume the derivative in (J) can be approximated by

$$\Delta(TTS + TTD)/DD$$

Thus we reexpress the average attenuation by

$$\frac{1}{\Delta(TTS + TTD)} \int_{DD} e^{-TTS - TTD} \, d(TTS + TTD)$$

This can be evaluated immediately as

$$DAMP = -\Delta e^{-TTS - TTD}/\Delta(TTS + TTD) \qquad (5.3\text{-}6)$$

The above trivial result is modified slightly by the inclusion of the phenomenon of refraction. The basic principle involved is that light travels not exactly in a straight line, but rather in a slightly curved line. At a point on the line, we let (n) denote the refractive index, (r) the distance to the earth center, and $\sin\theta$ the angle of incidence on a surface parallel to the earth. The curved line is described by

$$(n)(r)\sin\theta = \text{constant} \qquad (5.3\text{-}7)$$

where the constant is the nominal tangent height R_H of the scan line. Referring to the greatly exaggerated Figure 5.3-2, we see that where the unrefracted path would be intersecting the bottom of layer (L) at an angle whose sine is R_H/R_L, the refracted path is passing through a somewhat lower point and at a lesser angle. Let (y) be the nominal scan line, and (z) be the perpendicular displacement of the true path from the unrefracted one. Then the true angle is

$$\theta \approx \arcsin\left(\frac{R_H}{R_L}\right) - \arcsin\left(\frac{dz}{dy}\frac{R_H}{R_L}\right) \qquad (5.3\text{-}8)$$

We also have

$$\theta \approx \arcsin\left(\frac{R_H}{R_L}\ \text{RINDEX}_L\right) \qquad (5.3\text{-}9)$$

where RINDEX_L is the refractive index in layer (L). The derivative dz/dy can be isolated and simplified by appropriate series expansions. It is used in the code to develop the true path as a function of the nominal path, and so to provide the correct boundaries, etc., at which to evaluate (TTS) and (TTD).

Scattering Factor

Besides the average attenuation discussed in the preceding subsection, the contribution to the output from a path increment (DD) depends on the previously introduced scattering factor of the form

$$\sum_i \sigma_i\ p_i(\psi)\ \text{DD}$$

Since the atmosphere being modeled contains both Rayleigh and aerosol scatterers, there are two σ's and p's that have to be evaluated. In both cases, the (σ) is the local extinction coefficient, denoted as (RDTAU) for Rayleigh scatterers, and (ADTAU) for aerosol scatterers. Also in both cases, the polarized output (if any exists) can be expected to be linearly polarized in the plane perpendicular to the scattering plane, so that in both cases two polarization parameters of the phase function constitute sufficient input data. Finally, for both cases it is essential to specify the scattering angle (ψ). Actually, this is done by specifying the cosine of that angle (COPSI). We simply form the dot product of a vector representing the input sunlight and a vector representing the light traveling to the detector.

In the case of Rayleigh scattering, the phase function can be calculated analytically within the program. Ideally, the two polarization parameters are $6/16\pi$ and $6\ \text{COPSI}^2/16\pi$. Sometimes it is appropriate to modify this

slightly. But for aerosol scattering, the situation is much more complicated. At present, we read in the phase function for selected values of (COPSI), usually 46 in number, and interpolate on the basis of (COPSI).

Albedo

Scattering from the atmosphere is only one of two possible mechanisms whereby light reaches the detector. There is also scattering from the surface of the earth, or some cloud layer above it. The total fraction of the incident light scattered from such a surface is its albedo. The simplest, and most commonly used angular dependence for surface scattering is the well-known Lambert law:

$$\text{radiance out} = (\text{irradiance in})\ \text{ALBEDO}\ \frac{\mu_o}{\pi} \qquad (5.3\text{-}10)$$

where (μ_o) is the cosine of the incidence angle. It is known that natural surfaces usually are not Lambertian. Nevertheless, better models are only occasionally available. Our model has incorporated a Feugelson law for single scattering from clouds, but otherwise uses Lambert's Law. The Feugelson law for the approximate albedo (A_c) of a cloud of optical thickness (τ) is given by

$$A_c = 1 - \frac{7}{12}\ \frac{2\mu_o + 1}{1 + (1-\frac{c_1}{3})\tau} + \frac{7}{24}\ \frac{c_1\,\mu_o/3 + c_2(3\mu_o - 1)/8\ \{1 - 2\mu_o(c_1/3 - 1)\}}{1 + (1-\frac{c_1}{3})\tau} \qquad (5.3\text{-}11)$$

where $c_1 = 2.48$ and $c_2 = 3.70$.

5.3.3 Forward Scattering on the Sun Path

After single scattering, the next less simple mechanism whereby light reaches the detector includes one or more nearly forward scatters on the path from the sun to the primary scatter. This subsection details the way

in which this contribution is handled by adapting the methods already described in the preceding sections. That is, we discuss modifications to the geometry, the average attenuation, the scattering fraction, and the albedo calculation.

Geometry

The geometry used to calculate the contribution to the output that includes some forward scattering on the sun path differs from the single scattering geometry only in that what is assumed to propagate along the sun path is a stream rather than a plane wave. The explicit definition for the stream (Whitney, 1972) is radiance integrated against a $\cos^2$ weighting function. There occurs in the calculation a factor (FPRL), which is part of the stream definition, and factors (NORM) and (ESTPRL) that relate to the inversion of streams back to radiances at the output. This inversion is discussed in detail in a subsequent subsection on full multiple scattering.

Attenuation

The notion of a stream rather than a plane wave propagating along the sun path modifies the average attenuation in two ways. First, since forward scatters do not remove anything from the stream, forward scatters have to be excluded from the optical depths along the sun path. This is done by modifying the optical depths by a factor of (1-PHS), where (PHS) is a combination of streamlike phase function integrals that represents forward scattering from a stream into itself. The construction of (PHS) is detailed in the above mentioned paper. The modified optical depth from the sun is (MSTTS). With that replacement, the analog of (DAMP), the average attenuation, is

$$\text{MSDAMP} = -\Delta e^{-\text{MSTTS}} - \text{TTD}/\Delta(\text{MSTTS} + \text{TTD}) \qquad (5.3\text{-}12)$$

The second modification required is that we exclude from (MSDAMP) the case in which absolutely no scatters occur on the sun path, since we have already counted single scattering. This done by decreasing (MSDAMP) by that part of the average that represents just single scattering. Thus we put

$$\text{MSDAMP} = \text{MSDAMP} - \text{DAMP}$$

Scattering

The scattering factor is also affected by the inclusion of forward scattering along the sun path. Where before it was appropriate to have a plane-wave transformation, or phase function $p(\psi)$, it is now appropriate to have a stream transformation, or (PHS), evaluated for the nominal scattering angle (ψ). For both Rayleigh and aerosol scatterers, these PHS's are entered as data, precalculated at the angles that occur in the dodecahedral arrangement of streams introduced in (Whitney, 1972) namely 0°, 180°, 63° and 117°. An interpolation routine then obtains the (PHS) for the desired angle (ψ).

Albedo

The final modifications required to accommodate a stream on the sun path concern the albedo calculations. For a Lambertian surface, a discretized version of Lambert's law is required. The continuous law involves the factor $|\cos(\theta)|/\pi$, where

$$\pi = \int_{\text{hemisphere}} |\cos(\theta)| \, d\Omega$$

That is, the law is formulated to say that uniform radiance input provides uniform radiance output, just scaled down by the albedo. The discrete law must be formulated to say the same thing, but with the integral replaced by a sum over the dodecahedron angles, and the $|\cos(\theta)|$ replaced by averages of $|\cos(\theta)|$ with quadratic weighting functions. The normalization for all the averages is

$$\int_{\text{hemisphere}} (\hat{p}\cdot\hat{k})^2 \, d\Omega = 2\pi/3 \tag{5.3-13}$$

The actual averages are as follows: for 0^o,

$$\langle|\cos(\theta)|\rangle = \frac{3}{2\pi}\int_{\text{hemisphere}} (\hat{z}\cdot\hat{k})^3 \, d\Omega = 3/4 \tag{5.3-14}$$

for 63^o,

$$\begin{aligned}
\langle|\cos(\theta)|\rangle &= \frac{3}{2\pi}\int_{\text{hemisphere}} (\hat{z}\cdot\hat{k})\left[\left(\frac{\hat{z}}{\sqrt{5}} + \frac{2\hat{x}}{\sqrt{5}}\right)\cdot\hat{k}\right]^2 d\Omega \\
&= \frac{3}{2\pi}\int_{\text{hemisphere}} \frac{(\hat{z}\cdot\hat{k})^3}{5} + 4\hat{z}\cdot\hat{k}\frac{(\hat{x}\cdot\hat{k})^2}{5} \, d\Omega \\
&= \frac{3}{2\pi}\int_{\text{hemisphere}} \frac{(\hat{z}\cdot\hat{k})^3}{5} + \frac{2}{5}(\hat{z}\cdot\hat{k} - \hat{z}\cdot\hat{k}^3) \, d\Omega \\
&= 9/20
\end{aligned} \tag{5.3-15}$$

Thus the sum analogous to the integral is

$$3/4 + \sum_{5\ \text{terms}} 9/20 \equiv 3 \qquad (5.3\text{-}16)$$

Thus for the discrete case, the (π) in Lambert's law is replaced by a 3.

5.3.4 Forward Scattering on the Detector Path

We suppose now that the photons sustain one or more nearly forward scatters on their path from the primary scatter to the detector. This case is slightly more complicated than that discussed in the preceding section, and so entails a few more modifications, in regard to geometry, average attenuation, and scattering factor.

Geometry

The major geometric consideration with forward scattering on the detector path is the possibility of transfer of radiation from one line of sight to another at a slightly different angle. To handle this, we formulate for each line of sight an approximation for the probability that forward scattering ultimately contributes to that particular line of sight. This probability varies from zero for the uppermost line of sight to unity for a scan tangent to the earth. In between, the probability is approximated as follows: the difficult feature requiring approximation is that where forward scatters are concerned we must think not of contributions from a path increment, but rather from whole three dimensional regions. That is, if subsequent forward scatters are allowed, contributions to a given scan line come not from the line, but from a region surrounding the line. We formulate the above mentioned probability function as a line integral of the form

$$PM_m = \int e^{-\tau'}\, d\tau' \qquad (5.3\text{-}17)$$

where the path over which the integral is done traverses, roughly, the optical region that can, with no mechanism other than subsequent forward scattering, contribute to the m^{th} scan line. The path proceeds from the detector, through atmospheric layers down to and including the m^{th} one, and then out again. The $\Delta\tau'$ to be associated with any particular layer has to be approximated in a rather gross way, because with the curvature of the earth, the different propagation directions in a stream can traverse drastically different optical depths. We begin by formulating $\Delta\tau'$ in such a way that if the whole atmosphere were condensed in one uniform layer (whose geometric thickness would therefore be the atmospheric scale height), that layer would have the optical depth tangent through itself:

$$\Delta\tau' = \text{EXTINCTION } \sqrt{2\ \text{RE}\ \text{SH}} \tag{5.3-18}$$

Thus for a layer of thickness KM, we put

$$\Delta\tau' = \text{EXTINCTION } \sqrt{2\ \text{RE}\ \text{KM}}\ \sqrt{\text{KM}/\text{SH}} \tag{5.3-19}$$

This formulation guarantees that for very small (KM), (τ') converges to a well-defined function of the tangent height associated with (PM) and is insensitive to the number and geometric thickness of layers that happen to be used in the atmospheric model. Finally, we must consider the effect of the scattering phase function. Clearly in the case of extreme forward scattering, the contributing region that $\Delta\tau'$ represents should shrink to zero; that is, forward scattering becomes ineffective for transfer from one line of sight to another. We represent this volume effect by modifying $\Delta\tau'$ to $\Delta\tau'\,(1\text{-PHS})^3$.

Attenuation

The attenuation for contributions to the output that will undergo one or more forward scatters on the detector path is modified in several ways. First, the attenuation on the detector path is modified by a factor (1-PHS)

to omit forward scattering just as the attenuation along the sun path was. The modified optical depth on the detector path is (MSTTD), so that at each point the attenuation is

$$e^{-MSTTS - MSTTD}$$

Second, as we have already counted single scattering and forward scattering on the sun path, we have to subtract the portion of the function representing those events: $e^{-MSTTD-TTD}$. Third, and novel to the case where there are to be subsequent forward scatters, there is no one unique and readily identified path over which this function should be evaluated and averaged. Recall that instead of contributions from a path increment, we are considering contributions from a spatial region. Instead of attempting to average the attenuation over a region, we simply leave it as a point function, evaluated at representative points (e.g. the tangent points of scan lines directed to the bottom of each atmospheric layer).

Scattering

The absence of a particular path to integrate over is again evident in the scattering factor, for no particular path length (DD) appears. Instead, (DD) is replaced by a standard length for subsequent forward scattering, which is just the $\sqrt{2\ RE\ KM}\ \sqrt{KM/SH}$ previously introduced in connection with the PM's.

5.3.5 Full Multiple Scattering

The final and most complicated mechanism whereby light reaches the horizon profile detector involves two or more scatters that cannot be classified as nearly forward. This section discusses the application of a method that handles these events, and also incidentally provides some additional information concerning the other mechanisms already discussed. The method is basically that introduced in Whitney, 1972. In that paper, the integro-differential equation of radiative transfer is discretized as a set of twelve coupled differential equations for streams. For symmetry the streams are arranged pointing to the faces of a regular dodecahedron.

Geometry

The geometry of the horizon scan situation is modified slightly to achieve a speedy application of the method without significant loss of accuracy. Specifically, thicker layers are used (usually 20 km), and they are imagined to be flat until the final step, where curvature is introduced as a correction. Because the layers are flat, the introduction of a cloud is simplified; the analog of

$$SQ = \frac{\sqrt{KM} - \sqrt{SOLIDTIP}}{\sqrt{KM}} \qquad (5.3\text{-}20)$$

becomes simply

$$\frac{KM - SOLIDTIP}{KM}$$

Also because the layers are flat, the original continuous equation of radiative transfer can be expressed with inverse cosines of incidence angles. In the discrete case, these are all replaced by inverses of cosines averaged with quadratic weighting functions; that is, inverses of the values 3/4 and 9/20 previously derived in connection with the discrete analog of Lambert's Law.

Attenuation

The attenuation of contributions to the output is calculated in much the same way as it was in the preceding section. All optical depths are scaled by a factor of the form (1-PHS), in order to eliminate forward scattering from the calculation. Then the integrals are done exactly. The general form of the integral required is

$$\int e^{\tau_1/c_0} \frac{d\tau_1}{c_1} e^{\frac{\tau_2-\tau_1}{c_1}} \frac{d\tau_2}{c_2} e^{\frac{\tau_3-\tau_2}{c_2}} \cdots$$

where τ_1, τ_2, τ_3... are the optical depths at which the first, second, third ... scatters occur, and c_0, c_1, c_2 ... are the cosines for the stream traveling from the sun, from the first scatter, from the second scatter, ... The various τ's are constrained so that each of the exponentials is less than unity. The constraints are handled by a tree structure, or set of nested do-loops, that governs the calculations. The program first chooses the layer for the first interaction (L1), then the inclination for the scattered stream (P1), then its direction (Q1), and then the layer for the second scatter (L2), and so on. If the first inclination (P1) is upward (downward) the second layer (L2) is required not to be below (above) the first layer (L1).

In the code, the multiple attenuation integral is not done all at once, but in pieces; since the τ_3 integral is done in a loop which is within the loop that does the τ_2 integral, and which is in turn inside the loop that does the τ_1 integral. As an example, the τ_1 integral is just

$$e^{\tau_1 (1/c_0 - 1/c_1)} \frac{d\tau_1}{c_1}$$

Because it has been isolated from the functions of τ_2, it is no longer true that the exponential is necessarily less than unity; it may as well be greater. However, when all the required integrals are multiplied together, the result is less than unity, as is physically required.

A small novelty is required to handle the case where two or more scatters occur in sequence within the same layer. The problem for that layer is then a micro version of the problem for the atmosphere as a whole. We could handle it the same as the full atmosphere, breaking the layer into smaller sub layers. But such a procedure would be time consuming, so we attempt to get an approximate answer without resorting to it. For the case where all the scatters from (i) through (i+n) occur in one layer, we approximate the required integral with the product of the τ_i, τ_{i+1}, ... τ_{i+n} integrals, but with an important modification. Consider the case where

all the inclinations are the same. The problem then reduces to a familiar one in Poisson statistics, and the required integral is known to be simply the above product, but divided by (n!). Thus we induce that generally a factor of (1/n!) should be incorporated.

Scattering

We come now to the actual scattering operations for full multiple scattering. These are constructed by a procedure whose goal is to minimize the storage space and computational burden required. The main source of difficulty to be overcome is the inclusion of polarization, requiring four Stokes parameters s_0, s_1, s_2, s_3 to characterize a stream and, in general, sixteen parameters to characterize a stream transformation. The input stream transformations are provided for streams in the Z-X plane separated by the dodecahedral scattering angles 0°, 63°, 117°, and 180°. For these cases, symmetry reduces the sixteen parameters to far fewer, so that storage space is minimized. In particular, for 63° and 117°, there are only eight parameters: one 2x2 matrix operating on $\begin{pmatrix} s_0 \\ s_1 \end{pmatrix}$ and another operating on $\begin{pmatrix} s_2 \\ s_3 \end{pmatrix}$; and for 0° and 180° there are only three parameters, only two of which are independent. For any particular scatter that occurs in the code, the stream transformation is synthesized by combining the minimal stored information with appropriate rotations of the plane-polarization parameters $\begin{pmatrix} s_1 \\ s_2 \end{pmatrix}$. That is, first a 2x2 rotation is applied so that the polarization state in the nominal scattering plane acquires the name 1. Then the appropriate stream transformation is applied. Then another 2x2 rotation is applied to restore the polarization state in the nominal scattering plane to its final correct name.

Program Control

In the case of multiple scattering it is not enough simply to attenuate and scatter. The program must be prevented from expending excessive effort on negligible contributions to the output, and must be prevented from reconsidering the contributions it has more accurately calculated in the single scattering part of the code. These goals are accomplished by several tests in the code.

Of primary importance is the so-called twig pruning, or (ENDTEST) for multiple scattering. This test compares the current contribution to the output with a numerical standard. The standard is based on the output that was obtained from single scattering, on the total number of terms of the particular scattering order that are left to consider, and on an input parameter expressing the programmer's judgement of how accurate he wants to be. If the test is failed, it is judged unprofitable to further pursue that particular branch of the multiple scattering tree. Were it not for this test, the program would run for outlandishly long times without appreciably changing the output.

Inversion of Streams

The final step in creating the horizon profile is to take the streams $S_{\hat{p}}$ provided by the multiple scattering code, and invert them to estimates of physical radiance, $S(\hat{k})$. This problem is the inverse of that involved in forming the stream $S_{\hat{p}}$ from the radiance $S(\hat{k})$. Since forming $S_{\hat{p}}$ is analogous to performing an integral transform on $S(\hat{k})$, it follows that estimating $S(\hat{k})$ is analogous to inverting the transform. Because we do the original transform only for power n = 2, and not arbitrary (n), it is possible to invert only approximately. This section discusses what is thought to be an optimum procedure for approximating $S(\hat{k})$.

We begin by considering a simple case where $S(\hat{k})$ is assumed to be equal to $S(-\hat{k})$, and to have the form

$$S(\hat{k}) = \sum^{6 \text{ terms}} S(\hat{p}) \left(\frac{5}{4}(\hat{p}\cdot\hat{k})^2 - \frac{1}{4} \right) \qquad (5.3\text{-}21)$$

with this form, it can readily be verified that

$$S_{\hat{p}} = \frac{2\pi}{3} \left[S(\hat{p}) + \sum^{5 \text{ terms}} \frac{1}{5} S(\hat{p}') \right] \qquad (5.3\text{-}22)$$

Referring to Whitney, 1972, we see that the inverse of this relationship would be

$$S(\hat{p}) = \frac{3}{2\pi}\left[\frac{9}{8} S_{\hat{p}} - \sum^{5\ \text{terms}} \frac{1}{8} S_{\hat{p}'}\right] \qquad (5.3\text{-}23)$$

As in Whitney, 1972, we have to separate forward-traveling from backward traveling radiation by extending these simple six term relationships to twelve terms. For the numbers used, the analogous inverse is

$$S(+\hat{p}) = \frac{3}{\pi}\left[S_{+\hat{p}} + \frac{1}{8} S_{-\hat{p}} - \frac{3}{20} \sum^{5\ \text{terms}} S_{+\hat{p}'} + \frac{1}{40} \sum^{5\ \text{terms}} S_{-\hat{p}'}\right] \qquad (5.3\text{-}24)$$

This is the basic relationship currently used to invert the array of output streams in the code.

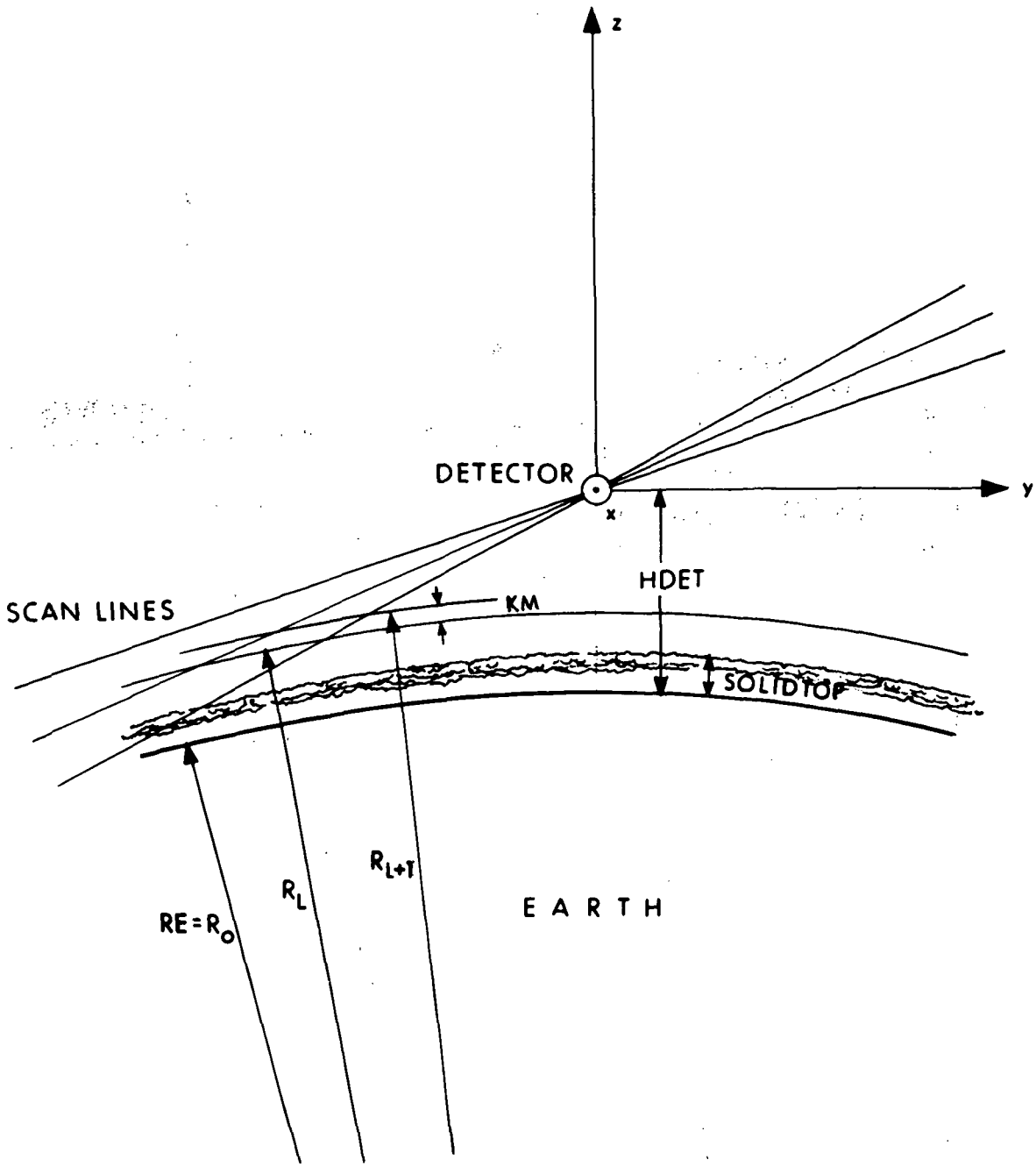

Fig. 5.3-1 Horizon Scan Geometry

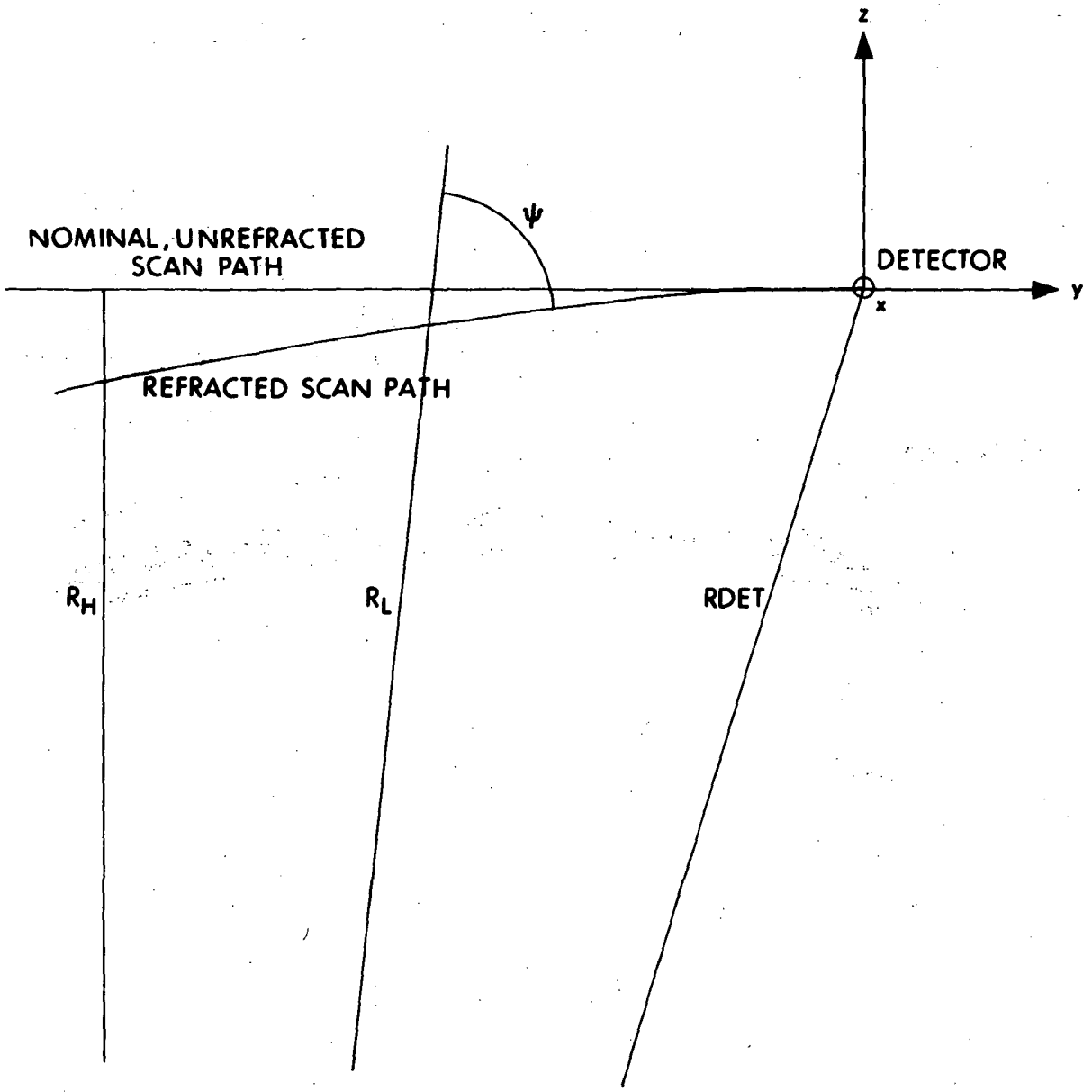

Fig. 5.3-2 Effect of Refraction

REFERENCES

SECTION 5

1) Groves, G.V., "Seasonal and Latitudinal Models of Atmospheric Temperature, Pressure, and Density", Air Force Surveys in Geophysics, No. 218, May, 1970.

2) Kondratyev, K.Ya., "Radiation in the Atmosphere", 386-399, Academic Press, New York and London, 1969.

3) Malchow, H.L., "Standard Models of Atmospheric Constituents and Radiative Phenomena for Inversion Simulation", MIT Aeronomy Program Internal Report No. AER 7-1, January, 1971.

4) Salah, J.E., "On the Nature and Distribution of Stratospheric Aerosols", Private Communications, February, 1971.

5) Valley, S.L., Handbook of Geophysics and Space Environment, McGraw-Hill, New York, 1965.

6) Whitney, C.K., "Implications of a Quadratic Stream Definition in Radiative Transfer Theory", J. Atm. Sci., 29, 1520-1530, 1972.

7) Wu, M.F., "Ozone Distribution and Variability", MIT Aeronomy Program Internal Report No. AER 1-2, August, 1970.